

UNIVERSIDAD DE LOS ANDES

DOCTORAL THESIS

---

# Non-equilibrium Strongly Interacting Quantum Many-Body Systems

---

*Author:*

Óscar Leonardo Acevedo Pabón

*Advisor:*

Luis Quiroga Puello

*A thesis submitted in fulfilment of the requirements  
for the degree of Doctor in Science-Physics  
in the research group:*

Grupo de Física de la Materia Condensada, FIMACO  
Departamento de Física



Bogotá D.C., Colombia  
September 2015

# Declaration of Authorship

I, Óscar Leonardo Acevedo Pabón, declare that this thesis titled, ‘Non-equilibrium Strongly Interacting Quantum Many-Body Systems’ and the work presented in it are my own. I confirm that:

- This work was done wholly or mainly while in candidature for a research degree at this University.
- Where any part of this thesis has previously been submitted for a degree or any other qualification at this University or any other institution, this has been clearly stated.
- Where I have consulted the published work of others, this is always clearly attributed.
- Where I have quoted from the work of others, the source is always given. With the exception of such quotations, this thesis is entirely my own work.
- I have acknowledged all main sources of help.
- Where the thesis is based on work done by myself jointly with others, I have made clear exactly what was done by others and what I have contributed myself.

Signed:

---

Date:

---

*“It is not in the nature of things for any one man to make a sudden violent discovery; science goes step by step, and every man depends on the work of his predecessors. When you hear of a sudden unexpected discovery —a bolt from the blue, as it were— you can always be sure that it has grown up by the influence of one man on another, and it is this mutual influence which makes the enormous possibility of scientific advance. Scientists are not dependent on the ideas of a single man, but on the combined wisdom of thousands of men, all thinking of the same problem, and each doing his little bit to add to the great structure of knowledge which is gradually being erected.”*

Ernest Rutherford

UNIVERSIDAD DE LOS ANDES

## *Abstract*

Facultad de Ciencias  
Departamento de Física

Doctor in Science-Physics

### **Non-equilibrium Strongly Interacting Quantum Many-Body Systems**

by Óscar Leonardo Acevedo Pabón

This thesis dissertation concerns the quantum dynamics of strongly interacting many-body systems under several non-equilibrium scenarios. Mimicking many real life settings, and especially some current major experiments, during most of this work we will deal with symmetrical interactions among the components, which will generate collective dynamics with high degree of correlation. The focus all throughout this work has been on the possibility of accurately control the quantum properties of the system, even at the microscopic level, by cleverly choosing macroscopic manipulation protocols. Our main results can be summarized as follows. First, we thoroughly investigate the irreversible defect formation when the Dicke model, a paradigmatic light-matter system, is made to cross its quantum phase transition (QPT). Furthermore, we have been able to explain this dynamical QPT for totally connected lattices, which had remained unresolved by well-known theories like the Kibble-Zurek mechanism. This was done by means of a broad encompassing critical function theory. Also, by going beyond semi-adiabatic evolutions, we have discovered that the dynamical QPT of the Dicke model has an intermediate regime where non-equilibrium processes provide a huge enhancing of quantum properties, far beyond the capabilities of equilibrium, quasi-equilibrium, or sudden quench schemes. Finally, we provided theoretical evidence and insights for the possibilities of quantum magnetism interactions in current high precision alkaline earth atom lattice clocks.

# *Acknowledgements*

There are many people I wish to thank for their support during this long and hard journey of my doctoral studies. First, I want to thank my mentors, starting with my advisor, Professor Luis Quiroga, whose dedication and guidance were crucial. Together with Prof. Quiroga, I thank for their contribution with such a great research experience to the other two co-authors of most of the published papers of my thesis: Professors Ferney Rodríguez and Neil Johnson. They were virtually co-advisors of my doctorate. I also must mention another great research supervisor: Professor Ana María Rey, who has offered me her unique expertise and amazing opportunities to venture into the field of theoretical AMO physics during my internship. The list of mentors would not be complete without acknowledging Professors Favio Cala and Ilia Mikhailov. Both were thesis advisors during my respective undergraduate studies. They have greatly influenced my path into Physics, the former since my high school years providing interesting philosophical insights, and the latter by initiating me in the discipline of scientific investigation. Prof. Mikhailov was also who rightly advised me to pursue my doctoral degree with Prof. Quiroga.

Besides the senior guides noted above, I also had the luck to share this academic adventure with great fellows. In the closest ‘academic family’, I mention my ‘siblings’: the older one Felipe Caycedo; and the younger and contemporary ones, Ángela Viviana Gómez, Adriana de Mendoza, Larry Castrillón, and Fernando Gómez. Another wonderful fellow has been Nathaly Marín. We shared discussions about broader scientific topics which are very useful to have some perspective. I also thank other colleague-friends: Mario Zapata, César Herreño, Nicolás Avilán, Juan Carlos Salazar, among others at ‘la casa capilla’ of Universidad de los Andes; together with Johannes Schachenmayer and Alexander Pikovski, etc., at JILA.

Finally, I want to thank the great support I received from Universidad de los Andes, especially the help from the Departamento de Fí academic and administrative staff, and the Facultad de Ciencias’ financial coverage of several research projects, including the ‘Proyectos Semilla’. I also express my gratitude for the hospitality received at JILA during my research internship. Another special mention is deserved by Colciencias, which with its Convocatoria 511 covered most of my academic expenses and sustenance during my doctoral studies.

# Contents

|   |             |
|---|-------------|
| <b>Declaration of Authorship</b>  | <b>i</b>    |
| <b>Abstract</b>   | <b>iii</b>  |
| <b>Acknowledgements</b>   | <b>iv</b>   |
| <b>Contents</b>   | <b>iv</b>   |
| <b>List of Figures</b>  | <b>vii</b>  |
| <b>Abbreviations</b>  | <b>viii</b> |
| <br>  |             |
| <b>Introduction</b>   | <b>1</b>    |
| <b>1 The Dicke Model and its dynamical QPT</b>                              | <b>4</b>    |
| 1.1 Introduction . . . . .  | 4           |
| 1.2 The Dicke Model . . . . .   | 5           |
| 1.3 Realization of the DM in cold atom settings . . . . .                   | 8           |
| 1.4 Quantum Hysteresis in the Dicke Model under a LZS cycle . . . . .       | 10          |
| 1.4.1 Theoretical background . . . . .                                      | 10          |
| 1.4.2 The Dicke Model under a LZS cycle . . . . .                           | 11          |
| 1.5 Conclusion . . . . .  | 13          |
| <b>2 Near-adiabatic dynamical scaling universality across a QPT</b>         | <b>14</b>   |
| 2.1 Introduction . . . . .  | 14          |
| 2.2 Models and methods . . . . .  | 17          |
| 2.3 The Kibble-Zurek Mechanism . . . . .                                    | 19          |
| 2.4 Final dynamical scaling collapse after the critical threshold . . . . . | 20          |
| 2.5 Continuous critical function scaling theory . . . . .                   | 23          |
| 2.6 The partition of the equilibrium universality class . . . . .           | 25          |
| 2.7 Conclusion . . . . .  | 26          |
| <b>3 The full dynamical QPT regime of Dicke Model</b>                       | <b>28</b>   |
| 3.1 Introduction . . . . .  | 28          |
| 3.2 Theoretical framework . . . . .   | 30          |
| 3.2.1 The open Dicke Model . . . . .  | 30          |

|          |   |            |
|----------|---|------------|
| 3.2.2    | Witnesses of quantum properties . . . . .   | 31         |
| 3.3      | Giant light-matter entanglement . . . . .   | 32         |
| 3.4      | Dynamical symmetry breaking . . . . .   | 33         |
| 3.5      | Enhancement of subsystem quantum properties . . . . .   | 34         |
| 3.6      | Non linear effective interactions . . . . .   | 36         |
| 3.7      | Matter-light quasi-probability behavior . . . . .   | 38         |
| 3.8      | Robustness against noise of non-equilibrium quantum correlations . . . . .                            | 39         |
| 3.8.1    | Robustness of light-matter entanglement . . . . .   | 39         |
| 3.8.2    | Robustness of subsystem results . . . . .   | 40         |
| 3.9      | Scaling of results . . . . .  | 42         |
| 3.10     | Conclusion . . . . .  | 43         |
| <b>4</b> | <b>Collective <math>SU(2)</math> quantum magnetism in a <math>^{87}\text{Sr}</math> lattice clock</b> | <b>45</b>  |
| 4.1      | Introduction . . . . .  | 45         |
| 4.2      | Derivation of the Hamiltonian . . . . .   | 48         |
| 4.3      | Mean field equations . . . . .  | 53         |
| 4.4      | Bloch vector dynamics . . . . .   | 54         |
| 4.4.1    | Total Bloch vector dynamics . . . . .   | 56         |
| 4.4.2    | Relative Bloch vector dynamics . . . . .  | 57         |
| 4.4.3    | Equal angle conditions . . . . .  | 59         |
| 4.5      | Dynamics of atom-atom correlations . . . . .  | 60         |
| 4.5.1    | Atom-atom correlations . . . . .  | 60         |
| 4.5.2    | Quantum Correlations . . . . .  | 62         |
| 4.6      | Conclusion . . . . .  | 63         |
|          | <b>Outlook</b>  | <b>65</b>  |
|          | <b>Bibliography</b>   | <b>78</b>  |
|          | <b>A Published and submitted papers. Chapter 1</b>  | <b>79</b>  |
|          | <b>B Published and submitted papers. Chapter 2</b>  | <b>83</b>  |
|          | <b>C Published and submitted papers. Chapter 3(a)</b>   | <b>95</b>  |
|          | <b>D Published and submitted papers. Chapter 3(b)</b>   | <b>103</b> |
|          | <b>E Support of Chapter 4</b>   | <b>118</b> |
| E.1      | Deduction of mean field equation . . . . .  | 118        |
| E.2      | Computing expectation values up to second order . . . . .   | 120        |
| E.3      | The squeezing parameter . . . . .   | 120        |
| E.4      | Expectation values: from macro to micro . . . . .   | 121        |
| E.5      | Failure of MFE: correlations and concurrence . . . . .  | 122        |
| E.6      | Analytic solutions under zero magnetic field . . . . .  | 123        |

# List of Figures

|     |  |    |
|-----|--|----|
| 1.1 | DM energy spectrum and experimental realization of the Dicke Model . . . . .           | 7  |
| 1.2 | Quantum Hysteresis in the Dicke Model . . . . .  | 11 |
| 1.3 | Non-reversibility seen in field Wigner Functions . . . . .                             | 12 |
| 2.1 | Dynamical crossing of the critical threshold in the DM . . . . .                       | 16 |
| 2.2 | Spin network schemes and illustration of the KZM . . . . .                             | 18 |
| 2.3 | Dynamical crossing of the critical threshold in the DM . . . . .                       | 21 |
| 2.4 | Dynamical critical exponent of final heating in the Kibble-Zurek regime . . . . .      | 22 |
| 2.5 | Universal critical functions . . . . .   | 24 |
| 2.6 | Continuous QPT dynamical universality . . . . .  | 25 |
| 3.1 | Giant dynamical magnification of light-matter entanglement . . . . .                   | 33 |
| 3.2 | Matter subsystem's QPT dynamic profiles . . . . .                                      | 35 |
| 3.3 | Field subsystem's QPT dynamic profiles . . . . .                                       | 37 |
| 3.4 | Matter subsystem states in the Bloch sphere . . . . .                                  | 38 |
| 3.5 | Field subsystem states in phase space . . . . .  | 39 |
| 3.6 | Open system effects on light-matter entanglement . . . . .                             | 41 |
| 3.7 | Open system effects on subsystem quantum properties . . . . .                          | 42 |
| 3.8 | Scaling in the dynamical regime . . . . .  | 43 |
| 4.1 | Different degrees of freedom in a $^{87}\text{Sr}$ optical lattice clock. . . . .      | 46 |
| 4.2 | Different collision strengths according to exchange symmetry . . . . .                 | 49 |
| 4.3 | Mean field Bloch vectors . . . . .   | 54 |
| 4.4 | Pancake $p(N)$ and dynamics of total Bloch vector under spectator conditions . . . . . | 55 |
| 4.5 | Relative Bloch vector dynamics under spectator conditions . . . . .                    | 58 |
| 4.6 | Bloch vector dynamics: both spins rotated . . . . .                                    | 60 |
| 4.7 | Total and relative correlations between atoms . . . . .                                | 61 |
| 4.8 | Wootters concurrence and squeezing under mostly equal angle conditions . . . . .       | 62 |
| 4.9 | Wootters concurrence under spectator conditions . . . . .                              | 63 |

# Abbreviations

|             |  |
|-------------|--|
| <b>AEA</b>  | <b>A</b> lkaline <b>E</b> arth <b>A</b> toms                 |
| <b>AV</b>   | <b>A</b> nnealing <b>V</b> elocity                           |
| <b>AWF</b>  | <b>A</b> garwal- <b>W</b> igner <b>F</b> unction             |
| <b>BEC</b>  | <b>B</b> ose- <b>E</b> instein <b>C</b> ondensate            |
| <b>GDM</b>  | <b>G</b> eneralized <b>D</b> icke <b>M</b> anifold           |
| <b>KZM</b>  | <b>K</b> ibble- <b>Z</b> urek <b>M</b> echanism              |
| <b>LMGM</b> | <b>L</b> ipkin- <b>M</b> eshkov- <b>G</b> lick <b>M</b> odel |
| <b>LZ</b>   | <b>L</b> andau- <b>Z</b> ener                                |
| <b>LZS</b>  | <b>L</b> andau- <b>Z</b> ener- <b>S</b> tückelberg           |
| <b>MFE</b>  | <b>M</b> ean <b>F</b> ield <b>E</b> quations                 |
| <b>OP</b>   | <b>O</b> rders <b>P</b> arameter                             |
| <b>QED</b>  | <b>Q</b> uantum <b>E</b> lectro <b>D</b> ynamics             |
| <b>QCP</b>  | <b>Q</b> uantum <b>C</b> ritical <b>P</b> oint               |
| <b>QPT</b>  | <b>Q</b> uantum <b>P</b> hase <b>T</b> ransition             |
| <b>TFIM</b> | <b>T</b> ransverse <b>F</b> ield <b>I</b> sing <b>M</b> odel |
| <b>TL</b>   | <b>T</b> hermodynamic <b>L</b> imit                          |

*Dedicated to my friends and family, whose faith has been always a standing encouragement.*

# Introduction

In the last decades, several experimental breakthroughs have been achieved in the realization of strongly interacting many-body quantum models, with a very high degree of control and fine monitoring [1]. This is especially true in condensed matter aggregates of real or artificial atoms in cavity QED and circuit QED [2, 3], as well as in trapped ultra-cold atomic systems [4, 5]. These advancements have stimulated a very active theoretical research on many phenomena exhibited by these systems, like quantum phase transitions, emergence of quantum chaos, non-reversible evolutions (memory effects), collective generation and propagation of entanglement, critical universality, and finite-size scalability. The level of understanding of these complex effects is particularly scarce in non-equilibrium situations, and this thesis dissertation summarizes our contribution to this research frontier. Our work have also been motivated by its implications to quantum control protocols, which can be of particular interest in quantum metrology, quantum simulations, quantum computation, and quantum information processing [6–8]. In many situations, the relevant dynamics can be expressed in terms of a symmetrical interaction of the components, leading to a highly coordinated all-to-all system. Our work is centered on these kind of situations. However, we have found that many of our conclusions can be extended beyond the all-to-all scenario.

Many-body quantum dynamics is at the core of many natural and technological phenomena, from understanding of superconductivity or magnetism through applications in quantum information processing as in adiabatic quantum computing [8]. Spin networks, many-body systems composed of the simplest quantum unit, are an evident starting point to start understanding those phenomena as they enclose much of their complex behavior in a highly controllable and tractable way. While it is the system as a whole the one that has been mostly investigated, a focus on specific parts of the system can be useful, either for trying to accomplish advantageous microscopic quantum control through macroscopic changes of the system, or for monitoring and characterizing the collective phenomena with a more specific perspective.

One big focus of our work have been the Dicke model (DM) [9, 10], when it is made to dynamically cross its quantum phase boundary. Irreversible effects of this crossing can be seen in quantum hysteresis curves of the ground state fidelity and system's heating [11]. Also, for the near adiabatic regime, the presence of a minimal energy gap in the phase boundary makes that

along the critical threshold the adiabatic condition breaks down. During this critical crossing, we have found a new dynamical *continuous* scaling universality, which goes beyond traditional critical exponent approaches like the Kibble-Zurek mechanism [12, 13]. We have proven that our new approach is not only valid for all-to-all systems like the DM or (its universality class related) the Lipkin-Meshkov-Glick model, but it can also be implemented in spatially distributed systems like the 1D Ising model. Due to the continuous character, the traditional equilibrium universality classes become partitioned under more stringent conditions, if the dynamical quantum phase crossing of two-different systems are meant to be equivalent.

Beyond quasi-adiabatic evolutions, we have found in the DM a dynamical phase transition to a highly complex light-matter entangled state, which had remained unnoticed because of previous research mainly aiming at the adiabatic or the sudden quench limits [14–16]. The new phase is characterized by quantum chaos, fragmented Wigner distributions, and the dynamical spontaneous breaking of symmetry [17, 18]. The field superradiance is dynamically enhanced during this chaotic phase. Additionally, the phase transition is preceded by a magnified separate light and matter squeezing, which is related to internal quantum entanglement. We have established a thorough understanding of the conditions at which this phase emerges, including its scaling according to system size and annealing velocity, separating the chaotic phase from the near adiabatic and sudden quench regimes.

One crucial aspect for the generation of high quantum correlations in the DM is its strong all-to-all interaction, which allows to macroscopically coordinate the state of the atoms. This effect, which is essentially a squeezing effect, has been recently employed to push forward the precision of time measurement standards in 2D confined atomic clocks of alkaline earth atoms [19]. However, atomic collisions complicate the behavior of these systems, and further theoretical understanding is needed. Under some realistic conditions,  $p$ -wave collisions dominate, and the effective Hamiltonian for the orbital states is a collective spin model in a Dicke manifold very similar to the DM [20]. In addition, an underlying  $SU(N)$  symmetry of the nuclear spins allows that very varied initial quantum state transfer conditions can be achieved by highly controlled Ramsey pulses. Taking advantage of the similarities in methods and concepts with the DM, we have extended our analysis of highly correlated all-to-all interaction to this cold atom setting. Importantly, some of the results can be expressed analytically. We have found several regimes at which the exchange interaction can be affected depending on conditions of external magnetic field and initial driving pulses. Our results open a starting point for quantum simulations of systems with magnetic order like perovskite-like crystals.

Our work has shed light on many aspects of the on time, out of equilibrium, macroscopical control of non-trivial collective quantum properties of many-body systems under strong coupling conditions, leading to all-to-all interactions, without resorting to any semi-classical approximation and always taking account of the relevance of finite-size effects. We have successfully

provided a broad and fully quantum picture that can even be extended to general theories, as is the case of universal critical functions in the dynamical crossing of quantum phase transitions.

# Chapter 1

## The Dicke Model and its dynamical QPT

This chapter is a preamble containing essential ingredients that will play a major role in the next two chapters, and gives the first impression of the kind of many-body non-equilibrium situation that has been at the center of this doctoral thesis. Besides giving an introduction to the Dicke model and its quantum phase transition, this chapter will discuss some aspects of the most prominent and recent experimental realizations of the model, which are in the branch of ultra-cold atomic physics. We also present our first set of original results concerning Landau-Zener-Stückelberg processes (quantum hysteresis) in the DM, preceded by some theoretical background that contextualize the results.

### 1.1 Introduction

During the last decades, there have been significant advances in the experimental realization and control of many-body quantum systems [1]. Many of these realizations can be regarded as particular cases of an interaction between matter and radiation (or some sort of bosonic excitation field). Also, from a theoretical point of view, in several cases these systems can be readily modeled as matter consisting of a single or several two-level systems (qubits) and radiation as a set of independent harmonic oscillators. The kinds of physical systems that could be approached by this perspective range from cavity Quantum Electrodynamics (QED) and circuit QED [2, 3, 21, 22], ultra-cold atomic physics [4, 5, 23–25], artificial atoms of semiconductor heterostructures interacting with light [26, 27] or with plasmonic excitations [28–30], and many more. Since these systems comprise several degrees of freedom, their theoretical study has been traditionally approached by approximate perturbative methods [31]. Most of these approximations rely on the assumption that the matter-radiation interaction is weak and/or entirely dissipative. These regimes are no longer a limit in many experimental realizations, and,

moreover, there is a bunch of effects of the strong structured interaction regime that could be of interest for quantum control and extended to applications in quantum information processing and quantum computation [32].

The major task of quantum control, especially in fields like quantum computation, is to reliably manipulate quantum systems while preserving advantageous properties such as coherence, entanglement, and purity. However, all realistic implementations must take into account that coherent control contains an error; and estimations say that the allowable error in the fidelity of an usable quantum operation must be of the order of  $10^{-4}$  or less [33]. Such aim has demonstrated to be considerably difficult to achieve, both because of the fine experimental requirements, and also because of the inherent complexity of the systems involved. The present work will concern about this second difficulty, and thus it will try to advance in the comprehension of the control and monitoring of many-body quantum systems.

One model that will occupy a big part of this thesis is the Dicke Model (DM) [9], a strongly interacting light-matter system arising over a wide range of applications on condensed matter physics as well as in atomic, molecular and optical physics. Despite significant knowledge has accumulated about its static properties across its parameter space, with the emergence of a superadiant quantum phase transition (QPT) [34], scarce is known about the dynamical crossing of this transition. In other words, much of the past work on this model has focused on static properties or equilibration schemes leaving many aspects of the non-equilibrium evolution as open problems. We advanced this state of knowledge by exploring the time dependent quantum control of DM by means of a tuned interaction, in regimes where strong correlations among the components play an essential role.

In this chapter we present the essential generalities of the DM in section 1.2, followed by an exposition of a very prominent experimental realization of it (section 1.3). Later, in section 1.4, the setting of the DM under a Landau-Zener-Stückelberg (LZS) cycle is brought up in order to give a first glance of the non-trivial dynamics that can emerge. Finally, we briefly summarize the main results in section 1.5.

## 1.2 The Dicke Model

The DM describes a radiation-matter system which, despite its simplicity, exhibits a wide arrange of complex collective phenomena, many of them specifically associated with the existence of a QPT [35–37]. The DM consists of a set of identical qubits symmetrically coupled to a single radiation mode. It can be described by the microscopic Hamiltonian [9],

$$\hat{H}(t) = \frac{\epsilon}{2} \sum_{i=1}^N \hat{\sigma}_z^{(i)} + \omega \hat{a}^\dagger \hat{a} + \frac{\lambda(t)}{\sqrt{N}} (\hat{a}^\dagger + \hat{a}) \sum_{i=1}^N \hat{\sigma}_x^{(i)} \quad (1.1)$$

where  $\hat{\sigma}_\alpha^{(i)}$  are Pauli matrices, and  $N$  is the number of qubits. Energies  $\epsilon$  and  $\omega$  represent the qubit and field transition frequencies respectively, while  $\lambda$  represent a scaled interaction parameter. Over the first three chapters of this thesis, we are going to deal with non-equilibrium scenarios when the DM is driven by this parameter  $\lambda$  as a mean of quantum control. That is why we state the time dependence  $\lambda(t)$  explicitly. Under many situations, as all the ones we consider in our work, the dynamics of the DM do not require the consideration of the  $2^{\otimes N} \otimes \mathbb{N}$  dimensional Hilbert state that takes into account all possible states of the qubits <sup>1</sup>. Instead,  $SU(2)$  collective operators  $\hat{J}_\alpha = \frac{1}{2} \sum_{j=1}^N \hat{\sigma}_\alpha^{(j)}$  can be used, and then Hamiltonian 1.1 can be written in the form,

$$\hat{H} = \epsilon \hat{J}_z + \omega \hat{a}^\dagger \hat{a} + \frac{2\lambda(t)}{\sqrt{N}} \hat{J}_x (\hat{a}^\dagger + \hat{a}). \quad (1.2)$$

Here, operators  $\hat{J}_\alpha$  act on the totally symmetric manifold, also known as the **Dicke manifold**, where the operator  $\hat{\mathbf{J}}^2 = \sum_\alpha \hat{J}_\alpha^2$  is a good quantum number (a constant of motion) with eigenvalue  $J(J+1)$ , and  $J = N/2$ . In this manifold, all qubits are treated in exactly the same way, as a set of  $N$  two-level indistinguishable bosons. This manifold is just  $N$  dimensional, instead of the original  $2^{\otimes N}$  dimension of the matter subsystem entire Hilbert space.

The DM is deemed to achieve its thermodynamic limit (TL) when its matter subsystem size goes to infinity, i.e., when  $N \rightarrow \infty$ . Much of the attractiveness of the DM lies on the presence of a second-order quantum phase transition (QPT) at this TL [35–37], which means that there is a significant change in the behavior of the ground state when its parameters are changed through a specific set of critical values. The phase-boundary is described by the equation  $\lambda_c = \frac{\sqrt{\epsilon\omega}}{2}$ . The scaling of the interaction parameter in Eq. 1.1 is devised in order to have its phase transition correctly defined in terms of  $\epsilon$  and  $\omega$ . When the coupling parameter  $\lambda$  is above the critical value, the ground state of the system is characterized by a non-zero expectation value of its excitation operators or order parameters (OP),

$$\langle \hat{N}_b \rangle \equiv \langle \hat{a}^\dagger \hat{a} \rangle, \quad \text{and} \quad \langle \hat{N}_q \rangle = \left\langle \hat{J}_z - \frac{N}{2} \right\rangle. \quad (1.3)$$

On the other hand, when  $\lambda < \lambda_c$ , the OPs are zero. Because of this property, the region when  $\lambda > \lambda_c$  is called ordered or superradiant phase, and the other one is called *normal phase*. Near the phase-boundary, and in the superradiant phase, there is a dependence of the OP  $\langle \hat{N}_b \rangle \propto (\lambda - \lambda_c)$  and  $\langle \hat{N}_q \rangle \propto (\lambda - \lambda_c)^{1/2}$  [34]. This power-law behavior is typical of second order phase transitions, since the OP function is continuous across the phase boundary, but has a discontinuity in its derivative. For that type of phase transitions, the critical exponents are a characteristic of the universality class to which the model belongs. The DM has also another important constant of motion that also has the advantage of commuting with  $\hat{\mathbf{J}}^2$ . This quantity is **parity**, defined as  $\hat{\Pi} \equiv e^{i(\hat{N}_q + \hat{N}_b)}$ . In the ordered quantum phase ( $\lambda > \lambda_c$ ), the  $\mathbb{Z}_2$  symmetry related to parity is spontaneously broken, in the sense that the TL ground state is two-fold

<sup>1</sup>As the qubits are usually regarded as generalized two level atoms, in many instances of this work we will refer to the set of qubits as the **matter subsystem**.

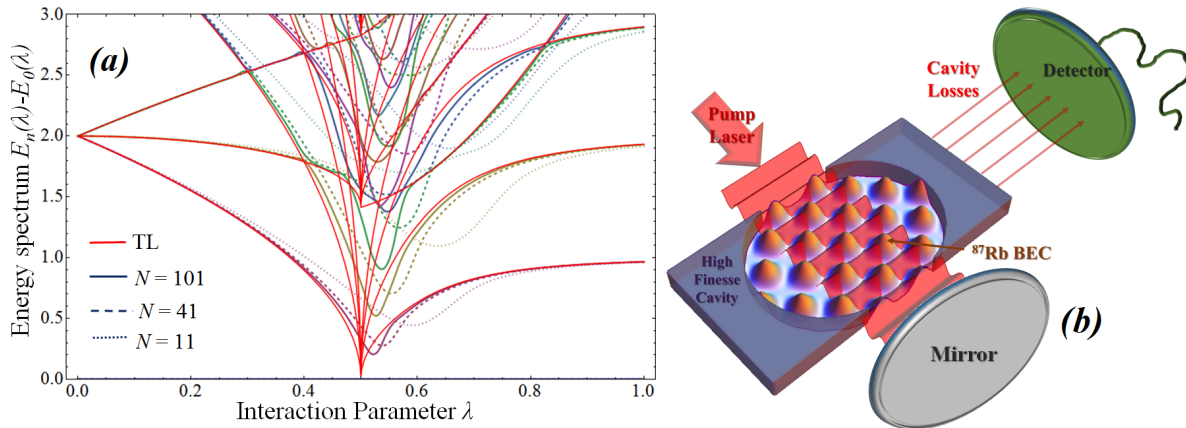


FIGURE 1.1: **(a)** Spectrum of the DM as a function of the interaction parameter  $\lambda$  both in the TL and for some finite sizes when  $\omega = \epsilon = 1$  in Eq. 1.2. All energies are measured with respect to the ground state energy. A second order QPT occurs at value  $\lambda = 0.5$  when the energy gap vanishes. This spectrum was computed in the even parity sector of the model. **(b)** Schematic of recent successful realizations of the DM in a BEC of  $^{87}\text{Rb}$  atoms confined by a magneto-optical trap, made to interact with the field mode of a high finesse cavity by means of a pumped transverse field [4, 5].

degenerate, corresponding to the two different eigenvalues of  $\hat{\Pi}$ . Also, at the quantum critical point (QCP)  $\lambda_c$ , the DM presents an infinitely degenerated vanishing energy gap [34], as it is shown in Fig. 1.1a. This zero energy gap in the TL poses an impossible barrier to dynamically cross the phase boundary, at any finite time, while maintaining the system in the ground state.

While current knowledge of the light and matter properties in the DM equilibrium ground state are relatively well known [38–42], its fully quantum out-of-equilibrium critical behavior is just starting to be understood [12, 14, 17, 18, 43]. Most of the properties previously described for the TL have manifestations for finite sizes versions of the model. We illustrate that fact in Fig. 1.1a by showing the spectrum for some chosen values of  $N$ . The QCP is not a zero gap point anymore, but a minimum finite gap that gets smaller and smaller as the system size grows. It also gets slightly stranded to higher values of  $\lambda$  as compared to the TL case. That kind of scaling properties, i.e. dependence on size, have been extensively studied in the DM in the equilibrium situation [38–42, 44–46]. This poses the question on how those scaling properties translate to the case when the Hamiltonian varies on time through variations of its parameters. This question plays a major role during most of this thesis, and is an inquiry that had been quite scarcely addressed. Something that contrasts with the big amount of literature that has been written about the static properties. The dynamical version of the QPT has nevertheless been explored. However, among the works that explored the issue of the critical dynamical evolution of DM, many exploit the TL at some level, and either resort to a semiclassical approximation [14, 47], or other perturbative approaches [48], or open system’s Langevin equations that fail to cross the phase-boundary [49]. In strong contrast, our approach will always tackle the problem at the very quantum level, something almost exclusively to contemporary research [12, 13, 17, 18, 43]. From the theoretical point of view, the dynamical crossing of the QPT in the DM is still a

non-trivial open problem concerning non-equilibrium effects in a strongly interacting quantum many-body system.

### 1.3 Realization of the DM in cold atom settings

Many experimental realizations of the DM have been discussed during the last decades, several of them being around implementations in circuit QED, where superconducting qubits play the role of the matter subsystem [2, 3, 21, 22]. Notwithstanding, it could be said that the branch of experiments that deserves most of the attention is that demonstrating DM superradiance in ultra-cold atom optical traps, especially  $^{87}\text{Rb}$  Bose-Einstein condensates [4, 5, 50, 51]. Those experiments are so prominent that a main description of them is pertinent. More excitingly, those experiments seem to approach a level of quantum control that it seems that soon at least some of the results of these thesis will be confirmed. Also, this explanation of experimental techniques provides a valuable concrete representation of the DM, that could help the reader to have an actual physical picture of our theoretical results. The following presentation is based on Refs. [4, 5, 50, 51], especially Ref. [5].

Figure 1.1b depicts a schematic drawing of the main components of the experiment. An ultra-cold cloud of  $N \sim 10^5$   $^{87}\text{Rb}$  atoms confined by a magneto-optical trap inside a high finesse Fabri-Perot cavity. The cloud is driven by a transverse pump laser whose wavelength is the same as that of the fundamental mode of the cavity. The combined cavity and pump laser setting produce an optical lattice potential that affects the motion of the atoms in the cloud through coupling with far-detuned atomic resonances. This coupling causes that the matter wave state of the atoms symmetrically interacts with each other through the mediating presence of the radiation mode. At low intensity pump power  $\epsilon_p$ , the Bose-Einstein Condensate (BEC) remains in its condensate (almost spatially uniform) translational ground state. However, when a critical value of  $\epsilon_p$  is reached, the ground state becomes a grid-like matter wave as the one shown in Fig. 1.1b. This change of configuration constitutes the QPT, whose spontaneous symmetry breaking is caused by the fact that two matter wave configurations, distinguishable only by a phase difference of  $\pi$ , have the same lowest possible energy. The effective two-level system (qubit) of this system is composed of the ground BEC translational state and the fundamental grid-like matter wave state for each atom<sup>2</sup>. There are several ways to monitoring the system. The two most fundamental manners are: addressing the radiation field by coupling one of the (unavoidably) leaky walls of the cavity to a detector, or using time of flight methods to measure the matter wave modes. It is interesting to see that each technique measures the state of one of the two main components of the DM, i.e., light and matter respectively.

We will now proceed to map the essential physics of the experiment into the DM Hamiltonian in Eq. 1.2. The degrees of freedom involved can be described by the mode creation (annihilation)

<sup>2</sup>A more realistic description would include more than these two translational states

operator  $\hat{a}$  ( $\hat{a}^\dagger$ ), the matter wave corresponding field operators  $\hat{\Psi}(\mathbf{r})$ , and the pumping laser amplitude  $\alpha_p(t)$  simulated by a  $c$ -number. The Hamiltonian then reads [52],

$$\hat{H}_{\text{BEC}} = \omega_0 \hat{a}^\dagger \hat{a} + \int d^2\mathbf{r} \hat{\Psi}^\dagger(\mathbf{r}) \left[ -\frac{\nabla_{\mathbf{r}}^2}{2m_a} + \Delta_0 \left( \hat{a}^\dagger \cos kz + \alpha_p^*(t) \cos ky \right) \left( \hat{a} \cos kz + \alpha_p(t) \cos ky \right) \right] \hat{\Psi}(\mathbf{r}), \quad (1.4)$$

where  $m_a$  is the mass of the atoms,  $\Delta_0$  is the light shift per intra-cavity photon, and  $\omega_0$  is the radiation mode frequency. Now, we approximate the field operator by a Fourier series in the grid plane (which we suppose is the  $zy$  plane),

$$\hat{\Psi}(x, y, z) \approx \hat{\Phi}_0(x) \sum_{n_z, n_y} A^{-1/2} \hat{c}_{n_z, n_y} e^{ik(n_z z + n_y y)}, \quad (1.5)$$

where the numbers  $n_z, n_y$  indicate the matter wave modes, and  $k$  the angular wave number. After this, we restrict the dynamics to the manifold generated by the field operator of the uniform BEC state  $\hat{c}_g = \hat{c}_{0,0}$ , and the fundamental first excited matter wave mode  $\hat{c}_e = \frac{1}{4}(\hat{c}_{1,1} + \hat{c}_{1,-1} + \hat{c}_{-1,1} + \hat{c}_{-1,-1})$ . Under these approximations, Hamiltonian in Eq. 1.4 can be written as,

$$\hat{H}_{\text{BEC}} \approx \frac{1}{2} |\alpha_p(t)|^2 \left( \hat{c}_e^\dagger \hat{c}_e + \hat{c}_g^\dagger \hat{c}_g \right) + \frac{k^2}{2m_a} \hat{c}_e^\dagger \hat{c}_e + \omega \hat{a}^\dagger \hat{a} + \frac{1}{2} \Delta_0 \hat{a}^\dagger \hat{a} \left( \hat{c}_e^\dagger \hat{c}_e + \hat{c}_g^\dagger \hat{c}_g \right) + \frac{\Delta_0}{4} \left( \hat{a}^\dagger \alpha_p(t) + \hat{a} \alpha_p^*(t) \right) \left( \hat{c}_e^\dagger \hat{c}_g + \hat{c}_g^\dagger \hat{c}_e \right). \quad (1.6)$$

After discarding global phases, going to rotation frame, and using as Dicke states,

$$|m\rangle = \frac{1}{\sqrt{m!(N-m)!}} \left( \hat{c}_e^\dagger \right)^m \left( \hat{c}_g^\dagger \right)^{N-m} |0\rangle, \quad (1.7)$$

we can obtain Hamiltonian in Eq. 1.2. Then, there exists the following equivalences among parameters,

$$\epsilon = \frac{k^2}{2m_a}, \quad \omega = \delta_c - \frac{1}{2} \Delta_0 N, \quad \lambda(t) = \frac{\sqrt{N}}{4} \Delta_0 |\alpha_p(t)|. \quad (1.8)$$

Where  $\delta_c$  is the the atom-laser frequency detuning. Notice how the laser becomes the actual control parameter, the knob for driving the DM across parameter space. This way, every time we speak about modulating  $\lambda(t)$ , we can think that process as changing the pumping laser power.

## 1.4 Quantum Hysteresis in the Dicke Model under a LZS cycle

### 1.4.1 Theoretical background

There is a model that probably constitutes the simplest possible case of a crossing of a QCP of a time-dependent Hamiltonian. This is the Landau-Zener (LZ) model and it reduces the situation to a two level system with the following Hamiltonian [53, 54],

$$\hat{H}_{LZ} = -\frac{\Delta_0}{2}\hat{\sigma}_x + \frac{\varepsilon_0 - \varepsilon(t)}{2}\hat{\sigma}_z. \quad (1.9)$$

The energy-gap between the ground state and the excited state is  $\Delta(t) = \sqrt{\Delta_0^2 + (\varepsilon(t) - \varepsilon_0)^2}$ . At the QCP  $\varepsilon = \varepsilon_0$ , the system reaches the minimal energy-gap  $\Delta = \Delta_0$ . The classical setting of the problem is to make a transition with a variation  $\varepsilon(t) = vt$  starting from  $t = -\infty$  in the ground state, that is, starting at  $|0\rangle$ <sup>3</sup>. The probability of ending in the excited state at  $t = \infty$ , which turns out to be  $|0\rangle$ , is a classical result in the LZ problem and it is given by,

$$P_{LZ} = \exp\left(-\frac{\pi\Delta_0^2}{v}\right), \quad (1.10)$$

where the ratio  $\frac{\Delta_0^2}{v}$  is called the adiabatic parameter. It is worth noticing that when  $v$  is very small, we have zero probability for the system to jump to the excited state. Therefore, the limit  $v \rightarrow 0$  accomplishes the perfect adiabatic evolution. One interesting aspect of the LZ problem is that much of its dynamics is determined during the short interval at which the minimum-gap is crossed. This is true to the point that a LZ can be seen as analogous to a beam-splitter [55], since the probability in Eq. 1.10 for the system staying in state  $|0\rangle$  can be seen as equivalent to a transmission coefficient which characterizes the odds for a beam to go through a partially reflecting mirror. The analogy with the beam-splitter could be extended, and then one may want to reverse the evolution of  $\varepsilon(t)$  and cross again the critical gap. This complete cycle is known as a Landau-Zener-Stückelberg (LZS) process. At the end of a LZS cycle, the probability of staying in the  $|0\rangle$  state can be approximated by the formula [55],

$$P_{LZS} = 4P_{LZ}(1 - P_{LZ}) \sin(\theta_{12} + \Phi_S), \quad \text{with} \quad \theta_{12} = \int_{t_1}^{t_2} \Delta(t)dt. \quad (1.11)$$

The time  $t_1$  and  $t_2$  defines the interval between the two crossings of the gaps. The phase  $\Phi_S$  is called Stokes phase and it is determined entirely by the form of the minimum gap, so it does not depend on the velocity  $v$ . On the other hand, the dynamical phase  $\theta_{12}$  is in inverse proportion to  $v$ ; or equivalently, in direct proportion to the total time of the cycle  $\tau \propto 2v^{-1}$ . That way, Eq. 1.11 implies that one should expect an oscillatory behavior with respect to  $\tau$  of the probability for finishing the cycle in the same state at which it was started, these are

<sup>3</sup>We mean by  $|0\rangle$  one of the two states of the qubit, the other one being  $|1\rangle$ . In this notation,  $\hat{\sigma}_z \equiv |1\rangle\langle 1| - |0\rangle\langle 0|$ .

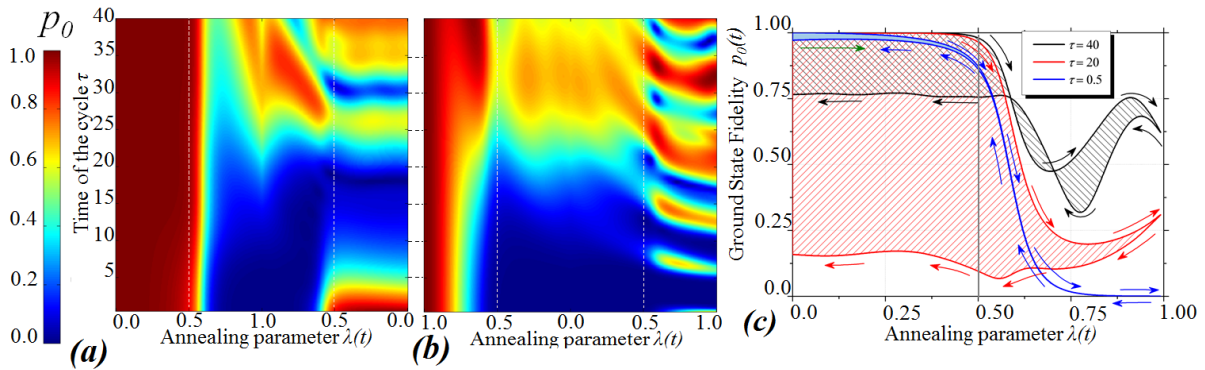


FIGURE 1.2: Quantum hysteresis profiles as measured by ground state fidelity  $p_0(t)$  as a function of  $\lambda(t)$  when the interaction parameter performs a LZS cycle as specified by Eq. 1.12. The DM system size is  $N = 15$ . The entire profile is shown for cycles starting at (a) the normal phase, or at (b) the  $\lambda > 0.5$  ordered phase. Bright and dark fidelity fringes to the right part of the graphs are Stückelberg oscillations. Some particular curves of the profile in (a) are shown in (c) in order to show the area enclosed by the non-reversible process, which show that LZS neither too fast nor too low are the ones with more hysteresis. The QPT boundary in the TL is marked by a white line in (a,b) and a grey one in (c).

known as *Stückelberg oscillations* [56]. Despite its simplicity, the LZ problem has found an enormous range of application in several experimental situations. Also, some generalizations of its concepts can be done to tackle the dynamics in more than two levels [57–59].

#### 1.4.2 The Dicke Model under a LZS cycle

Let us suppose resonant energies,  $\epsilon = \omega = 1$  in Hamiltonian of Eq. 1.2 and let us suppose that a DM undergoes a triangle-like LZS cycle described by,

$$\lambda(t) = \begin{cases} \lambda_1 + 2(\lambda_2 - \lambda_1)t/\tau, & t \leq \tau/2 \\ \lambda_2 + 2(\lambda_1 - \lambda_2)(t/\tau - 1/2), & t > \tau/2 \end{cases}; \quad (1.12)$$

where  $\lambda_1$  and  $\lambda_2$  are respectively zero (one) and one (zero) depending on whether the system starts (ends) in the normal (superradiant) phase. Let us also suppose that at  $t = 0$  the system is in the ground state corresponding to its starting value of  $\lambda$ . We will assume that this state is always in the even parity sector. The velocity of the cycle is characterized by its total time  $\tau$ . For any value of  $\lambda(t)$  there is a set of instantaneous eigenstates  $|\varphi_n(\lambda(t))\rangle$  of the DM Hamiltonian. If  $|\Psi(t)\rangle$  represents the actual dynamical state, we can express the probability of being in the instantaneous eigenstates as,

$$p_n(t) = |\langle \varphi_n(\lambda(t)) | \Psi(t) \rangle|^2. \quad (1.13)$$

In particular, the probability of being in the ground state  $p_0(t)$  is known as **fidelity**.

In fig. 1.2a-b we present dynamical profiles for  $p_0(t)$  over a wide range of cycle times  $\tau$  for an  $N = 15$  DM with both forms of performing the LZS cycle in Eq. 1.12. Very high values of  $\tau$  correspond to almost zero probability of exciting the system, so it almost follows the

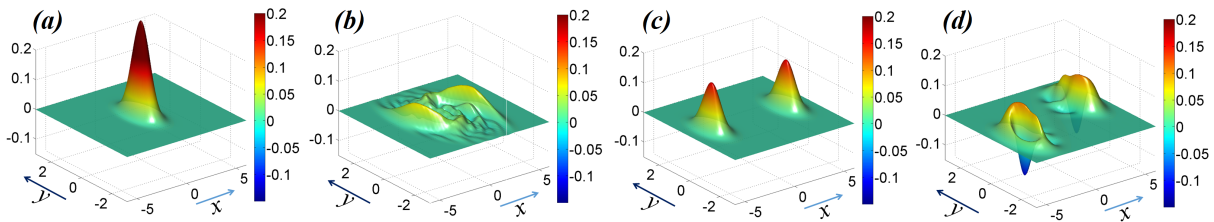


FIGURE 1.3: Non-reversibility of the dynamics as witnessed by the light Wigner distributions  $W_b$ , for a DM with  $N = 15$  and a LZS cycle time  $\tau = 20$ . **(a,c)** Initial states. **(b,d)** Final states. **(a-b)** Cycle start and ending point at the normal phase ( $\lambda = 0$ ). **(c-d)** Cycle start and ending point at the ordered phase ( $\lambda = 1$ ). The irreversible consequences of hysteresis are manifested in complex small structures **(b)** and negative regions **(d)** of  $W_b$ , these features are respectively related to quantum chaos and non-classical light.

instantaneous eigenstate during all the time evolution (adiabatic limit). In the other extreme, at very short times, the system simply is not able to respond to changing the Hamiltonian, so that it remains frozen in the initial state (sudden quench limit). In such a limit, the fall in the fidelity is due to differences between the instantaneous ground state and the starting one as predicted by the QPT. Thus, this change is concentrated around the QCP. On the other hand, the path between these two limits is not monotonous, and complex oscillations arise by varying the value of  $\tau$ . This is a many-body version of Stückelberg oscillations, as defined in Eq. 1.11.

In fig. 1.2c we chose particular ground state fidelity evolutions in order to see how they stand against the annealing parameter  $\lambda(t)$ . It is interesting to notice that they tend to enclose an area that may be called a *quantum hysteresis curve*, as it has been recognized in experimental realizations of the DM [5]. This curves measure the amount of irreversible excitations developed by the LZS cycle. Both adiabatic and sudden quench limits represent low degrees of hysteresis, while the intermediate regime have a very non-trivial evolution of excitations. In chapter 3 we will see that this intermediate regime of velocities are dominated by outstanding non-equilibrium processes.

In addition to ground state fidelity, we also present quantum hysteresis effects by means of the field Wigner quasi-probability distribution, which is a theoretical tool from Quantum Optics that contains the same information as the density matrix [60]. It is defined as,

$$W_b(\alpha, \hat{\rho}_b) = \sum_{n=0}^{\infty} (-1)^n \langle n | \hat{D}^\dagger(\alpha) \hat{\rho}_b \hat{D}(\alpha) | n \rangle, \quad (1.14)$$

where  $\hat{D}(\alpha) = e^{\alpha \hat{a}^\dagger - \alpha^* \hat{a}}$  is the displacement operator, and  $\alpha \in \mathbb{C}$  is related to the field quadratures by  $\sqrt{2}\alpha = x + ip$ . Despite their apparently abstract definition, Wigner functions can be reconstructed experimentally [61].

Figures 1.3a-d show how after intermediate  $\tau$  LZS processes, the final state of light gets very different from how it started. The initial Gaussian-like shapes of the distributions are appreciably distorted. Negative values of the distribution appear, especially for the cycles starting in

the superradiant phase (Figs. 1.3c-d). Also, for the cycle starting in the normal phase (Figs. 1.3a-b) the final stage is full of small wiggles that spread over the distribution. Negativity of Wigner function is related to distinctively quantum states of light, while small structures like the wiggles in Fig. 1.3b are associated to quantum chaos [62].

## 1.5 Conclusion

We have presented the DM Hamiltonian and the main properties that make it so interesting for studying highly correlated many-body systems, especially in the context of coupled matter-light systems. We have also explained a set of cold-atoms experiments that provides a more tangible intuition of the type of physical systems that can be involved under the DM physics. Finally, we have given a first glance of the kind of results that can emerge from submitting the DM under a driving over its interaction parameter. This has been done with a brief presentation of the behavior of the DM under LZS cycles. We have seen that highly non trivial behaviors can emerge, especially outside the relatively simple cases of sudden quench and adiabatic limits. In the next chapters we will substantially extend these initial remarks.

## Chapter 2

# Near-adiabatic dynamical scaling universality across a QPT

This chapter focus the study of non-equilibrium quantum critical phenomena (already introduced in the previous chapter) on the near-adiabatic regime, i.e, when the control parameter is varied at relatively slow rates. In such cases, the main effects are concentrated in the lower part of the excitation spectrum and then it is possible to find equivalent effects if the driving rate is adjusted to the system size, i.e., it is possible to find size-independent *scaling*. Also, in this chapter we will not restrict ourselves to the DM, despite being our central motivation. Now we add two other models that serve to establish a very general view of this QPT near-adiabatic scenario. The theory that we develop is so broad that allows us to group different models into an equivalence class, where properties of one model can be easily mirrored by many others, i.e., we will establish the foundations of *universality* in this non-equilibrium QPT context.

### 2.1 Introduction

Scaling is a widespread phenomenon in nature, which determines how the patterns of a definite system change as its size is varied. From allometric scaling on physiological features of an organism with respect to overall size in biology [63], to the relation between the frequency of a word and the size of a written text [64], these scaling phenomena have usually found an expression through a power-law formula relating the variables. In physics, this kind of relations have been also extensively discovered and, in particular, critical phenomena (behavior of physical systems near a phase transition) have been found to be governed by these power-laws [65]. However, instead of directly addressing a scaling subject to system size variations, in critical physical phenomena it has been largely understood through variations of state parameters like temperature or external fields, where the critical exponents of the power laws are only exact

near the phase boundary and in the TL, when the number of system components  $N$  goes to infinity [10].

This kind of scaling has been found even in non-equilibrium situations, and at the zero temperature limit of QPTs. The usual framework for describing the main dynamical scaling features of many-body QPTs has been the Kibble-Zurek mechanism (KZM) [66–68], a broad scope approach that can be applied to both classical [69] and quantum systems, and to finite [70, 71] and zero-temperature cases as well. However, the KZM only provides a way of estimating *final* power-law behavior of observables, and it is based on the critical exponents as they can be found in the TL. This KZM scheme has been successful for the case of adiabatic critical scaling of finitely connected spin networks like the Transverse-Field Ising Model (TFIM) and one-dimensional Bose-Hubbard models [72–78]. In those cases the lattice is short-range connected, in the sense that each qubit has only two nearest neighbors that interact directly with it. The KZM employs the presence of correlation lengths and critical exponents in order to make quantitative predictions, which casts serious doubts on whether it can be applied to systems with an undefined spatial distribution like the DM and the Lipkin-Meshkov-Glick model (LMGM) [79, 80]. Detailed explanations of adiabatic collapse have also usually focused on approximations that are only valid for very tiny excitations of the system, in adiabatic QPT theory [81, 82].

In this chapter we will depart from the traditional KZM and adiabatic QPT theory. We will see that scaling is to be found all along the dynamical evolution around the critical threshold, and that is valid for times scales that range from the really adiabatic ones up to the regime where the KZM is applied. We will demonstrate the existence of universal critical functions, that includes critical exponents only as precursors of these effects. It turns out that this continuous scaling structure present in the low-energy excitation spectrum of the system around the critical threshold is the only sufficient and necessary condition for near-adiabatic dynamical scaling. Given that this condition is also satisfied by the finitely connected models, our findings, further supported by analytical and numerical results, explain why the KZM is limited on understanding adiabatic dynamical scaling, and switch the attention to the really relevant mechanism leading to it. Scaling functions go beyond critical exponents by incorporating richer information about the dynamics of the underlying many-body system, including finite-size effects, and hence extending the range of validity over which theoretical predictions can describe empirical data [83].

One of the main interests for researching zero temperature near-adiabatic phenomena is its relevance for applications in what has been called adiabatic quantum computation [7, 84–86], which aims to achieve high-fidelity quantum information processing by varying external conditions at very low rates, taking advantage of the robustness of a many-body system. The scalability of the evolution is essential for many implementations of the adiabatic quantum protocols. As the system size gets bigger (and so the simultaneously processed information), longer computing

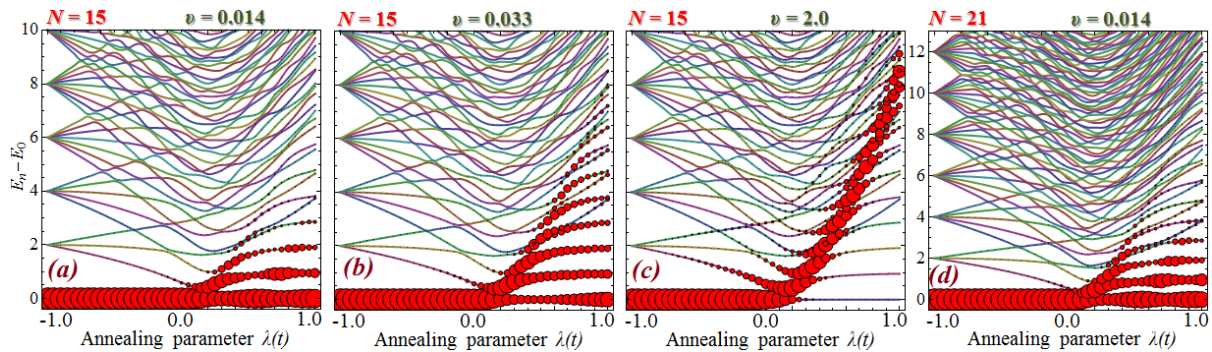


FIGURE 2.1: These figures overlap the  $\lambda$  dependent spectrum of a DM with (a-c)  $N = 15$  and (d)  $N = 21$  and the time evolution of the probability  $p_n(t)$  (see Eq. 1.13) of finding the system in a definite instantaneous eigen state, represented by the size of red circles. The dynamical crossing is a linear ramp from the ground state at  $\lambda = -1$  until  $\lambda = 1$  with constant annealing velocity (AV)  $v = \frac{d\lambda}{dt}$ . The TL critical value is at  $\lambda = 0$ . The faster the evolution, the harder is for the system to stay in the ground state, thus populating excited states and generating heating. A comparison between (a) and (d) shows that at the same AV, bigger system sizes will be more excited as the critical energy gap gets narrower. Notice that in the near-adiabatic regime, major changes only occur when fundamentally crossing the critical threshold.

times are required to obtain the same level of fidelity. As it is illustrated in Fig. 2.1, an interplay between size and driving rate arises. The process may be discarded as inviable if the computation times are not kept low enough as compared to decoherence times, other disturbing noises, or simply is impractical for the amount of quantum information required.

On the other hand, from the experimental perspective, applications in cold-atoms simulations are currently one of the most promising techniques to reach highly tunable realizations of model systems with QPTs, and then performing adiabatic processes on them. Starting from the striking achievement of the Bose-Hubbard model and its superfluid-Mott insulator transition [87], this area has greatly increased the accessible physics with respect to QPTs [25]. The presence of equilibrium universality properties in these models led to the exploration of whether zero-temperature universal dynamics are also possible, and several model systems have already been examined [73–76]. The sufficient conditions that the present results provide for adiabatic quantum simulations could extend the range of models effectively realized by these experiments. We will see with the systems with same values of critical exponents (same universality class) do not necessarily exhibit the same continuous near-adiabatic dynamics, as the critical functions pose more stringent conditions for universality than critical exponents. This is a crucial hint for adiabatic quantum simulations, in which a particular model is taken to act as experimental surrogates of another one [88]. The universal scaling functions reported here can be combined with experimental results and theoretical extensions of the core concepts to study phase transitions at finite temperature and/or classical systems.

This chapter is structured as follows. In section 2.2 we present the models and setting of near-adiabatic QPT we are going to consider. After that, a theoretical background of the KZM is given in section 2.3. We then show in section 2.4 that a regime with the characteristics of the

KZM is present in all three models under consideration, but the KZM fails in providing the correct critical dynamical exponents. In section 2.5 we present our novel continuous critical function theory, demonstrating its significantly wider scope as compared to the KZM and adiabatic QPT theory. Section 2.6 explains how the new continuous scaling picture changes the perspective of what should be considered as a dynamical equivalence class. Finally, section 2.7 highlights the central message of this chapter.

## 2.2 Models and methods

In this section we define the three models this chapter is about, review their basic properties, and define the general dynamical QPT scheme. The DM has been already introduced in chapter 1 so we will not discuss it again here. There is only a difference with respect to Eq. 1.1. The microscopic Hamiltonian for the DM used in this chapter will be,

$$\hat{H}_{\text{DM}}(t) = \frac{1}{2} \sum_{i=1}^N \hat{\sigma}_z^{(i)} + \hat{a}^\dagger \hat{a} + \frac{\lambda(t) + 1}{2\sqrt{N}} (\hat{a}^\dagger + \hat{a}) \sum_{i=1}^N \hat{\sigma}_x^{(i)}. \quad (2.1)$$

In other words, there is just a different convention for writing the interaction parameter. It is made for convenience, because that way many equations will be easier to write.

The next model is TFIM, which consists of a one dimensional chain of  $N$  qubits with nearest-neighbor couplings and under the action of an external transverse field. Its Hamiltonian is,

$$\hat{H}_{\text{TFI}}(t) = - \sum_{i=1}^N \left\{ \hat{\sigma}_z^{(i)} + (\lambda(t) + 1) \hat{\sigma}_x^{(i)} \hat{\sigma}_x^{(i+1)} \right\}, \quad (2.2)$$

where cyclical conditions are imposed in the sum ( $\hat{\sigma}_\alpha^{(1)} = \hat{\sigma}_\alpha^{(N+1)}$ ). This model is exactly solvable [89], and it has been recently simulated by ultra-cold atoms [90]. Finally, the LMGM is the totally connected version of the TFIM. Its Hamiltonian is of the form [91],

$$\hat{H}_{\text{LMG}} = \sum_{i=1}^N \hat{\sigma}_z^{(i)} + \frac{\lambda(t) + 1}{N} \left( \sum_{i=1}^N \hat{\sigma}_x^{(i)} \right)^2. \quad (2.3)$$

As well as it happens with the DM, the kind of states that are going to be relevant for the LMGM are those in the maximal Dicke manifold in such a way that Eq. 2.3 can be written with collective operators  $\hat{J}_\alpha$ . The dynamics will be also concentrated in the even parity sector, as this is also a conserved quantity in the LMGM. This model has analytical solutions [92], but their implementation is usually much more cumbersome than the numerical treatment. In fact, Hamiltonian in Eq. 2.3 generates a bidiagonal matrix, which renders feasible the handling of system sizes up to  $N = 2^{13}$ . Proposed realizations of the LMGM are widespread from BECs [93] to circuit QED [94]. Figure 2.2a depicts cartoons of the three models.

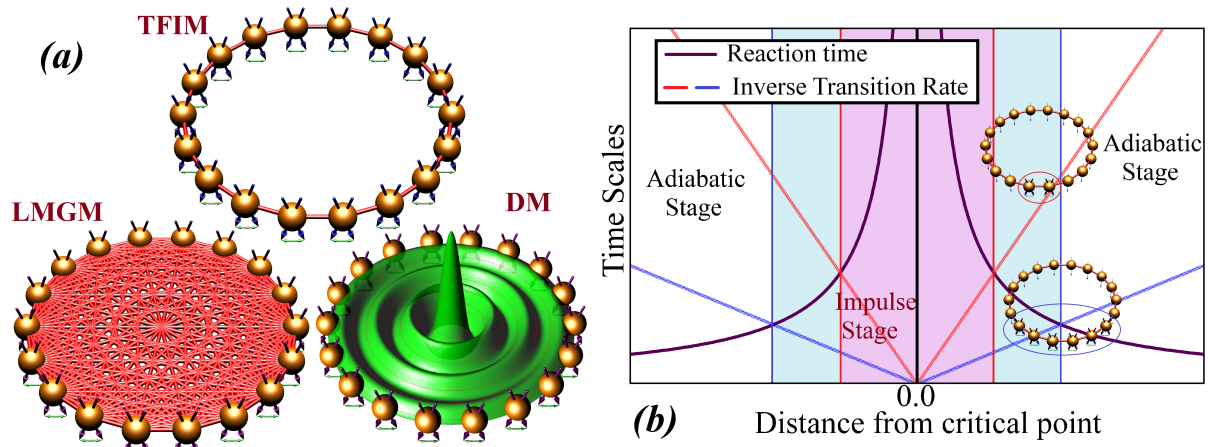


FIGURE 2.2: (a) Illustration of the three different spin networks we will consider in this chapter: the upper part picture represents the TFIM; the lower left part, the LMGM; and the lower right part, the DM. The TFIM have a 1D spatially distributed interaction, while both DM and LMGM are totally connected lattices which belong to the same equilibrium universality class. In the DM, the field mode can be seen as the mediator of the all-to-all interaction among the qubits, while in the LMGM the interaction is direct. (b) Schematics of the Kibble-Zurek mechanism across a QPT. When a system is made to dynamically cross a QPT at relatively low velocities, it can follow the adiabatic evolution during most part of the evolution except around the QCP, where it enters an impulse stage. At this stage the system has not enough time to adapt to the changing order of the ground state, and then only a partial order is gained after entering the adiabatic stage at the other side of the QPT. The level of order acquired during this process depends on the velocity at which the crossing is made, and also on the system size. The KZM makes predictions about the final results by means of simple scaling relations involving the equilibrium critical exponents.

All three models have a second order QPT at  $\lambda = 0$  in the TL [10, 35, 95], the  $\lambda < 0$  part is characterized by zero excitations (all qubits in  $-z$  state) while the  $\lambda > 0$  forms of superposition of  $x$  and  $-x$  states. Around the phase boundary, the TFIM model has a divergence in the correlation length of the form  $\xi \propto \lambda^{-\nu}$  and a behavior of the energy gap  $\Delta \propto \lambda^{\nu z}$ , with critical exponents  $\nu = z = 1$  [10]. The LMGM and DM belong to the same equilibrium universality class, which means that many aspects of their QPT have strong equivalences. In particular, they have the same critical exponents, being  $\nu = \frac{3}{2}$  and  $z = \frac{1}{3}$ . The interpretation of the critical exponent  $\nu$  in those totally connected spin networks is subtler than in spatially connected systems like the TFIM, since no clear correlation length can be defined. However, extrapolations of such exponent have been established by interpreting the systems as the infinite dimensional limit of finitely connected networks [96].

To describe the crossing of the QPT, we will analyze a simple case in which the annealing parameter evolves linearly as  $\lambda(t) = vt$  since it leads to relatively simple formulae, though we stress that extension to any power-law time-dependence is straightforward [12]. The control parameter rate  $v = \frac{d\lambda}{dt}$  will be called the annealing velocity (AV). We start in the ground state  $|\varphi_0(t_i)\rangle$  with  $\lambda(t_i) = -1$  at ‘negative’ time  $t_i = -v^{-1}$  (i.e. the zero of time is defined as the instant where the system passes through  $\lambda(t_i) = 0$ ). This starting state represent zero interaction among the qubits. The three systems will evolve with a time-dependent state  $|\Psi(t)\rangle$  across the QCP, until positive time  $t_f$  where  $\lambda(t_f) = 1$ . For slow enough AV, the system should

end in a final ground state  $|\varphi_0(\lambda(t_f))\rangle$  representing perfect adiabatic evolution. However the QCP hinders the many-body system from achieving this result, since the minimal energy gap makes it easy for the system to jump out of the ground state (see Fig. 2.1). Since this gap gets smaller as the system size increases, ever slower quenches are necessary to keep the system in the ground state. Hence the fundamental effect of the crossing of QPTs is the loss of adiabatic evolution.

In thermodynamics, at finite temperature, an adiabatic process is defined by the conservation of entropy. However, in close quantum systems this definition is not useful since entropy is conserved and set to zero during an unitary evolution. Instead, other indicators of adiabatic evolution must be chosen. During this chapter we employ two main indicators. The first one is **ground state fidelity**  $p_0$ , which was already defined in Eq. 1.13. It lies in the interval  $0 \leq p_0 \leq 1$  and has its maximum value for perfect adiabatic evolution. The second one is **heating**,

$$Q(t) = \langle \Psi(t) | \hat{H}(\lambda(t)) | \Psi(t) \rangle - E_0(\lambda(t)), \quad (2.4)$$

which is the difference between the actual expected value of energy and the instantaneous ground state energy. Heating is always non-negative, and for adiabatic evolution is zero [97].

## 2.3 The Kibble-Zurek Mechanism

The KZM is a paradigm for analyzing dynamical defect formations across phase boundaries. Despite it was originally devised for exploring the cosmological formation of structures [66–68], the general scheme of the KZM can be extended to the crossing of thermodynamic phase transitions and even to QPTs. The mechanism relies on an *adiabatic-impulse-adiabatic* approximation, where excitations only emerge during a finite window around the QCP. The interval of the impulse regime is defined by the moment when the characteristic time of the parametric driving is comparable to the reaction time estimated by the inverse first excitation energy gap [8].

In more specific words, the KZM for QPTs can be explained as follows. The rate at which the annealing parameter changes is essential for achieving adiabatic control, and a time scale like  $\tau_v \equiv \lambda(t) \left(\frac{d\lambda}{dt}\right)^{-1}$  perfectly characterizes this aspect and it is called inverse transition rate [8]. Also, the adiabatic theorem determines a time scale that measures the disposal of the system to achieve adiabatical evolution, let us call it reaction time  $\tau_R$ , and it can be thought as the time the system requires to adapt itself to the changes in its Hamiltonian in order to stay at the ground state. This reaction time is usually inversely proportional to the energy gap between the ground state and the first excited state [98]. In a neighborhood around the QCP, the reaction time tends to diverge and the inverse excitation rate cancels out, as Fig. 2.2b illustrates. Given the meaning of these time scales, one should expect that when  $\tau_R \ll \tau_v$  the conditions for

adiabatical driving are satisfied and the dynamics of the system consist of the trivial pursuit of the ground state; this regime of evolution is called the adiabatic stage. On the other hand, when this condition no longer holds, the system loses the ability of retaining the properties of the ground state and it enters an impulse stage. Then one proposes the *adiabatic-impulse-adiabatic* approximation, which predicts that the system *freezes* at the moment of entering the impulse stage and it remains so until returning to an adiabatic stage at the other side of the QCP. Therefore, the system enters the other phase *quenched*.

According to the definitions of critical exponents, divergence of the reaction time is characterized by a power law,

$$\tau_R \propto |\varepsilon|^{-\nu z}; \quad \xi \propto |\varepsilon|^{-\nu}, \quad (2.5)$$

where we have also included the divergent behavior of correlation length  $\xi$  inherent to the phase transition. Hence, the point at which the system freezes defines a characteristic time  $t_C$  and a characteristic length  $\xi_C$ . In terms of the AV  $v$ , these characteristic magnitudes are,

$$t_C \sim v^{-\frac{\nu z}{1+\nu z}}; \quad \xi_C \sim v^{-\frac{\nu}{1+\nu z}}. \quad (2.6)$$

It is at this point when the KZM becomes a predictive paradigm. It states that many final properties of the system after the crossing of the phase boundary can be simply estimated by dimensional analysis of the characteristic magnitudes in Eq. 2.6. For instance, if the system has some sort of excitation density  $n_{\text{exc.}}$ , it will be of the order  $\xi_C^{-d}$ , where  $d$  is the spatial dimension of the system. In the TFIM, this density can be thought as the inverse of average size of the domains that acquire the new phase order (see small TFIM cartoons in Fig. 2.2b). Despite the critical exponents present in the power-law scaling functions emerge from the TL, the effects can be extrapolated to the finite-size case. In fact, the KZM has been successfully applied to near-adiabatic QPT dynamics in spatially connected lattice models with finite size [72–75]. This extrapolation is possible thanks to the length scale defined by correlations, which makes the prediction essentially identical to the TL case if the system size is big enough to contain several ordered domains.

## 2.4 Final dynamical scaling collapse after the critical threshold

Figure 2.3 shows both heating  $Q(t)$  and ground state fidelity  $p_0(t)$  for  $\lambda \in [-1, 1]$  for the ramped crossing of the QPT in the TFIM, the LMGM, and DM as well. For  $\lambda < 0$ , the behavior at a given  $v$  is independent of size, with virtually no loss of adiabaticity. Above the critical threshold, however, excitations form following a **scaled annealing velocity** with respect to system size,

$$\Lambda = N v^\mu. \quad (2.7)$$

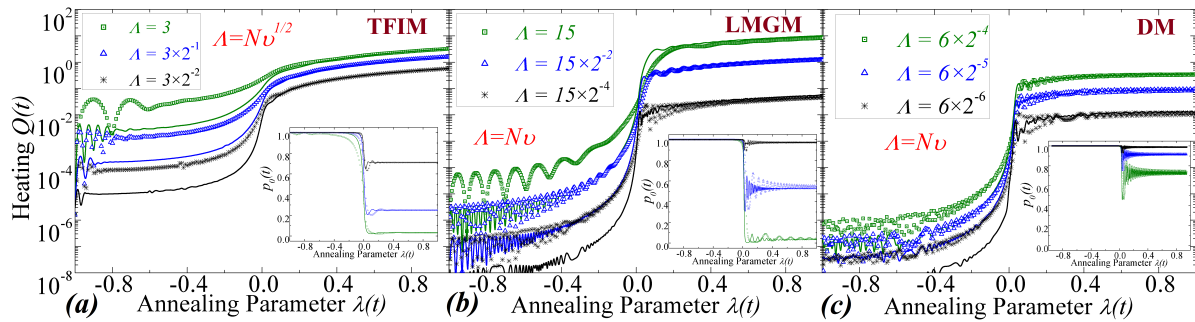


FIGURE 2.3: Time-evolution of heating  $Q(t)$  (insets show ground state fidelity  $p_0(t)$ ) for (a) TFIM, (b) LMGM, and (c) DM. Continuous lines represent results for  $N = 160$  (TFIM),  $N = 2^{11}$  (LMGM) and  $N = 2^9$  (DM) qubits, while symbols correspond to half that size. When annealing velocity  $v$  is scaled properly with  $N$ , data collapse to a single size-independent value occurs after crossing the QCP, around  $\lambda = 0$ .

Then, after the QPT, all systems exhibit a form of final value dynamical scaling. Also, the almost vertical step around  $\lambda = 0$  shows that the evolution is essentially adiabatic, except for the narrow interval around the QCP where the major excitations are formed. Furthermore, Fig. 2.4 shows that a power law relation exists in final heating of the TFIM, as well as in the LMGM and DM. A similar profile could be done with final ground state fidelity. This suggests that the KZM could be correct in all three spin networks considered in this chapter, provided the AV is scaled adequately in each case. The KZM is supposed to predict those final value dynamical exponents [8]. In the case of heating, from Eqs. 2.6 and 2.7, we have the KZM scaling exponent to be,

$$Q_f \sim 1/\tau(t_C) \sim t_C^{-1} \sim v^{\frac{\nu z}{\nu z + 1}} \sim \Lambda^{\frac{\nu z}{(\nu z + 1)\mu}}, \quad (2.8)$$

which is deduced from the energy gap when the impulse-adiabatic threshold is reached. For the TFIM, the KZM prediction is  $Q_f \sim \Lambda^1$ , which has been confirmed [73, 74]. By stark contrast, the totally connected models do not match this estimate: instead of the KZM exponent of  $1/3$ , a scaling  $Q_f \sim \Lambda^{3/2}$  has been found. This exponent was already established in the literature for the LMGM [79]; and we confirmed that the DM, its equilibrium universality class partner, has the same dynamical scaling.

We then conclude that the KZM is not entirely valid for all-to-all spin networks like the DM and LMGM. This should not be that surprising, as some assumptions of the KZM are not valid in the totally connected case. In fact, the DM and LMGM have *no definite length at all*. Any correlation for any pair of constituents is exactly the same. So, in this sense, they must be considered spaceless. This means that any spatial scaling and diffusion of excitations cannot be the cause of scaling dynamical behavior, contrasting with what has been portrayed for finite-range models in the traditional KZM explanation. However, it is clear from Figs. 2.3 and 2.4 that universal dynamical scaling is still possible. We will see that we must look closer to what is happening in the critical threshold. Then we will establish size-independent results not only at a final stage of the critical process, but all throughout the dynamical critical evolution. The cause will be a critical universal structure that is not only defined by the TL pair of critical

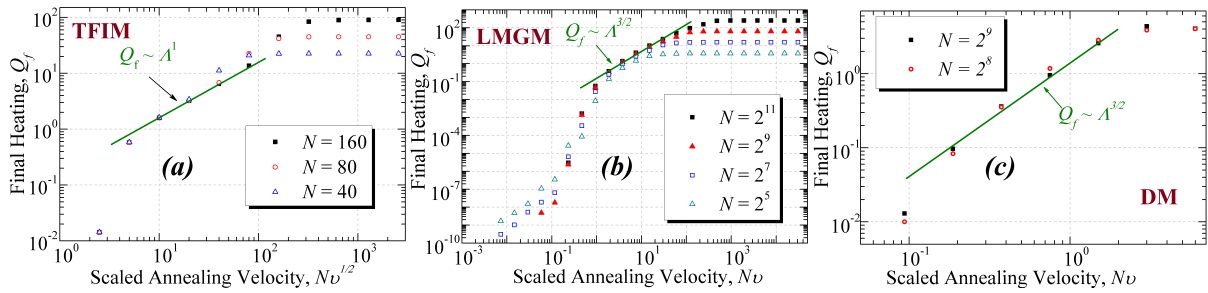


FIGURE 2.4: Dynamical scaling exponent of final heating in the near-adiabatic regime. The three models are presented in the same order as in Fig. 2.3. The KZM is able to explain the TFIM exponent since it takes into account the spatial size of the defects caused by the QPT dynamical crossing. However, this theory predicts an exponent of  $1/3$  for totally-connected models like the TFIM and the DM. This failure shows that the traditional KZM is not as broadly reliable. This justifies our development of continuous critical function scaling theory, which stays valid at both extremes of spin network connectivity. The theory has also more explanatory power, since it predicts continuous critical collapse instead of simple final defects scaling (see Fig. 2.6).

exponents; instead, we will construct a scaling theory all over the critical interval, in what could be called continuous critical function scaling.

The dynamical scaling for the DM and LMG set apart from those for the TFIM in one more aspect: the degree of collapse, i.e., the minimal system size at which non-scaled finite-size effects start to be negligible. This minimal size is much higher for totally connected networks. For system sizes over  $N = 60$ , the TFIM exhibits almost perfect scaling collapse [76]. On the other hand, it is clear in Fig. 2.3 that the DM needs much higher system sizes to make scaling apparent, and the LMG require even higher values of  $N$ . This difference lies in the way system sizes affect the critical threshold. All three systems depart from perfect adiabaticity because of infrared divergencies in the spectrum of low-energy modes in the TL [97]. These divergencies are cut off by the system's finite size itself and the more difficult this divergence is cut off by the system size, the weaker the scaling collapse that could be expected. In systems with finite-range interactions, excitations may be thought as quasiparticles along the lattice. Infrared divergencies are associated to quasiparticles of very long wavelengths and finite lattices set an upper bound to this length scale  $L$ . As  $N$  denotes the number of lattice vertices, it is easy to see that this length scale cut-off behaves as  $L \propto N^{1/d}$  where  $d$  is the lattice space dimension. Thus, higher dimension lattices, i.e., more connected lattices, require higher system sizes to exhibit universal dynamical behavior. This explains why the TFIM exhibits universal behavior at much lower system sizes as compared to both DM and LMG. The difference between the DM and LMG also has to do with the cutoff of infrared divergences, but not with respect to the connectivity of the lattice which for these models is the same. It has been argued that the cutoff can be made in open systems by a weak coupling to the environment, which would damp the very low energy excitations [97]. If the TL picture of the DM is compared with that of the LMG [34, 99], it can be observed that, for every single value of  $\lambda$ , the LMG looks composed by a single bosonic mode while the DM consists of two of them. In both cases, only one bosonic mode

suffers the vanishing of the energy gap while the second mode in the DM offers an effective dynamical bath, making easier for the system size to cut off the gap.

## 2.5 Continuous critical function scaling theory

We have already seen that the important aspects of the dynamical crossing of the QPT are defined around the critical threshold. Then we should look closer of what is happening there. But first, it is convenient to express the time evolution of the system in terms of instantaneous eigenstates:

$$|\Psi(t)\rangle = \sum_{n=0} a_n(t) e^{-i \int_{t_0}^t E_n(t') dt'} \left| \varphi_{\lambda(t)}^{(n)} \right\rangle, \quad (2.9)$$

where  $\hat{H}(t) \left| \varphi_{\lambda(t)}^{(n)} \right\rangle = E_n(\lambda(t)) \left| \varphi_{\lambda(t)}^{(n)} \right\rangle$  for every time  $t$ . The  $a_n(t)$  evolution follows

$$\frac{da_n(\lambda)}{d\lambda} = \sum_{m \neq n} e^{i v^{-1} \phi_{n,m}^{(N)}(\lambda)} \chi_{n,m}^{(N)}(\lambda) a_m(\lambda); \quad (2.10)$$

where  $\phi_{n,m}^{(N)}(\lambda) \equiv \int_0^\lambda \Delta_{n,m}^{(N)}(\lambda') d\lambda'$ , which is the integral of the energy gap between eigenstates  $n$  and  $m$ . The transition amplitudes  $\chi_{n,m}^{(N)} \equiv - \left\langle \varphi_{\lambda}^{(n)} \left| \frac{d}{d\lambda} \left( \left| \varphi_{\lambda}^{(m)} \right\rangle \right) \right. \right\rangle$  can be written as  $\chi_{n,m}^{(N)}(\lambda) = \frac{V_{n,m}^{(N)}(\lambda)}{\Delta_{n,m}^{(N)}(\lambda)}$  whenever eigenstates  $n$  and  $m$  are non-degenerate, and  $V_{n,m}^{(N)}$  are the matrix elements of the interaction part of the Hamiltonian, mediated by  $\lambda$ . The superscript  $(N)$  indicates that all the functions depend on the system size. Equation 2.10 is usually the central part of the Adiabatic Theorem [100], which states that if  $v \ll \left| \frac{\Delta_{n,m}}{\chi_{n,m}} \right|$ , then  $|a_n|$  remain constant. For sufficiently slow annealing, this is satisfied outside the QCP region, implying that only the eigenstates that reach a zero gap in the TL are relevant for the loss of adiabaticity. It is at this point that critical function enter the picture, since  $\chi_{n,m}$  and  $\Delta_{n,m}$  obey a scaling relation when  $|\lambda| \ll 1$  [40, 77, 101]:

$$\chi_{n,m}^{(N)}(\lambda) = N^{1/\nu} C_{n,m}(x), \quad (2.11)$$

$$\Delta_{n,m}^{(N)}(\lambda) = N^{-z} D_{n,m}(x); \quad (2.12)$$

where  $x \equiv N^{1/\nu} \lambda$  with  $\nu$  and  $z$  determined through the power-law behavior in the TL [10, 44]. Figures 2.5a-b confirm the existence of critical function in all three models. It can be seen that these functions start matching the TL power-law behavior for sufficiently large  $N$  and  $x$ .

The main result concerning continuous critical function scaling is that the evolution in Eq. 2.10 can now be cast in size-independent form:

$$\frac{da_n(x)}{dx} = \sum_{m \neq n} e^{i \Lambda^{-1/\mu} \Phi_{n,m}(x)} a_m(x) C_{n,m}(x), \quad (2.13)$$

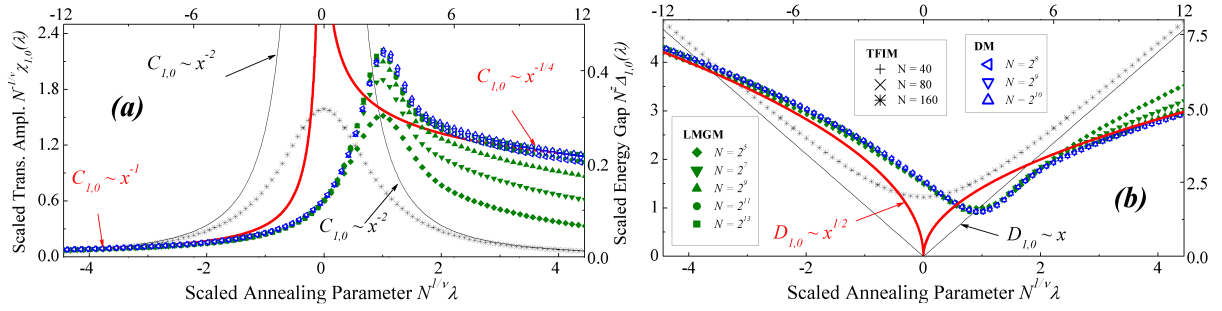


FIGURE 2.5: Universal behavior of finite-size critical functions (a)  $C_{1,0}$  and (b)  $D_{1,0}$  as defined in Eqs. 2.11 and 2.12. Symbols show results for system size  $N$  while continuous curves are power-law predictions in the TL. (Thick red line is for both DM and LMGM. Thin black line is for TFIM). Scales for the DM and LMGM are shown left-bottom and right-top respectively, and are set to show that critical functions for both models have the same shape since they belong to the same universality class. Horizontal scale for the TFIM is at the top, while vertical scale is not present, but it goes up to 25 in (a) and 0.25 in (b).

where the scaled velocity is again  $\Lambda = Nv^\mu$  ( $\mu = \frac{\nu}{1+z\nu}$ ), and the dynamical phase difference is,

$$\Phi_{n,m}(x) = \int_0^x D_{n,m}(x') dx' . \quad (2.14)$$

Equation 2.13 predicts universal results in terms of excitation probabilities  $p_n \equiv |a_n|^2$ , and the ground-state fidelity. As the energy spectrum has a regular behavior [34, 76, 99], the heating will also be universal since  $Q \equiv \sum_n p_n \Delta_{n,0}$ . This prediction is confirmed in Fig. 2.6 with both adiabatic quantifiers behaving in a size-independent manner across the critical region. Hence the generalization from critical exponents to critical functions expands the description from a restricted final value collapse in Fig. 2.3, to a complete temporal picture of the collapse in Fig. 2.6.

Our new continuous picture based on critical functions includes the traditional results predicted both by the KZM and by adiabatic QPT theory as special cases, since both can be expressed as power-law dependencies at the end of the quenching process [79]. Adiabatic phase transitions occur when there is even a lower probability of leaving the ground state than in the KZM. In such a limit, the following approximation of Eq. 2.13 holds for  $n \neq 0$ :

$$a_n(\lambda) \approx \int_{-1}^{\lambda} e^{iv^{-1}\phi_{n,0}(\lambda')} \chi_{n,0}(\lambda') d\lambda' . \quad (2.15)$$

Since the integrand is only non-negligible around the QCP, it follows that  $|a_n| \sim v$ , for which  $p_n \sim v^2$  and hence  $Q_f \sim \Lambda^{2/\mu}$ . The lower left part of Fig. 2.4b, shows that adiabatic exponent in the LMGM. The critical functions for totally connected networks give some hint of the way the KZM predictions fail. Figure 2.5a reveals that in the  $\lambda > 0$  phase, there is an anomalous  $x^{-1/4}$  dependence caused by a divergent  $\chi \sim N^{1/2}$  transition amplitude [102, 103]. Furthermore, in the  $\lambda < 0$  phase, a  $x^{-1}$  dependence is present. Such exponents are specific to all-to-all networks like the LMGM and DM, and this difference is not taken into account in the KZM. Other totally

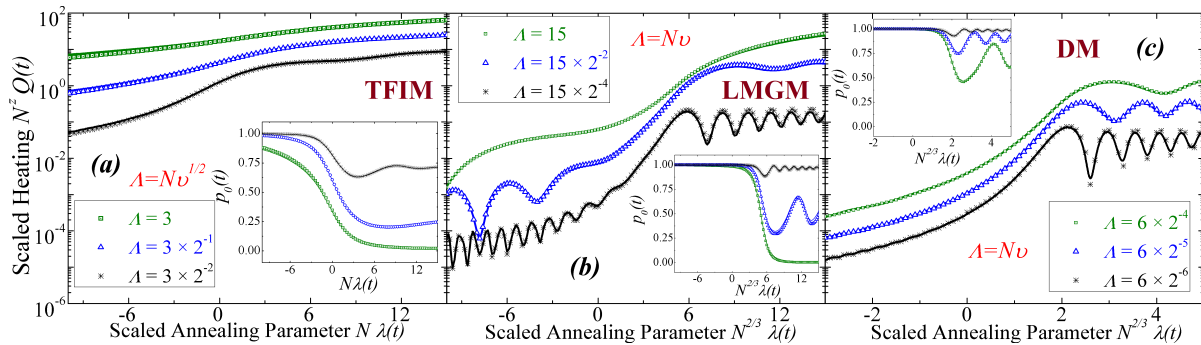


FIGURE 2.6: Magnification around QCP for the three models as in Fig. 2.3, with scaling of  $Q(t)$  and  $\lambda(t)$ . A continuous-in-time size-independent behavior is revealed, as predicted by Eq. 2.13 but outside the scope of critical exponent analysis.

connected models have been recently proven to follow KZM predictions [104], but those findings belong to the Rabi model, in the  $z = 2$  and  $\nu = 1/4$  universality class. We think that the absence of anomalies in the Rabi model as the ones we are seeing in the LMGM and DM has much to do with the success of the KZM in it.

Complete time-evolution curves of observables during linear ramping of a control parameter were already shown to collapse in one-dimensional networks like the TFIM [72, 76, 77]. But their explanations resorted to different approximations as adiabatic perturbation theory or the continuity of the density of states around the QCP. In such cases, the spatial distribution of the network was always acknowledged in the interpretation. All that hindered the full range of network connectivities and times scales at which the continuous dynamical scaling collapse is to be found. Instead, we present the scenario in its very essential components, which gives it much greater scope. We believe that this is a major step in extending the finite size scaling theory in critical phenomena started by Fisher and Barber [105], but now to the non-equilibrium situation of near-adiabatic crossing of a QPT.

## 2.6 The partition of the equilibrium universality class

The failure of the KZM prediction for LMGM and DM highlights the accuracy of a dynamical function approach as compared to power-law relations based on critical exponents. Dynamical critical functions provide a full time-resolved picture of dynamical scaling in the near-adiabatic regime, even around the critical threshold where excitations have not yet stabilized. The DM and the LMGM seem to still belong to the same dynamical universality class, at least in terms of their dynamical critical exponents, suggesting that they should evolve in a virtually equal manner. Then, it would be very interesting to have such a degree of equivalence in the continuous collapse we have unraveled through critical functions. This would have crucial implications for the design and cross-checking of QPT annealing schemes, and perhaps more importantly, for quantum simulations [88]. One could imagine adiabatic quantum simulation protocols, when

a specific model is used to explore realizations of another one in the same universality class. Examples in the TFIM and Bose-Hubbard models have demonstrated the viability of such approach [76, 90]. As the DM has been already experimentally realized with ultra-cold atom simulations while LMGM realizations is still ambiguously experimentally probed, the above possible equivalency will allow to test LMGM physics in the lab at the near-adiabatic regime. In the end, the LMGM can be seen as the DM where the interaction through the radiation mode is summarized by an effective qubit-qubit interaction [39].

The fact that the curves for LMGM and DM in Figs. 2.5a-b have essentially the same shape, might erroneously be taken as sufficient justification for using one as a quantum simulation of the other – however, this is not true. No matter how a dynamical curve in Fig. 2.6b is scaled, its shape will never completely match any curve of Fig. 2.6c. Instead, a thorough examination of Eq. 2.13 reveals that equivalence between both near-adiabatic evolutions can only be achieved if the functions  $\{C_{n,m}(x)\}$  scale as  $C_{n,m}^{\text{DM}}(\alpha x) = \alpha^{-1} C_{n,m}^{\text{LMGM}}(x)$ , which is a much more stringent condition that is undetectable through critical exponent analysis. In short, although equilibrium equivalence between systems around the QCP can be accomplished just by having identical critical exponents, achieving *continuous dynamical* equivalence requires further tuning of model parameters, thereby partitioning the traditionally static universality classes into *subsets* of dynamically equivalent systems. This new classification through continuous critical functions, that predicts near-adiabatic even qualitatively different for systems with exactly the same critical exponents, is another indication of how much restricted is the KZM with respect to our theory.

## 2.7 Conclusion

We revealed universal dynamical scaling behavior across near-adiabatic QPTs in networks ranging from traditional spatial systems (TFIM) to fully connected ones (DM and LMGM). Our findings, which lie beyond traditional critical exponent analysis like the KZM and adiabatic perturbation approximations, are applicable even where excitations have not yet stabilized and hence provide a time-resolved understanding of QPTs encompassing a wide range of near-adiabatic regimes. We show explicitly that even though two systems may traditionally belong to the same universality class, they can have very different adiabatic evolutions. This implies a partition of the equilibrium universality class into several dynamical ones. Because of that, more stringent conditions need to be imposed for quantum simulations, where one system is used as surrogate of the other. Thanks to the several peculiarities that totally connected lattices like the LMGM and DM exhibit in their near-adiabatic dynamical scaling across a second-order QPT, we have been able to isolate its only necessary and sufficient condition; namely the continuous critical function theory. These insights are valuable extensions of finite-size scaling theory

to the non-equilibrium continuous scenario with many valuable directives for applications in near-adiabatic quantum control.

## Chapter 3

# The full dynamical QPT regime of Dicke Model

In this chapter we continue addressing the dynamical crossing of the QPT of the DM. But now we depart from the near-adiabatic range of annealing velocities, and explore all the range of possibilities up to the sudden quench limit. In the process, we will discover that well in between those limit regimes lies a rich set of outstanding non-equilibrium phenomena that had remain unnoticed. The wealth of novel effects include giant magnification of light-matter entanglement, a dynamical separate enhancement of light and matter squeezing, robust many-body quantum states, and more. All of them among the most coveted quantum resources. We will thoroughly establish when and how each of these effects arise, including scaling of system size and control parameter rates. We will even evaluate the robustness of our results against disturbances caused by the environment. We believe that results present in this chapter open new horizons on the way strong interactions in light-matter systems under non-equilibrium can be used to accomplish greatly sought-after quantum control protocols.

### 3.1 Introduction

Many-body quantum dynamics lie at the core of many natural phenomena and proposed quantum technologies, including information processing through schemes such as adiabatic quantum computing [7, 84]. Achieving the controllable generation and manipulation of entanglement over many qubits is a key challenge, while doing so in light-matter systems is highly desirable for optoelectronic implementations [106]. QPTs can provide a naturally occurring entangled state and it is known that the entanglement can be enhanced at the critical point [38, 107]. The ground state, and hence entanglement, of a quantum system like the DM can be varied in a controlled way through adiabatic perturbations, though this is in principle an infinitely slow

process [8]. We will see that faster protocols can be far more advantageous to accomplish such quantum control goals.

Recent studies have focused on time-dependent perturbations around the QPT of the DM that are either very slow (adiabatic) [12] or very fast (sudden quench) [13]; or small dynamic oscillations around a phase space region [43]; or static coupling after a sudden quench [14, 15, 108–110]. Despite results of present chapter also encompass all dynamical regimes, including adiabatic to dispersive, we are going to be concerned on an unexplored yet very rich intermediate set of annealing velocities. In this regime, we have found a remarkable dynamical amplification of critical quantum effects as compared to the static or adiabatic QPT values. This includes giant light-matter entanglement [17], preceded by a remarkable amplification of squeezing for separate subsystems [18]. The high light-matter entanglement phase is also characterized by complex and chaotic properties of the matter and field subsystems, in what could be deemed as a dynamical chaotic phase with a spontaneous symmetry breaking. The chaotic stage also features increased superradiance. We provide a precise definition and understanding of the conditions at which this complex phase arises, including its scaling according to system size and annealing velocity. As light-matter systems are at the core of most realizations of macroscopic quantum control schemes, our assessment sheds light to processes important for applications ranging from quantum metrology [6, 111, 112], to quantum information technologies [113, 114]. Our results extend current understanding of coupled light-matter systems beyond the equilibrium ground state [38–42], and also beyond more recent studies of out-of-equilibrium critical behavior [12, 43, 48, 115, 116].

Our results will also clarify the interrelation of various forms of quantum correlations within a light-matter system. In the DM, both the matter and field are known to act as mediators of an effective non-linear self-interaction with each other [39, 42]. These non-linear interactions produce interesting phenomena in both atomic and optical systems [117, 118]. Among the most relevant effects, there is the strong collapse and revival of squeezing [119, 120], which in many matter states can be related to atom-atom entanglement [121]. As the non-linear interactions are only effective, it is of essential relevance to understand how the eventual matter-field correlations relates to the generation of quantum squeezing in each subsystem.

This chapter is structured as follows. Section 3.2 present the dynamical setting and methods of analysis. Section 3.3 explains the general profile of the dynamical evolution under the perspective of light-matter entanglement, highlighting the presence of dynamical magnification of it in the intermediate velocities regime. It is followed by section 3.4, which is an explanation of the different AV regimes by means of dynamical symmetry breaking. Matter and light subsystem dynamical profiles are presented in section 3.5, both for squeezing and their order parameters (OP). Then a general explanation of the results, both system-wide or at the subsystem level, is made in section 3.6 by the realization that the dynamics involve effective non-linear interactions. Section 3.7 gains further insight from the point of view of phase space representations of

the subsystems. The next two sections establish the consistency of our results, demonstrating their robustness under dissipative effects (section 3.8), and for different system sizes by means of scaling relations (section 3.9). Section 3.10 concludes with some final general remarks.

## 3.2 Theoretical framework

### 3.2.1 The open Dicke Model

As we are going to deal with losses later in this chapter, the state of the total DM system must be represented by a density matrix  $\hat{\rho}_S$ , evolving under a unitary part generated by Eq. 1.2, and a dissipative part caused by radiation losses of the field cavity. The time evolution is then expressed by a master equation [31],

$$\begin{aligned} \frac{d}{dt}\hat{\rho}_S &= -i \left[ \hat{H}, \hat{\rho}_S \right] \\ &+ \kappa (\bar{n} + 1) \left( 2\hat{a}\hat{\rho}_S\hat{a}^\dagger - \left\{ \hat{a}^\dagger\hat{a}, \hat{\rho}_S \right\} \right) + \kappa\bar{n} \left( 2\hat{a}^\dagger\hat{\rho}_S\hat{a} - \left\{ \hat{a}\hat{a}^\dagger, \hat{\rho}_S \right\} \right), \end{aligned} \quad (3.1)$$

where  $\kappa$  is the damping rate of the cavity, and  $\bar{n}$  is the thermal mean photon number. At initial time  $t = 0$ , the system state is

$$\hat{\rho}(0) = |-N/2\rangle_z \langle -N/2|_z \otimes \frac{e^{-\beta\hat{a}^\dagger\hat{a}}}{\text{tr}\{e^{-\beta\hat{a}^\dagger\hat{a}}\}}, \quad (3.2)$$

where  $e^{-\beta} = \bar{n}/(\bar{n} + 1)$ . Thus, the initial state at  $\lambda(0) = 0$  corresponds to an unentangled state formed by the qubit ground state times the field thermal equilibrium state at inverse temperature  $\beta = 1/(k_B T)$ , with  $k_B$  the Boltzmann constant. The controlled interaction will change with an annealing velocity (AV)  $v$  by a linear ramping:  $\lambda(t) = vt$ . The interval of interest is  $\lambda \in [0, 2]$ , well across the QPT. In this chapter we will analyze quantum properties of the main DM constituting subsystems. Any subsystem  $A$  will be described by a density matrix  $\hat{\rho}_A$ , defined as the trace with respect to the other degrees of freedom:  $\hat{\rho}_A(t) = \text{tr}_{S-A}\{\hat{\rho}_S\}$ .

We will explore the dynamical development of quantum properties in subsystems and in the composed coupled matter-light as well, caused by the ramped QPT crossing, without resorting to any common simplifications like mean-field, rotating wave or semi-classical approximations. As we have already mentioned, our main results lie at AV values outside the well-known adiabatic and sudden quench regimes, where quantum correlations such as entanglement and squeezing of each separate subsystem can get significantly enhanced. Exact numerical solutions have been obtained by integrating Eq. 3.1. When  $\kappa = 0$ , evolution lies on the pure Hilbert space and it is generated by the DM Hamiltonian. Otherwise, evolution lies in the space of density matrices and its generator is the total Liouvillian superoperator of Eq. 3.1 [31]. Thus, the dimension of the numerical evolution vector space is squared as soon as the unitary condition is broken.

As the dimension of the field Hilbert space is infinite, the Fock basis  $\{|n\rangle\}$  is truncated up to a number where numerical results converge. We have taken advantage of every simplifying condition, such as parity conservation when  $\kappa = 0$ . Also, as it has been in previous chapters, we set resonant energies in Eq. 1.2:  $\epsilon = \omega = 1$ .

### 3.2.2 Witnesses of quantum properties

Because of the all-to-all situation, the density matrix of any set of  $M \leq N$  qubits is the same and lies on the maximal Dicke manifold  $\hat{\mathbf{J}}^2 = (J + 1)J$ , with  $J = M/2$ . The first quantum property of matter that we address is entanglement, which for a 2 qubit subsystem is measured by Wootters concurrence  $c_W$  [122]. The second one is spin squeezing, which is highly related to multipartite entanglement and usually expressed in terms of a squeezing parameter  $\xi_q$  [123]. Under unitary evolution ( $\kappa = 0$ ), when parity of the total system is even and conserved,  $c_W$  and  $\xi_q$  are explicitly related whenever the concurrence is different from zero [124, 125],

$$1 - \xi_q^2 = (N - 1)c_W = \frac{2}{N} \left( \left| \langle \hat{J}_+^2 \rangle \right| + \langle \hat{J}_z^2 \rangle - \frac{N^2}{4} \right). \quad (3.3)$$

The factor  $N - 1$  in the concurrence is a direct manifestation of the monogamy of entanglement [126], since each qubit is equally entangled to any other one and hence the finite amount of possible entanglement is evenly distributed. There is also an analogous squeezing parameter in the field mode, though it cannot be directly related to a form of entanglement. It is expressed in terms of the variance and covariance of field quadratures [127],

$$\xi_b^2 = \text{var}(x) + \text{var}(p) - \sqrt{(\text{var}(x) - \text{var}(p))^2 + 4\text{cov}(x, p)^2}. \quad (3.4)$$

We will also use phase space representations of both main subsystem's density matrices. The field mode will be described by the Wigner distribution, already defined in Eq. 1.14. The matter states will be visualized by the Agarwal-Wigner function (AWF), which is a Bloch sphere representation of the qubit's density matrix [128],

$$W_q(\theta, \phi) = \sum_{l=0}^N \sum_{m=-l}^l T_{l,m} Y_{l,m}(\theta, \phi), \quad (3.5)$$

where  $Y_{l,m}$  are the spherical harmonics. Terms  $T_{l,m} = \text{tr} \left\{ \hat{\rho}_q \hat{T}_{l,m} \right\}$ , with  $\hat{\rho}_q$  the qubit subsystem density matrix, are the expected values of the multipole operator,

$$\hat{T}_{l,m} = \sum_{M, M'=-j}^j (-1)^{j-m} \sqrt{2l+1} \begin{pmatrix} j & l & j \\ -M & m & M' \end{pmatrix} |jM\rangle \langle jM'|, \quad (3.6)$$

where  $j = N/2$ , and  $\begin{pmatrix} j & l & j \\ -M & m & M' \end{pmatrix}$  is the Wigner  $3j$  symbol.

When global unitary condition is satisfied, the total composite system is always in a pure state, and both radiation and matter have the same value of the Von-Neumann entropy  $S_N$  due to Schmidt decomposition. Then, this entropy  $S_N$  provides a quantitative measure of the degree of entanglement between matter and light [32]. However, in order to have an idea of the decoherence effects of a leaky cavity, we had to analyze the DM as an open system, and then,  $S_N$  is no longer a good entanglement witness. Instead, we used quantum negativity in that case, whose non-zero value is a sufficient condition for bipartite entanglement in the open light-matter system [129]. Quantum negativity is defined as,

$$\mathcal{N}(\hat{\rho}) = \frac{\|\hat{\rho}^{\Gamma_q}\|_1 - 1}{2}, \quad (3.7)$$

where  $\hat{\rho}^{\Gamma_q}$  is the partial transpose of  $\hat{\rho}$  with respect to the matter subsystem, and  $\|\hat{A}\|_1 \equiv \text{tr} \left\{ \sqrt{\hat{A}^\dagger \hat{A}} \right\}$  is the trace norm.

### 3.3 Giant light-matter entanglement

Figure 3.1a summarizes the main finding of this chapter: A novel, dynamical light-matter regime with greatly enhanced system-wide properties including entanglement, when the light-matter coupling is driven at intermediate velocities. The peak entanglement value (purple) is far larger than the known equilibrium critical maximum [38], i.e. much larger than what can be achieved under adiabatic conditions. Also, this enhanced entanglement extends over a far broader range, well across the  $\lambda > \lambda_c$  region. As the AV increases, the critical onset point of light-matter entanglement is pushed toward larger  $\lambda$  values and is no longer represented by a sharp peak, but instead a wavy plateau. At much higher velocities beyond the giant entanglement regime,  $\lambda$  varies so fast that a sudden quench condition is achieved. Now the system is not quick enough to respond to the light-matter coupling, at least not in the  $\lambda \in [0, 2]$  interval of Fig. 3.1a.

Figure 3.1b demonstrates how the range of velocities that classify as ‘intermediate’ actually increases with increasing number of qubits  $N$ , meaning that the enhanced entanglement regime begins to dominate the space of behaviors as opposed to becoming a small niche. This regime can be imagined as lying between a lower bound AV  $v_{\min}$  which marks the adiabatic evolution, and an upper bound one  $v_{\max}$  defining the AV at which the sudden quench approximation starts to be valid. Specifically, Fig. 3.1b shows the dynamical phase diagram of the intermediate regime in which the giant entanglement occurs, including its scaling behavior. More details of scaling behavior will be given in section 3.9. It is clear that the adiabatic evolution is more difficult to achieve as the number of atoms increases. The other main variable is the value of  $\lambda_d$  reached by the annealing. The sudden quench condition requires higher AVs as this  $\lambda_d$  gets bigger. The oscillatory behavior near the adiabatic regime has been smoothed out in order to make the phase boundary visually clearer.

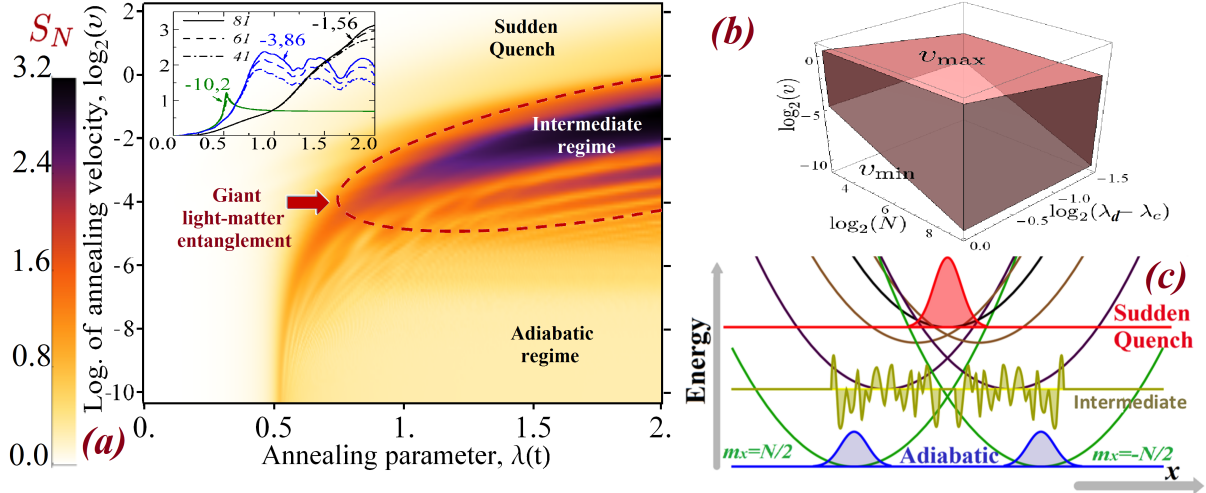


FIGURE 3.1: (a) We show the Von-Neumann entropy dynamic evolution profile (times varies from left to right) for a DM with  $N = 81$ . We use this quantity as a witness of light-matter entanglement when the system remains closed ( $\kappa = 0$ ). The figure span all regimes: from the adiabatic limit at the bottom, to the sudden quench limit at the top. The dashed line encloses an intermediate regime where giant dynamical magnification of light-matter entanglement occurs. The insets show the evolution for three selected values of  $\log_2 v$  (according to color) and three different system sizes (according to line style). (b) Schematic indicates energies of the three main outcomes when the light-matter coupling is increased at different velocities. Horizontal axis is the field position quadrature, both for sketches of the field Wigner function and for the harmonic confining potentials (parabola). The potential felt by the field depends on the eigenvalue  $m_x$  of the matter operator  $\hat{J}_x$ . If driving is very slow, the system stays cool in a symmetry broken ground state (blue curve) where each subsystem has entropy  $\log 2$  (low matter-light entanglement). If driving is very fast (sudden quench), the system still is in the initial  $\lambda = 0$  state (red curve), i.e. confined by the black parabola and light-matter entanglement is zero. For intermediate velocities, the system gets heated such that it occupies a complicated superposition of all the  $\hat{J}_x$  eigenvalues, and hence gets disturbed by all these potentials (yellow curve). (c) Dynamical phase diagram showing the new enhanced entanglement regime (shaded red) defined by instances where  $S_N > \log 2$  since  $S_N \rightarrow \log 2$  is the asymptotic value for the equilibrium ordered phase. For visual clarity in this figure, we take  $S_N > \log 2 + 0.05$ . Below a minimum annealing velocity  $v_{\min}$  the system's behavior is adiabatic, while for  $v > v_{\max}$  it corresponds to sudden quench. The adiabatic boundary depends on system size as  $v_{\min} \propto N^{-1}$ . The sudden quench boundary is size-independent, but depends on the value of  $\lambda$  that is reached during the driving:  $v_{\max} \propto (\lambda - \lambda_c)^{3/2}$ .

### 3.4 Dynamical symmetry breaking

We now develop a deeper theoretical understanding of the results in Fig. 3.1a, by analyzing the underlying quantum state in the three main dynamical regimes, as illustrated in Fig. 3.1c. We start by rewriting the Dicke Hamiltonian in Eq. 1.2 exactly as

$$\hat{H} = \omega \hat{b}^\dagger \hat{b} - \frac{4\lambda^2}{\omega N} \hat{J}_x^2 + \epsilon \hat{J}_z, \quad (3.8)$$

where  $\hat{b} = \hat{a} + \frac{2\lambda}{\omega\sqrt{N}} \hat{J}_x$ . In the  $\lambda > \lambda_c$  range, the last term becomes less and less relevant and the Dicke Hamiltonian can be seen as a radiation mode that feels a displaced harmonic potential whose values depend on the eigenstate  $|m_x\rangle$  of  $\hat{J}_x$  in which the matter system sits [13].

Specifically, if  $\lambda \gg \lambda_c$ , then

$$\hat{H} \approx \sum_{m_x} \left( \frac{1}{2} \omega \left[ \hat{p}^2 + \left( \hat{x} - \frac{2\lambda}{\omega\sqrt{N}} m_x \right)^2 \right] - \frac{4\lambda^2}{N} m_x^2 \right) |m_x\rangle \langle m_x|, \quad (3.9)$$

where we have used the quadrature operators of the radiation mode. The different confining potentials depending on the eigenvalue of  $\hat{J}_x$  are depicted by different parabolae in Fig. 3.1c. Importantly, the energy potential is symmetrical with respect to a change in sign in  $m_x$ , which is a source of degeneracy. In addition, as  $|m_x|$  gets bigger, the minimum value of the harmonic potential becomes lower. The ground state of this approximate Hamiltonian is any superposition of the form

$$|\psi_0\rangle = \cos \theta |N/2\rangle_{m_x} |-\beta\rangle + e^{i\varphi} \sin \theta | -N/2\rangle_{m_x} |\beta\rangle, \quad (3.10)$$

i.e. it corresponds to the two minimum parabolae. Hence the symmetry of the ground state is spontaneously broken. The field state  $|\beta\rangle$  is a coherent state with  $\beta = \frac{2\lambda}{\omega\sqrt{N}} m_x$ . As parity is preserved during the ramping, and adiabatic evolution keeps the energy in the lowest possible value, the projection of  $|\psi_0\rangle$  onto the even parity sub-space ( $\theta = \pi/4$  and  $\varphi = 0$  in Eq. 3.10) is the state achieved in this regime. Both the symmetry breaking and the adiabatic asymptotic value of entropy ( $S_N = \log 2$ ) in each subsystem can be explained by this double-well, since two coherent states are needed to describe each system.

The multiple potential picture in Fig. 3.1c and Eq. 3.9 is still valid for the intermediate and sudden quench regimes. As the AV increases, the process generates a relative heating with respect to the ground state. For high enough AV (sudden quench), the system stays essentially in its starting condition, and the heating is just the consequence of the initial state being very different from the instantaneous ground state. Despite this sudden heating being very high, the simplicity of the initial state (i.e. confined in the central energy potential) leads to no matter-light entanglement (i.e. one coherent state describes each subsystem). In the novel intermediate regime, by contrast, all confining potentials simultaneously perturb the system. A complicated superposition of non-trivial states for each parabola is generated, with complex and chaotic features. Since almost every eigenvalue of  $\hat{J}_x$  has a non-zero probability, the entropy of each subsystem is significantly higher than in the other two regimes. Due to its complex nature, there is no simple way to describe the structure of the dynamical state in the intermediate regime. This regime is embedded in the non-integrable part of the finite-size DM, which in the  $\lambda > 0.5$  phase has signatures of quantum chaos [44].

### 3.5 Enhancement of subsystem quantum properties

We now proceed to characterize our complex dynamical regime and the complete dynamical QPT profile by focusing on properties of each subsystem. Namely the matter subsystem composed by the all-to-all spin network, and the radiation mode subsystem.

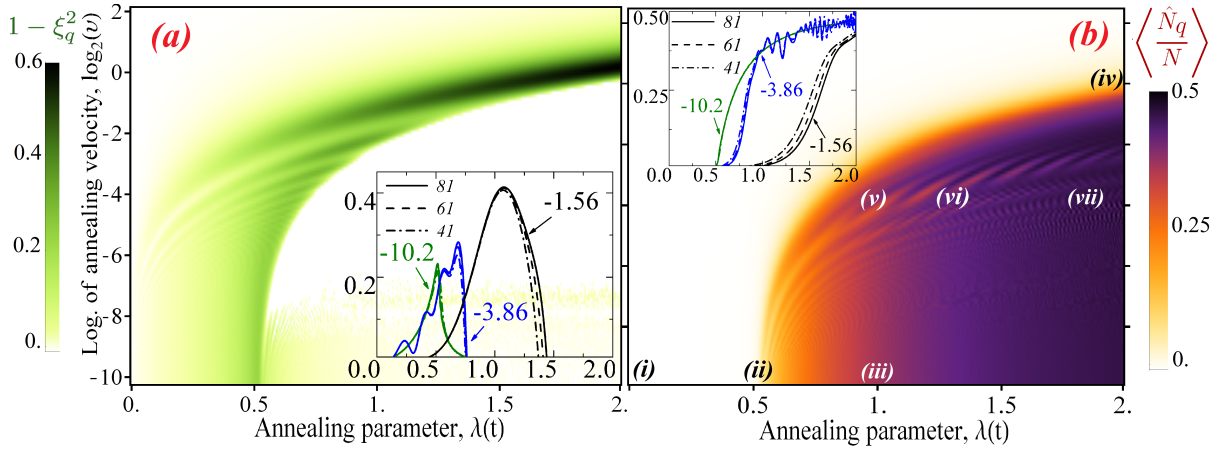


FIGURE 3.2: Dynamic profiles analogous to Fig. 3.1a of matter subsystem properties: (a) Two qubit concurrence  $c_W(N-1) = 1 - \xi_q^2$ , related to spin squeezing in Dicke manifold states (see Eq. 3.3), and (b) scaled order parameter (OP)  $\langle \hat{N}_q \rangle / N$  (see Eq. 1.3). In the insets we show that strong similarities exist for different values of  $N$ , pointing toward scaling properties of the results. Roman symbols in (b) hint at instants where phase space representations of subsystem states are depicted in Figs. 3.4 and 3.5.

A general picture of the time evolution of the matter quantum properties is revealed by means of spin squeezing (related to matter entanglement) and the expected value of its OP in Figs. 3.2a-b. We confirm again that under adiabatic conditions the spin squeezing or entanglement of the matter subsystem corresponds to those well known from the equilibrium QPT [38, 130]. Near the thermodynamic limit equilibrium phase transition  $\lambda = 0.5$ , adiabatic evolution exhibits a maximum value of entanglement followed by its decay and then the growth of the OP. The anti-correlation between squeezing and OP is present in the dynamical regime as well, but now there is a definite *sudden death* of entanglement, so that Figs. 3.2a and 3.2b are negative images of each other. As the range of high AV is entered, the position of the maximum point of squeezing and the onset point of the OP are pushed toward higher values of  $\lambda$ . Any value of  $v$  beyond the adiabatic limit leads to the dynamical regime, provided that the controlled interaction is ramped up to a high enough value. In other words, the sudden quench condition is only a consequence of the upper bound of  $\lambda$ .

More important than the position of maximum concurrence in the dynamical regime, is its value. It reaches up to three times the corresponding value of the adiabatic evolution (see Fig. 3.2a). This is a remarkable improvement for the collective generation of such a distinctive quantum property, and is due entirely to the system being in the non-equilibrium dynamical regime. For some given AV values, this magnified concurrence for different number of qubits  $N$  follows closely the scaling  $c_W(N-1)$  (see inset of Fig. 3.2a), keeping the spin squeezing parameter curves almost size independent, and gets modestly better as the system size grows. Some size dependent deviations are present in curves for the  $\log_2 v = -1.56$  case. The concurrence sudden death point is also virtually size-independent. The scaling properties of the dynamical regime will be discussed in section 3.9. Matter OP, for some chosen AVs, also shows very good

scaling collapse in its dynamical evolution, i.e., curves in inset of Fig. 3.2b are essentially size independent thanks to the scaling  $\hat{N}_q/N$  in the OP.

With respect to the maximum matter OP in Fig. 3.2b, it is bounded. Therefore independent of the regime, it cannot be increased. The kind of enhancement revealed by the OP is a magnification of *superradiance*, which is the traditional way to describe the QPT of DM [35]. The OP indicates the scaled number of excitations within the subsystem, which is bounded because of finiteness of  $N$ . In the dynamical regime, excitations develop more quickly (see blue curve in inset of Fig. 3.2b). In case of the eventual leakage of excitations through the cavity (see section 3.8 for cavity loss effects), it manifests itself as a sharp burst of photons which are suddenly released. Bursts like these are excellent indicators of the DM QPT in cold atom experimental realizations [4].

Qubit quantum properties are very important for applications in quantum computation and quantum information. However, the finite character of the matter subsystem conceals much of the complexity of the evolution. The field subsystem, with its own relevance in highly controlled quantum optics, does not have this restriction. Field dynamical profiles analogous to that of Fig. 3.2 are shown in Figs. 3.3a-b. Similarities with Figs. 3.2a-b are noticeable, though with relevant differences. A large dynamical magnification of the field quadrature squeezing is also present, but it dies off later than its matter counterpart. Thus the development of the field OP is delayed as compared to that of the qubits. Superradiance, as seen by value of the field OP, is now not only sharper, but it can be as much as twice the value attainable with adiabatic ramping at a given  $\lambda$ . This greatly enhances the intensity of superradiant bursts. Radiation intensity enhancements of this kind have also been predicted in the DM submitted to sudden quenches and a lossy cavity [13]. Dynamically enhanced and suppressed superradiance alternate after the first burst (see blue curve in inset of Fig. 3.3b), a behavior absent in the equilibrium QPT. A wavy plateau in figure 3.2b coincides with that alternating stage. The dynamical phase marked by these oscillations is the same characterized by giant light-matter entanglement in Fig. 3.1a.

### 3.6 Non linear effective interactions

The origin of the giant enhancement of the light-matter entanglement and spin squeezing discussed so far lies in a prolonged realization of effective non-linear interactions within both subsystems, after a preparation stage where the sudden quench approximation holds. As the light-matter coupling increases in time from zero into the  $\lambda > \lambda_c$  range, the system moves out of its frozen initial state. The interaction term in the Dicke Hamiltonian begins to dominate and each subsystem works as a mediator of the other's self-interaction. Matter-light interaction is in principle linear and generates little entanglement in the adiabatic limit, since the system has enough time to continuously stabilize in response to the perturbation. The intermediate regime

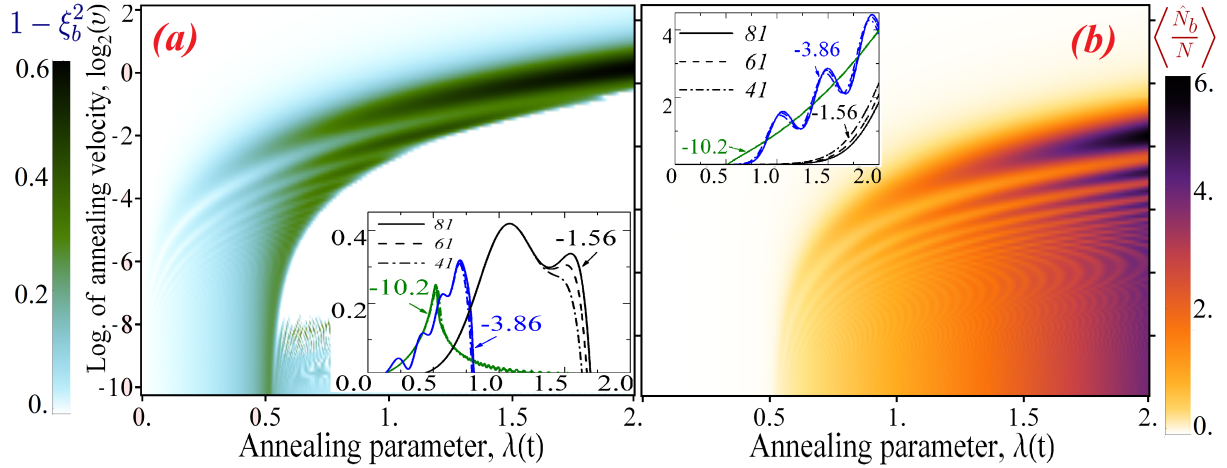


FIGURE 3.3: Corresponding dynamic profiles and insets of Figs. 3.2a and 3.3b, now for the field subsystem. (a) Evolution of  $1 - \xi_b^2$ , as defined in Eq. 3.4, whenever it is greater than zero (squeezed radiation). (b) Scaled OP of light  $\langle \hat{N}_b \rangle / N$ . Major tendencies of Fig. 3.2 are replicated here. However, the unbounded nature of the field OP allows an appreciation of the field intensity's oscillation (associated with superradiance) around the equilibrium values, with intervals of significant dynamical enhancement of superradiant bursts. The oscillatory behavior is related to a combined light-matter quantum chaotic stage that coincides with giant light-matter entanglement of Fig. 3.1a.

is the only one in which non-linearities can develop significantly. Then, the non-linear processes are realized as one axis squeezing with a transverse field for matter [120, 123], and Kerr-like interactions for radiation [118]. During these separate squeezing processes, both radiation and matter act as effective interaction mediators for each other. This extends to the non-equilibrium case static correspondences with matter-only [39], or radiation-only systems [42].

The process of separate squeezing does not last indefinitely: each subsystem starts to retain quantum information of the other, which is the moment when the entropy grows. The effective interaction is broken, leaving the qubits and radiation mode entangled with each other but not within themselves. Because of monogamy and the breaking of the effective non-linear interaction condition, separate squeezing, which is related to internal quantum entanglement, suddenly dies as soon as combined matter-light entanglement emerges. The field squeezing survives longer because of its greater information capacity. Despite being a single radiation mode, the field acts as a reservoir that dissipates the quantum correlations present in the spin squeezed state. If the qubits were not coupled to the field, squeezing could have revivals after its sudden death [120]. The enhanced internal entanglement in both the matter and light subsystems is subsequently transformed into the system-wide giant light-matter entanglement. These results have the interesting consequence that in terms of quantum processing, one can choose the moment of the control driving where a specific magnified quantum property is optimal, and that can be chosen among both forms of squeezing, light-matter entanglement, or other particular mixed situation. By contrast, in the adiabatic regime, entanglement within and between subsystems compete against each other, because they occur simultaneously at the critical point. Indeed,

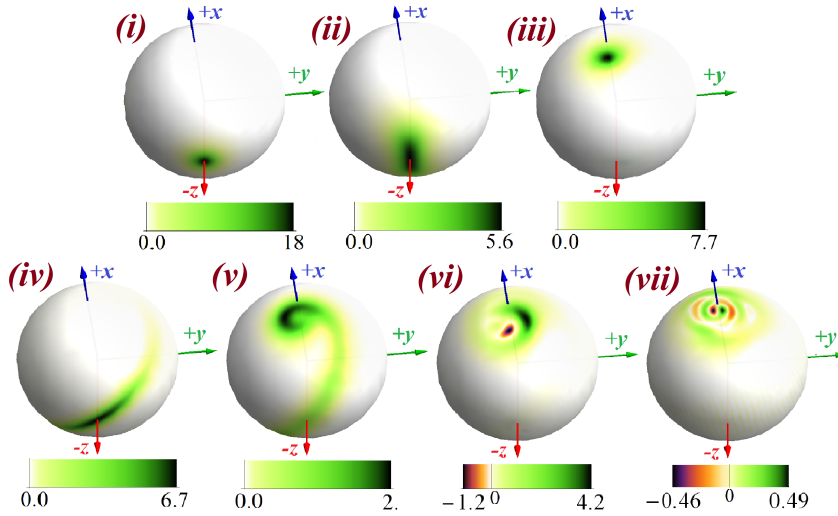


FIGURE 3.4: Agarwal-Wigner functions (AWF), as defined in Eq. 3.5, at the instants indicated in Fig. 3.2b by the corresponding number (dissipative effects are ignored,  $\kappa = 0$ ). They are phase space representations of the matter subsystem depicted in the Bloch sphere. Color scale of all Wigner functions can be very different. Maximal dynamical squeezing in (iv) is much greater than the adiabatic counterpart in (ii). Also, negative complex structures develop in the combined light-matter chaotic stage in (v-vii); which contrast with an adiabatic ordered state as in (iii). The stage in (iii,v-vii) has also no squeezing and no concurrence, since the Wigner function is now split along the  $x$  and  $-x$  directions and no longer concentrated around the initial state. Opposite Bloch hemispheres are not shown because of symmetry:  $W_q(\theta, \phi + \pi) = W_q(\theta, \phi)$ .

the non-equilibrium situation produces a very favorable separation between system-wide and subsystem concentrated quantum correlations.

### 3.7 Matter-light quasi-probability behavior

Complete state representations of the subsystems state reveal more details of the processes involved in the dynamical regime. Figures 3.4 and 3.5 show several snapshots of Wigner and AWF quasi-distributions at different instants. The enormous difference in the squeezing amount between the dynamical regime and the adiabatic one, as well as a difference in the direction of squeezing, is now graphically clear. This can be seen by comparing Figs. 3.4iv and 3.5iv with Figs. 3.4ii and 3.5ii, and was previously shown for different AV values in Figs. 3.2 and 3.3. At any regime, death of squeezing is associated with a splitting in half of the distributions, caused by the spontaneous symmetry breaking described in section 3.4. This splitting is symmetrical along the  $x$  and  $-x$  direction in both subsystems. The system's density of excitations, indicated by the OP, increases as the distributions become displaced away from the initial state.

Features of the complex light-matter entangled stage are clarified by Figs. 3.4v-vii and 3.5v-vii, which contrast with the adiabatic splitting in Figs. 3.4iii and 3.5iii. The dynamical splitting of the distribution leads to negative scars and complex patterns for both subsystems, though the phenomenon is far more conspicuous in radiation. Donut shapes with a negative centered AWF, such as that in Fig. 3.4vi, have been experimentally obtained in 3000 atoms with just a

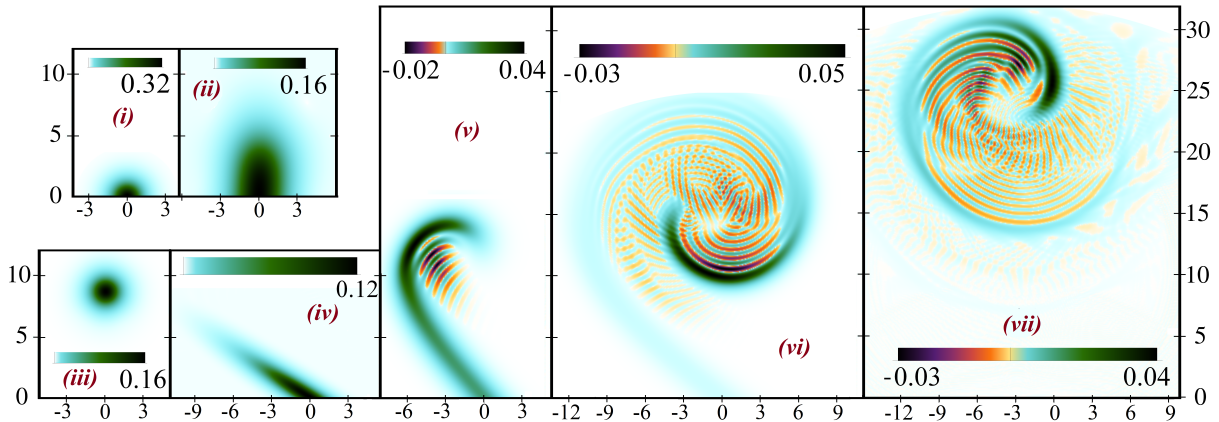


FIGURE 3.5: Analogous pictures of Fig. 3.4 but for the field Wigner distribution  $W_b$ . This is represented in the  $x - p$  plane of position (vertical) and momentum (horizontal) quadrature. All figures have the same  $x - p$  scale but color scale can be very different. The chaotic stage in (v-vii) exhibits sub-Planck structures. Negative regions of  $x$  are not shown because of symmetry:  $W_b(x, p) = W_b(-x, -p)$ .

single photon [131]. In addition, round-tailed interference patterns such as that in Fig. 3.5vi have been obtained for light in Kerr-like media following a Fokker-Planck equation [119], which confirms the presence of non-linear effective interactions. These results mean that the field is able to exhibit chaotic behavior itself, regardless of its entanglement to the matter subsystem. The field Wigner function is not only full of negatives regions (a marker of non-classical light), but it also contains abundant so-called sub-Planckian structures which have been related to quantum chaos [62]. The finite-size DM is non-integrable, and its ordered phase has been connected to chaotic features [44, 132]. This chaotic onset is responsible for the small size dependence on curves in insets of Figs. 3.1a, 3.2 and 3.3 for the  $\log_2 v = -1.56$  case, since the symmetry breaking occurs deeper in the ordered phase. As spin squeezing is very sensitive to chaos [109, 110], it is no surprise that its sudden death becomes irreversible once the light-matter entangled stage arises.

## 3.8 Robustness against noise of non-equilibrium quantum correlations

### 3.8.1 Robustness of light-matter entanglement

In section 3.3 we used Von Neumann entropy  $S_N$  as a measure of light-matter entanglement in the case that the entire system is pure. However, in order to have an idea of the decoherence effects, the DM must be treated as an open system, and then,  $S_N$  is no longer a good light-matter entanglement measure. Instead, we can use quantum negativity as defined in Eq. 3.7. One may wonder if switching from one form of entanglement measure to the other has any justification. Figure 3.6a shows a dynamical profile of the ramping process analogous to that of Fig. 3.6a,

but with logarithmic negativity  $\log_2(2\mathcal{N} + 1)$ . The resemblance with the  $S_N$  graphic is quite apparent, and the enhanced entanglement regime is again clearly noticeable. This should be no surprise as both measures virtually codified the same information. If total  $\hat{\rho}$  is a pure state, and  $\{p_i\}$  is the spectrum of  $\hat{\rho}_q$  in that case (which is the same as the spectrum of  $\hat{\rho}_b$  because of Schmidt decomposition), both negativity  $\mathcal{N}$  and  $S_N$  can be written in terms of that spectrum. The first one would be  $2\mathcal{N} + 1 = \sum_{i,j} \sqrt{p_i p_j}$ , while the second one is  $S_N = -\sum_i p_i \log p_i$ . Therefore, Fig. 3.6a confirms that both entanglement measurements are well connected and suitable for witnessing light-matter entanglement. The reason why  $S_N$  was preferred whenever it is a good measure is because its wider usage and well established connection to other quantum information concepts [32].

When we include cavity losses, we predict the survival of giant light-matter entanglement, as shown in Fig. 3.6b. Since the light-matter entanglement increases as  $N$  increases, we predict that experimental system sizes  $N \approx 10^5$  as those described in section 1.3 will develop significantly more robust light-matter entanglement against losses than for small systems. By contrast, entanglement generation in the well-studied near-adiabatic regime cannot be achieved under current experimental setups, since decoherence times are much shorter than the annealing times required by this regime. It should be noticed that the system sizes  $N$  accessible to open system numerical solution are well smaller than the ones examined in the pure case. This could cast doubt on whether the conclusions brought from this small size result have any general validity. However, there are good signatures that giant light-matter entanglement only gets stronger as  $N$  increases. This means that, provided the open system's parameters like  $\kappa$  and  $\bar{n}$  remain the same, any deleterious effect caused by the leakage of quantum information to the environment is only weaker with sizes of the order  $N = 81$  than the ones that we present.

### 3.8.2 Robustness of subsystem results

Figures 3.7a-e address how the presence of losses in the cavity affect the dynamical enhancement of quantum properties at subsystem level. All the main results found in  $\kappa = 0$  evolution survive very well if decoherence towards the environment is two orders of magnitudes lower than the main energy scale. Even if dissipation is at values of just an order of magnitude below, spin squeezing effects remain highly robust, with increasing noise resistance with system size. Field squeezing surprisingly survives to dissipation regimes comparable to the Hamiltonian dynamics itself. On the other hand, detailed features of the chaotic stage (such as OP oscillations, negative regions, and Sub-Planck structures) are far more sensitive to decoherence, requiring losses to be at levels of  $\kappa = 0.01$ . These very sensitive features have been proposed as tools for measuring very weak forces [133]. In our analysis, we have found that small finite values of  $\bar{n}$  (such as those typical at the ultra-low temperatures of most experimental realizations) do not change dramatically the conclusions; they just slightly intensify the process of decoherence. Previous works on non-equilibrium DM under different settings have also confirmed that some

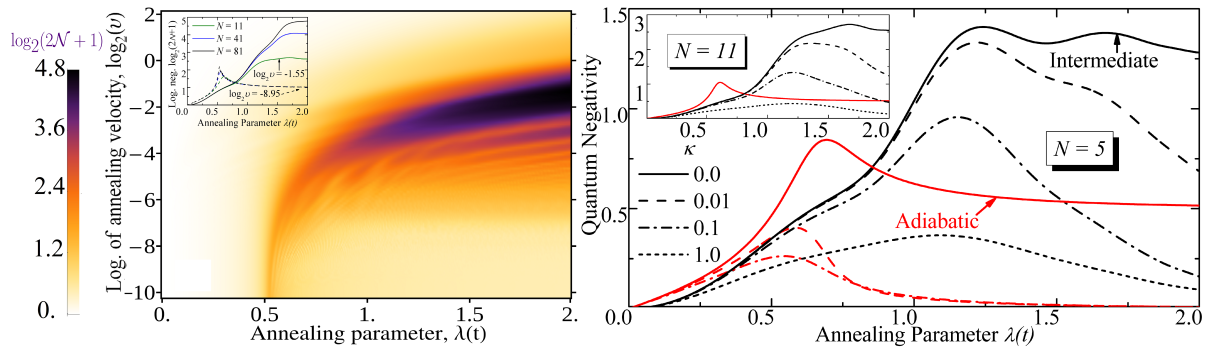


FIGURE 3.6: **(a)** Dynamical profile analogous to Fig. 3.1a but now for logarithmic negativity  $\log_2(2\mathcal{N} + 1)$ . There is strong resemblance between both profiles. This justifies the use of  $S_N$  as the entanglement witness for the closed system case while changing to  $\mathcal{N}$  when the system is open. The inset shows that even with relative small system sizes,  $\mathcal{N}$  has qualitatively similar behaviors for the same  $v$ , so that conclusions about the robustness of the dynamic light-matter entanglement against decoherence can be extrapolated to bigger  $N$ . **(b)** Effect of cavity losses on light-matter entanglement generation in terms of  $\mathcal{N}$ . Cavity's field decay rate is  $\kappa$  (different line style). Black curves depict giant entanglement regime  $\log_2(v) = -1.58$ , while red curves represent adiabatic one  $\log_2(v) = -8.96$ . Main figure is for  $N = 5$  system's size while inset represents analogous  $N = 11$  results. Dynamical entanglement regime is bigger and more robust against open system losses as  $N$  increases. In opposition, near-adiabatic entanglement vanishes even for weak losses since annealing time is too long as compared to decoherence time. Zero temperature has been assumed and  $\kappa$  is measured in units of field free frequency  $\omega$ . Finite temperature cases have very similar tendencies.

major phenomena present here, such as spin squeezing, survive losses. Enhanced superradiance can be detected [13], and squeezing can still have time to develop [15, 119]. We note that, despite perturbing the quantum state of the system, a lossy cavity compensates by providing the experimental possibility to monitor the dynamic evolution of the field in time [134].

The robustness of quantum correlations suggests that some of the effects described in this chapter may be accessible under current experimental realizations of the DM. We have already explained in section 1.3 that the control described by  $\lambda(t)$  can be realized as a pump laser power increasing over time. The noise present in current experiments, like the ones performed by Klinder et al., is well inside the levels where some of our predictions remain robust, nearly analogous to our  $\kappa = 0.1$  case [5]. Furthermore, the experimental annealing velocities correspond very well to the giant entanglement regime predicted by our analysis. As field squeezing is the most robust quantum correlation (see Fig. 3.7e) and it is experimentally accessible thanks to a leaky mirror, tomographic techniques and photon statistics could be the first front for experimental comparisons with our predictions [134]. Other tomographic techniques could also analyze properties of the matter subsystem state [135]. But, given the specific degrees of freedom forming the qubit states in current realizations (basically matter wave modes) [5], suitable equivalences of those state resolving techniques to this kind of degrees of freedom should be devised. In the same sense, in order to directly witness light-matter entanglement, further advancements in experimental procedures may be required.

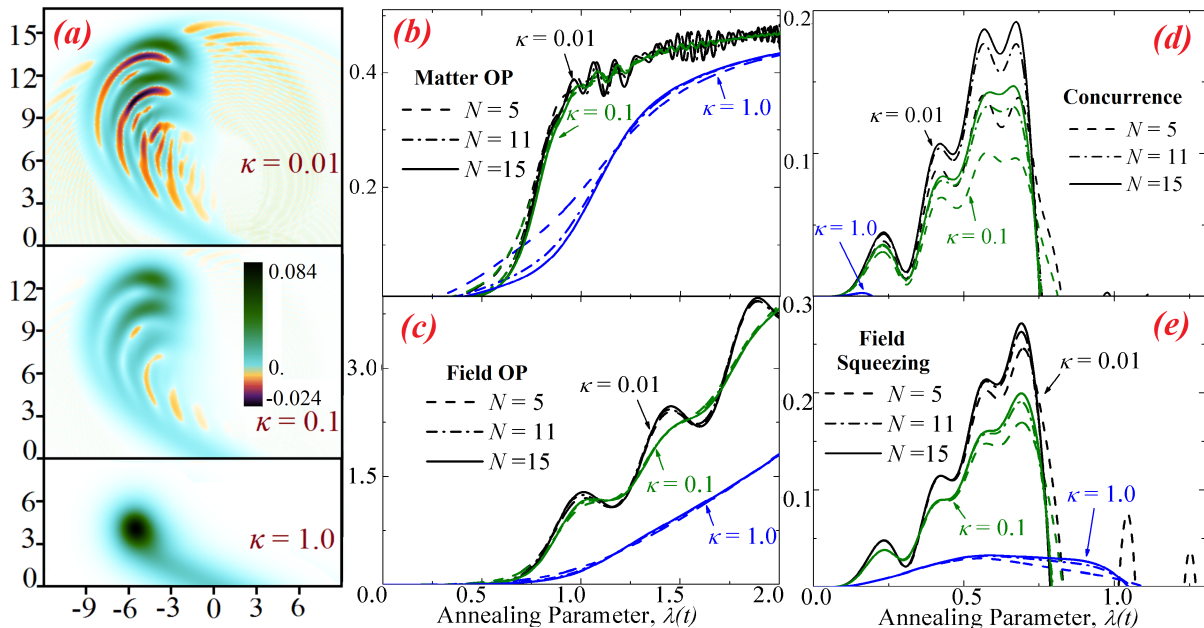


FIGURE 3.7: Effect of a leaky field cavity (expressed in terms of cavity decay rate  $\kappa$ ) on the dynamical enhancement of subsystem quantum properties. **(a)** Wigner distribution for AV  $\log_2 v = -1.58$ ,  $N = 15$  qubits at instant  $\lambda = 2$ . **(b-e)** Different field and matter properties as function of time for  $\log_2 v = -3.86$ , and three different system sizes. Quantum chaos signatures (sub-Planck structures, negative Wigner distributions, and oscillations in OPs) are highly sensitive to dissipative perturbations. On the other hand, squeezing and internal entanglement effects are far more robust, especially for field squeezing. In all figures  $\bar{n} = 0$ .

### 3.9 Scaling of results

Our results exhibit substantial size invariance, as the insets of Figs. 3.1a, 3.2, and 3.3 show. Even the small system sizes in lossy cavity results in Figs. 3.7b-e are highly size independent, which justifies our claim that the conclusions drawn there can be taken as general trends. Figures 3.8a-b show that the onset point of the dynamical regime occurs at points  $\lambda_d$  following a power law,  $(\lambda_d - \lambda_c) \propto v^{2/3}$ . This kind of scaling relation is typical in QPT critical properties [10]. This scaling laws extends our previous results on adiabatic scaling theory in near-adiabatic regime of chapter 2 to faster regimes. Even though we have used the same kind of scaling variables as in the near adiabatic case, many results in the dynamic regime collapse very well without any re-scaling of  $\lambda$ .

The origin of the scaling exponent can be understood in a rather simple way, using concepts from the KZM [8]. The scaled time is the instant where the healing time of the system (as measured by the inverse mean energy gap in the spectrum  $\Delta^{-1}$ ) has the same order of magnitude, i.e., when  $t\Delta \approx 1$ . As  $\Delta \propto (\lambda_d - \lambda_c)^{1/2}$  in the ordered phase [39], and  $t \propto (\lambda_d - \lambda_c)v^{-1}$ , we get the exponent  $2/3$  present in all lines of Figs. 3.8a-b. The fact that equilibrium critical exponents have been used reveals that, even though the emergence of the dynamical regime is well inside the  $\lambda > 0.5$  range, its mechanism is still related to the QPT, and so many critical phenomena get dynamically enhanced. On the other hand, the fact that the evolutions are very similar in

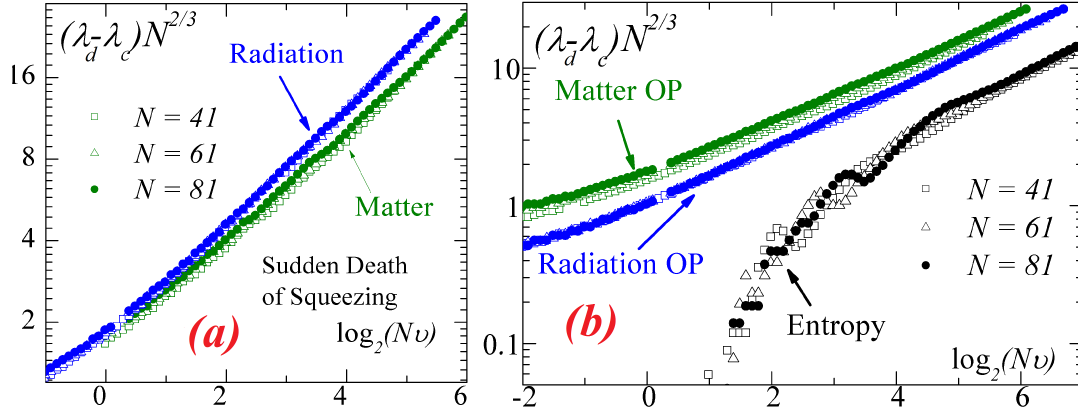


FIGURE 3.8: Size-independence of the instant  $\lambda_d$  when field and qubits organize in a combined light-matter excited state. **(a)** Instant of a sudden death of squeezing, in both matter and radiation subsystems. **(b)** Instant when each system reaches a significant value of its OP or  $S_N$ . These values are  $\langle \hat{N}_q \rangle = 0.1N$ ,  $\langle \hat{N}_b \rangle = 0.0123N$ , and  $S_N = 0.125 \log(N+1)$ . At sufficiently high AVs, all the instances chosen are related by the same scaling power law relation  $(\lambda_d - \lambda_c) \propto v^{2/3}$ .

the chaotic region, despite the different sizes, has to do with the relatively equal structure of the interaction well inside the superradiant phase, provided it has not bounced against the finite limits of the matter subsystem. There is a good chance that this scaling of dynamical features is related to the existence of excited state quantum phase transitions [136], whose existence has been already established in the DM [137], and have already provided insights in the sudden quench limit [138].

### 3.10 Conclusion

We have found that, in between the traditional driving schemes (neither near-adiabatic, nor sudden quench), a previously unnoticed intermediate annealing regime emerges, and that this regime can be seen as advantageous for many quantum control processes. The onset of this intermediate phase is marked by induced non-linear self-interactions in both matter and field subsystems, developing squeezed states in each of them that are related to internal entanglement. This squeezing process is much stronger than what can be achieved in near-adiabatic evolutions, since the internal entanglement does not have to compete against the matter-field entanglement that arises in later stages.

We have also found that the dynamical squeezing mechanism is succeeded by the development of a chaotic and entangled radiation-matter dynamical phase. Clear signatures of quantum chaos, such as fragmented Wigner functions, have been identified in this phase. This stage has its own dynamically enhanced properties such as superradiance, phase order, and sensibility to weak forces. We have established the robustness of all the quantum enhancing processes under dispersive conditions and its invariance to system size. We have shown that this last invariance condenses into a power-law relation associated with critical exponents. We hope

this understanding will prove important for developing schemes to generate squeezed and other entangled states, as have been proposed in the contexts of quantum metrology and quantum information processing.

## Chapter 4

# Collective $SU(2)$ quantum magnetism in a $^{87}\text{Sr}$ lattice clock

In the previous chapters we showed how the coupling between an all-to-all spin network and a field mode (i.e., the DM) can generate distinctive highly correlated quantum behavior when submitted to non-equilibrium conditions. This chapter deals with a very similar situation, but now the other coupled system is not a bosonic mode but a copy of the spin network itself. This duplication of the network is caused by another degree of freedom that also produces a two level system per particle (each particle has an  $SU(2) \times SU(2)$  state). In a sense, the system of this chapter is more similar to a LMGM with two different spin species, but with additional interactions. The non-equilibrium condition now is neither associated to a QPT, nor is caused by a time dependent Hamiltonian as before. Nevertheless, we will see that already familiar non-linear processes, like one axis squeezing with a transverse field, are also involved in dynamical entanglement generation. In fact, we will find that an interplay of this and other correlations are at the core of the dynamics of this pair of strongly interacting collective (pseudo)spins. Finally, it should be mentioned that the system discussed in this chapter has the invaluable attractiveness of being realizable by an experiment, namely a  $^{87}\text{Sr}$  lattice clock, that constitutes a true milestone and a current end technology of quantum control.

### 4.1 Introduction

The search for more and more stable time standards is a main driving force for research in ultra high precision atomic physics. Advancements in atomic clocks has led to establish as the definition of the second for the international system of units my means of the Caesium standard since 1960 [139]. Further improvements of these time measurements are still intensively pursued [140]. The importance of these achievements in the measurement of such a fundamental physical magnitude are impossible to overestimate, suffice it to mention that they have been used in the

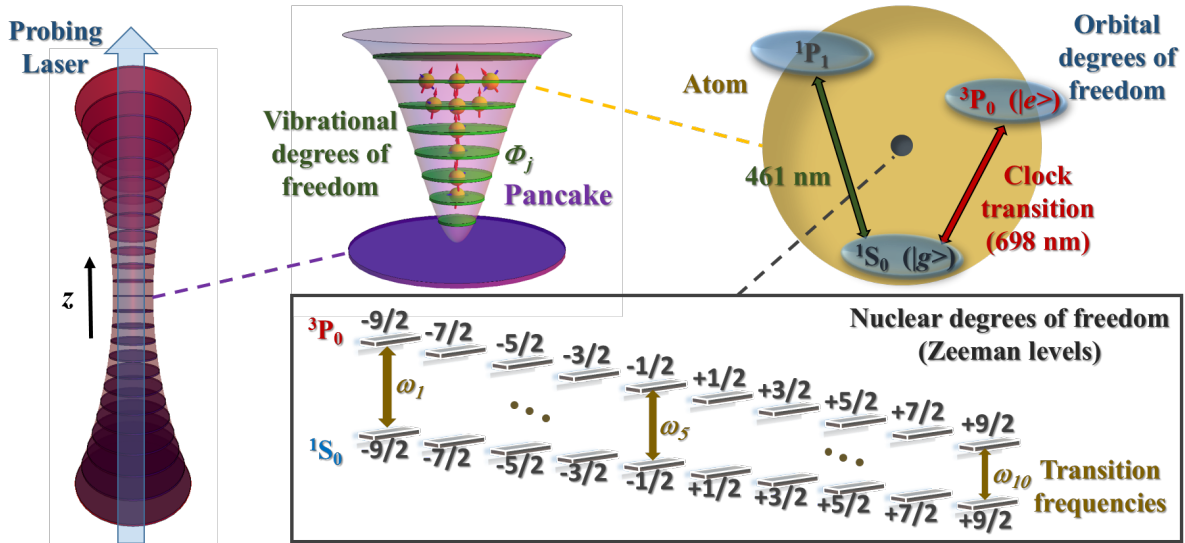


FIGURE 4.1: Schematic picture of the optical lattice clock with  $^{87}\text{Sr}$  atoms, and the degrees of freedom involved. (a) Optical trap with much stronger longitudinal confinement ( $\nu_z \approx 80$  kHz) producing a 1D ‘pancake’-lattice structure. (b) Different vibrational levels  $\Phi_j$  in each pancake produced by the transversal relatively weak confinement ( $\nu_R \approx 450$  Hz). (c) Electronic (orbital) energy level structure, with the clock transition defined between the ground  $|g\rangle$  and the first  $|e\rangle$  excited state. (d) Zeeman energy levels produced by the nuclear spin with vanishing hyperfine interaction (underlying  $SU(N)$  symmetry). However, a weak hyperfine structure in the  $^3P_0$  state allows to address each nuclear state with a different Rabi frequency  $\Omega_i$ .

some of the most stringent tests up to date for the stability of our basic physical constants [141]. The atomic system studied in this chapter belongs to this tradition. It consists of a set of ultra-cold *fermionic* alkaline-earth atoms (AEA) atoms (temperatures of  $\sim 1\mu\text{K}$ ) confined in an optical trap forming a 1D lattice structure as illustrated in Fig. 4.1a. This ultra-precise clock has been allowed by major advancements in the quantum manipulation of trapped ultra-cold atoms [142], ultra-stable lasers [143], and the formidable spectroscopic resolution with which they can be measured thanks to frequency comb technologies [144]. One major atomic species used in these experiments has been  $^{87}\text{Sr}$ , and from now on we are going to focus on it, by using its measured parameters to perform calculations. Notwithstanding, many of the methods involving  $^{87}\text{Sr}$  clocks could also be implemented in other fermionic lattice clocks with AEA-like species, the other major one currently investigated being  $^{171}\text{Yb}$  [20]. These AEA lattice atomic clocks have reached time measurement precision of the order of  $10^{-18}$  [19, 145], beyond the best current caesium standard [146], and single-ion optical clocks [147].

The scheme of using trapped fermionic atoms arranged as in Fig. 4.1a. was devised in order to take advantage of several features of the setting [148]:

- When the atoms are trapped in regions smaller than the clock transition wavelength, Doppler and collisional shifts are avoided (Lamb-Dicke regime), which greatly increases the precision with respect to ballistic atoms. Other shifts may be prevented by choosing *magic wavelength* optical traps [149].

- By interrogating many atoms at the same time, the stability of the clock is greatly increased, bypassing the projection noise of single absorber clocks.
- Finally, by using *polarized fermions*, the exclusion principle is expected to suppress atom-atom interactions (at least up to the level of  $s$ -wave collisions) which otherwise would affect the accuracy and precision of the clock. This could be done with bosonic species as well, but then special ways to circumvent atomic overlapping should be implemented.

It is this last issue that mostly concerns us in this chapter, since if we see it in the opposite way, the presence of such interactions could be a perfect platform to investigate many-body quantum physics in an outstandingly controllable setting. These interactions may be small with respect to time measurements, but since they are the remnant dominant interactions, the emergent quantum system can be effectively seen as strong interacting. Furthermore, these interactions can be experimentally probed thanks to the wonderful current resolution capabilities. The nature of the interaction in the  $^{87}\text{Sr}$  clock has been continuously discussed in the last years. Initially, at precision of 2Hz, no collision interaction was detected [150, 151]. With the increase of precision, finally some collision measured as density dependent frequency shifts were found [152], and were attributed to  $s$ -wave collisions allowed by inhomogeneous excitations which would make the atoms to be distinguishable [153, 154]. Later it was seen that the  $p$ -wave collisions could be the leading elastic channel [155].

In this chapter we are going to investigate many-body interactions in the  $^{87}\text{Sr}$  lattice clock under the assumption of an all-to-all approximation and neglecting loss effects. The interaction between atoms will be entirely through  $p$ -wave collisions. Nuclear spin of  $^{87}\text{Sr}$  is  $F = 9/2$ , and there is a vanishing hyperfine interaction in the clock transition. This decoupling of the nuclear degrees of freedom to the orbital clock states would mean an underlying  $SU(\mathcal{N})$  symmetry in the system. However, we will see that, because of symmetry considerations, the degrees of freedom can be coupled to the orbital states producing an exchange interaction. The group symmetry determined by  $\mathcal{N}$  depends on how many nuclear states are initially populated, we are going to deal only with the case  $\mathcal{N} = 2$ . The resulting exchange interaction can be seen as a coupling of collective pseudo-spin associated to each nuclear spin, a situation that can be designated as collective  $SU(2)$  quantum magnetism.

This chapter will be structured as follows. We will start in section 4.2 by giving an exact definition of the system of interest: we will explain the steps that led to the Hamiltonian, and we will establish the initial conditions. Section 4.3 will present the relatively simple mean field equations that emerge in the problem, which will prove to be very valuable for the interpretation of results. Section 4.4.1 will present and discuss results concerning Bloch vector dynamics, i.e., the time evolution of first order expected values of collective orbital pseudospin. Section 4.5 will extend the analysis to second order expected values, which will allow to explore the emergence

of atom-atom correlations and even quantum phenomena like entanglement and spin squeezing. Finally, we will give some concluding remarks in 4.6.

## 4.2 Derivation of the Hamiltonian

Let us first describe the Hilbert space in which the state of each pancake lies. These states can be generated by applying the following field creator operators to the zero particle state [52, 156],

$$\hat{\Psi}_{a,i}^\dagger(X, Y, Z) = \phi_0(Z) \sum_j \hat{c}_{a,i,j}^\dagger \Phi_j(X, Y), \quad (4.1)$$

where  $a \in \{e, g\}$  defines the orbital clock states, and  $i \in \{1, 2, \dots, 2F + 1\}$  denotes the nuclear magnetic state. The number  $j$  indexes collectively the transversal translational modes  $\Phi$  (see Fig. 4.1b), while we assume that only the longitudinal fundamental mode  $\phi_0$  is populated. Operators  $\hat{c}_{a,i,j}^\dagger$  creates an atom in a state described by these three indexes. As the atoms are fermions, this operators anti-commute, i.e.,

$$\{\hat{c}_{a_1, i_1, j_1}^\dagger, \hat{c}_{a_2, i_2, j_2}^\dagger\} = \delta_{a_1, a_2} \delta_{i_1, i_2} \delta_{j_1, j_2}, \quad (4.2a)$$

$$\{\hat{c}_{a_1, i_1, j_1}^\dagger, \hat{c}_{a_2, i_2, j_2}\} = \{\hat{c}_{a_1, i_1, j_1}^\dagger, \hat{c}_{a_2, i_2, j_2}^\dagger\} = 0. \quad (4.2b)$$

The basis generated by the field operators in  $\hat{c}_{a,i,j}^\dagger$  is expected to be an eigenbasis of the translational Hamiltonian  $\hat{H}_T = \int d^3\mathbf{R} \hat{\Psi}^\dagger(\mathbf{R}) \left(-\frac{1}{2m} \nabla^2 + U_{\text{ext}}(\mathbf{R})\right) \hat{\Psi}(\mathbf{R})$ . Assuming that the optical trap is in the *magic wavelength* [149], the confining Hamiltonian is supposed to be the same independently of  $a$  and  $i$ .

One of the main assumptions to further simplify the Hamiltonian is the *frozen modes* approximation, that supposes that the set of modes  $j$  that are excited in each pancake is fixed [20]. This approximation neglects the probability of mode changing interactions, which is justified by the fact that the Gaussian transversal confining potential (due the laser waist) has a non-degenerate spectrum whose energy differences are of about two order of magnitudes higher than the mean interaction energies. It also neglects losses caused by either single or atom-atom collisions, which is justified if the probing time of the system is shorter than the decay times of these dissipative effects. Therefore, from now on we are supposing a fixed number  $N$  of atomic translational modes excited in each pancake, and we can think of each mode  $j$  as a distinguishable atom that can have each of the  $2(2F + 1)$  states described by the numbers  $a$  and  $i$ . As a further simplification, we will assume that only two nuclear spin states are populated, which we will be denoted by the numbers 1 and 2 throughout this chapter. This simplification can be achieved thanks to a slight difference in the Zeeman amplitudes for each nuclear component (see Fig. 4.1d), which allows to selectively populate only some desired nuclear states  $i$ . In that case, each mode  $j$  has four possible internal states  $(a, i) \in \{e2, e1, g2, g1\}$ . For the orbital degree of

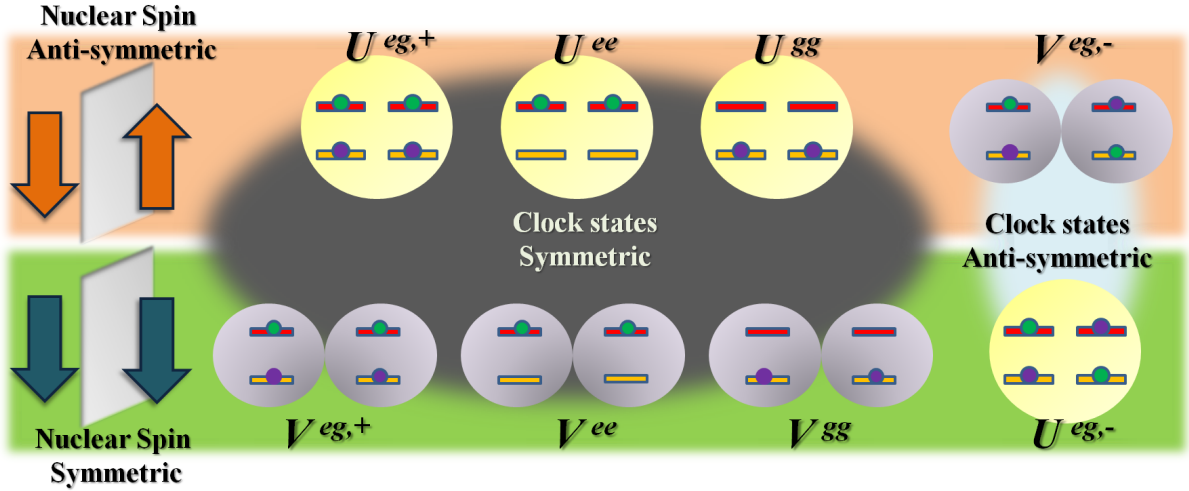


FIGURE 4.2: This Table contains all eight possible two particle collision eigen-energies in Eq. 4.4. Letters  $V$  correspond for spatially antisymmetric collisions ( $p$ -wave) while  $U$  indicates  $s$ -wave spatially symmetric collisions. The energy also depends on the kind of clock state superposition involved, either the three symmetric possibilities (triplet, left), or one anti-symmetric superposition (singlet, right). Nuclear states are only related to these collision terms because their exchange symmetry must guarantee that the total state remains anti-symmetric (fermions). Any state with the composite nuclear and orbital states totally symmetric (generalized Dicke manifold) will have the  $s$ -wave interactions suppressed.

freedom, we can define a pseudo-spin operator,

$$\tilde{t}_{i,\alpha}^j = \frac{1}{2} \sum_{a,b} \sigma_{a,b}^\alpha \hat{c}_{a,i,j}^\dagger \hat{c}_{b,i,j}, \quad (4.3)$$

where  $\sigma_{a,b}^\alpha$  are Pauli matrix components and  $\alpha \in \{x, y, z\}$ . Notice that the  $\tilde{t}_{i,\alpha}^j$  operator projects on the nuclear state  $i$  and that one can define an operator without that projection,  $\hat{t}_\alpha^j = \tilde{t}_{1,\alpha}^j + \tilde{t}_{2,\alpha}^j$ . An analogous definition could be made for the nuclear degrees of freedom with operators  $\hat{s}_{a,\alpha}^j$  and  $\hat{s}_\alpha^j$ .

Once we have settled the Hilbert space, we continue with the atom-atom collisions, which are dominated by the  $s$ -wave and  $p$ -wave interactions, the former occurs for spatially symmetric collisions, and the latter for spatially antisymmetric ones. Also, the collision length will depend on the pair of orbital states involved and whether these pairs are in a symmetric or an antisymmetric superposition. This gives eight possible collision lengths, as illustrated in Fig. 4.2. On the other hand, thanks to the virtually zero hyperfine structure, the collision length will be independent of nuclear spin states. However, the kind of collision allowed will depend on whether the nuclear states are in a symmetric or an antisymmetric superposition, because the total wave function must remain antisymmetric. An eigenvector of the collision Hamiltonian  $\hat{H}_{j,l}^c$  for a pair of modes  $j, l$  will be a product of spatial, orbital and nuclear states with defined symmetry [20]. This Hamiltonian can be casted in a symmetric and antisymmetric part of nuclear spins,

$$\hat{H}_{j,l}^{c,\pm} = \hat{\Pi}^\pm \left[ G_{j,l} \hat{\mathbf{t}}^j \cdot \hat{\mathbf{t}}^l + X_{j,l}^\pm \hat{t}_z^j \hat{t}_z^l + C_{j,l}^\pm (\hat{t}_z^j + \hat{t}_z^l) + K_{j,l}^\pm \right], \quad (4.4)$$

where  $\hat{\Pi}^\pm$  is the projection on the singlet or triplet subspace of combined  $j, l$  nuclear states. The coefficients for the triplet projection are,

$$G_{j,l} = U_{j,l}^{eg,+} - V_{j,l}^{eg,-}, \quad (4.5a)$$

$$X_{j,l} = U_{j,l}^{ee} + U_{j,l}^{gg} - 2U_{j,l}^{eg,+}, \quad (4.5b)$$

$$C_{j,l} = U_{j,l}^{ee} - U_{j,l}^{gg}, \quad (4.5c)$$

$$K_{j,l} = \frac{1}{4} \left( U_{j,l}^{ee} + U_{j,l}^{gg} + U_{j,l}^{eg,+} + V_{j,l}^{eg,-} \right). \quad (4.5d)$$

The letters  $U$  and  $V$  mark  $s$ -wave and  $p$ -wave terms respectively, and the super-index specifies the superposition of orbital states involved in the collision (plus and minus are symmetric and antisymmetric respectively). The coefficients for the singlet projection are analogous, but one must change the  $V$ s for  $U$ s. The form of the Hamiltonian in Eq. 4.4 is that of the Kugel-Khomskii model [157], which can be used to understand magnetic properties of crystals with perovskite-like structure [158]. Hence, this cold alkaline-earth atom setting can be used as a platform for quantum simulations for such condensed matter systems [155]. The total collision Hamiltonian will be  $\hat{H}^c = \sum_{j<l} (\hat{H}_{j,l}^{c,+} + \hat{H}_{j,l}^{c,-})$ .

In general, the value of coefficients in Eq. 4.5 (which are in fact eigen-energies of the collision Hamiltonian) will depend on the translational modes involved. This asymmetry would demand each mode to be described separately, and then the evolution will be guaranteed to lie in a  $4^N$ -dimensional Hilbert space. This exponential complexity can be overcome under the *all-to-all* approximation and the restriction to a Generalized Dicke Manifold (GDM), which eliminates this mode pair dependence under a collective description of all the modes. The GDM is spanned by the totally symmetric states defined uniquely by the four non-negative integers  $\{n_{e2}, n_{e1}, n_{g2}, n_{g1}\}$ , restricted to  $\sum_{a,i} n_{a,i} = N$ . Those states are of the form,

$$|n_{e2}, n_{e1}, n_{g2}, n_{g1}\rangle = \left( \frac{N!}{n_{e2}!n_{e1}!n_{g2}!n_{g1}!} \right)^{-1/2} \sum_{p \in P(n_{e2}, n_{e1}, n_{g2}, n_{g1})} p(|e2, \dots, e2, e1, \dots, e1, g2, \dots, g2, g1, \dots, g1\rangle), \quad (4.6)$$

where  $P(n_{e2}, n_{e1}, n_{g2}, n_{g1})$  is the set of all the  $\frac{N!}{n_{e2}!n_{e1}!n_{g2}!n_{g1}!}$  different permutations between atoms. In other words, the GDM spanning states are only specified by how many modes have each of the four possible internal states. The dimension of the GDM grows cubically with the number of modes:  $d = \frac{1}{6}(N+3)(N+2)(N+1)$ . If the system lies in the GDM,  $s$ -wave interactions are immediately suppressed, as the spatial collision must be antisymmetric in order to keep the total state fermionic (the combined nuclear and orbital state is always symmetric in the GDM). Once the  $p$ -wave collisions are dominant, then the dependence on the particular pair of modes in Eq. 4.5 becomes negligible [20, 155], which further guarantees that the interaction is only totally symmetric, reinforcing the possibility of the all to all approximation. As a matter of fact, thermal effects also help to make the collective description more accurate. Even with

the presence of  $s$ -wave terms, the  $p$ -wave collision terms become more and more dominant as the occupied vibrational modes are higher in energy because of thermal excitation [159], keeping the system mainly in the initial GDM. These highly excited states have also a much reduced mode dependence of the collision terms, which is further averaged out by the thermal fluctuations. Despite these last conditions would demand thermal master equations for the very exact description of the state, the assumption of a unitary evolution of a pure state of the system still captures the essential physics involved. We will be concerned with collective squeezing and exchange interaction, both of them being relatively robust against noise.

In the GDM, and defining collective operators  $\hat{T}_\alpha = \sum_{j=1}^N \hat{t}_\alpha^j$ , the collision Hamiltonian can be rewritten as,

$$\hat{H}^c = (V^{eg,+} - V^{eg,-}) \hat{\mathbf{T}}^2 + \frac{1}{2} (V^{ee} + V^{gg} - 2V^{eg,+}) \hat{T}_z^2 + \frac{1}{2} (N-1) (V^{ee} - V^{gg}) \hat{T}_z. \quad (4.7)$$

There remains the interaction that the atoms can have with other electromagnetic fields as the Ramsey pulses of a driving laser, or an external magnetic field  $B$ . This part of the Hamiltonian can be written as,

$$\hat{H}^L = -\delta \hat{T}_z - \sum_{i=1,2} \Omega_i \hat{T}_{i,y} + B \Delta g \sum_{i=1,2} m_{F,i} \hat{T}_{i,z} + B \bar{g} \sum_{i=1,2} m_{F,i} \sum_{j=1}^N \hat{\pi}_i^j, \quad (4.8)$$

where  $\delta$  is the laser detuning with respect to clock frequency in the absence of magnetic field. Coefficients  $\Omega_i$  are the Rabi frequencies of the laser Ramsey driving, which depend on the nuclear spin states and the clock dipole transition. These two terms are just for state preparation and read-out so they are not that relevant for the dynamics. What is important to notice in them is that atoms can be driven to different pulse angles depending on the nuclear state. The last two terms in Eq. 4.8 are due to the Zeeman splitting caused by an external magnetic field, where  $\Delta g$  and  $\bar{g}$  are respectively the differential and average Landé factors. The numbers  $m_{F,i}$  are the single atom magnetic nuclear quantum number, while the operators  $\hat{\pi}_i^j$  are projectors onto the  $i$ th nuclear state. The resolution of each nuclear state can also be exploited to read the state of each nuclear spin separately. Taking both Hamiltonians in Eqs. 4.7 and 4.8 into account, the system evolution during dark Ramsey time is generated by,

$$\hat{H} = \kappa \hat{\mathbf{T}}^2 + X \hat{T}_z^2 + (N-1) C \hat{T}_z + C' \hat{T}_z + \alpha (\hat{T}_2 - \hat{T}_1) + \gamma \hat{S}_z. \quad (4.9)$$

This will be the Hamiltonian to use for the rest of this chapter. Experimental estimations of these coefficients in Sr clocks are as follows [160]. Coefficient  $\kappa = V^{eg,+} - V^{eg,-}$  is of the order of 1.7 Hz. This value can be bigger, as  $s$ -wave collisions may also be involved in it. Coefficient  $X = \frac{1}{2} (V^{ee} + V^{gg} - 2V^{eg,-})$  takes values around 1.3 Hz. Coefficient  $C = \frac{1}{2} (V^{ee} - V^{gg})$  is around  $-0.39$  Hz. Another coefficient is  $C' = \frac{m_{F,2} + m_{F,1}}{2} \Delta g B$ , which can be made zero by choosing for instance  $m_{F,2} = 1/2$  and  $m_{F,1} = -1/2$ . The only relevant magnetic field term

will be that with  $\alpha = \frac{m_{F,2} - m_{F,1}}{2} \Delta g B$ , with  $\Delta g \sim 109 \text{ Hz/G}$ , so  $\alpha = 54.5B \text{ Hz}$  [151], if the magnetic field is measured in Gauss and  $m_{F,2} - m_{F,1} = 1$ . Finally, the last coefficient is  $\gamma = B\bar{g}(m_{F,2} - m_{F,1})$ , with  $\bar{g} \sim 185 \text{ Hz/G}$ . We will see that because of the operators we are interested in, and the initial conditions, this last term –dependent on magnetic field– will not be relevant either.

Finally, we must establish the initial conditions. We are going to assume we start in the Dicke Manifold of total nuclear spin, i.e.,  $\mathbf{S}^2 = S(S+1)$  and  $S = N/2$ . We are going to assume that the nuclear states form an angle  $\beta$  with respect to the axis  $S_z = -N/2$  and direction  $+x$ . This kind of initial nuclear state, even addressing only a pair of Zeeman levels, is experimentally feasible [161]. As far as we are going to be concerned with observables that depend only on operators  $\hat{T}_{i,\alpha}$ , the term proportional to  $\gamma$  in Eq. 4.9 can be ignored. Each GDM state with a definite value of  $S_z$  also yields a definite quantum number for operators  $\mathbf{T}_1^2 = (T_1 + 1)T_1$  and  $\mathbf{T}_2^2 = (T_2 + 1)T_2$ , which are  $T_1 = (N - s)/2$  and  $T_2 = s/2$  respectively; i.e., the  $S_z = s - N/2$  manifold has dimension  $d = (N - s + 1)(s + 1)$ . In general, concerning the orbital degrees of freedom, we are going to assume that we start by having all the clock states initially polarized in  $g$ , and then applying different Ramsey pulses to each nuclear spin forming different angles  $\theta_i$  with respect to  $T_z = -N/2$ . Explicitly, the initial condition is,

$$|\psi(0)\rangle = \sum_{s=0}^N \binom{N}{s}^{1/2} \left(\sin \frac{\beta}{2}\right)^s \left(\cos \frac{\beta}{2}\right)^{N-s} \sum_{l_1=0}^{N-s} \sum_{l_2=0}^s \binom{N-s}{l_1}^{1/2} \binom{s}{l_2}^{1/2} \left(-\sin \frac{\theta_1}{2}\right)^{l_1} \left(-\sin \frac{\theta_2}{2}\right)^{l_2} \left(\cos \frac{\theta_1}{2}\right)^{N-s-l_1} \left(\cos \frac{\theta_2}{2}\right)^{s-l_2} |s, l_1, l_2\rangle_1, \quad (4.10)$$

where first factors are binomial coefficients,  $\theta_i$  is the Ramsey pulse area, and non-negative integers  $l_i$  define an eigenvalue of  $T_{i,z} = l_i - T_i$ . The subindex in the ket is because there is an alternative basis, which would be the eigenbasis of Eq. 4.9 with zero magnetic field, namely  $|s, l, J\rangle_2$ , where  $T_z = l - J$  and  $\mathbf{T}^2 = J(J+1)$ . Clebsch-Gordan coefficients mediate between both bases. From the initial condition in Eq. 4.10, it can be seen that the expectation value of any observable  $\hat{B}$  that depends only of operators  $\hat{T}_{i,\alpha}$  could be written as,

$$\langle \hat{B} \rangle = \sum_{s=0}^N \binom{N}{s} \left(\sin^2 \frac{\beta}{2}\right)^s \left(\cos^2 \frac{\beta}{2}\right)^{N-s} \langle \hat{B} \rangle_s, \quad (4.11)$$

where  $\langle \hat{B} \rangle_s$  is the expectation value in the submanifold with  $S_z = s - N/2$ . Therefore, any expectation value would be a weighted average over each  $s$ -definite submanifold. This fact will be very relevant in order to have better estimations in the mean field theory. All over this chapter we will assume symmetrical mixing of the nuclear states, i.e., we will always assume  $\beta = \pi/2$ .

We are going to be concerned about two main kinds of initial angle settings. The first set of conditions can be called **spectator conditions**, in which  $i = 1$  states remain in the ground

state (*spectator* atoms) while only atoms with  $i = 2$  are rotated (*interrogated* atoms). As the terminology suggests, this kind of conditions are devised to address the possibility of state transfer induced by exchange interaction: in the sense that Hamiltonian 4.9 couples nuclear and orbital degrees of freedom by means of purely fermionic antisymmetry arguments, and that this Hamiltonian may produce the transfer of information from the interrogated atoms to the spectator atoms and the other way around. The second set is the **equal angle conditions**, i.e.,  $\theta_1 = \theta_2$  so that we start with zero relative Bloch vector  $\hat{\mathbf{T}}_2 - \hat{\mathbf{T}}_1$ . This relative Bloch vector will remain zero if there is no magnetic field  $B$ . However, state transfer will appear if  $B \neq 0$ , as Zeeman splitting would generate differences between the nuclear states. As state transfer is the essence of systems interacting through quantum magnetism, most of the attention will be directed to situations with that kind of interaction.

### 4.3 Mean field equations

Despite being only accurate when correlations among particles are negligible, mean field equations (MFE) can illustrate many qualitative aspects of the physics involved. There are many ways to derive these equations, either by changing the quantum field operators in Eq. 4.1 by  $c$ -numbers, or by approximating the state of the total system as an uncorrelated product of individual particles  $|\psi(t)\rangle \langle\psi(t)| \approx \hat{\rho}(t)^{\otimes N}$ . For more details, the reader can see section E.1 in the appendices. The MFE of Hamiltonian in Eq. 4.9 can be written in vectorial form,

$$\frac{d\mathbf{t}_2}{d\tau} = [2\mathbf{t}_1 + (2\chi Z + a + c)\mathbf{e}_z] \times \mathbf{t}_2, \quad (4.12a)$$

$$\frac{d\mathbf{t}_1}{d\tau} = [2\mathbf{t}_2 + (2\chi Z - a + c)\mathbf{e}_z] \times \mathbf{t}_1, \quad (4.12b)$$

where  $\tau = \kappa Nt$ ,  $a = \alpha/(N\kappa)$ ,  $c = C/\kappa$ , and  $\chi = X/\kappa$ . Vectors  $\mathbf{t}_i$  represent the single particle expectation value of  $\hat{t}_j^\alpha$ , which is the same for all particles thanks to the all-to-all condition. Vector  $\mathbf{e}_z$  is the unitary vector along the  $z$  direction. The number  $Z = t_{1,z} + t_{2,z}$  is a constant of motion. The part of Eqs. 4.12 that depends on  $x$  and  $c$  causes only a precession of the entire system around the  $z$  axis. Therefore, they are going to be ignored by going to a rotating frame, whose angular velocity is  $\boldsymbol{\Omega} = (2\chi Z + c)\mathbf{e}_z$ . By considering initial conditions in Eq. 4.10, both  $\mathbf{t}_2$  and  $\mathbf{t}_1$  start in the  $z - x$  plane forming angles  $\theta_2$  and  $\theta_1$  with respect to  $\mathbf{e}_z$ .

In terms of relative coordinates  $\mathbf{R} = \mathbf{t}_2 + \mathbf{t}_1$  and  $\mathbf{r} = \mathbf{t}_2 - \mathbf{t}_1$ , the MFE are simplified to,

$$\frac{d\mathbf{R}}{d\tau} = a\mathbf{e}_z \times \mathbf{r}, \quad (4.13a)$$

$$\frac{d\mathbf{r}}{d\tau} = 2\mathbf{R} \times \mathbf{r} + a\mathbf{e}_z \times \mathbf{R}. \quad (4.13b)$$

These equations have rather easy interpretations in the limits  $a \rightarrow 0$  and when  $a \rightarrow \infty$  as illustrated in Figs. 4.3a-b. In the zero magnetic field limit, the total vector  $\mathbf{R}$  remains constant

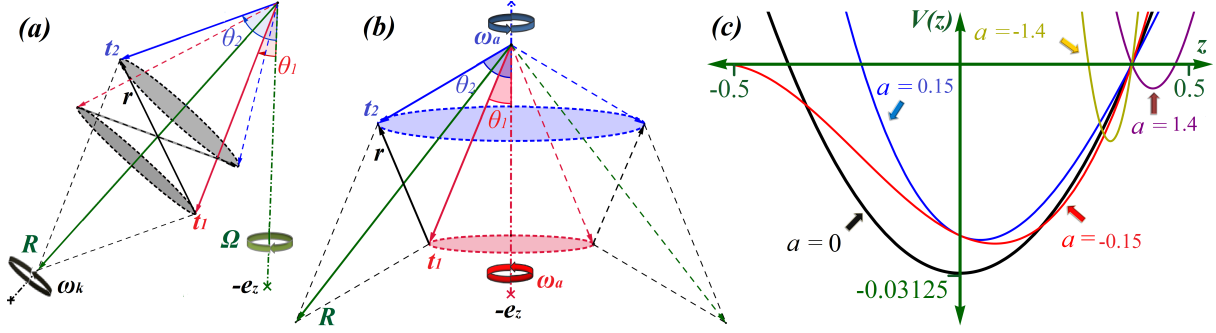


FIGURE 4.3: (a,b) Time evolution of vectors  $\mathbf{t}_1$ ,  $\mathbf{t}_2$  and their total and relative ones  $\mathbf{R}$  and  $\mathbf{r}$ . The evolution in (a) is the  $a \rightarrow 0$  limit of Eqs. 4.13, while (b) is for the  $a \rightarrow \infty$  limit (great magnetic field). Population transfer, as measured by the variation of  $z$  component of  $\mathbf{r}$ , is suppressed by high magnetic fields. (c) Confining potential felt by  $z = r_z$  under different values of  $a$ . Initial conditions are  $t_1 = t_2 = 0.25$ ,  $\theta_2 = 3\pi/4$  and  $\theta_1 = \pi/4$ . Motion of  $z$  is confined to  $V(z) < 0$ . At small values, magnetic field can enhance or suppress population transfer as compared to zero field (black harmonic potential). However, at high values it only pegs the value of  $z$  to a narrow interval.  $\Omega$  rotations in (a) are ignored because of the rotating frame interaction picture.

and the relative  $\mathbf{r}$  precesses around it, a precession that also applies to vectors  $\mathbf{t}_1$  and  $\mathbf{t}_2$ . In the opposite limit of infinite magnetic field,  $\mathbf{t}_1$  and  $\mathbf{t}_2$  precess around the  $z$  axis in opposite directions but with the same frequency, varying vectors  $\mathbf{R}$  and  $\mathbf{r}$  accordingly. As the laboratory frame  $xy$  components would depend also on the rotating terms, it is the relative component  $r_z = z$  the most interesting for these simplified MFE. This component express the relative population of modes in state  $e_2$  with respect to those in state  $e_1$ . This relative population oscillates around the mean value  $Z/2$  in the zero magnetic field limit, while it remains fixed at infinite magnetic field. It is then clear that an intense magnetic field can act as a suppressor of population transfer.

Outside the two simple magnetic field limits, the time evolution of  $z$  is described by,

$$\ddot{z} = 6(z - z_0)^2 - 4 \left[ (a - z_0)^2 + R_0^2 - z_0^2 \right] (z - z_0) + \ddot{z}_0 = -\partial V / \partial z, \quad (4.14)$$

where  $\dot{z}$  represents derivative with respect to  $\tau$ , subindex zero is initial value, and  $R_0 = |\mathbf{R}(0)|$ . Potential  $V(z)$  is cubic, which is an alteration of the zero magnetic field harmonic potential. Figure 4.3c shows that, if the magnetic field is not so intense, it can enhance or suppress population transfer according to the initial population imbalance. We will see this simple classical picture drawn from the MFE are a good guide to understand results even in the exact quantum domain.

## 4.4 Bloch vector dynamics

This section is concerned about results that are obtainable either by means of MFE as in previous section and also a full quantum treatment. So, it is mainly focused on Bloch vector dynamics.

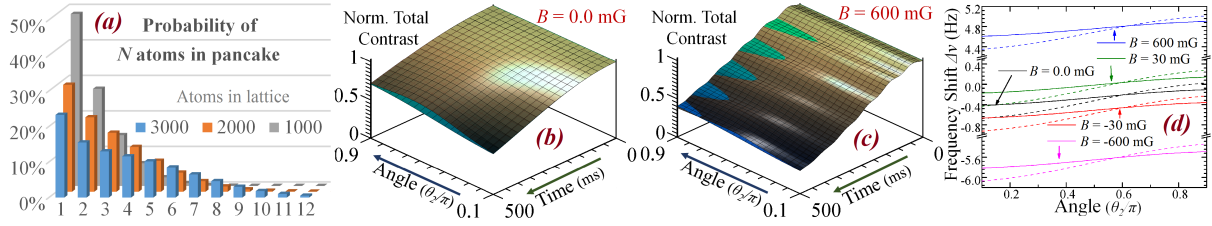


FIGURE 4.4: **(a)** Probability of having a pancake with  $N$  atoms in it, which depends on the total number of atoms in the optical lattice. **(b,c)** Time evolution of normalized total contrast,  $\frac{|\langle \hat{\mathbf{T}}_{xy}(t) \rangle|}{|\langle \hat{\mathbf{T}}_{xy}(0) \rangle|}$  under spectator conditions ( $\theta_1 = 0$ ) with different Ramsey angle  $\theta_2$  and two different magnetic fields  $B$ . This data is the average over all pancakes with one thousand atoms in the entire lattice. **(d)** Frequency shift of total Bloch vector under the same conditions of **(b,c)** and also other values of  $B$ . Notice the pair of big breaks in the vertical scale in order to represent the high  $B$  shifts. Cold colored surfaces in **(b,c)** and solid lines in **(d)** represent the exact quantum results while MFE predictions are depicted with warm colored surfaces and dashed lines respectively. Total Bloch dynamics clearly demands high experimental resolution in order to find beyond MFE physics; for instance, frequency resolution should be of the order of  $\sim 0.1\text{Hz}$ .

We understand as Bloch vector dynamics the time evolution of expectation values like  $\langle \hat{\mathbf{T}}_{i,\alpha} \rangle$ , their microscopic counterparts  $\langle \hat{\mathbf{t}}_{i,\alpha}^j \rangle$ , or any other information extracted from them. The main objective of this section is to answer the question of whether it is possible to distinguish between the MFE predictions and the exact quantum ones, by focusing on the most available kind of data currently available in the  $^{87}\text{Sr}$  atomic clocks with Ramsey spectroscopy techniques (i.e., Bloch vector dynamics themselves).

Before going further, we need to give an additional clarification of the experimental data at disposal under current realizations of the  $^{87}\text{Sr}$  atomic clock, which will be the focus of this section. If attention is paid to Fig. 4.1a, it should be noticed that the probing laser under current clock operations simultaneously scans all pancakes in the 1D lattice. This means that the more readily available data from these experiments concerns predictions not of a single pancake, like that of Eq. 4.11, but an average of a signal generated by all pancakes simultaneously. This available experimental data is equivalent to having expectation values of the form,

$$\langle \hat{\mathbf{T}}_{i,\alpha} \rangle = \sum_N p_N \langle \hat{\mathbf{T}}_{i,\alpha} \rangle_N, \quad (4.15)$$

where  $p_N$  is the probability of having  $N$  atoms in a pancake, which depends on the total number of atoms in the lattice. Figure 4.4a depicts some of the possible probability distributions  $p_N$ , which were experimentally determined. All over this section, we will discuss results obtained by means of averages like Eq. 4.15 for the specific case that there are a thousand atoms in the entire lattice. This is a relatively small amount of atoms, as numbers up to 4000 are quite common, but that is not so relevant for discussing the main tendencies.

The initial conditions are specified by Eq. 4.10 with atoms having initial Ramsey angles  $\theta_i$  depending on the nuclear spin state. Both quantum and MFE results were obtained by numerically solving the evolution for a particular value of  $s$  and  $N$ , by using Hamiltonian 4.9 as

generator or integrating Eqs. 4.12. After that, mean values are obtained by subsequently applying Eqs. 4.11 and 4.15. However, not all results were obtained numerically. There are instances where expectation values of the problem are expressible in analytic forms. Under zero magnetic field, and in the exact quantum realm, all expectation values of total orbital pseudo-spin  $\hat{\mathbf{T}}$  are readily computable (see section E.6 in the appendices). Also, the MFE can be reduced to a superposition of harmonic oscillators or constant angular frequency rotations, as Fig. 4.3a illustrates.

We are going to analyze our Bloch vector dynamics under two categories: *total Bloch vector* dynamics when expectation values for both nuclear states are added (vector  $\mathbf{R}$  in Figs. 4.3a-b), and *relative Bloch vector* dynamics when differences between those vectors are considered (vector  $\mathbf{r}$  in Figs. 4.3a-b). This makes the description simpler and allows to separate objectives, since total dynamics are more interesting for clock implementations and metrology, while the relative ones are related to state transfer and quantum magnetism.

#### 4.4.1 Total Bloch vector dynamics

Total Bloch vector dynamics under spectator conditions are shown in Figs. 4.4b-d. The two first surfaces (Figs. 4.4b-c) show time evolution of total contrast, which is the  $xy$  magnitude of the Bloch vector (see caption for equation). This nomenclature come from the fact that this parameter is associated to the amplitude of fringes in Ramsey spectroscopy. Figure 4.4b may seem wrong, at least if one thinks about the prediction Eq. 4.13, which states that at zero magnetic field total contrast should remain constant. However, we must remember that results in Fig. 4.4b are averages over different values of  $s$  (see Eq. 4.11), and different number of atoms in pancake  $N$  (see Eq. 4.15). Different values of  $s$  and  $N$  mean different lengths for  $NR_z$  in Fig. 4.3a, which would give different precession frequencies  $\Omega$  (see Eq. 4.12), and even a different definition of  $\tau$ . All this means that the initial composition of Bloch vectors becomes increasingly dephased, accumulating a destructive interference, which explains why measurable total contrast decays. This relative dephasing is less intense for small angles  $\theta_2$ , which indicates that the distribution of precession frequencies is less relevant in that case. Also, the fact that the quantum decay tends to be bigger than the classical one is related to the fact that the quadratic term in Hamiltonian 4.9 induce additional phase fluctuations not considered in the MFE. Figure 4.4c can be explained similarly, but now we must take into account that under strong magnetic field, Eq. 4.13 predicts oscillations of  $R_{xy}$  with angular frequency  $a$ , which depends only on  $N$ . However, Fig. 4.3b shows clearly that if  $\theta_1 = 0$  and  $B$  dominates,  $R_{xy}$  should not oscillate at all. This means that the total contrast decay for high  $B$  is almost exclusively related to interference with different pancake signals with a small component due to coupling with relative Bloch vector which causes a small dependence on  $\theta_2$ . If  $B$  were totally dominant, the decay would be independent of  $\theta_2$ . Quantum deviations in Figs. 4.4b-c from MFE are not very big, which means that total Bloch vector dynamics under spectator conditions require good experimental

resolutions in order to distinguish atom-atom correlations and quantum fluctuations. Also, these deviations concentrate differently when strong magnetic field is applied (at large  $\theta_2$  angles) than in zero magnetic field (around  $\theta_2 = \pi/2$ ), which suggest different behavior of the correlations associated to total Bloch vector in each case.

The other total Bloch vector quantity we are going to discuss for spectator conditions is the *frequency shift* [162]. This is defined as,

$$2\pi\Delta\nu = \frac{\Delta\phi}{\Delta t}, \quad (4.16)$$

where  $\Delta\phi$  is the azimuthal ( $xy$  plane) rotation angle of total Bloch vector after a time  $\Delta t = 100\text{ms}$ . Other  $\Delta t$  values give similar results as the azimuthal angular frequency starts being relatively constant. This frequency shift is density dependent, in the sense that it will be greater if we have a bigger nadir angle, i.e, if we have a bigger initial population of excited atoms. The shift is also bigger when more atoms are trapped in the lattice. Thus, frequency shift is one of the big challenges for the many-body AEA lattice system to be used as a clock [159]. The collective behavior helps to have great stability and then improved precision with respect to single atom or single ion clocks, but this shift caused by atom-atom interactions would introduce a systematic error in the frequency standard. Figure 4.4d depicts the frequency shift estimated for the same conditions of Figs. 4.4b-c. Then, it is shown that a resolution of  $\sim 0.1\text{Hz}$  would be needed in order to make the atomic collision effects apparent and to distinguish the quantum evolution from the MFE. Then, no wonder that in previous experiments with not very great resolution the interactions were unnoticed. In Fig. 4.4d we see that  $\Delta\nu$  behaves as expected, increasing with zenith angle, and in fact its dependence is linear with respect to  $\cos\theta_2$ . If azimuthal rotation angle were really constant, then the crossing with  $\Delta\nu = 0$  could be chosen to avoid clock systematic errors but the non-linear character of Hamiltonian in Eq. 4.9 discards that possibility. Higher number of atoms and equal angle conditions would give more noticeable shifts [160].

#### 4.4.2 Relative Bloch vector dynamics

Switching to relative Bloch vector dynamics under spectator conditions in Fig. 4.5 gives a different perspective. For instance, while the  $z$  component of total Bloch vector is always constant, that is not longer true for the relative one, which allows to talk about *population transfer*. This is defined as,

$$\mathcal{Z} = \frac{n_{e2} - n_{e1}}{n_{e2} + n_{e1}}, \quad (4.17)$$

where  $n_{\alpha i}$  are the expected number of atoms in nuclear state  $i$  and orbital state  $\alpha$  as in Eq. 4.6. An equivalent definition of  $\mathcal{Z}$  is given in caption of Fig. 4.5. The quantum exchange populations between states  $e2$  and  $e1$  represented by  $\mathcal{Z}$  can be thought as multiple bosons in a double well potential, with the possibility of tunneling across the mid barrier. This kind

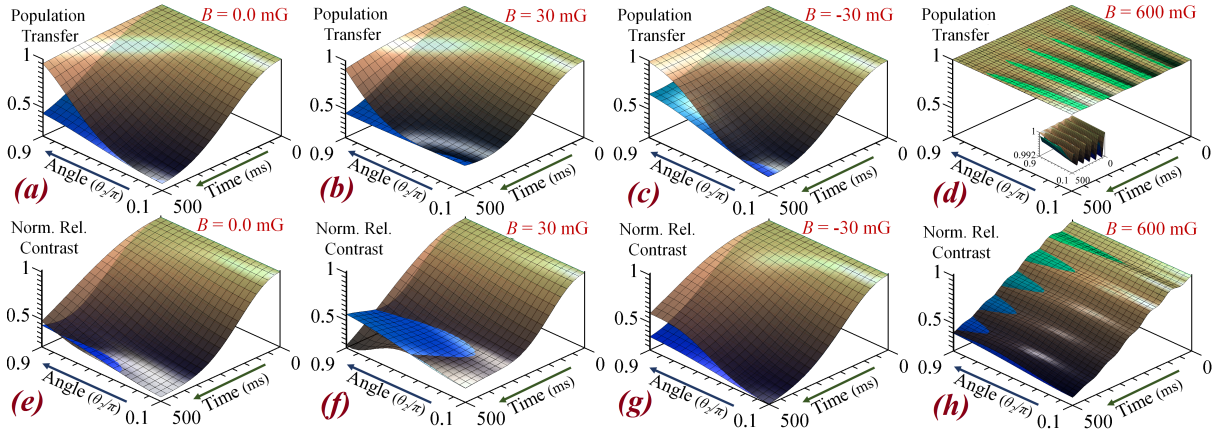


FIGURE 4.5: (a-d) Dynamics of population transfer  $\mathcal{Z} = \frac{\langle \hat{T}_{2,z} - \hat{T}_{1,z} \rangle}{\langle \hat{T}_z + N/2 \rangle}$ , and (e-h) normalized relative contrast  $\frac{|\langle \hat{T}_{2,xy}(t) - \hat{T}_{1,xy}(t) \rangle|}{|\langle \hat{T}_{2,xy}(0) - \hat{T}_{1,xy}(0) \rangle|}$  under the same conditions specified in Figs. 4.4b-d. Now, deviations from the MFE can be resolved much easier as compared to the total case, especially for (a-c) and (e-g), i.e., for large angles  $\theta_2 > \pi/2$  and not very big  $B$ . This suggests cases with significant correlations between Bloch vectors  $\hat{\mathbf{T}}_1$  and  $\hat{\mathbf{T}}_2$ . In contrast, the large  $B$  case (d,h) have very good agreement with MFE. Also, notice the magnetic field suppression of exchange transfer in (d). In that case, transfer is only visible by means of a big zoom in the inset.

of quantum problem has been famously associated to tunneling across Josephson junctions in superconductor physics [163]. Oscillations between wells depend on the conditions on the relative strength of tunneling hopping, barrier height, and interaction energy in each well. In particular, when the chemical potential associated to the differences in population and interaction energy between wells dominate the dynamics, the population oscillation is suppressed, in a phenomenon known as macroscopic self-trapping. This effect has been recently confirmed in bosonic cold-atom systems [164] and excitonic condensates [165]. At zero magnetic field a precession around total Bloch vector is predicted (see Fig. 4.3a), but its frequency depends on the initial value of  $\theta_2$ , with bigger values being for initial big population imbalance. In phenomenon similar to macroscopic self-trapping, high values of  $\theta_2$  will have very slight change of  $\mathcal{Z}$ , as can be seen in Fig. 4.5a.

Figure 4.5d shows the suppression of population transfer predicted in the MFE and illustrated in Figs. 4.3b-c. A similar picture would have been obtained if magnetic field were directed in negative direction. In the double well picture, this would mean that the magnetic field creates an energy difference between both nuclear states so high that hopping terms (proportional to  $\kappa$  in eq. 4.9) cannot longer make the populations to oscillate. However, under weak magnetic terms (Figs. 4.5b-c) the effect of  $B$  suppression of  $\mathcal{Z}$  oscillation is not so clear, since they can enhance or diminish the state transfer depending on direction. This direction asymmetry was already predicted in Fig. 4.3c, which shows that small values of  $a$  can broaden or tighten the confinement of  $\mathcal{Z}$  depending on the direction, i.e., precessions around  $\mathbf{R}$  and  $\mathbf{e}_z$  in Fig. 4.3b can cancel or reinforce each other. The asymmetry between negative and positive small magnetic

fields is also present in relative contrast in Figs. 4.5f-g with a complex dependence on the initial Ramsey angle  $\theta_2$ .

Relative contrast under zero magnetic field should oscillate between a positive and maximum value as depicted in Fig. 4.3a when  $\mathbf{r}$  is projected onto the  $xy$  plan. Also, its frequency of oscillation will depend on the magnitude of total Bloch vector. Both amplitude and frequency will be bigger for small  $\theta_2$ , as it is evidenced in Fig. 4.5e. However, this tendency deducible from Fig. 4.3a is obscured by high interference among different frequencies, caused again by different Bloch vectors  $\mathbf{t}_1$  and  $\mathbf{t}_2$  lengths which will greatly vary the length of total  $\mathbf{R}$ . Equation 4.13 shows that when  $B$  is dominant, both relative and total contrast behave the same, that is why Fig. 4.4c is so similar to 4.5h.

### 4.4.3 Equal angle conditions

We have reserved results for equal angle conditions to this separate section. This in part due to the fact they have been analyzed, at least partially and in the zero magnetic field case, in Ref. [20]. That specific case, which has analytical solutions as expressed in E.6, does not make any use of the presence of the nuclear degrees of freedom, and as such it is not much related to our aim of investigating  $SU(2)$  quantum magnetism. We have included it as a reference for certain comparisons, especially spin squeezing in section 4.5.2. In this analytically solvable case, for any value of  $\hat{S}_z$ , the system will be always in an eigenvalue of  $\hat{\mathbf{T}}^2$ , i.e., it will always lie in the Dicke manifold of total orbital pseudo-spin. This presence of a good quantum number and the fact that the contrast profile in Fig. 4.6a. greatly resembles Fig. 4.4b indicates that the interference that causes contrast decay is mostly due to different pancake signals. Also, as there are less dephasing explainable in terms of MFE, we see that quantum effects are more easily seen in Fig. 4.6a. with respect to Fig. 4.4b, which we will see that this has to do to with a squeezing process in the former. Now, for intense  $B$  as in 4.6b, the oscillations predicted by the MFE are totally visible, since they have maximum amplitude, but can be damped by dephasing of azimuthal frequencies  $\Omega$ , with zero dephasing when  $\theta_2 = \theta_1 = \pi/2$ . Quantum fluctuations, instead, introduce dephasing at all angles.

Concluding the Bloch vector review, we show in Fig. 4.6c that the magnetic field under equal angle conditions induces a population transfer provided  $B$  is not too intense<sup>1</sup>. That is exclusive of the small  $B$  regime. Population transfer is initially zero and it will remain so if no field is applied. In the other extreme, if  $B$  is too intense, the suppression of state transfer is activated. Only when all terms in Hamiltonian 4.9 are relevant it is possible to have significant population transfer under equal angle conditions. Which is also the most convoluted possibility.

<sup>1</sup>We do not show an equivalent to Fig. 4.6c with negative angle, but it is easily deducible, as inverting the direction of  $B$  is equivalent to interchange  $\hat{\mathbf{t}}_2$  and  $\hat{\mathbf{t}}_1$ . Then, a figure for  $B = -30\text{mG}$  would be very similar to Fig. 4.6c but with negative values of  $\mathcal{Z}$ .

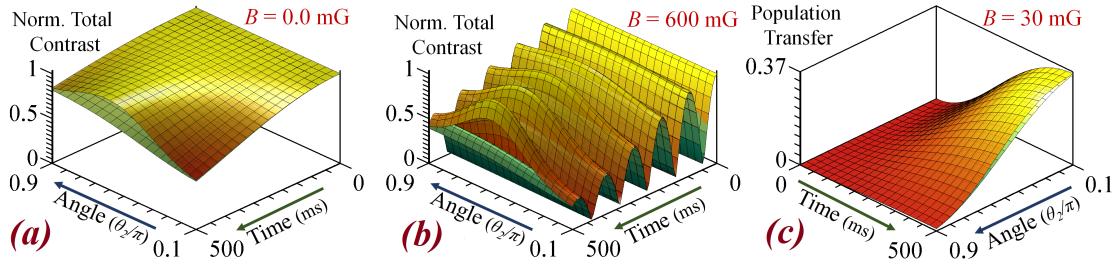


FIGURE 4.6: Bloch vector dynamics results under both spins rotated conditions, i.e.,  $\theta_1 = \theta_2$ ; all the rest is as specified in Figs. 4.4b-d except that the warm and cold color palette is different. **(a-b)** Total contrast results, conditions with equal initial Ramsey angles produce more distinguishable deviations from MFE. **(c)** Even though at  $B = 0$  both Bloch vectors would behave equally under these initial conditions, not too big  $B \neq 0$  induces a population transfer and in general an exchange interaction.

## 4.5 Dynamics of atom-atom correlations

In order to see the role correlations play in previous results and tendencies, it is time to explore information beyond single point functions. Ways of computing them are explained in appendix section E.2. As we are now dealing with correlations between particle, it has no sense to keep investigating signals when all pancakes are included, since there are no correlations between particles belonging to different pancakes. Then, we will focus on a single pancake so that an average like Eq. 4.15 is no longer needed. All through the rest of this chapter, we are going to present results with  $N = 16$ . Tendencies are essentially the same with other values of atoms in the pancake. Besides that, all other settings and conditions defined in previous sections are maintained.

### 4.5.1 Atom-atom correlations

The basic supposition of MFE is explained in appendix section E.1. Then, it is explained in appendix E.5 that an implication of the mean field approximation is the absence of microscopic correlations, that is, that microscopic expected values like  $\langle \hat{\mathbf{t}}_{i,\alpha}^{j_1} \rangle$  and  $\langle \hat{\mathbf{t}}_{j,\beta}^{j_2} \rangle$  are statistically independent for any pair of different atoms  $j_1 \neq j_2$ . As a converse, we could use correlation measures like linear covariances between particles to establish when and how do we expect to find a failure in the MFE. Examining these correlations is tantamount to probe the level of exchange interaction at the atom-atom level, providing a crucial evaluation of the kind of highly correlated systems that could be suitable for quantum simulation in the AEA lattice clock platform.

We have chosen some forms of maximum covariances as correlation parameters (see E.5) since they have a direct interpretation as the statistical interrelation between certain Bloch vectors of each atom. Given that in the previous section we stressed a separation between total and relative Bloch vector, we are going to mention here just the correlation parameters more relevant

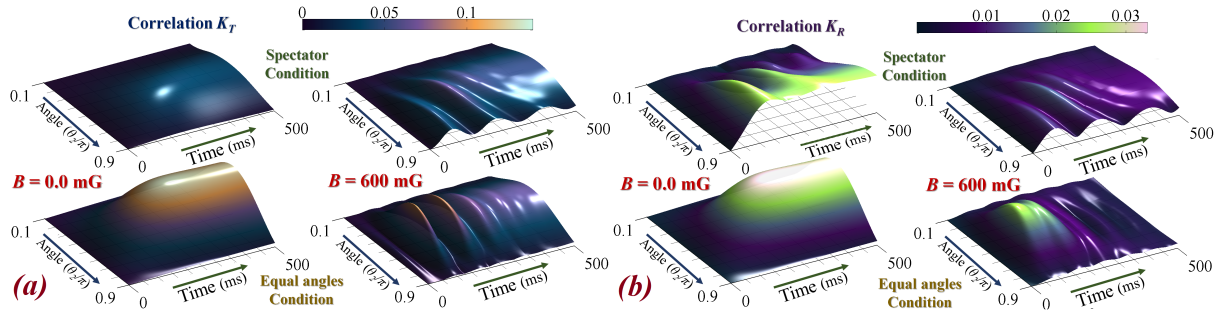


FIGURE 4.7: (a) Total correlation parameter  $K_T$  and (b) relative correlation parameter  $K_R$  as a function of time and under different initial conditions. These parameters establish the maximum covariance between the Bloch vectors of a pair of different atoms ( $j_1 \neq j_2$ ) interacting within a pancake with a total of  $N = 16$  atoms. As the name suggests, the Bloch vectors in each case are different, being total vectors  $\mathbf{t}^{j_1}$  and  $\mathbf{t}^{j_2}$  in the former, while in the latter it is between  $\mathbf{t}_2^{j_1}$  and  $\mathbf{t}_1^{j_2}$ . Instances with high values of these covariances would imply evolution conditions at which the MFE predictions concerning the involved macroscopic Bloch vectors fail.

for both kinds of Bloch vector, respectively  $K_T$  and  $K_R$ . Figures 4.7a-b give a general picture of the behavior of both kind of covariances. We should clarify that the smaller scale for  $K_R$  does not mean that we have considerably less relative correlations as compared to the absolute one. Far from that, the reason of the different scale is that the maximum possible value of  $K_T$  is 0.25 while it is only a quarter of that for  $K_R$ , due to the probability below unity of both particles having a definite nuclear state.

It is quite consistent to see that there are strong similarities between the pair of surfaces in Figs. 4.7a and 4.7b in the same way that it happened in Figs. 4.4c and 4.5h. This reveals that even at the level of correlations and in the pure quantum realm, it is maintained the identical behavior of relative and total Bloch vector predicted by MFE 4.13 under dominating magnetic field. Also, correlations in Figs. 4.7a and 4.7b are small, something that justifies the level of similarity between the quantum solution and MFE when magnetic field is intense. This correspondence is maintained even for particular times and initial angle conditions, with the general rule of thumb: less correlations, better accuracy between MFE and exact quantum solution. All of this despite Figs. 4.4c and 4.5h have extra information coming from pancakes with different kind of atoms. Keeping this rule of thumb in mind, it is clear that total Bloch vectors do not reveal much quantum behavior under spectator conditions, but they certainly do when both nuclear spins are equally rotated. That is quite apparent in the fact that upper graphs in Fig. 4.7a are much less prominent than the lower ones. As a general tendency, we can say that spectator conditions are not well suited for generating high correlations in the total Bloch vector, as they disperse the evolution on different values of  $\langle \hat{\mathbf{T}}^2 \rangle$ . In other words, spectator conditions tend to cause the nuclear states to be a dispersive environment for total Bloch vector correlations. In next subsection we will see that this is also a deleterious effect on squeezing and total quantum concurrences.

On the other hand, relative correlations for spectator conditions shown in Fig. 4.7b are much

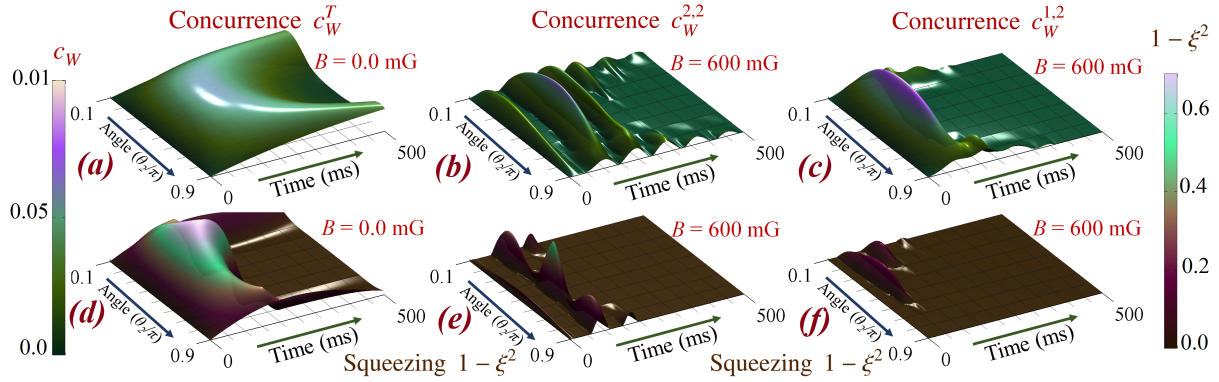


FIGURE 4.8: Evolution of (a-c) concurrence, and (d-f) spin squeezing under mostly equal angle conditions. With the exception of (f), which is under spectator conditions. The absence of exchange interaction in (a) and (d) represent pure cases of one axis squeezing with a transverse field, already mentioned in section 3.6. Especially at middle angles, when total Bloch vector is perpendicular to the non linear term. Total quantum correlations are absent in any other case since the exchange interaction and the magnetic field tend to blurred them out. However, if two qubit density matrices with definite nuclear spin are considered (see Eq. E.17), then there can be some instances of two particle entanglement as in (b-c).

more promising, at least for zero or weak magnetic field <sup>2</sup>. Relative Bloch vector quantities under small  $B$  are certainly the more adequate for showing distinctive quantum behavior for the spectator conditions, as it was anticipated in Figs. 4.5a-c and 4.5e-g. This relative Bloch vector quantum behavior, and the relative quantum correlations we will see in next subsection, confirm the existence of true quantum magnetism in the  $^{87}\text{Sr}$  lattice clock, in the sense of strongly correlated and even often quantum entangled exchange interaction between the pseudo-spin of atoms with different (but definite) nuclear spin state <sup>3</sup>.

## 4.5.2 Quantum Correlations

Hamiltonian in Eq. 4.9 has an interesting quadratic term proportional to  $X$ , which is the interaction term in the LMGM, and has been already seen to produce spin squeezing when the initial term is perpendicular to  $\hat{T}_z$  [120, 123]. This kind of process is seen as favorable for clock operations, as it tends to reduce the phase uncertainty (and hence the inaccuracies of time keeping)[166]. In Figs. 4.8a and 4.8d, such a squeezing process is confirmed, and is best manifested, as expected, in the perpendicular initial conditions. In contrast, under any other condition, be it because of magnetic field, or because of exchange interaction, total concurrence and squeezing is virtually negligible so that it was pointless to present graphs for them. Under all those other situations, the system is no longer in the maximally symmetric Dicke manifold and dephasing between the different Bloch vectors with definite nuclear spin state cancel the quantum correlations. Total spin squeezing is momentarily generated in other situations like

<sup>2</sup>In this section we have skipped the presentation of results for  $B = \pm 30\text{mG}$  under spectator conditions because it would greatly saturate the presentation of results. As a general tendency, they are distorted versions of the results for zero magnetic field, much in the same sense as Figs. 4.5a-c and 4.5e-g.

<sup>3</sup>Correlations parameters like  $K_1$  and  $K_2$  defined in appendix section E.5 for spectator conditions are not shown in Fig. 4.7b, but they are very similar to their  $K_R$  counterparts.

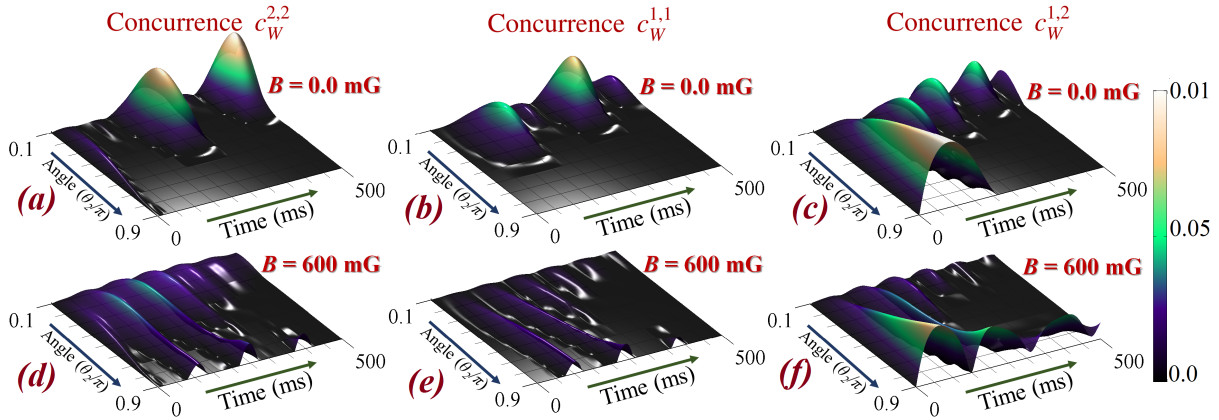


FIGURE 4.9: Time dependence of concurrence as a measure of entanglement between a pair of atoms when (a,b) both are made to collapse onto nuclear state 2, (c,d) both onto 1, or one onto 2 and the other one onto 1. All results are for spectator conditions and a pancake with  $N = 16$  atoms.

in Figs.e-f, as in those situations there are slight coordination between Bloch vectors at early stages.

Besides the initially disappointing findings for total concurrence and spin squeezing, we should not quickly conclude that only the  $B = 0 \wedge \theta_2 = \theta_1$  initial condition is the only interesting case for studying quantum correlations. A different picture is drawn if only two qubit density matrices with definite nuclear spin are considered. Then it is possible to talk about quantum correlations between specific Bloch vectors  $\hat{\mathbf{t}}_i$ . That kind of entanglement is present for equal angle conditions, as in Figs. 4.8b-c, which are well related to the correspondent graph in Fig. 4.7b. However, it is under spectator conditions and zero magnetic field (Figs. 4.9a-c), when exchange interaction occurs from start, that definite nuclear spin quantum concurrences tell the most interesting story. Early after starting point, concurrences appear between both nuclear states at 1 or between 1 and 2 at Ramsey angles near the  $-z$  direction. Later, the entanglement initially developed in the (1,1) pair is transmitted back and forward to the (2,2) pair, while the relative concurrence (1,2) follows that beating with twice the frequency. This reveals that exchange interaction not only induces transfer of state, but also transfer of entanglement. The low concurrences in 4.9d-f only confirms that once the state transfer is suppressed, also the transfer of entanglement is diminished, with the exception of an emergent beating at high angles in 4.9f.

## 4.6 Conclusion

We have theoretically demonstrated the existence of  $SU(2)$  quantum magnetism in a  $^{87}\text{Sr}$  lattice clock assuming all-to-all conditions and totally unitary evolution. We have shown that this exchange interaction is noticeable even under current Bloch vector measurements of multiple pancakes at the same time, however obscured by the average process. When zooming on a pair

of particles in each pancake, we have found not only that Bloch vector state transfer occurs between them, but also that strong correlations and even quantum entanglement is developed during the dynamics. An even more curious finding has been that quantum entanglement may alternate between the pair of nuclear states from which the two particle clock states density matrix is extracted, in a sort of exchange of concurrence. The source of entanglement has been identified as non-linear processes frequently found to generate spin squeezing, and indeed very similar to those found in chapter 3. In general, we have found that the presence of this exchange interaction, whenever is clearly manifest (for instance, under spectator conditions), has a negative impact on favorable phenomena for metrology applications like spin squeezing on the total all-to-all state or total concurrence between single atom clock states.

We evaluated the effect of a magnetic field on the exchange interactions as well, which, whenever is too intense, suppress the state transfer and even the quantum entanglement transfer. Instead, when atoms have all a totally defined nuclear state (equal angle conditions), spin squeezing is generated and the magnetic field is not that effective in deleting correlations. The quantum magnetism we unraveled during this chapter takes the system further from ideal clock operations, but makes it much more interesting as a quantum simulator. Thus, quantum magnetism results greatly contrast with the stability and accuracy of clock operation under fully polarized nuclear spins, as was the focus of precedent works on the system. Finally, we must recall that the relatively simple classical ‘rotor’ picture we developed by means of MFE proved to be useful for the interpretation of many results.

# Outlook

We started by exploring the generalities of the DM both for the TL and finite size version, with a special focus on the QPT and related critical boundary. After presenting a remarkable experimental realization of the DM, we established the main tendencies of the system being irreversibly excited when made to dynamically cross the critical threshold, in a process of quantum hysteresis. After that, we discovered a new theoretical approach to describe this defect formation, namely the dynamical critical function theory. It turned out that our theory was able to tackle previously well understood systems like the TFIM, as well as the DM and LMGM. For the latter ones, traditional explanations such as the KZM fail.

When we went higher in the annealing velocities range, we stumbled upon a previously unnoticed dynamical regime that generated greatly magnified quantum properties as spin-squeezing and light-matter entanglement. Much more encouraging, we found out that many of these collective quantum effects were quite robust against dissipation caused by the environment. We were able to give a thorough demarcation of that complex dynamical regime by establishing its scaling behavior both in terms of system size and annealing velocity. Symmetry breaking, non-linear effective interactions and quantum chaos were all incorporated in our insights about this exciting discovery.

We then switched to the exchange interactions between clock state collective pseudo-spin networks in a  $^{87}\text{Sr}$  lattice clock, concocted by a suitable mixture of the fermionic nature of particles, the highly symmetrical  $p$ -wave interaction between vibrational modes, and the underlying  $SU(N=2)$  symmetry related to vanishing hyperfine interactions. We demonstrated strong correlations and exchange interaction between nuclear spin states, which confirmed the handiness of such a system for quantum magnetism simulations. Already familiar non-linear processes were found in this problem, that involved the transfer not only of orbital states, but also of quantum correlations. We found a trade-off between clock accuracy and transfer interactions.

A common thread all throughout this thesis was the concern about macroscopic control of quantum many-body systems, in particular the ones that involve all-to-all spin networks. In chapters 1 (quantum hysteresis) and 2, we found the restrictions experimented by adiabatic quantum control protocols when confronted to scalability with system size. Furthermore, we did it with a novel and broad ranged theory. In contrast, chapters 3 and 4 provided a more positive

perspective of non-equilibrium highly correlated collective interactions as means for quantum control techniques. Indeed, novel and highly profitable regimes have been identified. In both cases, different objectives could be achieved with a very good degree of tunability. The level of control in chapter 3 resided fundamentally in the annealing parameter, including its velocity and the value up to which is raised. On the other hand, in chapter 4, the maneuverability was the Ramsey pulses applied during initial state preparation, and in some sense, even the presence of the magnetic field.

Finally, we want to stress that all the topics dealt within this work have also in common a high degree of current interest, both theoretically and experimentally. In fact, quantum hysteresis procedures have been recently experimentally investigated for the DM [5]. Also, the dynamical crossing of QPT is one of the major open problems in current research [167], and the robustness of our results against noise makes us confident that soon we will see experimental confirmation of some of them. Finally, the  $^{87}\text{Sr}$  lattice clock is well ahead in the research race, either in the sense of ultra-high precision clocks, or as highly tunable quantum simulators [20]. We have found very rewarding to produce contributions that push further these knowledge frontiers.

# Bibliography

- [1] Y. Han, Z. Wang, and G.-C. Guo, *A new epoch of quantum manipulation*, [Natl. Sci. Rev.](#) **1**, 91 (2013).
- [2] P. Nataf and C. Ciuti, *No-go theorem for superradiant quantum phase transitions in cavity QED and counter-example in circuit QED*, [Nature Comm.](#) **1**, 1 (2010).
- [3] O. Viehmann, J. von Delft, and F. Marquardt, *Superradiant phase transitions and the standard description of circuit QED*, [Phys. Rev. Lett.](#) **107**, 113602 (2011).
- [4] K. Baumann, C. Guerlin, F. Brennecke, and T. Esslinger, *Dicke quantum phase transition with a superfluid gas in an optical cavity*, [Nature](#) **464**, 1301 (2010).
- [5] J. Klinder, H. Keßler, M. Wolke, L. Mathey, and A. Hemmerich, *Dynamical phase transition in the open Dicke model*, [Proc. Natl. Acad. Sci. U. S. A.](#) **112**, 3290 (2015).
- [6] A. M. Rey, L. Jiang, and M. Lukin, *Quantum-limited measurements of atomic scattering properties*, [Phys. Rev. A](#) **76**, 053617 (2007).
- [7] R. Schützhold and G. Schaller, *Adiabatic quantum algorithms as quantum phase transitions: First versus second order*, [Phys. Rev. A](#) **74**, 060304 (2006).
- [8] J. Dziarmaga, *Dynamics of a quantum phase transition and relaxation to a steady state*, [Adv. Phys.](#) **59**, 1063 (2010).
- [9] R. H. Dicke, *Coherence in spontaneous radiation processes*, [Phys. Rev.](#) **93**, 99 (1954).
- [10] S. Sachdev, *Quantum Phase Transitions* (Cambridge University Press, 2011).
- [11] O. Acevedo, L. Quiroga, F. Rodríguez, and N. F. Johnson, *Quantum emitters dynamically coupled to a quantum field*, [AIP Conf. Proc.](#) **1566**, 560 (2013).
- [12] O. L. Acevedo, L. Quiroga, F. J. Rodríguez, and N. F. Johnson, *New dynamical scaling universality for quantum networks across adiabatic quantum phase transitions*, [Phys. Rev. Lett.](#) **112**, 030403 (2014).
- [13] S. Fuchs, J. Ankerhold, M. Blencowe, and B. Kubala, *Non-equilibrium dynamics of the Dicke model for mesoscopic aggregates: signatures of superradiance*, (2015), [arXiv:1501.07841 \[quant-ph\]](#) .

- [14] A. Altland and F. Haake, *Equilibration and macroscopic quantum fluctuations in the Dicke model*, [New J. Phys. \*\*14\*\*, 073011 \(2012\)](#).
- [15] A. Alvermann, L. Bakemeier, and H. Fehske, *Collapse-revival dynamics and atom-field entanglement in the nonresonant Dicke model*, [Phys. Rev. A \*\*85\*\*, 043803 \(2012\)](#).
- [16] V. M. Bastidas, J. H. Reina, C. Emary, and T. Brandes, *Entanglement and parametric resonance in driven quantum systems*, [Phys. Rev. A \*\*81\*\*, 012316 \(2010\)](#).
- [17] O. L. Acevedo, L. Quiroga, F. J. Rodríguez, and N. F. Johnson, *Enhanced light-matter entanglement from driving neither too fast nor too slow*, Accepted for publication in Phys. Rev. A (2015), [arXiv:1503.05470 \[quant-ph\]](#).
- [18] O. L. Acevedo, L. Quiroga, F. J. Rodríguez, and N. F. Johnson, *Robust quantum correlations in out-of-equilibrium matter-light systems*, Accepted for publication in New J. Phys. (2015), [arXiv:1504.04260 \[quant-ph\]](#).
- [19] B. J. Bloom, T. L. Nicholson, J. R. Williams, S. L. Campbell, M. Bishof, X. Zhang, W. Zhang, S. L. Bromley, and J. Ye, *An optical lattice clock with accuracy and stability at the  $10^{-18}$  level*, [Nature \*\*506\*\*, 71 \(2014\)](#).
- [20] A. Rey, A. Gorshkov, C. Kraus, M. Martin, M. Bishof, M. Swallows, X. Zhang, C. Benko, J. Ye, and N. Lemke, *Probing many-body interactions in an optical lattice clock*, [Ann. Phys. \*\*340\*\*, 311 \(2014\)](#).
- [21] F. Dimer, B. Estienne, A. S. Parkins, and H. J. Carmichael, *Proposed realization of the Dicke-model quantum phase transition in an optical cavity QED system*, [Phys. Rev. A \*\*75\*\*, 013804 \(2007\)](#).
- [22] N. Lambert, Y.-n. Chen, R. Johansson, and F. Nori, *Quantum chaos and critical behavior on a chip*, [Phys. Rev. B \*\*80\*\*, 165308 \(2009\)](#).
- [23] D. Porras and J. I. Cirac, *Effective quantum spin systems with trapped ions*, [Phys. Rev. Lett. \*\*92\*\*, 207901 \(2004\)](#).
- [24] J. Ye, H. J. Kimble, and H. Katori, *Quantum state engineering and precision metrology using state-insensitive light traps*, [Science \*\*320\*\*, 1734 \(2008\)](#).
- [25] I. Bloch, J. Dalibard, and W. Zwerger, *Many-body physics with ultracold gases*, [Rev. Mod. Phys. \*\*80\*\*, 885 \(2008\)](#).
- [26] H. Kamada, H. Gotoh, J. Temmyo, T. Takagahara, and H. Ando, *Exciton Rabi oscillation in a single quantum dot*, [Phys. Rev. Lett. \*\*87\*\*, 246101 \(2001\)](#).
- [27] F. H. L. Koppens, C. Buizert, K. J. Tielrooij, I. T. Vink, K. C. Nowack, T. Meunier, L. P. Kouwenhoven, and L. M. K. Vandersypen, *Driven coherent oscillations of a single electron spin in a quantum dot*, [Nature \*\*442\*\*, 766 \(2006\)](#).

- [28] Y. N. Chen, G. Y. Chen, D. S. Chuu, and T. Brandes, *Quantum-dot exciton dynamics with a surface plasmon: Band-edge quantum optics*, [Phys. Rev. A](#) **79**, 033815 (2009).
- [29] A. V. Akimov, A. Mukherjee, C. L. Yu, D. E. Chang, A. S. Zibrov, P. R. Hemmer, H. Park, and M. D. Lukin, *Generation of single optical plasmons in metallic nanowires coupled to quantum dots*, [Nature](#) **450**, 402 (2007).
- [30] B. Min, E. Ostby, V. Sorger, E. Ulin-Avila, L. Yang, X. Zhang, and K. Vahala, *High-Q surface-plasmon-polariton whispering-gallery microcavity*, [Nature](#) **457**, 455 (2009).
- [31] H. P. Breuer and F. Petruccione, *The Theory of Open Quantum Systems* (Oxford University Press, 2007).
- [32] M. A. Nielsen and I. L. Chuang, *Quantum Computation and Quantum Information* (Cambridge University Press, 2010).
- [33] D. Gottesman, *An introduction to quantum error correction and fault-tolerant quantum computation*, (2009), [arXiv:0904.2557 \[quant-ph\]](#) .
- [34] C. Emary and T. Brandes, *Chaos and the quantum phase transition in the Dicke model*, [Phys. Rev. E](#) **67**, 066203 (2003).
- [35] K. Hepp and E. H. Lieb, *On the superradiant phase transition for molecules in a quantized radiation field: the Dicke maser model*, [Ann. Phys.](#) **76**, 360 (1973).
- [36] Y. K. Wang and F. T. Hioe, *Phase transition in the Dicke model of superradiance*, [Phys. Rev. A](#) **7**, 831 (1973).
- [37] F. T. Hioe, *Phase transitions in some generalized Dicke models of superradiance*, [Phys. Rev. A](#) **8**, 1440 (1973).
- [38] N. Lambert, C. Emary, and T. Brandes, *Entanglement and the phase transition in single-mode superradiance*, [Phys. Rev. Lett.](#) **92**, 073602 (2004).
- [39] J. Reslen, L. Quiroga, and N. F. Johnson, *Direct equivalence between quantum phase transition phenomena in radiation-matter and magnetic systems: Scaling of entanglement*, [Europhys. Lett.](#) **69**, 8 (2005).
- [40] J. Vidal and S. Dusuel, *Finite-size scaling exponents in the Dicke model*, [Europhys. Lett.](#) **74**, 817 (2006).
- [41] T.-L. Wang, L.-N. Wu, W. Yang, G.-R. Jin, N. Lambert, and F. Nori, *Quantum Fisher information as a signature of the superradiant quantum phase transition*, [New J. Phys.](#) **16**, 063039 (2014).
- [42] T. C. Jarrett, A. Olaya-Castro, and N. F. Johnson, *Optical signatures of quantum phase transitions in a light-matter system*, [Europhys. Lett.](#) **77**, 34001 (2007).

- [43] V. M. Bastidas, C. Emary, B. Regler, and T. Brandes, *Nonequilibrium quantum phase transitions in the Dicke model*, *Phys. Rev. Lett.* **108**, 043003 (2012).
- [44] C. Emary and T. Brandes, *Quantum chaos triggered by precursors of a quantum phase transition: The Dicke model*, *Phys. Rev. Lett.* **90**, 044101 (2003).
- [45] Q.-H. Chen, Y.-Y. Zhang, T. Liu, and K.-L. Wang, *Numerically exact solution to the finite-size Dicke model*, *Phys. Rev. A* **78**, 051801 (2008).
- [46] C. Wang, Y.-Y. Zhang, and Q.-H. Chen, *Quantum correlations in collective spin systems*, *Phys. Rev. A* **85**, 052112 (2012).
- [47] M. J. Bhaseen, J. Mayoh, B. D. Simons, and J. Keeling, *Dynamics of nonequilibrium Dicke models*, *Phys. Rev. A* **85**, 013817 (2012).
- [48] V. M. Bastidas, J. H. Reina, and T. Brandes, *Non-equilibrium entanglement in a driven many-body spin-boson model*, *J. Phys.: Conf. Ser.* **167**, 012063 (2009).
- [49] G. Vacanti, S. Pugnetti, N. Didier, M. Paternostro, G. M. Palma, R. Fazio, and V. Vedral, *Photon production from the vacuum close to the superradiant transition: Linking the dynamical Casimir effect to the Kibble-Zurek mechanism*, *Phys. Rev. Lett.* **108**, 093603 (2012).
- [50] C. Hamner, C. Qu, Y. Zhang, J. Chang, M. Gong, C. Zhang, and P. Engels, *Dicke-type phase transition in a spin-orbit-coupled Bose-Einstein condensate*, *Nature Comm.* **5**, 4023 (2014).
- [51] M. P. Baden, K. J. Arnold, A. L. Grimsmo, S. Parkins, and M. D. Barrett, *Realization of the Dicke model using cavity-assisted Raman transitions*, *Phys. Rev. Lett.* **113**, 020408 (2014).
- [52] C. J. Pethick and H. Smith, *Bose-Einstein Condensation in Dilute Gases* (Cambridge University Press, 2008).
- [53] C. Zener, *Non-adiabatic crossing of energy levels*, *Proc. R. Soc. A* **137**, 696 (1932).
- [54] E. Majorana, *Atomi orientati in campo magnetico variabile*, *Nuovo Cimento* **9**, 43 (1932).
- [55] P. Huang, J. Zhou, F. Fang, X. Kong, X. Xu, C. Ju, and J. Du, *Landau-Zener-Stückelberg interferometry of a single electronic spin in a noisy environment*, *Phys. Rev. X* **1**, 011003 (2011).
- [56] E. Stückelberg, *Theorie der unelastischen Stöße zwischen Atomen*, *Helv. Phys. Acta* **5**, 369 (1932).
- [57] A. Altland, V. Gurarie, T. Kriecherbauer, and A. Polkovnikov, *Nonadiabaticity and large fluctuations in a many-particle Landau-Zener problem*, *Phys. Rev. A* **79**, 042703 (2009).

- [58] A. Altland and V. Gurarie, *Many body generalization of the Landau-Zener problem*, [Phys. Rev. Lett.](#) **100**, 063602 (2008).
- [59] G. Sun, X. Wen, B. Mao, J. Chen, Y. Yu, P. Wu, and S. Han, *Tunable quantum beam splitters for coherent manipulation of a solid-state tripartite qubit system*, [Nature Comm.](#) **1**, 1 (2010).
- [60] D. Walls and G. J. Milburn, *Quantum Optics* (Springer, 2008).
- [61] V. Bužek, G. Adam, and G. Drobný, *Reconstruction of Wigner functions on different observation levels*, [Ann. Phys.](#) **245**, 37 (1996).
- [62] W. H. Zurek, *Sub-Planck structure in phase space and its relevance for quantum decoherence*, [Nature](#) **412**, 712 (2001).
- [63] G. B. West, J. H. Brown, and B. J. Enquist, *A general model for the origin of allometric scaling laws in biology*, [Science](#) **276**, 122 (1997).
- [64] H. S. Heaps, *Information Retrieval: Computational and Theoretical Aspects* (Academic Press, New York, 1978).
- [65] H. E. Stanley, *Scaling, universality, and renormalization: Three pillars of modern critical phenomena*, [Rev. Mod. Phys.](#) **71**, S358 (1999).
- [66] W. H. Zurek, *Cosmological experiments in superfluid helium?*, [Nature](#) **317**, 505 (1985).
- [67] W. H. Zurek, *String-seeded spirals: Origin of rotation and the density of the halo*, [Phys. Rev. Lett.](#) **57**, 2326 (1986).
- [68] T. W. B. Kibble, *Topology of cosmic domains and strings*, [J. Phys. A: Math. Gen.](#) **9**, 1387 (1976).
- [69] T. Kibble, *Phase-transition dynamics in the lab and the Universe*, [Physics Today](#) **60**, 47 (2007).
- [70] A. Yates and W. H. Zurek, *Vortex formation in two dimensions: When symmetry breaks, how big are the pieces?*, [Phys. Rev. Lett.](#) **80**, 5477 (1998).
- [71] P. Laguna and W. H. Zurek, *Density of kinks after a quench: When symmetry breaks, how big are the pieces?*, [Phys. Rev. Lett.](#) **78**, 2519 (1997).
- [72] A. Polkovnikov, K. Sengupta, A. Silva, and M. Vengalattore, *Colloquium : Nonequilibrium dynamics of closed interacting quantum systems*, [Rev. Mod. Phys.](#) **83**, 863 (2011).
- [73] W. H. Zurek, U. Dorner, and P. Zoller, *Dynamics of a quantum phase transition*, [Phys. Rev. Lett.](#) **95**, 105701 (2005).

- [74] L. Cincio, J. Dziarmaga, M. M. Rams, and W. H. Zurek, *Entropy of entanglement and correlations induced by a quench: Dynamics of a quantum phase transition in the quantum Ising model*, [Phys. Rev. A \*\*75\*\*, 052321 \(2007\)](#).
- [75] F. M. Cucchietti, B. Damski, J. Dziarmaga, and W. H. Zurek, *Dynamics of the Bose-Hubbard model: Transition from a Mott insulator to a superfluid*, [Phys. Rev. A \*\*75\*\*, 023603 \(2007\)](#).
- [76] M. Kolodrubetz, B. K. Clark, and D. A. Huse, *Nonequilibrium dynamic critical scaling of the quantum Ising chain*, [Phys. Rev. Lett. \*\*109\*\*, 015701 \(2012\)](#).
- [77] S. Deng, G. Ortiz, and L. Viola, *Dynamical non-ergodic scaling in continuous finite-order quantum phase transitions*, [Europhys. Lett. \*\*84\*\*, 67008 \(2008\)](#).
- [78] V. M. Bastidas, C. Emary, G. Schaller, and T. Brandes, *Nonequilibrium quantum phase transitions in the Ising model*, [Phys. Rev. A \*\*86\*\*, 063627 \(2012\)](#).
- [79] T. Caneva, R. Fazio, and G. E. Santoro, *Adiabatic quantum dynamics of the Lipkin-Meshkov-Glick model*, [Phys. Rev. B \*\*78\*\*, 104426 \(2008\)](#).
- [80] G. Engelhardt, V. M. Bastidas, C. Emary, and T. Brandes, *ac-driven quantum phase transition in the Lipkin-Meshkov-Glick model*, [Phys. Rev. E \*\*87\*\*, 052110 \(2013\)](#).
- [81] C. De Grandi, V. Gritsev, and A. Polkovnikov, *Quench dynamics near a quantum critical point*, [Phys. Rev. B \*\*81\*\*, 012303 \(2010\)](#).
- [82] A. Polkovnikov, *Universal adiabatic dynamics in the vicinity of a quantum critical point*, [Phys. Rev. B \*\*72\*\*, 161201 \(2005\)](#).
- [83] S. Papanikolaou, F. Bohn, R. L. Sommer, G. Durin, S. Zapperi, and J. P. Sethna, *Universality beyond power laws and the average avalanche shape*, [Nature Phys. \*\*7\*\*, 316 \(2011\)](#).
- [84] E. Farhi, J. Goldstone, S. Gutmann, J. Lapan, A. Lundgren, and D. Preda, *A quantum adiabatic evolution algorithm applied to random instances of an NP-complete problem*, [Science \*\*292\*\*, 472 \(2001\)](#).
- [85] S. Boixo, T. F. Rønnow, S. V. Isakov, Z. Wang, D. Wecker, D. A. Lidar, J. M. Martinis, and M. Troyer, *Evidence for quantum annealing with more than one hundred qubits*, [Nature Phys. \*\*10\*\*, 218 \(2014\)](#).
- [86] S. Santra, G. Quiroz, G. Ver Steeg, and D. A. Lidar, *Max 2-SAT with up to 108 qubits*, [New J. Phys. \*\*16\*\*, 045006 \(2014\)](#).
- [87] M. Greiner, O. Mandel, T. Esslinger, T. W. Hansch, and I. Bloch, *Quantum phase transition from a superfluid to a Mott insulator in a gas of ultracold atoms*, [Nature \*\*415\*\*, 39 \(2002\)](#).

- [88] A. Trabesinger, *Quantum simulation*, [Nature Phys.](#) **8**, 263 (2012).
- [89] J. Dziarmaga, *Dynamics of a quantum phase transition: Exact solution of the quantum Ising model*, [Phys. Rev. Lett.](#) **95**, 245701 (2005).
- [90] J. Simon, W. S. Bakr, R. Ma, M. E. Tai, P. M. Preiss, and M. Greiner, *Quantum simulation of antiferromagnetic spin chains in an optical lattice*, [Nature](#) **472**, 307 (2011).
- [91] H. Lipkin, N. Meshkov, and A. Glick, *Validity of many-body approximation methods for a solvable model: (I). exact solutions and perturbation theory*, [Nucl. Phys.](#) **62**, 188 (1965).
- [92] F. Pan and J. Draayer, *Analytical solutions for the LMG model*, [Phys. Lett. B](#) **451**, 1 (1999).
- [93] J. I. Cirac, M. Lewenstein, K. Mølmer, and P. Zoller, *Quantum superposition states of Bose-Einstein condensates*, [Phys. Rev. A](#) **57**, 1208 (1998).
- [94] J. Larson, *Circuit QED scheme for the realization of the Lipkin-Meshkov-Glick model*, [Europhys. Lett.](#) **90**, 54001 (2010).
- [95] P. Ribeiro, J. Vidal, and R. Mosseri, *Thermodynamical limit of the Lipkin-Meshkov-Glick model*, [Phys. Rev. Lett.](#) **99**, 050402 (2007).
- [96] R. Botet, R. Jullien, and P. Pfeuty, *Size scaling for infinitely coordinated systems*, [Phys. Rev. Lett.](#) **49**, 478 (1982).
- [97] A. Polkovnikov and V. Gritsev, *Breakdown of the adiabatic limit in low-dimensional gapless systems*, [Nature Phys.](#) **4**, 477 (2008).
- [98] M. S. Sarandy, L.-A. Wu, and D. A. Lidar, *Consistency of the adiabatic theorem*, [Quantum Information Processing](#) **3**, 331 (2004).
- [99] P. Ribeiro, J. Vidal, and R. Mosseri, *Exact spectrum of the Lipkin-Meshkov-Glick model in the thermodynamic limit and finite-size corrections*, [Phys. Rev. E](#) **78**, 021106 (2008).
- [100] A. Messiah, *Quantum Mechanics*, Vol. 2 (North Holland, 1981).
- [101] S. Dusuel and J. Vidal, *Finite-size scaling exponents of the Lipkin-Meshkov-Glick model*, [Phys. Rev. Lett.](#) **93**, 237204 (2004).
- [102] C.-Y. Leung, W. C. Yu, H.-M. Kwok, S.-J. Gu, and H.-Q. Lin, *Scaling behavior of the ground-state fidelity in the Lipkin-Meshkov-Glick model*, [Int. J. Mod. Phys. B](#) **26**, 1250170 (2012).
- [103] M. A. Bastarrachea-Magnani, O. Castaños, E. Nahmad-Achar, R. López-Peña, and J. G. Hirsch, *Fidelity, susceptibility and critical exponents in the Dicke model*, [J. Phys.: Conf. Series](#) **492**, 012012 (2014).

- [104] M.-J. Hwang, R. Puebla, and M. B. Plenio, *Quantum phase transition and universal dynamics in the Rabi model*, (2015), [arXiv:1503.03090 \[quant-ph\]](#) .
- [105] M. E. Fisher and M. N. Barber, *Scaling theory for finite-size effects in the critical region*, [Phys. Rev. Lett. \*\*28\*\*, 1516 \(1972\)](#).
- [106] M. Kira, S. W. Koch, R. P. Smith, A. E. Hunter, and S. T. Cundiff, *Quantum spectroscopy with Schrödinger-cat states*, [Nature Phys. \*\*7\*\*, 799 \(2011\)](#).
- [107] J. Vidal, *Concurrence in collective models*, [Phys. Rev. A \*\*73\*\*, 062318 \(2006\)](#).
- [108] L. Bakemeier, A. Alvermann, and H. Fehske, *Dynamics of the Dicke model close to the classical limit*, [Phys. Rev. A \*\*88\*\*, 043835 \(2013\)](#).
- [109] K. Furuya, M. Nemes, and G. Pellegrino, *Quantum dynamical manifestation of chaotic behavior in the process of entanglement*, [Phys. Rev. Lett. \*\*80\*\*, 5524 \(1998\)](#).
- [110] L. Song, D. Yan, J. Ma, and X. Wang, *Spin squeezing as an indicator of quantum chaos in the Dicke model*, [Phys. Rev. E \*\*79\*\*, 046220 \(2009\)](#).
- [111] V. Giovannetti, S. Lloyd, and L. Maccone, *Advances in quantum metrology*, [Nature Photon. \*\*5\*\*, 222 \(2011\)](#).
- [112] R. Schnabel, N. Mavalvala, D. E. McClelland, and P. K. Lam, *Quantum metrology for gravitational wave astronomy*, [Nature Comm. \*\*1\*\*, 121 \(2010\)](#).
- [113] S. L. Braunstein, *Quantum information with continuous variables*, [Rev. Mod. Phys. \*\*77\*\*, 513 \(2005\)](#).
- [114] L. Amico, A. Osterloh, and V. Vedral, *Entanglement in many-body systems*, [Rev. Mod. Phys. \*\*80\*\*, 517 \(2008\)](#).
- [115] A. L. Grimsmo, A. S. Parkins, and B.-S. Skagerstam, *Rapid steady-state convergence for quantum systems using time-delayed feedback control*, [New J. Phys. \*\*16\*\*, 065004 \(2014\)](#).
- [116] W. Kopylov, C. Emary, E. Schöll, and T. Brandes, *Time-delayed feedback control of the Dicke-Hepp-Lieb superradiant quantum phase transition*, [New J. Phys. \*\*17\*\*, 013040 \(2015\)](#).
- [117] M. Kitagawa and M. Ueda, *Squeezed spin states*, [Phys. Rev. A \*\*47\*\*, 5138 \(1993\)](#).
- [118] G. Kirchmair, B. Vlastakis, Z. Leghtas, S. E. Nigg, H. Paik, E. Ginossar, M. Mirrahimi, L. Frunzio, S. M. Girvin, and R. J. Schoelkopf, *Observation of quantum state collapse and revival due to the single-photon Kerr effect*, [Nature \*\*495\*\*, 205 \(2013\)](#).
- [119] M. Stobińska, G. Milburn, and K. Wódkiewicz, *Wigner function evolution of quantum states in the presence of self-Kerr interaction*, [Phys. Rev. A \*\*78\*\*, 013810 \(2008\)](#).

- [120] C. Law, H. Ng, and P. Leung, *Coherent control of spin squeezing*, [Phys. Rev. A \*\*63\*\*, 055601 \(2001\)](#).
- [121] X. Wang and K. Mølmer, *Pairwise entanglement in symmetric multi-qubit systems*, [Europ. Phys. J. D \*\*18\*\*, 385 \(2002\)](#).
- [122] W. K. Wootters, *Entanglement of formation of an arbitrary state of two qubits*, [Phys. Rev. Lett. \*\*80\*\*, 2245 \(1998\)](#).
- [123] J. Ma, X. Wang, C. Sun, and F. Nori, *Quantum spin squeezing*, [Phys. Rep. \*\*509\*\*, 89 \(2011\)](#).
- [124] X. Wang and B. Sanders, *Spin squeezing and pairwise entanglement for symmetric multiqubit states*, [Phys. Rev. A \*\*68\*\*, 012101 \(2003\)](#).
- [125] X. Yin, X. Wang, J. Ma, and X. Wang, *Spin squeezing and concurrence*, [J. Phys. B: At. Mol. Opt. Phys. \*\*44\*\*, 015501 \(2010\)](#).
- [126] M. Koashi and A. Winter, *Monogamy of quantum entanglement and other correlations*, [Phys. Rev. A \*\*69\*\*, 022309 \(2004\)](#).
- [127] D. F. Walls, *Squeezed states of light*, [Nature \*\*306\*\*, 141 \(1983\)](#).
- [128] J. Dowling, G. Agarwal, and W. Schleich, *Wigner distribution of a general angular-momentum state: Applications to a collection of two-level atoms*, [Phys. Rev. A \*\*49\*\*, 4101 \(1994\)](#).
- [129] G. Vidal and R. F. Werner, *Computable measure of entanglement*, [Phys. Rev. A \*\*65\*\*, 032314 \(2002\)](#).
- [130] L. Bakemeier, A. Alvermann, and H. Fehske, *Quantum phase transition in the Dicke model with critical and noncritical entanglement*, [Phys. Rev. A \*\*85\*\*, 043821 \(2012\)](#).
- [131] R. McConnell, H. Zhang, J. Hu, S. Čuk, and V. Vuletić, *Entanglement with negative Wigner function of almost 3,000 atoms heralded by one photon*, [Nature \*\*519\*\*, 439 \(2015\)](#).
- [132] P. Qin, W.-g. Wang, G. Benenti, and G. Casati, *Complexity and instability of quantum motion near a quantum phase transition*, [Phys. Rev. E \*\*89\*\*, 032120 \(2014\)](#).
- [133] F. Toscano, D. Dalvit, L. Davidovich, and W. Zurek, *Sub-Planck phase-space structures and Heisenberg-limited measurements*, [Phys. Rev. A \*\*73\*\*, 023803 \(2006\)](#).
- [134] A. I. Lvovsky, *Continuous-variable optical quantum-state tomography*, [Rev. Mod. Phys. \*\*81\*\*, 299 \(2009\)](#).
- [135] R. Schmied and P. Treutlein, *Tomographic reconstruction of the Wigner function on the Bloch sphere*, [New J. Phys. \*\*13\*\*, 065019 \(2011\)](#).

- [136] M. Caprio, P. Cejnar, and F. Iachello, *Excited state quantum phase transitions in many-body systems*, [Ann. Phys. \*\*323\*\*, 1106 \(2008\)](#).
- [137] T. Brandes, *Excited-state quantum phase transitions in Dicke superradiance models*, [Phys. Rev. E \*\*88\*\*, 0321133 \(2013\)](#).
- [138] P. Pérez-Fernández, P. Cejnar, J. M. Arias, J. Dukelsky, J. E. García-Ramos, and A. Relaño, *Quantum quench influenced by an excited-state phase transition*, [Phys. Rev. A \*\*83\*\*, 033802 \(2011\)](#).
- [139] L. Essen and J. V. L. Parry, *An atomic standard of frequency and time interval: A caesium resonator*, [Nature \*\*176\*\*, 280 \(1955\)](#).
- [140] P. Gill, *When should we change the definition of the second?*, [Phil. Trans. of the R. Soc. A \*\*369\*\*, 4109 \(2011\)](#).
- [141] T. Chiba, *Squeezed atomic states and projection noise in spectroscopy*, [Prog. Theor. Phys. \*\*126\*\*, 993 \(2011\)](#).
- [142] C. E. Wieman, D. E. Pritchard, and D. J. Wineland, *Atom cooling, trapping, and quantum manipulation*, [Rev. Mod. Phys. \*\*71\*\*, S253 \(1999\)](#).
- [143] T. Kessler, C. Hagemann, C. Grebing, T. Legero, U. Sterr, F. Riehle, M. J. Martin, L. Chen, and J. Ye, *A sub-40-mHz-linewidth laser based on a silicon single-crystal optical cavity*, [Nature Photon. \*\*6\*\*, 687 \(2012\)](#).
- [144] J. L. Hall, *Nobel lecture: Defining and measuring optical frequencies*, [Rev. Mod. Phys. \*\*78\*\*, 1279 \(2006\)](#).
- [145] N. Hinkley, J. A. Sherman, N. B. Phillips, M. Schioppo, N. D. Lemke, K. Beloy, M. Pizzocaro, C. W. Oates, and A. D. Ludlow, *An atomic clock with  $10^{-18}$  instability*, [Science \*\*341\*\*, 1215 \(2013\)](#).
- [146] A. D. Ludlow, T. Zelevinsky, G. K. Campbell, S. Blatt, M. M. Boyd, M. H. G. de Miranda, M. J. Martin, J. W. Thomsen, S. M. Foreman, J. Ye, and et al., *Sr lattice clock at  $10^{-16}$  fractional uncertainty by remote optical evaluation with a Ca clock*, [Science \*\*319\*\*, 1805 \(2008\)](#).
- [147] T. Rosenband, D. B. Hume, P. O. Schmidt, C. W. Chou, A. Brusch, L. Lorini, W. H. Oskay, R. E. Drullinger, T. M. Fortier, J. E. Stalnaker, and et al., *Frequency ratio of  $Al^+$  and  $Hg^+$  single-ion optical clocks; metrology at the 17th decimal place*, [Science \*\*319\*\*, 1808 \(2008\)](#).
- [148] T. Akatsuka, M. Takamoto, and H. Katori, *Optical lattice clocks with non-interacting bosons and fermions*, [Nature Phys. \*\*4\*\*, 954 \(2008\)](#).

- [149] M. Bishof, Y. Lin, M. D. Swallows, A. V. Gorshkov, J. Ye, and A. M. Rey, *Resolved atomic interaction sidebands in an optical clock transition*, [Phys. Rev. Lett. \*\*106\*\*, 250801 \(2011\)](#).
- [150] M. M. Boyd, T. Zelevinsky, A. D. Ludlow, S. M. Foreman, S. Blatt, T. Ido, and J. Ye, *Optical atomic coherence at the 1-Second time scale*, [Science \*\*314\*\*, 1430 \(2006\)](#).
- [151] M. M. Boyd, T. Zelevinsky, A. D. Ludlow, S. Blatt, T. Zanon-Willette, S. M. Foreman, and J. Ye, *Nuclear spin effects in optical lattice clocks*, [Phys. Rev. A \*\*76\*\*, 022510 \(2007\)](#).
- [152] G. K. Campbell, M. M. Boyd, J. W. Thomsen, M. J. Martin, S. Blatt, M. D. Swallows, T. L. Nicholson, T. Fortier, C. W. Oates, S. A. Diddams, and et al., *Probing interactions between ultracold fermions*, [Science \*\*324\*\*, 360 \(2009\)](#).
- [153] S. Blatt, J. W. Thomsen, G. K. Campbell, A. D. Ludlow, M. D. Swallows, M. J. Martin, M. M. Boyd, and J. Ye, *Rabi spectroscopy and excitation inhomogeneity in a one-dimensional optical lattice clock*, [Phys. Rev. A \*\*80\*\*, 052703 \(2009\)](#).
- [154] A. M. Rey, A. V. Gorshkov, and C. Rubbo, *Many-body treatment of the collisional frequency shift in fermionic atoms*, [Phys. Rev. Lett. \*\*103\*\*, 260402 \(2009\)](#).
- [155] N. D. Lemke, J. von Stecher, J. A. Sherman, A. M. Rey, C. W. Oates, and A. D. Ludlow, *p-Wave cold collisions in an optical lattice clock*, [Phys. Rev. Lett. \*\*107\*\*, 103902 \(2011\)](#).
- [156] H. Ritsch, P. Domokos, F. Brennecke, and T. Esslinger, *Cold atoms in cavity-generated dynamical optical potentials*, [Rev. Mod. Phys. \*\*85\*\*, 553 \(2013\)](#).
- [157] K. I. Kugel' and D. I. Khomskii, *The Jahn-Teller effect and magnetism: transition metal compounds*, [Sov. Phys. Usp. \*\*25\*\*, 231 \(1982\)](#).
- [158] Y. Tokura, *Orbital physics in transition-metal oxides*, [Science \*\*288\*\*, 462 \(2000\)](#).
- [159] M. D. Swallows, M. Bishof, Y. Lin, S. Blatt, M. J. Martin, A. M. Rey, and J. Ye, *Suppression of collisional shifts in a strongly interacting lattice clock*, [Science \*\*331\*\*, 1043 \(2011\)](#).
- [160] M. J. Martin, M. Bishof, M. D. Swallows, X. Zhang, C. Benko, J. von Stecher, A. V. Gorshkov, A. M. Rey, and J. Ye, *A quantum many-body spin system in an optical lattice clock*, [Science \*\*341\*\*, 632 \(2013\)](#).
- [161] X. Zhang, M. Bishof, S. L. Bromley, C. V. Kraus, M. S. Safronova, P. Zoller, A. M. Rey, and J. Ye, *Spectroscopic observation of  $SU(N)$ -symmetric interactions in Sr orbital magnetism*, [Science \*\*345\*\*, 1467 \(2014\)](#).
- [162] Z. Yu and C. J. Pethick, *Clock shifts of optical transitions in ultracold atomic gases*, [Phys. Rev. Lett. \*\*104\*\*, 010801 \(2010\)](#).

- [163] B. Josephson, *Possible new effects in superconductive tunnelling*, [Phys. Lett. \*\*1\*\*, 251 \(1962\)](#).
- [164] M. Albiez, R. Gati, J. Fölling, S. Hunsmann, M. Cristiani, and M. K. Oberthaler, *Direct observation of tunneling and nonlinear self-trapping in a single bosonic Josephson junction*, [Phys. Rev. Lett. \*\*95\*\*, 010402 \(2005\)](#).
- [165] M. Abbarchi, A. Amo, V. G. Sala, D. D. Solnyshkov, H. Flayac, L. Ferrier, I. Sagnes, E. Galopin, A. Lemaître, G. Malpuech, and J. Bloch, *Macroscopic quantum self-trapping and Josephson oscillations of exciton polaritons*, [Nature Phys. \*\*9\*\*, 275 \(2013\)](#).
- [166] D. J. Wineland, J. J. Bollinger, W. M. Itano, and D. J. Heinzen, *Squeezed atomic states and projection noise in spectroscopy*, [Phys. Rev. A \*\*50\*\*, 67 \(1994\)](#).
- [167] J. Eisert, M. Friesdorf, and C. Gogolin, *Quantum many-body systems out of equilibrium*, [Nature Phys. \*\*11\*\*, 124 \(2015\)](#).
- [168] F. T. Arecchi, E. Courtens, R. Gilmore, and H. Thomas, *Atomic coherent states in quantum optics*, [Phys. Rev. A \*\*6\*\*, 2211 \(1972\)](#).
- [169] A. Usha Devi, X. Wang, and B. Sanders, *Spin squeezing criterion with local unitary invariance*, [Quantum Inf. Process. \*\*2\*\*, 207 \(2003\)](#).
- [170] T. L. Nicholson, M. J. Martin, J. R. Williams, B. J. Bloom, M. Bishof, M. D. Swallows, S. L. Campbell, and J. Ye, *Comparison of two independent Sr optical clocks with  $10^{-17}$  stability at  $10^3$  s*, [Phys. Rev. Lett. \*\*109\*\*, 230801 \(2012\)](#).

# Appendix A

## Published and submitted papers.

### Chapter 1

In the following pages we have decided to add complete papers (organized as appendices [A](#), [B](#), [C](#), and [D](#)) that have been published and/or submitted during the author's doctoral research. This papers are related to chapters [1-3](#) and are organized in that order. We stress that all these papers are fundamentally published forms of the doctoral research this thesis is about, and are included with the consent of the other authors.



**Quantum emitters dynamically coupled to a quantum field**

O. L. Acevedo, L. Quiroga, F. J. Rodríguez, and N. F. Johnson

Citation: [AIP Conference Proceedings](#) **1566**, 560 (2013); doi: 10.1063/1.4848534

View online: <http://dx.doi.org/10.1063/1.4848534>

View Table of Contents: <http://scitation.aip.org/content/aip/proceeding/aipcp/1566?ver=pdfcov>

Published by the [AIP Publishing](#)

---

## Quantum emitters dynamically coupled to a quantum field

O. L. Acevedo\*, L. Quiroga\*, F. J. Rodríguez\* and N. F. Johnson†

\*Departamento de Física, Universidad de los Andes, A.A. 4976, Bogotá, Colombia

†Department of Physics, University of Miami, Coral Gables, Miami, FL 33124, USA

**Abstract.** We study theoretically the dynamical response of a set of solid-state quantum emitters arbitrarily coupled to a single-mode microcavity system. Ramping the matter-field coupling strength in round trips, we quantify the hysteresis or irreversible quantum dynamics. The matter-field system is modeled as a finite-size Dicke model which has previously been used to describe equilibrium (including quantum phase transition) properties of systems such as quantum dots in a microcavity. Here we extend this model to address non-equilibrium situations. Analyzing the system's quantum fidelity, we find that the near-adiabatic regime exhibits the richest phenomena, with a strong asymmetry in the internal collective dynamics depending on which phase is chosen as the starting point. We also explore signatures of the crossing of the critical points on the radiation subsystem by monitoring its Wigner function; then, the subsystem can exhibit the emergence of non-classicality and complexity.

**Keywords:** Dicke model, parametrical driving, irreversibility.

**PACS:** 0.5.30.Rt

Recent experimental advances are allowing the controlled coupling of semiconductor quantum emitters, like quantum dots or NV-centers, within a confined quantum field (photons/plasmons/phonons) [1]. The Dicke model (DM) is a matter-radiation interaction system with potential realizations in those condensed matter scenarios, as well as in quantum optics and atomic physics. Realizations has been proposed in Circuit and Cavity QED [2], and there has been an especially successful realization using ultracold atoms [3]. Much of the attractiveness of the DM lies on the presence of a second-order Quantum Phase Transition (QPT) at its thermodynamic limit [4]. Most of works about the DM have focused in static effects of the QPT, both in the thermodynamic limit and in finite-size systems [5]. However, the dynamical aspects of the QPT in the DM have been scarcely addressed [6]. In this work, we will tackle the problem at the very quantum level by using reliable computational solutions. We will examine the effects of dynamically changing the parameters of finite size DMs starting from their ground state. This problem is important for the context of adiabatic quantum computation [7], as some quantum operations through different ground states on parameter space can be discarded as impractical if they cross critical points where increasing the number of qubits extremely increases the time required by the process.

The DM consists of a set of identical qubits symmetrically coupled to a single bosonic mode. The Hamiltonian of the model is,

$$\hat{H}_D = \varepsilon \hat{J}_z + \omega \hat{a}^\dagger \hat{a} + 2n_q^{-1/2} \lambda(t) \hat{J}_x (\hat{a}^\dagger + \hat{a}), \quad (1)$$

where  $n_q$  is the number of qubits, the operators  $\hat{J}_i = \frac{1}{2} \sum_{j=1}^{n_q} \hat{\sigma}_j^{(i)}$  denote collective operators of the set of

qubits ( $\hat{\sigma}^{(i)}$  are Pauli matrices), and operator  $\hat{a}^\dagger$  ( $\hat{a}$ ) is a creation (annihilation) operator of the bosonic mode. For results, we have set resonance between qubits and bosonic mode ( $\omega = \varepsilon$ ) and we have set it as the energy scale ( $\omega = 1$ ). The parametrical driving will be performed through the interaction parameter  $\lambda$  between the values 0 and 1; at the center of this interval there would be a QPT in the thermodynamic limit separating a normal phase ( $\lambda < 0.5$ ) from a superradiant phase ( $\lambda > 0.5$ ). The system will undergo triangle-like cyclical drivings of  $\lambda(t)$  described by,

$$\lambda(t) = \begin{cases} \lambda_1 + 2(\lambda_2 - \lambda_1)t/\tau, & t \leq \tau/2 \\ \lambda_2 + 2(\lambda_1 - \lambda_2)(t/\tau - 1/2), & t > \tau/2 \end{cases}; \quad (2)$$

where  $\lambda_1$  and  $\lambda_2$  are respectively zero (one) and one (zero) depending on whether the system starts/ends in the normal (superradiant) phase. The velocity of the cycle is characterized by its total time  $\tau$ . For any instantaneous value of  $\lambda$  there is a ground state  $|\Theta_{\lambda(t)}\rangle$ , and we will compare it with the actual dynamical state  $|\Psi(t)\rangle$  through the total fidelity  $f_T(t) = |\langle \Theta_{\lambda(t)} | \Psi(t) \rangle|^2$ . Also, we will probe the non-reversibility of the process through the Wigner distribution of the bosonic mode subsystem,

$$W(\alpha, \rho) = \sum_{n=0}^{\infty} (-1)^n \langle n | \hat{D}^\dagger(\alpha) \hat{\rho} \hat{D}(\alpha) | n \rangle, \quad (3)$$

where  $\hat{D}(\alpha) = e^{\alpha \hat{a}^\dagger - \alpha^* \hat{a}}$  is the displacement operator and  $\hat{\rho}$  is the bosonic mode density matrix.

In fig. 1-a there are shown different hysteresis curves of  $F_T(t)$  for selected values of  $\tau$ . The diabatic regime ( $\tau = 0.5$ ) is characterized by a sudden fall in the quantum fidelity as the critical value of  $\lambda = 0.5$  is crossed. But,

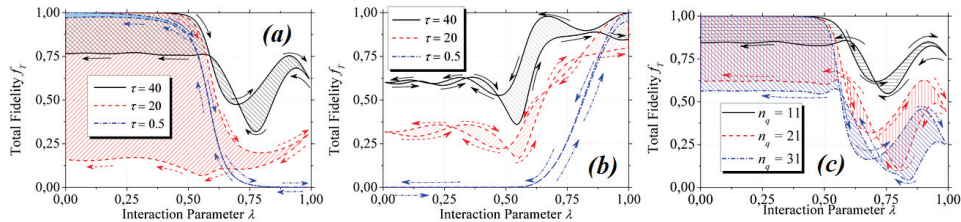


**FIGURE 1.** Quantum hysteresis curves of  $f_T$  as a function of  $\lambda$ . **(a,b)** Comparison of different cycle times  $\tau$  for a DM with size  $n_q = 15$  starting from **(a)** the normal phase, or **(b)** superradiant phase. **(c)** Effect on the hysteresis curves of the size of the system for cycles with  $\tau = 40$  and starting at the normal phase.

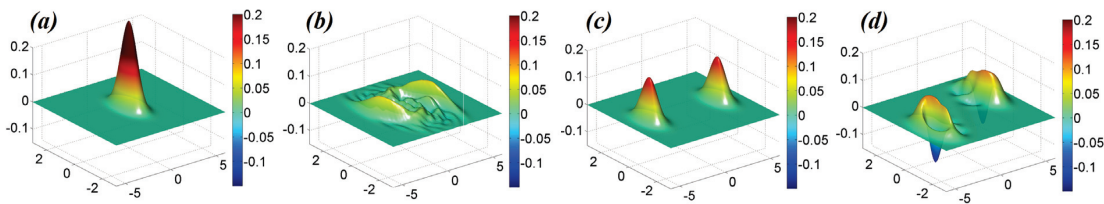


**FIGURE 2.** Non-reversibility of the dynamics as witnessed by the bosonic mode's Wigner distributions, for a resonator interacting with  $n_q = 15$  qubits and cycle times  $\tau = 20$ . **(a,c)** Initial states. **(b,d)** Final states. **(a,b)** Cycle start and ending point at the normal phase ( $\lambda = 0$ ). **(c,d)** Cycle start and ending point at the superradiant phase ( $\lambda = 1$ ).

as the parametric driving goes back, almost the same fidelity is achieved, embedding little area inside the curve. This high reversibility is caused by a sudden quench condition, i.e., the system remains virtually in the starting state and the fall in the fidelity is due to differences between the instantaneous ground state and the starting state as predicted by the QPT. On the other hand, the approach to the adiabatic limit is not monotonous, and complex oscillations arise. The falling in the hysteresis in the inverse cycle (fig. 1-b) is not so marked because the superradiant phase has a bigger difference between the ground states for different points in parameter space. The reversibility for this kind of cycles is higher but the oscillations are also much more pronounced. The rightmost fig. 1-c shows how the size of the system exacerbates the hysteresis effects.

Figures 2-(a-d) show results for the Wigner distribution. Both pairs of figures, (a,b) and (a,c), compare the state of the subsystem at the same point in parameter space but figs. 2-b and 2-d reveal results after the cycle is performed. The initial Gaussian-like shapes of the distribution are appreciably distorted and negative values of the distribution appear. Also, as the ground state reveals the Planckian scale, we conclude that a sub-Planckian structure is irreversibly formed. These features (negativity and sub-Planckian structure) are related to quantumness of the state and quantum chaos respectively [8].

In conclusion, we have revealed the emergence of irreversible complex behaviors in finite size DMs as a conse-

quence of dynamical crossing of the QPT when the adiabatic regime is approached. Counter-intuitively, the diabatic regime is almost reversible and order-preserving.

## ACKNOWLEDGMENTS

The authors acknowledge financial support from Proyectos Semilla, Dept. Física-Facultad de Ciencias at Universidad de los Andes (2010-2012). O. L. A. acknowledges financial support from Colciencias, Convocatoria 511.

## REFERENCES

1. A. V. Akimov et al., *Nature* **450**, 402-406 (2007); O. Arcizet et al., *Nature Physics* **7**, 879-883 (2011).
2. F. Dimer et al., *Phys. Rev. A* **75**, 013804 (2007); N. Lambert et al., *Phys. Rev. B* **80**, 165308 (2009).
3. K. Baumann et al., *Nature* **464**, 1301 (2010).
4. K. Hebb and E.H. Lieb, *Annals of Physics* **76**, 360 (1973).
5. C. Emary and T. Brandes, *Phys. Rev. Lett.* **90**, 044101 (2003).
6. M. J. Bhaseen et al., *Phys. Rev. A* **85**, 013817 (2012); V. M. Bastidas et al., *Phys. Rev. Lett.* **108**, 043003 (2012).
7. R. Schützhold and G. Schaller, *Phys. Rev. A* **74**, 060304 (2006); E. Farhi et al., *Science* **292**, 472 (2001).
8. A. Kenfack and K. Życzkowski, *J. Opt. B: Quantum Semiclass. Opt.* **6**, 396 (2004); F. Toscano et al., *Phys. Rev. A* **73**, 023803 (2006).

## Appendix B

Published and submitted papers.

### Chapter 2

## New Dynamical Scaling Universality for Quantum Networks Across Adiabatic Quantum Phase Transitions

O. L. Acevedo,<sup>1</sup> L. Quiroga,<sup>1</sup> F. J. Rodríguez,<sup>1</sup> and N. F. Johnson<sup>2</sup>

<sup>1</sup>*Departamento de Física, Universidad de los Andes, A.A. 4976, Bogotá, Colombia*

<sup>2</sup>*Department of Physics, University of Miami, Coral Gables, Miami, Florida 33124, USA*

(Received 19 September 2013; revised manuscript received 22 November 2013; published 22 January 2014)

We reveal universal dynamical scaling behavior across adiabatic quantum phase transitions in networks ranging from traditional spatial systems (Ising model) to fully connected ones (Dicke and Lipkin-Meshkov-Glick models). Our findings, which lie beyond traditional critical exponent analysis and adiabatic perturbation approximations, are applicable even where excitations have not yet stabilized and, hence, provide a time-resolved understanding of quantum phase transitions encompassing a wide range of adiabatic regimes. We show explicitly that even though two systems may traditionally belong to the same universality class, they can have very different adiabatic evolutions. This implies that more stringent conditions need to be imposed than at present, both for quantum simulations where one system is used to simulate the other and for adiabatic quantum computing schemes.

DOI: 10.1103/PhysRevLett.112.030403

PACS numbers: 05.30.Rt, 64.60.an, 64.60.Ht

Scaling is ubiquitous in nature, with critical exponents being used to characterize universal phase transition phenomena in both equilibrium and nonequilibrium systems [1]. Scaling functions go beyond critical exponents by incorporating richer information about the dynamics of the underlying many-body system, including finite-size effects, and hence extending the range of validity over which theoretical predictions can describe empirical data [2]. In the field of critical phenomena, much attention has recently been directed to adiabatic quantum phase transitions (QPTs). In addition to their fundamental role as zero-temperature many-body quantum phenomena [3], QPTs represent a key ingredient of current quantum computation schemes [4,5].

Recent studies show that as a QPT phase boundary is crossed slowly in models with finitely connected lattices [6–11], the short-range interaction allows a correlation length to be defined and, hence, scaling to be examined through the Kibble-Zurek mechanism (KZM) [6,12]. However, an implicit limiting assumption of the KZM is that adiabatic evolution holds except for a small threshold around the critical point, during which spatial defects in the order parameter are created and power-law relations emerge, defined by critical exponents. For slower quench rates, adiabatic perturbation theory (APT) can be invoked instead and excitations predicted in terms of quasiparticles [9,13]. However, totally connected lattice models such as the Dicke model (DM) and the Lipkin-Meshkov-Glick model (LMGM) [14] have no spatial order parameter and, hence, lack a clear connection to existing theories such as KZM. This may explain the lack of general results to date for the adiabatic QPT regime, with the exception of bosonic excitation estimates in the DM using simplifying mean-field and rotating wave approximations [15], scaling of

final excitations in the LMGM [16], and dynamical characterizations of the QPT through a monochromatic modulation of the annealing parameter [17].

In a QPT, critical exponents are extracted from the power-law behavior in the thermodynamic limit (TL), of equilibrium quantities such as energy gaps and susceptibilities around the quantum critical point (QCP) [6]. However, when finite-size scaling is considered, continuous functions emerge at the phase boundary. Here we show that, contrary to common belief, these critical functions—but not critical exponents—provide a unified description of QPT dynamics, as encoded by nonadiabatic indicators such as heating and ground-state fidelity. Furthermore, they encompass both finite-range [e.g., transverse field Ising model (TFIM)] and fully connected systems (e.g., DM and LMGM [18]) and, hence, overcome the limitations of KZM and APT. In addition to applications in adiabatic quantum computing [4,5], QPTs have been experimentally realized using ultracold atomic systems [19,20]. By revealing continuous-time details of the size-independent dynamical behavior of quantum many-body systems, our analysis goes beyond critical exponent analyses such as KZM and connects to studies of avalanche-like events across classical phase boundaries [2]. KZM-like and an APT-like regime are both naturally incorporated in and illuminated by this new framework. We find that the traditional universality of critical exponents is insufficient to describe the analogous dynamical evolutions of different models, thereby casting doubt on an implicit assumption of quantum simulations [21] in which particular models are taken to act as experimental surrogates of each other.

We focus on three models for which experimental realizations exist or have been proposed [22]. Each features  $N$  qubits with differing interaction connectivities

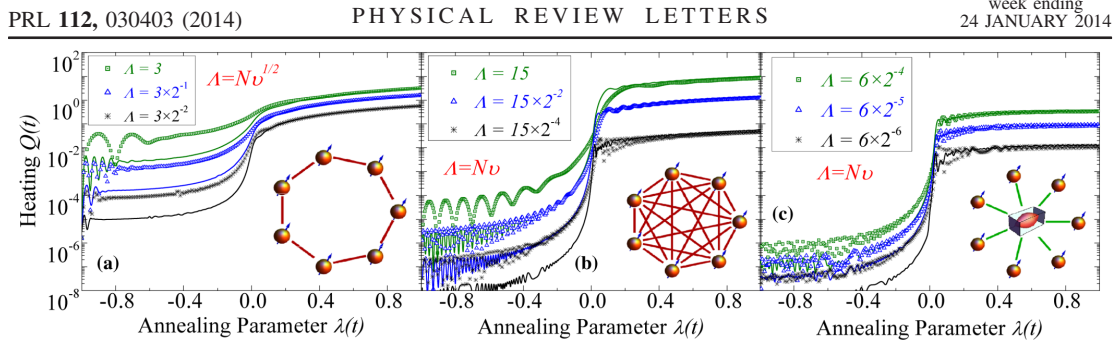


FIG. 1 (color online). Time evolution of heating  $Q(t)$  for (a) TFIM, (b) LMGM, and (c) DM. Insets show how the qubits interact in these three models. In each panel, we present results for three different scaled annealing velocities  $\Lambda$  (different colors) and two system sizes: TFIM, continuous lines ( $N = 160$ ) and symbols ( $N = 80$ ); LMGM, continuous lines ( $N = 2^{11}$ ) and symbols ( $N = 2^9$ ); DM, continuous lines ( $N = 2^9$ ) and symbols ( $N = 2^8$ ). Notice that for well inside the ordered phase ( $\lambda > 0$ ) for arbitrarily connected models, curves with the same  $\Lambda$  but different size  $N$  collapse.

(Fig. 1 insets). The following generic, dimensionless, time-dependent Hamiltonian ( $\hbar = 1$ ) describes the TFIM and LMGM:

$$\hat{H}(t) = - \sum_{i=1}^N \hat{\sigma}_z^{(i)} - \frac{\lambda(t) + 1}{N^s} \sum_{(i,j)} \hat{\sigma}_x^{(i)} \hat{\sigma}_x^{(j)}, \quad (1)$$

where  $\{\hat{\sigma}\}$  are Pauli matrices and  $(i, j)$  denotes pairs of interacting qubits. We choose the interaction strength  $\lambda(t)$  as the annealing parameter. In the TFIM, only pairs of nearest neighbors in a circular lattice interact, whereas in the LMGM all pair interactions are present. At  $\lambda = 0$  in the TL, the system is at the QCP [3,23], where a minimum-value energy gap arises between the ground state and the first excited accessible state.  $N^s$  in the denominator normalizes the interaction parameter according to size for the LMGM;  $s = 0$  in the TFIM, while  $s = 1$  in the LMGM. Like the LMGM, the DM has a totally connected lattice, but the qubit-qubit interaction is mediated by a boson mode: when the qubits and boson mode are in resonance, the Hamiltonian becomes

$$\hat{H}(t) = \sum_{i=1}^N \hat{\sigma}_z^{(i)} + \hat{a}^\dagger \hat{a} + \frac{\lambda(t) + 1}{2\sqrt{N}} (\hat{a}^\dagger + \hat{a}) \sum_{i=1}^N \hat{\sigma}_x^{(i)} \quad (2)$$

where  $\hat{a}^\dagger$  ( $\hat{a}$ ) is the mode's creation (annihilation) operator. The QCP in the TL is also at  $\lambda = 0$  [24].

To describe the crossing of the QPT, we show a simple case in which the annealing parameter evolves linearly as  $\lambda(t) = vt$  since it leads to relatively simple formulas, though we stress that extension to any power-law time dependence is straightforward (Supplemental Material [25]). We start in the ground state  $|\varphi_0(t_i)\rangle$  with  $\lambda(t_i) = -1$  at “negative” time  $t_i = -v^{-1}$  [i.e., the zero of time is defined as the instance where the system passes through  $\lambda(t_i) = 0$ ]. The systems in Eqs. (1) and (2) evolve with a

time-dependent state  $|\Psi(t)\rangle$  across the QCP, until positive time  $t_f$  where  $\lambda(t_f) = 1$ . For slow enough quench, the system should end in a final ground state  $|\varphi_0(\lambda(t_f))\rangle$  representing perfect adiabatic evolution. However, the QCP hinders the many-body system from achieving this result, since the minimal energy gap makes it easy for the system to jump out of the ground state. Because this gap gets smaller as the system size increases, ever slower quenches are necessary to keep the system in the ground state. Hence, the fundamental effect of the crossing of QPTs is the loss of adiabatic evolution. We employ two indicators to probe this result: (1) Ground-state fidelity  $p_0(t) = |\langle \varphi_0(t) | \Psi(t) \rangle|^2$  measuring the overlap between the actual dynamical state  $|\Psi(t)\rangle$  and  $|\varphi_0(t)\rangle$ . It lies in the interval  $0 \leq p_0 \leq 1$  and has its maximum value for perfect adiabatic evolution. (2) Heating  $Q(t) = \langle \Psi(t) | \hat{H}(t) | \Psi(t) \rangle - E_0(t)$ , which is always non-negative, and for adiabatic evolution is zero [26]. [ $E_0(t)$  is the instantaneous ground-state energy]. Details of the calculation are shown in the Supplemental Material [25].

Figure 1 shows the heating  $Q(t)$  for  $\lambda \in [-1, 1]$ . For  $\lambda < 0$ , the behavior at a given  $v$  is independent of size, with virtually no loss of adiabaticity provided  $v$  is small enough [13]. The stronger heating behavior that emerges above the QCP results from excitations forming, following a scaled velocity  $\Lambda$ . The almost vertical step around  $\lambda = 0$  shows that the evolution is essentially adiabatic, except for the narrow interval around the QCP where the major excitations are formed. Since the important aspects of the quenching are defined around the QCP, we analyze the system's state in terms of instantaneous eigenstates

$$|\Psi(t)\rangle = \sum_{n=0} a_n(t) e^{-i \int_{t_0}^t E_n(t') dt'} |\phi_{\lambda(t)}^{(n)}\rangle, \quad (3)$$

where  $\hat{H}(t) |\phi_{\lambda(t)}^{(n)}\rangle = E_n(\lambda(t)) |\phi_{\lambda(t)}^{(n)}\rangle$  for every time  $t$ . The  $a_n(t)$  evolution follows

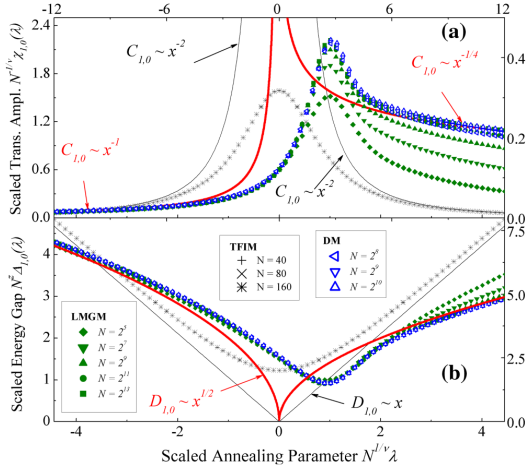


FIG. 2 (color online). Universal behavior of finite-size critical functions (a)  $C_{1,0}$  and (b)  $D_{1,0}$  as defined in Eqs. (5) and (6). Symbols show results for system size  $N$  while continuous curves are power-law predictions in the TL. (Thick red line is for both DM and LMGM. Thin black line is for TFIM). Scales for the DM and LMGM are given at the left bottom and right top, respectively, and show that the critical functions for both models have the same shape since they belong to the same universality class. Horizontal scale for the TFIM is at the top, while the vertical scale is not present but goes up to 25 in (a) and 0.25 in (b).

$$\frac{da_n(\lambda)}{d\lambda} = \sum_{m \neq n} e^{i\nu^{-1}\phi_{n,m}^{(N)}(\lambda)} \chi_{n,m}^{(N)}(\lambda) a_m(\lambda), \quad (4)$$

where  $\phi_{n,m}^{(N)}(\lambda) \equiv \int_0^\lambda \Delta_{n,m}^{(N)}(\lambda') d\lambda'$ , which is the integral of the energy gap between eigenstates  $n$  and  $m$ . The transition amplitudes  $\chi_{n,m}^{(N)} \equiv -\langle \varphi_\lambda^{(n)} | \frac{d}{d\lambda} (|\varphi_\lambda^{(m)}\rangle) \rangle$  can be written as  $\chi_{n,m}^{(N)}(\lambda) = [V_{n,m}^{(N)}(\lambda)] / [\Delta_{n,m}^{(N)}(\lambda)]$  whenever eigenstates  $n$  and  $m$  are nondegenerate, and  $V_{n,m}^{(N)}$  are the matrix elements of the interaction part of the Hamiltonian, mediated by  $\lambda$ . The superscript ( $N$ ) indicates that all the functions depend on the system size. Equation (4) is usually the central part of the adiabatic theorem [27], which states that if  $v \ll |\Delta_{n,m}/\chi_{n,m}|$ , then  $\{a_n\}$  remain constant. For sufficiently slow annealing, this is satisfied outside the QCP region, implying that only the eigenstates that reach a zero gap in the TL are relevant for the loss of adiabaticity. It is at this point that dynamical critical functions enter the picture, since  $\chi_{n,m}$  and  $\Delta_{n,m}$  obey a scaling relation when  $|\lambda| \ll 1$  [9,23,28]

$$\chi_{n,m}^{(N)}(\lambda) = N^{1/\nu} C_{n,m}(x), \quad (5)$$

$$\Delta_{n,m}^{(N)}(\lambda) = N^{-z} D_{n,m}(x), \quad (6)$$

where  $x \equiv N^{1/\nu} \lambda$  with  $\nu$  and  $z$  determined through the power-law behavior in the TL [24,3]. Figures 2(a) and 2(b) present these critical functions between the ground and first-excited states and show how they start matching the TL power-law behavior for sufficiently large  $N$  and  $x$ . It follows that  $\nu = z = 1$  for the TFIM and  $\nu = 3/2$  and  $z = 1/3$  for DM and LMGM [3,29].

Our main result is that the evolution in Eq. (4) can now be cast in size-independent form

$$\frac{da_n(x)}{dx} = \sum_{n \neq m} e^{i\Lambda^{-1/\mu} \Phi_{n,m}(x)} a_m(x) C_{n,m}(x), \quad (7)$$

where the scaled velocity  $\Lambda = Nv^\mu$ , the dynamical phase difference  $\Phi_{n,m}(x) = \int_0^x D_{n,m}(x') dx'$ , and  $\mu = \nu/(1+z\nu)$ . Equation (7) predicts universal results in terms of excitation probabilities  $p_n \equiv |a_n|^2$  and the ground-state fidelity. Since the energy spectrum has a regular behavior, the heating will also be universal since  $Q \equiv \sum_n p_n \Delta_{n,0}$ . This prediction is confirmed in Fig. 3 with both adiabatic quantifiers behaving in a size-independent manner across the critical region. We note that the collapse only occurs during and after the critical threshold, because it is around the QCP that the adiabatic indicators are significantly affected, and it is in this region that universal functions exist. Once the QCP is passed ( $\lambda > 0$  stage), the evolution is again essentially adiabatic and the accumulated nonadiabatic effects of crossing the critical threshold remain dominant, clamping the subsequent collapsed evolution. Therefore, our results show that by generalizing from critical exponents to critical functions, we expand the traditional description focused on scaling at a fixed final value of  $\lambda$  as in Fig. 1, to a complete temporal collapse picture as shown in Fig. 3 around the QCP.

This new picture includes well-known results predicted by KZM and APT as special cases, since both can be expressed as power-law dependencies at the end of the quenching process [16]. In the lower velocity APT regime where there is low probability of leaving the ground state, the following approximation holds for  $n \neq 0$ :

$$a_n(\lambda) \approx \int_{-1}^\lambda e^{i\nu^{-1}\phi_{n,0}(\lambda')} \chi_{n,0}(\lambda') d\lambda'. \quad (8)$$

Since the integrand is only non-negligible around the QCP, it follows that  $|a_n| \sim v$ , for which  $p_n \sim v^2$  and, hence,  $Q_f \sim v^2$ . The higher velocity KZM regime is characterized by excitations being large enough to discard APT, replacing it by an adiabatic-impulse-adiabatic approximation in which the size of the threshold at which major excitations are created is defined by a definite time  $t_K$  or, equivalently, a critical value of  $x_K = vN^{1/\nu} t_K$ .

In the traditional KZM, as is the case of the TFIM, a healing time has been directly related to the inverse energy gap [6], making  $t_K \Delta(t_K) = t_k (vt_K)^{\nu z} \sim 1$  and then

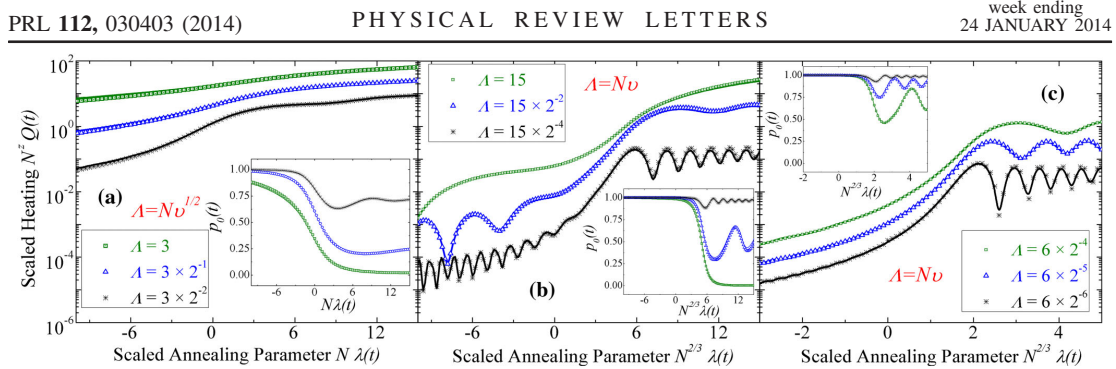


FIG. 3 (color online). Magnification and rescaling of the results in Fig. 1 around QCP, as described by Eq. (7). Collapse is no longer restricted to a nearly constant value well after the QCP. Instead, a continuous-in-time, size-independent behavior is revealed, a prediction that lies outside the scope of critical exponent analysis. Insets show continuous scaling also present for the ground-state fidelity  $p_0(t)$ . Exponent  $z = 1$  for the TFIM, whereas  $z = 1/3$  for both LMGM and DM.

$x_K \sim \Lambda^{1/\nu}$ . With this estimate, an adiabatic indicator such as heating can be predicted through  $Q_f \sim D(x_K) \sim \Lambda^z$ . For the TFIM ( $z = 1$ ), this KZM prediction has been confirmed [7]. By stark contrast, totally connected models do not match this estimate: instead of an exponent  $1/3$ , a scaling  $Q_f \sim \Lambda^{3/2}$  has been found [16]. However, Fig. 2(a) reveals that in the  $\lambda > 0$  phase, there is an anomalous  $x^{-1/4}$  dependence caused by a divergent  $\chi \sim N^{1/2}$  transition amplitude [29]. Furthermore, in the  $\lambda < 0$  phase, an  $x^{-1}$  dependence is present. Such exponents are specific to infinite dimensional lattices such as the LMGM and DM, and this difference is not taken into account in the KZM.

The failure of the KZM prediction for LMGM and DM highlights the accuracy of a dynamical function approach as compared to power-law relations based on critical exponents. Dynamical critical functions provide a full time-resolved picture of dynamical scaling in the near-adiabatic regime, even around the critical threshold where excitations have not yet stabilized—hence, understanding their properties is crucial for the design and cross-checking of annealing schemes in quantum simulations. The fact that the curves for LMGM and DM in Figs. 2(a) and 2(b) have essentially the same shape might erroneously be taken as sufficient justification for using one as a quantum simulation of the other—however, this is not true. No matter how a dynamical curve in Fig. 3(b) is scaled, its shape will never completely match any curve of Fig. 3(c). Instead, a thorough examination of Eq. (7) reveals that equivalence between both near-adiabatic evolutions can only be achieved if the functions  $\{C_{n,m}(x)\}$  scale as  $C_{n,m}^{\text{DM}}(\alpha x) = \alpha^{-1} C_{n,m}^{\text{LMGM}}(x)$ , which is a stringent condition that is undetectable through critical exponent analysis. In short, although equilibrium equivalence between systems around the QCP can be accomplished just by having identical critical exponents, achieving *dynamical* equivalence requires further tuning of model parameters, thereby

partitioning the traditionally static universality classes into *subsets* of dynamically equivalent systems.

The authors thank Ana Maria Rey for a critical reading of the manuscript. O. L. A., L. Q., and F. J. R. acknowledge financial support from Proyectos Semilla-Facultad de Ciencias at Universidad de los Andes and project “Quantum control of non-equilibrium hybrid systems,” UniAndes. O. L. A. acknowledges financial support from Colciencias, Convocatoria 511.

- [1] H. E. Stanley, *Rev. Mod. Phys.* **71**, S358 (1999).
- [2] S. Papanikolaou, F. Bohn, R. L. Sommer, G. Durin, S. Zapperi, and J. P. Sethna, *Nat. Phys.* **7**, 316 (2011).
- [3] S. Sachdev, *Quantum Phase Transitions* (Cambridge University Press, Cambridge, England, 2011).
- [4] E. Farhi, J. Goldstone, S. Gutmann, J. Lapan, A. Lundgren, and D. Preda, *Science* **292**, 472 (2001); R. Schützhold and G. Schaller, *Phys. Rev. A* **74**, 060304 (2006).
- [5] S. Boixo, T. F. Rønnow, S. V. Isakov, Z. Wang, D. Wecker, D. A. Lidar, J. M. Martinis, and M. Troyer, arXiv:1304.4595; S. Santra, G. Quiroz, G. V. Steeg, and D. Lidar, arXiv:1307.3931.
- [6] J. Dziarmaga, *Adv. Phys.* **59**, 1063 (2010).
- [7] W. H. Zurek, U. Dorner, and P. Zoller, *Phys. Rev. Lett.* **95**, 105701 (2005); L. Cincio, J. Dziarmaga, M. M. Rams, and W. H. Zurek, *Phys. Rev. A* **75**, 052321 (2007).
- [8] F. M. Cucchietti, B. Damski, J. Dziarmaga, and W. H. Zurek, *Phys. Rev. A* **75**, 023603 (2007).
- [9] S. Deng, G. Ortiz, and L. Viola, *Europhys. Lett.* **84**, 67008 (2008).
- [10] A. Polkovnikov, K. Sengupta, A. Silva, and M. Vengalattore, *Rev. Mod. Phys.* **83**, 863 (2011).
- [11] M. Kolodrubetz, B. K. Clark, and D. A. Huse, *Phys. Rev. Lett.* **109**, 015701 (2012).
- [12] T. Kibble, *J. Phys. A* **9**, 1387 (1976); W. H. Zurek, *Nature (London)* **317**, 505 (1985).

PRL **112**, 030403 (2014)

PHYSICAL REVIEW LETTERS

week ending  
24 JANUARY 2014

- [13] A. Polkovnikov, *Phys. Rev. B* **72**, 161201 (2005); C. De Grandi, V. Gritsev, and A. Polkovnikov, *ibid.* **81**, 012303 (2010).
- [14] R. H. Dicke, *Phys. Rev.* **93**, 99 (1954); H. Lipkin, N. Meshkov, and A. Glick, *Nucl. Phys.* **62**, 188 (1965).
- [15] A. Altland and V. Gurarie, *Phys. Rev. Lett.* **100**, 063602 (2008); A. Altland, V. Gurarie, T. Kriecherbauer, and A. Polkovnikov, *Phys. Rev. A* **79**, 042703 (2009).
- [16] T. Caneva, R. Fazio, and G. E. Santoro, *Phys. Rev. B* **78**, 104426 (2008).
- [17] V. M. Bastidas, C. Emary, B. Regler, and T. Brandes, *Phys. Rev. Lett.* **108**, 043003 (2012); G. Engelhardt, V. M. Bastidas, C. Emary, and T. Brandes, *Phys. Rev. E* **87**, 052110 (2013).
- [18] J. Reslen, L. Quiroga, and N. F. Johnson, *Europhys. Lett.* **69**, 8 (2005).
- [19] M. Greiner, O. Mandel, T. Esslinger, T. W. Hansch, and I. Bloch, *Nature (London)* **415**, 39 (2002).
- [20] I. Bloch, J. Dalibard, and W. Zwerger, *Rev. Mod. Phys.* **80**, 885 (2008).
- [21] A. Trabesinger, *Nat. Phys.* **8**, 263 (2012).
- [22] D. Porras and J. I. Cirac, *Phys. Rev. Lett.* **92**, 207901 (2004); K. Baumann, C. Guerlin, F. Brennecke, and T. Esslinger, *Nature (London)* **464**, 1301 (2010); J. Simon, W. S. Bakr, R. Ma, M. E. Tai, P. M. Preiss, and M. Greiner, *Nature (London)* **472**, 307 (2011).
- [23] S. Dusuel and J. Vidal, *Phys. Rev. Lett.* **93**, 237204 (2004).
- [24] C. Emary and T. Brandes, *Phys. Rev. Lett.* **90**, 044101 (2003).
- [25] See the Supplemental Material at <http://link.aps.org/supplemental/10.1103/PhysRevLett.112.030403> for details of the calculations and derivations.
- [26] A. Polkovnikov and V. Gritsev, *Nat. Phys.* **4**, 477 (2008).
- [27] A. Messiah, *Quantum Mechanics* (North Holland, Amsterdam, 1981), Vol. 2.
- [28] J. Vidal and S. Dusuel, *Europhys. Lett.* **74**, 817 (2006).
- [29] R. Botet, R. Jullien, and P. Pfeuty, *Phys. Rev. Lett.* **49**, 478 (1982); C. Emary and T. Brandes, *Phys. Rev. E* **67**, 066203 (2003).

**Supplementary material to “New dynamical scaling universality  
for quantum networks across adiabatic quantum phase  
transitions”**

O. L. Acevedo,<sup>1</sup> L. Quiroga,<sup>1</sup> F. J. Rodríguez,<sup>1</sup> and N. F. Johnson<sup>2</sup>

<sup>1</sup>*Departamento de Física, Universidad de los Andes, A.A. 4976, Bogotá, Colombia*

<sup>2</sup>*Department of Physics, University of Miami,  
Coral Gables, Miami, FL 33124, USA*

**Abstract**

In this Supplementary Material (SM), we provide details of the computational strategies employed in the main paper, in order to obtain exact numerical results for adiabatically crossing quantum phase transitions (QPT) using finite-size versions of the Dicke Model (DM), Lipkin-Meshkov-Glick Model (LMGM) and Transverse-Field Ising Model (TFIM). These results can be extended in a relatively straightforward way to the case of a non-linear time-dependence of the annealing parameter.

## SOLUTION OF THE TFIM PROBLEM

The TFIM has the advantage of being integrable [1]. After a Jordan-Wigner transformation, and a Fourier transform [2], its Hamiltonian can be decomposed as a sum of two-dimensional block Hamiltonians  $\hat{H}(t) = \sum_k \hat{H}_k(t)$ , where,

$$\hat{H}_k(t) = \hat{\sigma}_z^{(k)} + [1 - \lambda(t)] (\cos k \hat{\sigma}_z^{(k)} + \sin k \hat{\sigma}_x^{(k)}), \quad (1)$$

and  $k = \frac{\pi}{N}(2n + 1)$ , with  $n = 0, 1, \dots, N/2 - 1$ . Mode  $k$  represents a pair of fermionic excitations  $\{k, -k\}$ . These excitations are generated in even numbers because of parity conservation, where the operator is  $\hat{\Pi} = \bigotimes_{i=1}^N \hat{\sigma}_z^{(i)}$ . The decomposition in Eq. 1 means that instead of solving a  $2^N$ -dimensional Schrodinger equation, only  $N/2$  two-dimensional equations of the form  $\frac{d}{dt} |\psi_k(t)\rangle = -i\hat{H}_k(t) |\psi_k(t)\rangle$  need to be solved numerically, which are essentially Landau-Zener problems [3]. The total solution will be just the direct product  $|\Psi(t)\rangle = \bigotimes_k |\psi_k(t)\rangle$ . Furthermore, total heating can be expressed as the sum of the heating for each independent solution  $Q(t) = \sum_k Q^{(k)}(t)$ , while total fidelity is expressed as a product  $p_0(t) = \prod_k p_0^{(k)}(t)$ . As Eq. 1 allows exact diagonalization, exact forms for dynamical critical functions are possible and so the first-excited energy gap and transition amplitude are:

$$\Delta_{1,0}^{(N)}(t) = 2\sqrt{[\lambda(t) + \cos(\pi/N) - 1]^2 + \sin^2(\pi/N)}, \quad (2)$$

$$\chi_{1,0}^{(N)}(t) = \frac{\sin(\pi/N)/2}{[\lambda(t) + \cos(\pi/N) - 1]^2 + \sin^2(\pi/N)}. \quad (3)$$

## SOLUTION OF THE LMGM PROBLEM

The LMGM is a non-integrable model, so it does not have an exact diagonalization, in contrast to the TFIM in the previous section. However, its conserved quantities can be exploited in order to greatly simplify its numerical simulation. As in the TFIM, parity is constant, and in addition total angular momentum  $\hat{\mathbf{J}}^2$  is conserved [4] in the sense of collective operators  $\hat{J}_i = \frac{1}{2} \sum_{j=1}^{n_q} \hat{\sigma}_i^{(j)}$ . This last symmetry permits us to cast the Hamiltonian in the form:

$$\hat{H}(t) = -2\hat{J}_z - 4\frac{\lambda(t) + 1}{N} \hat{J}_x^2. \quad (4)$$

The even parity ( $\Pi = 1$ ), maximum angular momentum subspace ( $J = N/2$ ) will be the one containing the entire adiabatic evolution of the system. In this sense, despite the total Hilbert space of the LMGM growing exponentially as  $2^N$ , the effective Hamiltonian is of

the order  $N/2$ . In the basis of the even-parity eigenstates of  $\hat{J}_z$ , the Hamiltonian in Eq. 4 is bidiagonal which renders feasible the handling of systems sizes up to  $N = 2^{13}$ . Both dynamical evolution and instantaneous eigenstates were obtained with this basis.

## SOLUTION OF THE DM PROBLEM

The DM solution is significantly harder to obtain. It has, as the LMGM, total angular momentum as a conserved quantity, and again the dynamics will lie in the  $J = N/2$  subspace which allows its Hamiltonian to be expressed as:

$$\hat{H}(t) = \hat{J}_z + \hat{a}^\dagger \hat{a} + \frac{\lambda(t) + 1}{\sqrt{N}} \hat{J}_x (\hat{a}^\dagger + \hat{a}). \quad (5)$$

The DM has also parity  $\hat{\Pi} = e^{i\pi(\hat{a}^\dagger \hat{a} + \hat{J}_z - N/2)}$  as a conserved quantity [5]. However, the DM poses more computational complications: besides being non-integrable, this model lies on an infinite-dimensional Hilbert space, and its conserved quantities do not decompose its Hamiltonian into a sum of finite-dimensional blocks. The traditional computational solution to this difficulty is to work with *big enough* truncated versions of the Hilbert space. For adiabatic evolution situations like the ones we are interested in, this approach can be successful since the state-vectors of interest virtually *lie* on finite subspaces, i.e., their projections onto these subspaces are almost identical to the state-vectors themselves. The success of this solution can be easily tested by extending the truncation limit and then noticing that the results do not change (convergence test). The naivest application of this solution to the DM would be to work with vectors of the form  $|m\rangle_z \otimes |n\rangle$ , where the first one is an eigenvector of  $\hat{J}_z$  and the last one is a bosonic Fock state. The problem with this first approach is that it is not cost-efficient, especially when analyzing large systems during the symmetry-breaking phase ( $\lambda > 0$ ). This is because during that phase, the ground state has an expectation value of the number operator  $\hat{a}^\dagger \hat{a}$  that grows with the annealing parameter  $\lambda(t)$  and the number of qubits  $N$ , therefore requiring more Fock states to adequately represent the dynamics.

To confront that problem, Chen et al. have proposed a very useful basis that adapts itself to the behavior of the system as  $\lambda$  changes [6]. This basis has shown spectacular performances for calculating finite-size static properties of the ground-state of the system, even when  $N$  is very large. We have adapted this basis in order to take into account the

conservation of parity. We find an enormous improvement in computational performance with respect to the basis from Fock states. If we define  $G(t) = N^{-1/2} [1 + \lambda(t)]$ , the adapted vectors that form a basis for the Hilbert space have the form:

$$|\Phi_{m,k}(G)\rangle = \frac{1}{\sqrt{2}} \left( |m\rangle_x |\varphi_{m,k}(G)\rangle + (-1)^k |-m\rangle_x |\varphi_{-m,k}(G)\rangle \right). \quad (6)$$

Here the states  $|m\rangle_x$  are eigenvectors of the  $\hat{J}_x$  operator with eigenvalue  $m$ . The states  $|\varphi_{m,k}(G)\rangle$  would be eigenvectors of the Dicke Hamiltonian if the qubit free-term were zero. They have the form:

$$|\varphi_{m,k}(G)\rangle = \frac{\left(\hat{A}_m^\dagger\right)^k}{\sqrt{k!}} |-mG\rangle, \quad (7)$$

where  $\hat{A}_m^\dagger = \hat{a} + mG$  and  $|-mG\rangle$  is a coherent state that works as a ‘displaced vacuum’, and therefore these states can be seen as displaced Fock states. The basis consists of vectors  $|\Phi_{m,k}(G)\rangle$  where  $m$  ranges over all the non-negative eigenvalues of  $\hat{J}_x$  and  $k$  ranges over all non-negative integers; except when  $m = 0$ , where only even values of  $k$  are relevant. The truncation is performed on the displaced Fock states in terms of the values of  $k$ , from  $k = 0$  and up to a maximum value  $M$ . Truncation values as low as  $M = 8$  are enough to exactly diagonalize the Hamiltonian.

Despite the usefulness of the adapted basis in Eq. 6 for diagonalizing the DM at any value of  $\lambda$ , when this basis is used to dynamically simulate the adiabatic crossing, the computing time becomes prohibitively large. This is true even for system sizes of just  $N = 2^5$ , well below the size at which scaling effects are clearly manifested. In this case, dynamical evolution requires a further step. It turns out that the condition of near-adiabaticity is a great advantage, and the strategy is to solve the dynamics in terms of instantaneous eigenstates, as in Eq. 4 of the main text, focusing on the lower part of the spectrum. It requires being careful in continuously interpolating each eigenstate  $|\varphi_{\lambda(t)}^{(n)}\rangle$  as  $\lambda$  varies, even in the presence of (i) level crossings, (ii) almost critical behavior around the phase boundary, or (iii) spurious phases at each instance of diagonalization. This strategy was confronted with dynamical solutions for systems small enough to be directly evolved with the adapted basis, yielding excellent matching. It was even employed in the case of the LMGM and TFIM, in order to set more confidence on its equivalence, and also to ensure the accuracy of those results.

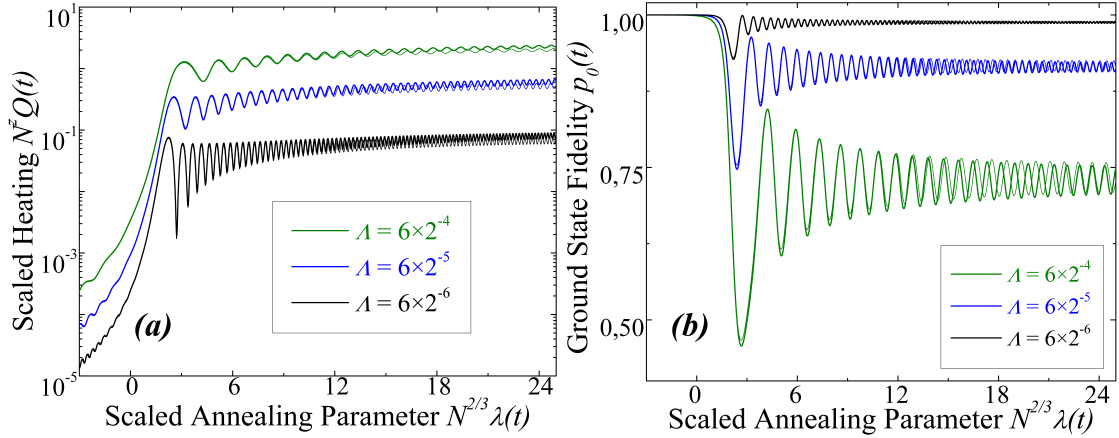


FIG. 1. Extended data interval corresponding to results shown for the DM in Fig. 3-c of main manuscript. (a) Scaled heating. (b) Ground state fidelity. Data for  $N = 2^8$  are plotted as thin curves while data for  $N = 2^9$  are plotted as thick curves.

### EXTENSIONS TO NON-LINEAR ANNEALING

In the main text, results were presented for an annealing parameter with linear time-dependence,  $\lambda(t) = vt$ . However, we stress that any power-law dependence of the form  $\lambda(t) = v\text{sign}(t)|t|^\kappa$  will exhibit this same size-independent behavior. The generalization to this case would imply the phase term in Eq. 4 of main text becoming

$$\exp\left(i\frac{v^{-1/\kappa}}{\kappa}\int_0^\lambda \text{sign}(\lambda')|\lambda'|^{\frac{1-\kappa}{\kappa}}\Delta_{n,m}^{(N)}(\lambda')d\lambda'\right).$$

At the same time in Eq. 7 of the main text, the phase would be redefined as  $\Phi_{n,m}(x) = \int_0^x \text{sign}(x')|x'|^{\frac{1-\kappa}{\kappa}}D_{n,m}(x')dx'$ , while  $\mu = \frac{\kappa v}{\kappa v z + 1}$  and  $\Lambda = \kappa^{-\mu}v^{\mu/\kappa}N$ . It is clear that the case  $\kappa = 1$  would imply less convoluted formulas and that is why it was chosen as the example in the main paper.

### COLLAPSE WELL BEYOND THE CRITICAL THRESHOLD

It might be asked whether some notorious differences between system sizes  $N$  in panels of Fig. 1 should be present in the respective panel of Fig. 3 if bigger values of  $\lambda$  of the main manuscript were investigated. In order to better appreciate that collapsed curves in Fig. 3 are effectively the continuous dynamical scaled version of data in Fig. 1, a larger

range of values of  $\lambda$  is illustrated in SM-Fig.1 for the DM. The chosen interval goes up to  $\lambda = 0.62$  for  $N = 2^8$  and to  $\lambda = 0.39$  for  $N = 2^9$  in the  $\lambda > 0$  ordered phase present in Fig. 1. Therefore, these new plots have a time scale comparable to that of Fig. 1 of main manuscript. In order to have clear curves with a fine mesh resolution, thinner curves have been used for  $N = 2^8$  instead of symbols. SM-Fig.1 shows that most differences between system sizes  $N$  in Fig. 1 of main manuscript are either because continuous finite-size scaling has not yet been applied and/or slightly because mesh resolution is not enough to show the complete oscillations appreciable in Fig. 3 of main manuscript. In SM-Fig.1, it is clear that collapse in both heating and fidelity is preserved well beyond the critical point albeit two non relevant discrepancies emerge for significantly large values of  $\lambda$ . The first one occurs only for the heating, and it consists of a gradual departure between analogous curves with different  $N$ . This departure is consistent with the fact that, at very high values of  $\lambda$ , the scaling of heating by  $N^z$  is no longer necessary and a collapse in terms of non-scaled heating, as seen in Fig. 1 of main manuscript, is what it must be expected. The second difference is an occasional loss of oscillation synchronization in the curves corresponding to different  $N$ . This discrepancy is also negligible, as the mean value of fidelity curves collapses very thoroughly. Both discrepancies are in fact connected, since the cause of oscillations is the accumulated phase difference between instantaneous eigenstates in terms of their respective energy difference, hence the loss of synchronization is also due to the fact that energy differences no longer scale with  $N^z$  for high values of  $\lambda$ .

- 
- [1] W. H. Zurek, U. Dorner, and P. Zoller, Phys. Rev. Lett. **95**, 105701 (2005).
  - [2] M. Kolodrubetz, B. K. Clark, and D. A. Huse, Phys. Rev. Lett. **109**, 015701 (2012).
  - [3] C. Zener, Proc. R. Soc. Lond. A **137**, 696 (1932).
  - [4] S. Dusuel and J. Vidal, Phys. Rev. Lett. **93**, 237204 (2004).
  - [5] C. Emary and T. Brandes, Phys. Rev. E **67**, 066203 (2003).
  - [6] Q.-H. Chen, Y.-Y. Zhang, T. Liu, and K.-L. Wang, Phys. Rev. A **78** (2008), 10.1103/Phys-RevA.78.051801.

## Appendix C

# Published and submitted papers.

## Chapter 3(a)

This paper has been accepted for publication in *Physical Review A*.

## Enhanced dynamic light-matter entanglement from driving neither too fast nor too slow

O. L. Acevedo,<sup>1,\*</sup> L. Quiroga,<sup>1</sup> F. J. Rodríguez,<sup>1</sup> and N. F. Johnson<sup>2</sup>

<sup>1</sup>*Departamento de Física, Universidad de los Andes, A.A. 4976, Bogotá D. C., Colombia*

<sup>2</sup>*Department of Physics, University of Miami, Coral Gables, Miami, FL 33124, USA*

A significant problem facing next-generation quantum technologies is how to generate and manipulate macroscopic entanglement in light and matter systems. Here we report a new regime of dynamical light-matter behavior in which a giant, system-wide entanglement is generated by varying the light-matter coupling at *intermediate* velocities. This enhancement is far larger, broader-ranged, and more experimentally accessible, than that occurring near the quantum phase transition of the same model under adiabatic conditions. By appropriate choices of the coupling within this intermediate regime, the enhanced entanglement can be made to spread system-wide or to reside in each subsystem separately.

PACS numbers: 03.67.Bg, 05.30.Rt, 05.45.Mt, 42.50.Dv, 42.50.Nn

### I. INTRODUCTION

Many-body quantum dynamics lie at the core of many natural phenomena and proposed quantum technologies, including information processing through schemes such as adiabatic quantum computing [1]. Achieving the controllable generation and manipulation of entanglement over many qubits is a key challenge, while doing so in light-matter systems is highly desirable for optoelectronic implementations. The ground state, and hence entanglement, of a quantum system can be varied in a controlled way through adiabatic perturbations, though this is in principle an infinitely slow process. Quantum Phase Transitions (QPTs) can provide a naturally occurring entangled state and it is known that the entanglement can be enhanced at the critical point [2]. Recent studies have focused on time-dependent perturbations around QPTs that are either very slow (adiabatic) [3] or very fast (sudden quench) [4]; or small dynamic oscillations around a phase space region [5]; or static coupling after a sudden quench [6–9].

Here we consider, by contrast, the regime of intermediate perturbation velocities that has so far been overlooked. We consider the experimentally realized light-matter system of the Dicke Model (DM) [10], which has been realized in a variety of systems (e.g. circuit QED [11] and cold atom settings [12, 13]). We uncover a level of quantum complexity that is far richer than either the adiabatic or fast-quench regimes. The system-wide entanglement is dramatically enhanced over the static or adiabatic QPT values. Our results extend current understanding of coupled light-matter systems beyond the equilibrium ground state [2, 14–17], and also they also stand apart from more recent studies of out-of-equilibrium critical behavior [3, 5–9, 18]. Moreover, our fully quantum analysis covers all dynamical regimes from very slow adiabatic through to sudden quench, capturing

at each stage the emergent non-linear self interactions and correlations within and between each subsystem.

Our calculations employ the DM Hamiltonian [10]:

$$\hat{H} = \epsilon \hat{J}_z + \omega \hat{a}^\dagger \hat{a} + 2 \frac{\lambda(t)}{\sqrt{N}} \hat{J}_x (\hat{a}^\dagger + \hat{a}), \quad (1)$$

where  $N$  is the number of matter qubits, the operators  $\hat{J}_i = \frac{1}{2} \sum_{j=1}^N \hat{\sigma}_i^{(j)}$  denote collective operators of the qubits, and operator  $\hat{a}^\dagger$  ( $\hat{a}$ ) is the creation (annihilation) operator of the radiation field. In the thermodynamic limit ( $N \rightarrow \infty$ ), the critical value of the light-matter coupling parameter  $\lambda$  is  $\lambda_c = \sqrt{\omega \epsilon} / 2$  while its finite- $N$  equivalent is slightly different [15, 19]. We treat the Hamiltonian exactly using a large basis set [20] and avoid common simplifications such as rotating-wave or semiclassical approximations. The total system evolves unitarily under Hamiltonian  $\hat{H}$ , starting at  $t = 0$  from the instantaneous ground state at  $\lambda = 0$ . The light-matter coupling parameter is characterized by an annealing velocity (AV)  $v$  under a linear ramping  $\lambda(t) = vt$ . More complicated time-dependencies can be treated but further complicate the understanding. The interval of interest in this paper is  $\lambda \in [0, 2]$ , meaning that the driving passes across a broad range of coupling strengths below and above the QPT. While the evolution of the total system  $S$  is described by a pure state  $|\Psi(t)\rangle$ , any subsystem  $A$  is described by a density matrix  $\hat{\rho}_A$  defined as the trace with respect to the other degrees of freedom not present in  $A$ :  $\rho_A(t) = \text{tr}_{S-A}(|\Psi(t)\rangle\langle\Psi(t)|)$ . Because of the global unitary condition and Schmidt decomposition, both radiation and matter have the same value of entropy  $S_N$ , and it provides a quantitative measure of the degree of entanglement between them [21].

This work is structured as follows: In section II we present the main result of our work, namely an enhanced dynamical light-matter regime at intermediate annealing velocities. It is followed, in section III, by a deeper theoretical explanation of our findings in terms of a dynamical symmetry-breaking and effective non-linear interactions. Then, in section IV, we establish the prevalence of our

\* ol.acevedo53@uniandes.edu.co

2

results for a wide range of system sizes and even if the system is submitted to a dissipating environment. Finally, we provide some concluding remarks in section V.

## II. ENHANCED DYNAMICAL LIGHT-MATTER ENTANGLEMENT

Figure 1 summarizes our main finding: A novel, dynamical light-matter regime with greatly enhanced system-wide properties including entanglement, when the light-matter coupling is driven at intermediate velocities. The peak entanglement value (purple) is far larger than the known equilibrium critical maximum [2], i.e. much larger than what can be achieved under adiabatic conditions. Also, this enhanced entanglement extends over a far broader range, well across the  $\lambda > \lambda_c$  region. As the annealing velocity increases, the critical onset point of light-matter entanglement is pushed toward larger  $\lambda$  values and is no longer represented by a sharp peak, but instead a wavy plateau. At much higher velocities beyond the giant entanglement regime,  $\lambda$  varies so fast that a sudden quench condition is achieved. Now the system is not quick enough to respond to the light-matter coupling, at least not in the  $\lambda \in [0, 2]$  interval of Fig. 1.

Besides exhibiting greatly enhanced values of light-matter entanglement, the intermediate regime has also some crucial practical advantages. Dotted lines in Fig. 1 show how different are the time scales for optimal maximum light-matter entanglement in the intermediate regime as compared to the adiabatic one. In the adiabatic regime, the optimal value of light-matter entanglement is at the critical point  $\lambda_c$ . By contrast, in the intermediate regime the optimal values are achieved well inside the  $\lambda > \lambda_c$  phase and require evolution times that are just a tiny fraction of the time needed to reach the critical point in the adiabatic regime. In any realistic implementation, the system loses quantum information towards the environment. If these open system effects are not negligible, the intermediate regime is the only viable way to achieve optimal light-matter entanglement, before the dissipation of the environment becomes relevant.

## III. DYNAMICAL SYMMETRY-BREAKING AND EFFECTIVE NON-LINEAR INTERACTIONS

We now develop a deeper theoretical understanding of the results in Fig. 1, by analyzing the underlying quantum state in the three main dynamical regimes, as illustrated in Fig. 2. We start by rewriting the Dicke Hamiltonian exactly as

$$\hat{H} = \omega \hat{b}^\dagger \hat{b} - \frac{4\lambda^2}{\omega N} \hat{J}_x^2 + \epsilon \hat{J}_z, \quad (2)$$

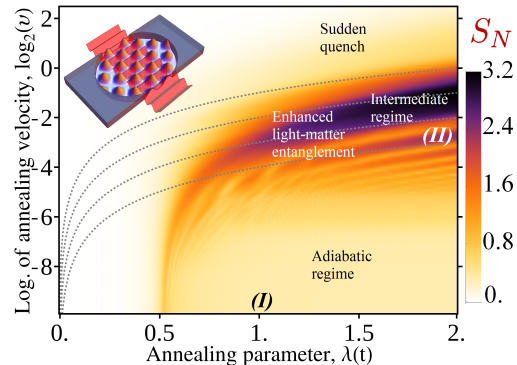


FIG. 1. (color online) Dynamic evolution of the Von-Neumann entropy  $S_N$  (time varies from left to right) for the Dicke Model (DM) with  $N = 81$  qubits. For simplicity we set  $\epsilon = \omega = 1$  in Eq. 1 for this figure, as well as for Figs. 3 and 4. The velocity range spans all regimes: from adiabatic (bottom) to sudden quench (top). Roman numerals mark where the field (Wigner) and matter (Agarwal-Wigner) distributions are depicted in Fig. 3. Dotted lines represent instants of equal time  $t$  passed after initial condition (from up to down:  $t = 2, 4, 8, 16$ ). In between those curves there is a region of novel dynamical light-matter behavior with greatly enhanced entanglement (purple) as compared to the QPT. It arises for intermediate velocities and lies well inside the coupling regime for the conventional ordered phase ( $\lambda > \lambda_c = 0.5$ ). The QPT corresponds to  $\lambda \rightarrow 0.5$  as  $v \rightarrow 0$  and hence as  $\log v \rightarrow -\infty$  (i.e. it tends toward  $\lambda = 0.5$  on the horizontal axis of the diagram). Inset: a schematic representation of the DM which mimics various experimental realizations.

where  $\hat{b} = \hat{a} + \frac{2\lambda}{\omega\sqrt{N}}\hat{J}_x$ . In the  $\lambda > \lambda_c$  range, the last term becomes less and less relevant and the Dicke Hamiltonian can be seen as a radiation mode that feels a displaced harmonic potential whose values depend on the eigenstate  $|m_x\rangle$  of  $\hat{J}_x$  in which the matter system sits [4]. Specifically, if  $\lambda \gg \lambda_c$ , then

$$\hat{H} \approx \sum_{m_x} \left( \frac{1}{2} \omega \left[ \hat{p}^2 + \left( \hat{x} - \frac{2\lambda}{\omega\sqrt{N}} m_x \right)^2 \right] - \frac{4\lambda^2}{N} m_x^2 \right) |m_x\rangle \langle m_x|, \quad (3)$$

where we have used the quadrature operators of the radiation mode. The different confining potentials depending on the eigenvalue of  $\hat{J}_x$  are depicted by different parabolae in Fig. 2. Importantly, the energy potential is symmetrical with respect to a change in sign in  $m_x$ , which is a source of degeneracy. In addition, as  $|m_x|$  gets bigger, the minimum value of the harmonic potential becomes lower. The ground state of this approximate Hamiltonian is any superposition of the form

$$|\psi_0\rangle = \cos \theta |N/2\rangle_{m_x} |-\beta\rangle + e^{i\varphi} \sin \theta |-N/2\rangle_{m_x} |\beta\rangle, \quad (4)$$

i.e. it corresponds to the two minimum parabolae. Hence the symmetry of the ground state is spontaneously bro-

ken. The field state  $|\beta\rangle$  is a coherent state with  $\beta = \frac{2\lambda}{\omega\sqrt{N}}m_x$ . As parity is preserved during the ramping, and adiabatic evolution keeps the energy in the lowest possible value, the projection of  $|\psi_0\rangle$  onto the even parity subspace ( $\theta = \pi/4$  and  $\varphi = 0$  in Eq. 4) is the state achieved in this regime. Both the symmetry breaking and the adiabatic asymptotic value of entropy ( $S_N = \log 2$ ) in each subsystem can be explained by this double-well, since two coherent states are needed to describe each system.

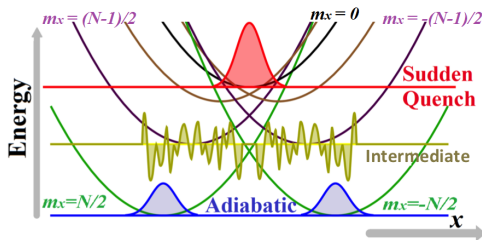


FIG. 2. (color online) Schematic indicates energies of the three main outcomes when the light-matter coupling is increased at different velocities. Horizontal axis is the field position quadrature, and for sketches of the field Wigner function and for the harmonic confining potentials (parabola). The potential felt by the field depends on the eigenvalue  $m_x$  of the matter operator  $\hat{J}_x$ . If driving is very slow, the system stays cool in a symmetry broken ground state (blue curve) where each subsystem has entropy  $\log 2$  (low matter-light entanglement). If driving is very fast (sudden quench), the system still is in the initial  $\lambda = 0$  state (red curve) and light-matter entanglement is zero. For intermediate velocities, the system gets heated such that it occupies a complicated superposition of all the  $\hat{J}_x$  eigenvalues, and hence gets disturbed by all these potentials (yellow curve).

The multiple potential picture in Fig. 2 and Eq. 3 is still valid for the intermediate and sudden quench regimes. As the AV increases, the process generates a relative heating with respect to the ground state. For high enough AV (sudden quench), the system stays essentially in its starting condition, and the heating is just the consequence of the initial state being very different from the instantaneous ground state. Despite this sudden heating being very high, the simplicity of the initial state leads to no matter-light entanglement (i.e. one coherent state describes each subsystem). In the novel intermediate regime, by contrast, all confining potentials simultaneously perturb the system. A complicated superposition of non-trivial states for each parabola is generated, with complex and chaotic features. The distribution of probabilities shows a complex distribution across  $J_x$  eigenvalues, leading to an entropy of each subsystem that is significantly higher in the intermediate regime than in the other two regimes. Due to its complex nature, there is no simple way to describe the structure of the dynamical state in the intermediate regime. Other forms of dynamically enhanced non-adiabatic entanglement generation

are possible, including the dynamical evolution preceded by a sudden quench [22].

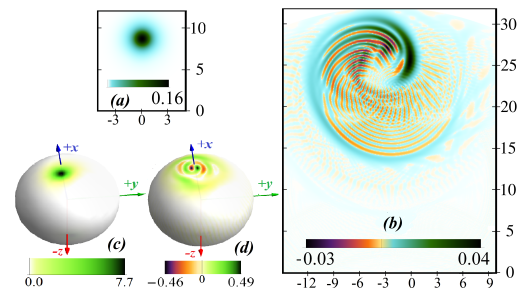


FIG. 3. (color online) (a,b) Field Wigner distributions at the same instants as the Roman numerals marked in Fig. 1: (I) becomes (a) and (II) becomes (b). Horizontal scales are for  $p$  momentum quadrature, while vertical ones are for the  $x$  position quadrature. Both figures have same  $x-p$  scale but the color scale is very different.  $-x$  part of the distribution not shown because it is symmetrical due to parity:  $W(x,p) = W(-x,-p)$ . (c,d) Respective Agarwal-Wigner distributions of the qubits in the Bloch sphere. Negative regions and fragmentation (yellow curve of Fig. 2) are a characteristic of the giant entanglement regime. Opposite hemispheres are not shown, but can be inferred from the symmetry relation  $W(\theta, \phi + \pi) = W(\theta, \phi)$  due to conserved parity.

The distinct behavior in the intermediate regime can also be interpreted in terms of the realization of non-linear self-interactions in each subsystem [14, 17], with qubits subjected to One-Axis Spin Squeezing with a Transverse Field [23, 24]. As the light-matter coupling increases in time from zero into the  $\lambda > \lambda_c$  range, the system moves out of its frozen initial state. The interaction term in the Dicke Hamiltonian begins to dominate and each subsystem works as a mediator of the other's self-interaction. Matter-light interaction is in principle linear and generates little entanglement in the adiabatic limit, since the system has enough time to continuously stabilize in response to the perturbation. The intermediate regime is the only one in which non-linearities can develop significantly. High values of squeezing in both subsystems are then generated [20]. However, this process does not last indefinitely: each subsystem starts to retain quantum information of the other, which is the moment when the entropy grows. The effective interaction is broken, leaving the qubits and radiation mode entangled with each other but not within themselves. Despite being a single radiation mode, the field acts as a reservoir that dissipates the quantum correlations present in the squeezed states of each subsystem. The quantum correlations developing in the field system can be represented by the Wigner quasi-probability distribution in Figs. 3(a) and (b). See appendix A for definitions of these distributions. This shows that the distribution becomes highly fragmented yet retains some order, reflecting the com-

plexity of the light subsystem in the intermediate regime. Round-tailed interference patterns as in Fig. 3 have been obtained in light with a non-linear Kerr-like interaction following a Fokker-Planck equation [25]. This confirms that the field experiences an effective non-linear interaction. Similar signatures of complexity arise in the matter subsystem, specifically the matter density matrices, as shown in the spherical Agarwal-Wigner functions in Figs. 3(c) and (d) [26].

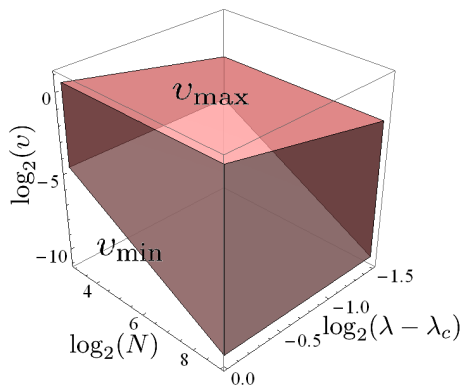


FIG. 4. (color online) Dynamical phase diagram showing the new enhanced entanglement regime (shaded red) defined by instances where  $S_N > \log 2$  since  $S_N \rightarrow \log 2$  is the asymptotic value for the equilibrium ordered phase. For visual clarity in this figure, we take  $S_N > \log 2 + 0.05$ . Below a minimum annealing velocity  $v_{\min}$  the system's behavior is adiabatic, while for  $v > v_{\max}$  it corresponds to sudden quench. The adiabatic boundary depends on system size as  $v_{\min} \propto N^{-1}$ . The sudden quench boundary is size-independent, but depends on the value of  $\lambda_d$  that is reached during the driving:  $v_{\max} \propto (\lambda_d - \lambda_c)^{3/2}$ . See appendix B for more details.

#### IV. PERSISTENCE OF RESULTS AGAINST DISSIPATION AND DIFFERENT SYSTEM SIZES

Figure 4 demonstrates how the range of velocities that classify as 'intermediate' actually increases with increasing number of qubits  $N$ , meaning that the enhanced entanglement regime (EER) begins to dominate the space of behaviors as opposed to becoming a small niche. The EER can be imagined as lying between a lower bound AV  $v_{\min}$  which marks the adiabatic evolution, and an upper bound one  $v_{\max}$  defining the AV at which the sudden quench approximation starts to be valid. Specifically, Fig. 4 shows the dynamical phase diagram of the intermediate regime in which the giant entanglement occurs, including its scaling behavior (dependence on system size  $N$ ). The adiabatic evolution is more difficult to achieve as the number of atoms increases. The other main variable is the value of  $\lambda_d$  reached by the annealing. The

sudden quench condition requires higher AVs as this  $\lambda_d$  gets bigger. The oscillatory behavior near the adiabatic regime has been smoothed out in order to make the phase boundary visually clearer. More details on how this diagram was obtained are given in appendix B.

In section II, we used Von Neumann entropy  $S_N$  as a measure of light-matter entanglement in the case that the entire system is pure. However, in order to have an idea of the decoherence effects of a leaky cavity we have to analyze the DM as an open system, and then,  $S_N$  is no longer a good entanglement witness. Instead, we use quantum negativity, whose non-zero value is a sufficient condition for bipartite entanglement in the open light-matter system [27]. Quantum negativity is defined as,

$$\mathcal{N}(\hat{\rho}) = \frac{\|\hat{\rho}^{\Gamma_q}\|_1 - 1}{2}, \quad (5)$$

where  $\hat{\rho}^{\Gamma_q}$  is the partial transpose of  $\hat{\rho}$  with respect to the matter subsystem, and  $\|\hat{A}\|_1 \equiv \text{tr} \{ \sqrt{\hat{A}^\dagger \hat{A}} \}$  is the trace norm. However, one may wonder if switching from

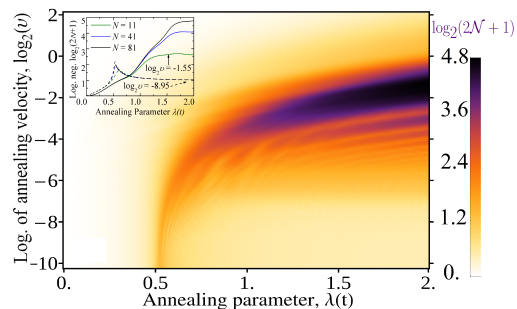


FIG. 5. (color online) Dynamical profile analogous to Fig. 1 but now for logarithmic negativity  $\log_2(2\mathcal{N} + 1)$ . There is strong resemblance between both profiles. This justifies the use of  $S_N$  as the entanglement witness for the closed system case while changing to  $\log_2(2\mathcal{N} + 1)$  when the system is open. The inset shows the dynamical evolution of logarithmic negativity for a near-adiabatic ramping velocity  $\log_2(v) = -8.95$  (dashed lines) and an intermediate one  $\log_2(v) = -1.55$  (solid lines). Different line colors represent different system sizes. This inset shows that even with relative small system sizes,  $\log_2(2\mathcal{N} + 1)$  has qualitatively similar behaviors for the same  $v$ , so that conclusions about the robustness of the dynamic light-matter entanglement against decoherence can be extrapolated to bigger  $N$ .

one form of entanglement measure to the other has any justification. Figure 5 shows a dynamical profile of the ramping process analogous to that of Fig. 1 (same parameters, unitary evolution, and system size  $N = 81$ ), but with logarithmic negativity  $\log_2(2\mathcal{N} + 1)$ . The resemblance with the  $S_N$  graphic is quite apparent, and the EER is again clearly noticeable. This should be no surprise as both measures virtually codified the same information. If total  $\hat{\rho}$  is a pure state, and  $\{p_i\}$  is the

spectrum of  $\hat{\rho}_q$  in that case (which is the same as the spectrum of  $\rho_b$  because of Schmidt decomposition), both negativity  $\mathcal{N}$  and  $S_N$  can be written in terms of that spectrum. The first one would be  $2\mathcal{N} + 1 = \sum_{i,j} \sqrt{p_i p_j}$ , while the second one is  $S_N = -\sum_i p_i \log p_i$ . Therefore, Fig. 5 confirms that both entanglement measures are well connected and suitable for witnessing light-matter entanglement. The reason why  $S_N$  was preferred in section II is because its wider usage and well established connection to other quantum information concepts [21].

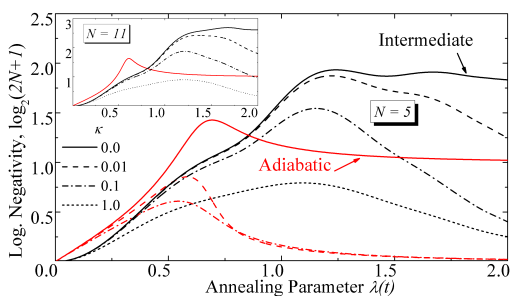


FIG. 6. (color online) Effect of cavity losses on light-matter entanglement generation, witnessed by quantum logarithmic negativity. Cavity's field decay rate is  $\kappa$  (different line style). Black curves depict giant entanglement regime  $\log_2(v) = -1.58$ , while red curves represent adiabatic one  $\log_2(v) = -8.96$ . Main figure is for  $N = 5$  system's size while inset represents analogous  $N = 11$  results. Dynamical entanglement regime is bigger and more robust against open system losses as  $N$  increases. In opposition, near-adiabatic entanglement vanishes even for weak losses since annealing time is too long as compared to decoherence time. Zero temperature has been assumed and  $\kappa$  is measured in units of field free frequency  $\omega$ . Finite temperature cases have very similar tendencies.

It should be stressed that the giant entanglement regime, central to present work, is accessible under current experiments very similar to the sketch in inset of Fig. 1 [12, 13]. In particular, Klinder et al. have been able to ramp a cold atom Bose-Einstein condensate whose dynamics are governed by the DM, and with annealing velocities corresponding very well to the giant entanglement regime predicted by our analysis [13]. Moreover, cavity decay rates, which measure the importance of losses, are an order of magnitude lower than the main evolution energy  $\omega$ , and can be well simulated by open cavity master equations [13]. Our analysis including losses predicts the survival of giant light-matter entanglement in those experiments – indeed it occurs even when open system losses are present, as shown in Fig. 6. We use quantum negativity as the light-matter entanglement measure for the open system case [27] since  $S_N$  will no longer be a good bipartite entanglement measure. Details of the definition of quantum negativity and the open system solution, are given in the appendix C. Since the light-matter

entanglement increases as  $N$  increases, we predict that experimental system sizes  $N \approx 10^5$  will develop significantly more robust light-matter entanglement against losses than for small systems. By contrast, entanglement generation in the well-studied near-adiabatic regime cannot be achieved under current experimental setups, since decoherence times are much shorter than the annealing times required by this regime.

We have then established the persistence of the EER for a wide range of system sizes and even under the effect of dissipation effects. A remnant concern could be that the system sizes  $N$  accessible to open system numerical solution in the present work are well smaller than the ones examined in the pure case. This could cast doubt on whether the conclusions brought from this small size result have any general validity. The inset of figure 5 shows that despite even at  $N = 11$ , there are good signatures of the dynamical phase with giant light-matter entanglement, and that it only gets stronger as  $N$  increases. This means that, provided the open system's parameters like  $\kappa$  and  $\bar{n}$  remain the same, any deleterious effect caused by the leakage of quantum information to the environment is only weaker with sizes of the order  $N = 81$  than the ones numerically accessible.

## V. CONCLUSIONS

We have unraveled a previously unnoticed dynamical regime where enhanced light-matter entanglement arises at intermediate ramping velocities. We have provided theoretical insights of this phenomenon by means of a dynamical symmetry breaking and effective non-linear self-interactions. We have further argued that our main results are still present under more realistic settings, as those already accessible by current experiments, with bigger system sizes and a dissipating environment. Finally, we note that by moving around the parameter space in time in Fig. 1, the enhanced squeezing and entanglement can be altered within the matter and light subsystems separately, and then transferred by means of the light-matter coupling. Potential applications include high precision quantum metrology and a range of quantum information processing technologies [28–30].

## ACKNOWLEDGMENTS

O.L.A, L.Q. and F.J.R. acknowledge financial support from Proyectos Semilla-Facultad de Ciencias at Universidad de los Andes (2010-2014) and project *Quantum control of non-equilibrium hybrid systems*, UniAndes-2013. O. L. A. acknowledges financial support from Colciencias, Convocatoria 511.

### Appendix A: Subsystem quasi-probabilities distributions

In order to provide a visual depiction of both matter and field subsystems in the main text, we employed phase space representations of the density matrix by means of Wigner functions. The matter states were represented by the Agarwal-Wigner function (AWF), which is a Bloch sphere representation of the subsystem's density matrix  $\hat{\rho}_q$  [26],

$$W_q(\theta, \phi) = \sum_{l=0}^N \sum_{m=-l}^l T_{l,m} Y_{l,m}(\theta, \phi), \quad (\text{A1})$$

where  $Y_{l,m}$  are the spherical harmonics; and terms  $T_{l,m} = \text{tr} \{ \hat{\rho}_q \hat{T}_{l,m} \}$  are expected values of the multipole operator,

$$\hat{T}_{l,m} = \sum_{M,M'=-j}^j (-1)^{j-m} \sqrt{2l+1} \begin{pmatrix} j & l & j \\ -M & m & M' \end{pmatrix} |jM\rangle \langle jM'|, \quad (\text{A2})$$

where  $j = N/2$ , and  $\begin{pmatrix} j & l & j \\ -M & m & M' \end{pmatrix}$  is the Wigner 3j symbol.

The respective Wigner function for the field density matrix  $\hat{\rho}_b$  is [4, 31],

$$W_b(\alpha, \hat{\rho}_b) = \sum_{n=0}^{\infty} (-1)^n \langle n | \hat{D}^\dagger(\alpha) \hat{\rho}_b \hat{D}(\alpha) | n \rangle, \quad (\text{A3})$$

where  $\hat{D}(\alpha) = e^{\alpha \hat{a}^\dagger - \alpha^* \hat{a}}$  is the displacement operator, and  $\alpha \in \mathbb{C}$ . The displacement parameter  $\alpha$  can be expressed in terms of the field's position ( $x$ ) and momentum ( $p$ ) quadratures as its real and imaginary part,  $\sqrt{2}\alpha = x + ip$ .

### Appendix B: Numerical evidence of phase diagram

This section provides a detailed explanation on how we obtained the phase diagram of the EER depicted in Fig. 4 of main text. The EER was defined as the dynamical region in Fig. 1 of main text where entropy is bigger than  $\log 2 + 0.05$  well inside the ordered  $\lambda > \lambda_c$  phase. This region can be seen as bounded by a maximum AV  $v_{\max}$  over which the sudden quench approximation is valid, and a minimum AV  $v_{\min}$  below which the adiabatic condition is fulfilled.

From Fig. 1 of main text, it is clear that  $v_{\min}$  does not depend on the value  $\lambda_d$  of the annealing parameter reached (the lower boundary forms an horizontal line in the figure). This is expected as the ground state in all the ordered phase has an asymptotic value of  $S_N \rightarrow \log 2$ , and the adiabatic condition should only depend on the

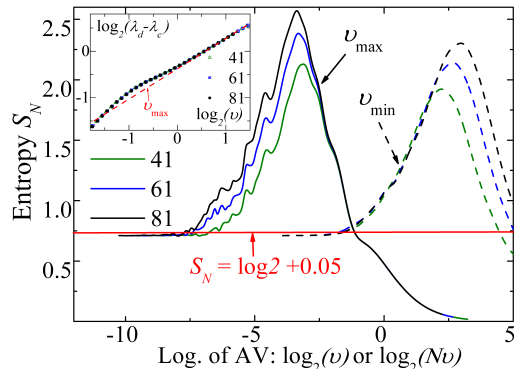


FIG. 7. (color online) Numerical evidence for constructing the dynamical phase diagram of Fig. 4 of main text. Solid (dashed) curves depict the value of  $S_N$  as a function of  $\log_2(v)$  ( $\log_2(Nv)$ ) when  $\lambda = 2.0$  for different system sizes. Point  $v_{\max}$  ( $Nv_{\min}$ ) is obtained in a size-independent way where curves touch the red horizontal line, which is the defining value for the dynamical phase boundary. The inset shows the dependence of point  $v_{\max}$  on the value of  $\lambda_d$  reached, and its fitting to the  $v_{\max} \propto (\lambda_d - \lambda_c)^{3/2}$  dependence (red dashed line). In opposition, the point  $Nv_{\min}$  is independent of the value of  $\lambda_d$  reached. In principle, solid and dashed curves represent the same data, but dashed curves have been smoothed in order to establish a cleaner boundary for  $v_{\min}$ .

system size  $N$ . The scaling  $v_{\min} \propto N^{-1}$  comes from a well established relation of the minimal energy gap  $\Delta$  at the critical threshold [3, 19], and it is confirmed in the dashed curves of Fig. 7 where using this kind of scaling of the AV makes the lower boundary of the EER size independent. The upper bound,  $v_{\max}$  depends on  $\lambda_d$  and the inset of Fig. 7 shows that the fitting  $v_{\max} \propto (\lambda_d - \lambda_c)^{3/2}$  is a good approximation. On the other, it is clear that  $v_{\max}$  does not depend on system size, as all three solid curves of Fig. 7 reach the red line at the same point. The relations  $v_{\max} \propto (\lambda_d - \lambda_c)^{3/2}$  and  $v_{\min} \propto N^{-1}$  with the addition of one particular point (as the ones obtained in Fig. 7) is all that is needed to produce Fig. 3 in main text.

### Appendix C: Open System Evolution

The composed DM light-matter density matrix  $\hat{\rho}(t)$  evolves under a unitary part generated by  $\hat{H}$  (see Eq. 1 of main text) and a dissipative part due to a field lossy cavity. The evolution of  $\hat{\rho}(t)$  is modeled by a Master Equation in Lindblad form [32],

$$\frac{d}{dt} \hat{\rho} = -i [\hat{H}, \hat{\rho}] + 2\kappa (\bar{n} + 1) \mathcal{D}(\hat{\rho}; \hat{a}) + 2\kappa \bar{n} \mathcal{D}(\hat{\rho}; \hat{a}^\dagger), \quad (\text{C1})$$

where  $\kappa$  is the damping rate of the cavity, and  $\bar{n}$  is the thermal mean photon number. Also, for any operator  $\hat{A}$ , the Lindblad superoperator  $\mathcal{D}$  is defined as ( $\{, \}$  denotes anti-commutator),

$$\mathcal{D}(\hat{\rho}; \hat{A}) = \hat{A}\hat{\rho}\hat{A}^\dagger - \frac{1}{2}\{\hat{A}^\dagger\hat{A}, \hat{\rho}\}. \quad (\text{C2})$$

The general initial condition (when  $\lambda(0) = 0$ ) consist of an unentangled light-matter state,

$$\hat{\rho}(0) = |-N/2\rangle_z \langle -N/2|_z \otimes \frac{e^{-\beta\hat{a}^\dagger\hat{a}}}{\text{tr}\{e^{-\beta\hat{a}^\dagger\hat{a}}\}}, \quad (\text{C3})$$

where  $e^{-\beta} = \bar{n}/(\bar{n} + 1)$ , and  $\beta = 1/T$  is the inverse temperature in natural units. This condition means zero

excitations in the matter state and field thermalization. The field state is in fact the steady equilibrium state for the respective terms in Eq. C1.

We have obtained exact numerical solutions of Eq. C1, either in the pure DM Hilbert state when  $\kappa = 0$ , or in the space of density matrices otherwise, using the DM Hamiltonian or the Liouvillian superoperator as the respective dynamical generator [32]. Since the dimension of the numerical evolution vector space is squared as soon as the unitary condition is broken, only relatively small values of  $N$  can be investigated under open conditions. As the field Hilbert space is infinite dimensional, we have truncated its Fock basis  $\{|n\rangle\}$  up to a number where numerical results converge.

- 
- [1] J. Dziarmaga, *Adv. Phys.* **59**, 1063 (2010).  
[2] N. Lambert, C. Emary, and T. Brandes, *Phys. Rev. Lett.* **92**, 073602 (2004).  
[3] O. L. Acevedo, L. Quiroga, F. J. Rodríguez, and N. F. Johnson, *Phys. Rev. Lett.* **112**, 030403 (2014).  
[4] S. Fuchs, J. Ankerhold, M. Blencowe, and B. Kubala, (2015), arXiv:1501.07841 [quant-ph].  
[5] V. M. Bastidas, C. Emary, B. Regler, and T. Brandes, *Phys. Rev. Lett.* **108**, 043003 (2012).  
[6] A. Altland and F. Haake, *New J. Phys.* **14**, 073011 (2012).  
[7] A. Alvermann, L. Bakemeier, and H. Fehske, *Phys. Rev. A* **85**, 043803 (2012).  
[8] L. Bakemeier, A. Alvermann, and H. Fehske, *Phys. Rev. A* **88**, 043835 (2013).  
[9] K. Furuya, M. C. Nemes, and G. Q. Pellegrino, *Phys. Rev. Lett.* **80**, 5524 (1998); L. Song, D. Yan, J. Ma, and X. Wang, *Phys. Rev. E* **79**, 046220 (2009).  
[10] R. H. Dicke, *Phys. Rev.* **93**, 99 (1954).  
[11] P. Nataf and C. Ciuti, *Nature Comm.* **1**, 1 (2010); O. Viehmann, J. von Delft, and F. Marquardt, *Phys. Rev. Lett.* **107**, 113602 (2011).  
[12] K. Baumann, C. Guerlin, F. Brennecke, and T. Esslinger, *Nature* **464**, 1301 (2010); C. Hamner, C. Qu, Y. Zhang, J. Chang, M. Gong, C. Zhang, and P. Engels, *Nature Comm.* **5**, 4023 (2014); M. P. Baden, K. J. Arnold, A. L. Grimsmo, S. Parkins, and M. D. Barrett, *Phys. Rev. Lett.* **113**, 020408 (2014).  
[13] J. Klinder, H. Keßler, M. Wolke, L. Mathey, and A. Hemmerich, *Proc. Natl. Acad. Sci. U. S. A.* **112**, 3290 (2015).  
[14] J. Reslen, L. Quiroga, and N. F. Johnson, *Europhys. Lett.* **69**, 8 (2005).  
[15] J. Vidal and S. Dusuel, *Europhys. Lett.* **74**, 817 (2006).  
[16] T.-L. Wang, L.-N. Wu, W. Yang, G.-R. Jin, N. Lambert, and F. Nori, *New J. Phys.* **16**, 063039 (2014).  
[17] T. C. Jarrett, A. Olaya-Castro, and N. F. Johnson, *Europhys. Lett.* **77**, 34001 (2007).  
[18] J. Eisert, M. Friesdorf, and C. Gogolin, *Nature Phys.* **11**, 124 (2015).  
[19] C. Emary and T. Brandes, *Phys. Rev. Lett.* **90**, 044101 (2003); *Phys. Rev. E* **67**, 066203 (2003).  
[20] O. L. Acevedo, Ph.D. Thesis, Universidad de Los Andes (2015).  
[21] M. A. Nielsen and I. L. Chuang, *Quantum Computation and Quantum Information* (Cambridge University Press, 2010).  
[22] V. Alba and F. Heidrich-Meisner, *Phys. Rev. B* **90**, 075144 (2014).  
[23] J. Ma, X. Wang, C. Sun, and F. Nori, *Phys. Rep.* **509**, 89 (2011).  
[24] C. K. Law, H. T. Ng, and P. T. Leung, *Phys. Rev. A* **63**, 055601 (2001).  
[25] M. Stobińska, G. J. Milburn, and K. Wódkiewicz, *Phys. Rev. A* **78**, 013810 (2008).  
[26] J. P. Dowling, G. S. Agarwal, and W. P. Schleich, *Phys. Rev. A* **49**, 4101 (1994).  
[27] G. Vidal and R. F. Werner, *Phys. Rev. A* **65**, 032314 (2002).  
[28] V. Giovannetti, S. Lloyd, and L. Maccone, *Nature Photon.* **5**, 222 (2011); R. Schnabel, N. Mavalvala, D. E. McClelland, and P. K. Lam, *Nature Comm.* **1**, 121 (2010); A. M. Rey, L. Jiang, and M. D. Lukin, *Phys. Rev. A* **76**, 053617 (2007).  
[29] S. L. Braunstein, *Rev. Mod. Phys.* **77**, 513 (2005).  
[30] L. Amico, A. Osterloh, and V. Vedral, *Rev. Mod. Phys.* **80**, 517 (2008).  
[31] D. Walls and G. J. Milburn, *Quantum Optics* (Springer, 2008).  
[32] H. P. Breuer and F. Petruccione, *The Theory of Open Quantum Systems* (Oxford University Press, 2007).

## Appendix D

# Published and submitted papers.

## Chapter 3(b)

This paper has been accepted for publication in *New Journal of Physics*.

## Robust quantum correlations in out-of-equilibrium matter-light systems

**O. L. Acevedo**

Departamento de Física, Universidad de los Andes, A.A. 4976, Bogotá, Colombia

E-mail: [ol.acevedo53@uniandes.edu.co](mailto:ol.acevedo53@uniandes.edu.co)

**L. Quiroga**

Departamento de Física, Universidad de los Andes, A.A. 4976, Bogotá, Colombia

**F. J. Rodríguez**

Departamento de Física, Universidad de los Andes, A.A. 4976, Bogotá, Colombia

**N. F. Johnson**

Department of Physics, University of Miami, Coral Gables, Miami, FL 33124, USA

**Abstract.** High precision macroscopic quantum control in interacting light-matter systems remains a significant goal toward novel information processing and ultra-precise metrology. We show that the out-of-equilibrium behavior of a paradigmatic light-matter system (Dicke model) reveals two successive stages of enhanced quantum correlations beyond the traditional schemes of near-adiabatic and sudden quenches. The first stage features magnification of matter-only and light-only entanglement and squeezing due to effective non-linear self-interactions. The second stage results from a highly entangled light-matter state, with enhanced superradiance and signatures of chaotic and highly quantum states. We show that these new effects scale up consistently with matter system size, and are reliable even in dissipative environments.

PACS numbers: 03.67.Bg, 05.30.Rt, 05.45.Mt, 42.50.Dv, 42.50.Nn

*Robust quantum correlations in out-of-equilibrium matter-light systems*

2

Many-body quantum dynamics are at the core of many natural and technological phenomena, from understanding of superconductivity or magnetism, to applications in quantum information processing as in adiabatic quantum computing [1]. Critical phenomena, defect formation, symmetry breaking, finite-size scaling are all aspects that emerge from the collective properties of the system [2]. Spin networks, many-body systems composed of the simplest quantum unit, are an obvious starting point to understand those phenomena, as they enclose much of their complex behavior in a highly controllable and tractable way. However, if the system under investigation includes a radiation subsystem, new opportunities arise for monitoring and characterizing the resulting collective phenomena [3, 4]. By devising driving protocols of the light-matter interaction, high precision macroscopic control then becomes a possibility, regardless of whether the focus is on the matter subsystem, the light, or the composite manipulation of both. This is particularly true for the Dicke model (DM) [5], which is the subject of the present work.

The DM describes a radiation-matter system which, despite its simplicity, exhibits a wide arrange of complex collective phenomena, many of them specifically associated with the existence of a quantum phase transition (QPT) [6]. Experimental realizations of the DM have been presented in different settings, from proposed realizations in circuit quantum electrodynamics [7], to the recent very successful demonstrations of DM superradiance in various cold atom experiments [8]. While the light and matter properties in the equilibrium ground state are relatively well known [9–13], its fully quantum out-of-equilibrium critical behavior is just starting to be understood [14, 15].

In the DM, both the matter and field are known to act as mediators of an effective non-linear self-interaction involving each other [10, 13]. These non-linear interactions produce interesting phenomena in both atomic and optical systems [16, 17]. Among the most relevant effects, there is the strong collapse and revival of squeezing [18, 19], which in many matter states can be related to atom-atom entanglement [20]. Applications of such effects are widespread, including high precision quantum metrology [21], and quantum information technologies [22]. As the non-linear interactions are only effective, it is of essential relevance to understand how the eventual matter-field correlations could affect the generation of the desirable quantum squeezing in each subsystem. We will theoretically address this problem in the particular setting of the finite size DM, when it is ramped across the critical threshold starting from its initial equilibrium non-interacting state.

Some previous works have already examined the dynamical emergence of quantum effects on each subsystem of the DM. However they focused on the semi-classical limit and a static coupling after a sudden quench [23–26], small dynamic oscillations around a phase space region [14], or under time-delayed feedback control [27]. Our work goes beyond this by giving a fully quantum analysis of the process of continuously turning on

the interaction, in order to assess the emergent effects of the non-linear self interaction in each subsystem. We have carried this out across all dynamical regimes: from the very slow adiabatic regime, where the equilibrium ground state results apply, to the sudden quench regime which is the initial preparation scheme for most previous non-equilibrium results. In between these limits, we have found an unexplored yet very rich intermediate set of annealing velocities featuring remarkable amplification of critical quantum effects as compared to the near-equilibrium results. This magnification of critical properties is followed by a novel chaotic dynamical phase, characterized by giant light-matter entanglement [28], negative Wigner quasi-distributions, and signatures of quantum chaos.

This paper is structured as follows. Section 1 presents the model, dynamical setting, and methods of analysis. Section 2 explains the general profile of the dynamical evolution under the perspective of matter and light quantum properties, namely squeezing and the order parameter (OP). Section 3 gains further insight from the point of view of phase space representations of the subsystems. Section 4 establishes the consistency of our results, even under dissipative effects, and for different system sizes, by means of a power-law relation. Section 5 concludes with some general remarks.

## 1. Theoretical framework

The DM describes a totally symmetric interaction of  $N$  matter qubits with a radiation mode. Its Hamiltonian is [5],

$$\hat{H} = \epsilon \hat{J}_z + \omega \hat{a}^\dagger \hat{a} + 2 \frac{\lambda(t)}{\sqrt{N}} \hat{J}_x (\hat{a}^\dagger + \hat{a}). \quad (1)$$

Symbols  $\hat{J}_i = \frac{1}{2} \sum_{j=1}^N \hat{\sigma}_i^{(j)}$  represent collective operators of the qubits, and symbol  $\hat{a}^\dagger$  ( $\hat{a}$ ) is the creation (annihilation) operator of the radiation field. Coefficients  $\epsilon$  and  $\omega$  are single qubit and single mode excitation energies respectively. From now on, we set resonant energies,  $\epsilon = \omega = 1$ . The thermodynamic limit ( $N \rightarrow \infty$ ) phase boundary of the controlled interaction is  $\lambda_c = \sqrt{\epsilon\omega}/2 = 0.5$ , which is slightly different at finite values of  $N$  [11]. The total system  $S$ , represented by a density matrix  $\hat{\rho}_S$ , evolves under a unitary part generated by  $\hat{H}$ , and a dissipative part caused by radiation losses of the field cavity. The time evolution is then expressed by a master equation [29],

$$\begin{aligned} \frac{d}{dt} \hat{\rho}_S = & -i [\hat{H}, \hat{\rho}_S] \\ & + \kappa (\bar{n} + 1) (2\hat{a} \hat{\rho}_S \hat{a}^\dagger - \{\hat{a}^\dagger \hat{a}, \hat{\rho}_S\}) + \kappa \bar{n} (2\hat{a}^\dagger \hat{\rho}_S \hat{a} - \{\hat{a} \hat{a}^\dagger, \hat{\rho}_S\}), \end{aligned} \quad (2)$$

where  $\kappa$  is the damping rate of the cavity, and  $\bar{n}$  is the thermal mean photon number. At initial time  $t = 0$  the system starts at

$$\hat{\rho}(0) = |-N/2\rangle_z \langle -N/2|_z \otimes \frac{e^{-\beta \hat{a}^\dagger \hat{a}}}{\text{tr} \{e^{-\beta \hat{a}^\dagger \hat{a}}\}}, \quad (3)$$

where  $e^{-\beta} = \bar{n}/(\bar{n} + 1)$ . Thus, the initial state at  $\lambda(0) = 0$  corresponds to an unentangled state formed by the qubit ground state times the field thermal equilibrium

state at inverse temperature  $\beta = 1/(k_B T)$ , with  $k_B$  the Boltzmann constant. The controlled interaction will change with an annealing velocity (AV)  $v$  by a linear ramping:  $\lambda(t) = vt$ . The interval of interest is  $\lambda \in [0, 2]$ , well across the QPT. This work is focused on subsystem properties. Any subsystem  $A$  will be described by a density matrix  $\hat{\rho}_A$ , defined as the trace with respect to the other degrees of freedom:  $\hat{\rho}_A(t) = \text{tr}_{S-A} \{\hat{\rho}_S\}$ .

We explore the dynamical development of the quantum properties in subsystems of the matter-light system, caused by this ramped QPT crossing, without resorting to any common simplifications like mean-field, rotating wave or semi-classical approximations. Our main results lie at AV values outside the well-known adiabatic and sudden quench regimes, where quantum correlations such as entanglement and squeezing of each separate subsystem can get significantly enhanced. Exact numerical solutions have been obtained by integrating Eq. 2. When  $\kappa = 0$ , the evolution lies on the pure Hilbert space and is generated by the DM Hamiltonian. Otherwise, the evolution lies in the space of density matrices and its generator is the total Liouvillian superoperator of Eq. 2 [29]. Thus, the dimension of the numerical evolution vector space is squared as soon as the unitary condition is broken. As the dimension of the field Hilbert space is infinite, the Fock basis  $\{|n\rangle\}$  is truncated up to a number where numerical results converge. We have taken advantage of every simplifying condition, such as parity conservation when  $\kappa = 0$ .

The state of any set of  $M$  qubits is the same (all qubits are equivalent) and lies on the maximal Dicke manifold  $\hat{\mathbf{J}}^2 = (J + 1)J$ , with  $J = M/2$ . The first quantum property of matter that we address is entanglement, which for a 2 qubit subsystem is measured by the Wootters concurrence  $c_W$  [30]. The second one is spin squeezing, which is highly related to multipartite entanglement and usually expressed in terms of a squeezing parameter  $\xi_q$  [31]. Under unitary evolution ( $\kappa = 0$ ), when parity of the total system is even and conserved,  $c_W$  and  $\xi_q$  are explicitly related whenever the concurrence is different from zero [32]:

$$1 - \xi_q^2 = (N - 1)c_W = \frac{2}{N} \left( \left| \langle \hat{J}_+^2 \rangle \right| + \langle \hat{J}_z^2 \rangle - \frac{N^2}{4} \right). \quad (4)$$

The factor  $N - 1$  in the concurrence is a direct manifestation of the monogamy of entanglement [33], since each qubit is equally entangled to any other one and hence the finite amount of possible entanglement is evenly distributed. Any qubit state can be visualized by the Agarwal-Wigner function (AWF), which is a Bloch sphere representation of the qubit's density matrix [34],

$$W_q(\theta, \phi) = \sum_{l=0}^N \sum_{m=-l}^l T_{l,m} Y_{l,m}(\theta, \phi), \quad (5)$$

and  $Y_{l,m}$  are the spherical harmonics. Terms  $T_{l,m} = \text{tr} \left\{ \hat{\rho}_q \hat{T}_{l,m} \right\}$ , with  $\hat{\rho}_q$  the qubit subsystem density matrix, are the expected values of the multipole operator,

$$\hat{T}_{l,m} = \sum_{M,M'=-j}^j (-1)^{j-m} \sqrt{2l+1} \begin{pmatrix} j & l & j \\ -M & m & M' \end{pmatrix} |jM\rangle \langle jM'|, \quad (6)$$

where  $j = N/2$ , and  $\begin{pmatrix} j & l & j \\ -M & m & M' \end{pmatrix}$  is the Wigner  $3j$  symbol.

In addition to the matter subsystems, the DM has the presence of a radiation mode that is usually much more experimentally accessible, thanks to the radiation leaked by the cavity and properties disclosed by tomographic techniques [3]. The general state of the mode can be condensed in the form of its Wigner quasi-probability distribution [35, 36],

$$W_b(\alpha, \hat{\rho}_b) = \sum_{n=0}^{\infty} (-1)^n \langle n | \hat{D}^\dagger(\alpha) \hat{\rho}_b \hat{D}(\alpha) | n \rangle, \quad (7)$$

where  $\hat{D}(\alpha) = e^{\alpha \hat{a}^\dagger - \alpha^* \hat{a}}$  is the displacement operator, and  $\alpha \in \mathbb{C}$ . There is also an analogous squeezing parameter in the field mode, though it cannot be directly related to a form of entanglement. It is expressed in terms of the variance and covariance of field quadratures [37],

$$\xi_b^2 = \text{Var}(x) + \text{Var}(p) - \sqrt{(\text{Var}(x) - \text{Var}(p))^2 + 4\text{Cov}(x, p)^2}. \quad (8)$$

The displacement operator in Eq. 7 is related to the quadratures by  $\sqrt{2}\alpha = x + ip$ .

## 2. Out-of-equilibrium enhancement of quantum correlations

A general picture of the time evolution of the matter quantum properties is revealed by means of spin squeezing (related to matter entanglement) and the expectation value of its OP in Figs. 1a-b. All the relevant AV are considered in each plot, from the adiabatic limit (bottom of vertical axis) to the sudden quench (top). If the adiabatic condition is fulfilled, the spin squeezing or entanglement of the matter subsystem corresponds to those well known from the equilibrium QPT [9, 38]. In the sudden quench limit, there are no appreciable changes since the system essentially stays where it started. In between those limits, a complex dynamical regime emerges. Near the thermodynamic limit equilibrium phase transition  $\lambda = 0.5$ , adiabatic evolution exhibits a maximum value of entanglement followed by its decay and then the growth of the OP. The anti-correlation between squeezing and OP is present in the dynamical regime as well, so that Figs. 1a and 1b are effectively negative images of each other. As the range of high AV is entered, the position of the maximum point of squeezing and the onset point of the OP are pushed toward higher values of  $\lambda$ . Any value of  $v$  beyond the adiabatic limit leads to the dynamical regime, provided that the controlled interaction is ramped up to a high enough value. In other words, the sudden quench condition is only a consequence

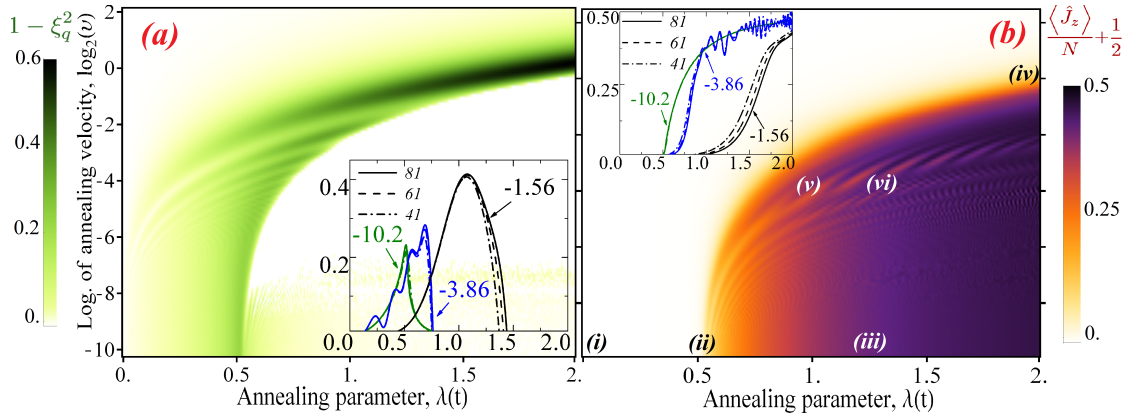


**Figure 1.** Dynamic profiles (time varies from left to right) of matter subsystem properties. **(a)** Two qubit concurrence  $c_W(N-1) = 1 - \xi_q^2$ , related to spin squeezing in Dicke manifold states (see Eq. 4). **(b)** Scaled order parameter (OP)  $\langle \hat{J}_z \rangle / N + 1/2$ . Results are for  $N = 81$ , and unitary evolution ( $\kappa = 0$ ). Dynamic regimes range from adiabatic (bottom) to sudden quench (top) annealing velocities (AV). Compared to what is possible in near-equilibrium (lower part), dynamic magnification of squeezing occurs at higher AV preceded by the emergence of the order parameter at delayed values of  $\lambda$ . The insets show the evolution for three selected values of  $\log_2 v$  (according to color) and three different system sizes (according to line style). Strong similarities exist for different values of  $N$ , pointing toward scaling properties of the results. Roman symbols in **(b)** hint at instants where phase space representations of subsystem states are depicted in Fig. 3.

of the upper bound of  $\lambda$ .

More important than the position of maximum concurrence in the dynamical regime, is its value. It reaches up to three times the corresponding value of the adiabatic evolution (see Fig. 1a). This is a remarkable improvement for the collective generation of such a distinctive quantum property, and is due entirely to the system being in the non-equilibrium dynamical regime. For some given AV values, this magnified concurrence for different number of qubits  $N$  follows closely the scaling  $c_W(N-1)$  (see inset of Fig. 1a), keeping the spin squeezing parameter curves almost size independent, and gets modestly better as the system size grows. Some size dependent deviations are present in curves for the  $\log_2 v = -1.56$  case. The sudden death point of concurrence is also virtually size-independent. The scaling properties of the dynamical regime will be discussed in section 4. The matter OP, for some chosen AVs, also shows very good scaling collapse in its dynamical evolution, i.e. the curves in the inset of Fig. 1b are essentially size independent thanks to the scaling  $\hat{J}_z/N$  in the OP.

With respect to the maximum matter OP in Fig. 1b, it is bounded. Therefore independent of the regime, it cannot be increased. The kind of enhancement revealed by the OP is a magnification of *superradiance*, which is the traditional way to describe

the QPT of DM [39]. The OP indicates the scaled number of excitations within the subsystem, which is bounded because of finiteness of  $N$ . In the dynamical regime, excitations develop more quickly (see blue curve in inset of Fig. 1b). In the case of eventual leakage of excitations through the cavity (see Section 4 for cavity loss effects), it manifests itself as a sharp burst of photons which are suddenly released. Bursts like these are excellent indicators of the DM QPT in cold atom experimental realizations [8].

Qubit quantum properties are very important for applications in quantum computation and quantum information. However, the finite character of the matter subsystem conceals much of the complexity of the evolution. The field subsystem, with its own relevance in highly controlled quantum optics, does not have this restriction. Field dynamical profiles analogous to that of Fig. 1 are shown in Figs. 2a-b. Similarities with Figs. 1a-b are noticeable, though with relevant differences. A large dynamical magnification of the field quadrature squeezing is also present, but it dies off later than its matter counterpart. Thus the development of the field OP is delayed as compared to that of the qubits. Superradiance, as seen by value of the field OP, is now not only sharper, but it can be as much as twice the value attainable with adiabatic ramping at a given  $\lambda$ . This greatly enhances the intensity of superradiant bursts. Radiation intensity enhancements of this kind have also been predicted in the DM submitted to sudden quenches and a lossy cavity [36]. Dynamically enhanced and suppressed superradiance alternate after the first burst (see blue curve in inset of Fig. 2b), a behavior absent in the equilibrium QPT. A wavy plateau in figure 1b coincides with that alternating stage. The dynamical phase marked by these oscillations is characterized by giant light-matter entanglement, with emergent quantum properties beyond the critical ones [28].

Magnification of squeezing and the other effects discussed so far are caused by a prolonged realization of effective non-linear interactions within both subsystems, after a preparation stage where the sudden quench approximation holds. Then, the non-linear processes are realized as one axis squeezing with a transverse field for matter [19, 31], and Kerr-like interactions for radiation [17]. During these separate squeezing processes, both radiation and matter act as effective interaction mediators for each other. This extends to the non-equilibrium case static correspondences with matter-only [10], or radiation-only systems [13]. Separate squeezing, which is related to internal quantum entanglement, suddenly dies as soon as combined matter-light entanglement emerges, because of monogamy and the breaking of the effective non-linear interaction condition. As the field has more information capacity, its squeezing can survive longer. By contrast, in the adiabatic regime, entanglement within and between subsystems compete against each other, because they occur simultaneously at the critical point.

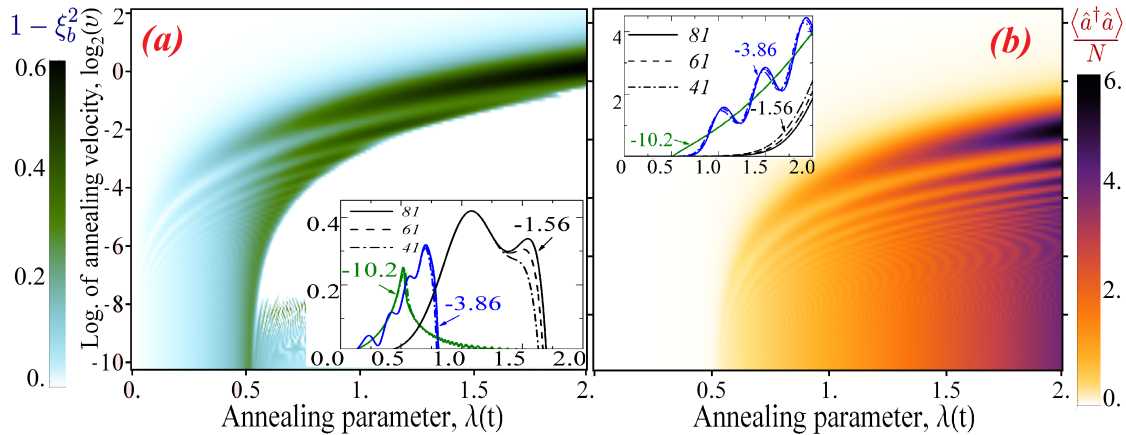


**Figure 2.** Corresponding dynamic profiles and insets of Figs. 1a and 2b, now for the field subsystem. (a) Evolution of  $1 - \xi_b^2$ , as defined in Eq. 8, whenever it is greater than zero (squeezed radiation). (b) Scaled OP of light  $\langle \hat{a}^\dagger \hat{a} \rangle / N$ . Major tendencies of Fig. 1 are replicated here. However the unbounded nature of the field OP allows an appreciation of the field intensity's oscillation (associated with superradiance) around the equilibrium values, with intervals of significant dynamical enhancement of superradiant bursts. The oscillatory behavior is related to a combined light-matter quantum chaotic stage.

### 3. Matter-light quasi-probability behavior

Complete state representations of the subsystems state reveal more details of the processes involved in the dynamical regime. Figures 3 and 4 show several snapshots of Wigner and AWF quasi-distributions at different instants. The enormous difference in the squeezing amount between the dynamical regime and the adiabatic one, as well as a difference in the direction of squeezing, is now graphically clear. This can be seen by comparing Figs. 3-4 (iv) with Figs. 3-4 (ii), and was previously shown for different AV values in Figs.1 and 2. In any regime, death of squeezing is associated with a splitting in half of the distributions, caused by the spontaneous symmetry breaking of the QPT [28]. This splitting is symmetrical along the  $x$  and  $-x$  direction in both subsystems. The system's density of excitations, indicated by the OP, increases as the distributions become displaced away from the initial state.

Features of the complex light-matter entangled stage are clarified by Figs. 3-4 (v-vi), which contrast with the adiabatic splitting in Figs. 3-4 (iii). The dynamical splitting of the distribution leads to negative scars and complex patterns for both subsystems, though the phenomenon is far more conspicuous in radiation. Donut shapes with a negative centered AWF such as that in Fig. 3 (vi), have been experimentally obtained in 3000 atoms with just a single photon [4]. In addition, round-tailed interference patterns such as that in Fig. 4 (vi) have been obtained for light in Kerr-like media following a Fokker-Planck equation [18], which confirms the presence of non-linear effective in-

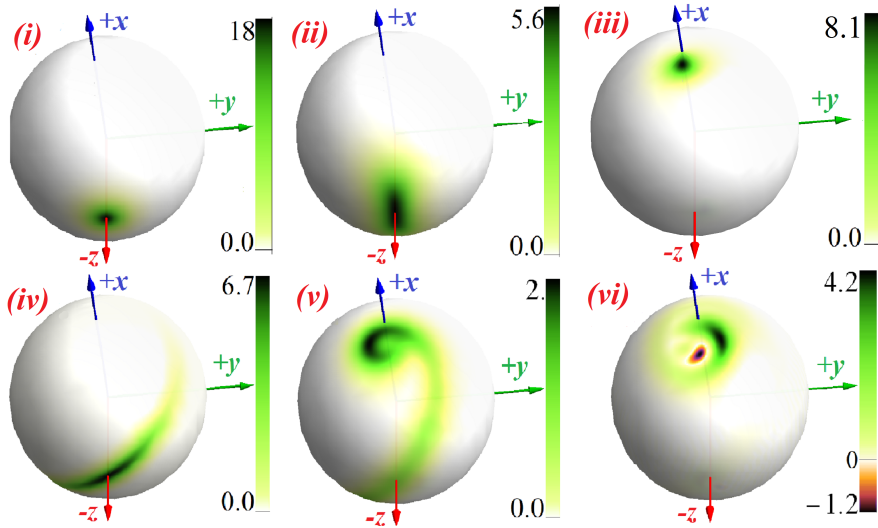


**Figure 3.** Agarwal-Wigner  $W_q$  at the instants indicated in Fig. 1b by the corresponding number (dissipative effects are ignored,  $\kappa = 0$ ). They are phase space representations of the matter subsystem, depicted on the Bloch sphere. Color scale of all Wigner functions can be very different. Maximal dynamical squeezing in (iv) is much greater than the adiabatic counterpart in (ii). Also, negative complex structures develop in the combined light-matter chaotic stage in (v-vi); which contrast with an adiabatic ordered state as in (iii). The stage in (iii,v,vi) has also no squeezing and no concurrence, since the Wigner function is now split along the  $x$  and  $-x$  directions and no longer concentrated around the initial state. Opposite Bloch hemispheres are not shown because of symmetry:  $W_q(\theta, \phi + \pi) = W_q(\theta, \phi)$ .

interactions. These results mean that the field is able to exhibit chaotic behavior itself, regardless of its entanglement to the matter subsystem. Despite being a single radiation mode, the field acts as a reservoir that dissipates the quantum correlations present in the squeezed states of each subsystem. If the qubits were not coupled to the field, squeezing could have revivals after its sudden death [19]. The field Wigner function is not only full of negatives regions (a marker of non-classical light), but it also contains abundant so-called sub-Planckian structures which have been related to quantum chaos [40]. The finite-size DM is non-integrable, and its ordered phase has been connected to chaotic features [6, 41]. This chaotic onset is responsible for the small size dependence on curves in insets of Figs. 1 and 2 for the  $\log_2 v = -1.56$  case, since the symmetry breaking occurs deeper in the ordered phase. As spin squeezing is very sensitive to chaos [26], it is no surprise that its sudden death becomes irreversible once the light-matter entangled stage arises.

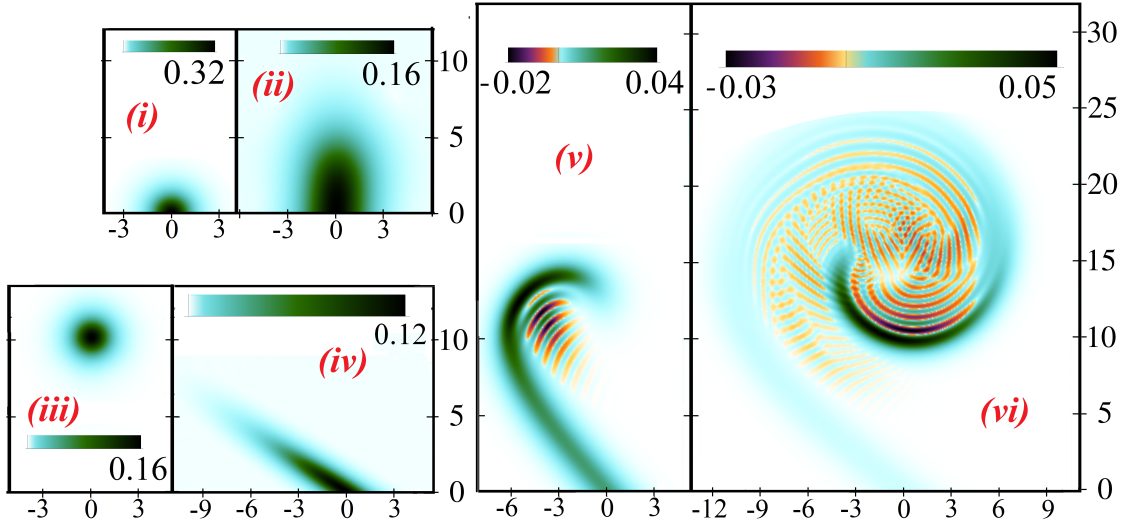


**Figure 4.** Analogous pictures of Fig. 3 but for the field Wigner distribution  $W_b$ . This is represented in the  $x - p$  plane of position (vertical) and momentum (horizontal) quadrature. All figures have the same  $x - p$  scale but color scale can be very different. The chaotic stage in (iv-v) exhibits sub-Planck structures. Negative regions of  $x$  are not shown because of symmetry:  $W_b(x, p) = W_b(-x, -p)$ .

## 4. Scaling and robustness of non-equilibrium quantum correlations

### 4.1. Robustness of results

So far, unitary evolution have been assumed in this work. Figures 5a-e address how the presence of losses in the cavity affect the dynamics. All the main results found in  $\kappa = 0$  evolution survive very well if decoherence towards the environment is two order of magnitudes lower than the main energy scale. Even if dissipation is at values of just an order of magnitude below, spin squeezing effects remain highly robust, with increasing noise resistance with system size. Field squeezing surprisingly survives to dissipation regimes comparable to the Hamiltonian dynamics itself. On the other hand, detailed features of the chaotic stage (such as OP oscillations, negative regions, and sub-Planckian structures) are far more sensitive to decoherence, requiring losses to be at levels of  $\kappa = 0.01$ . These very sensitive features have been proposed as tools for measuring very weak forces [42]. In our analysis, we have found that small finite values of  $\bar{n}$  (such as those typical at the ultra-low temperatures of most experimental realizations) do not change dramatically the conclusions; they just slightly intensify the process of decoherence. Previous works on non-equilibrium DM under different settings have also confirmed that some major phenomena present here, such as spin squeezing, survive losses. Enhanced superradiance can be detected [36], and squeezing can still have time to develop [18, 24]. We note that, despite perturbing the quantum state of the system, a lossy cavity compensates by providing the experimental possibility to monitor the dynamic evolution of the field in time [3].

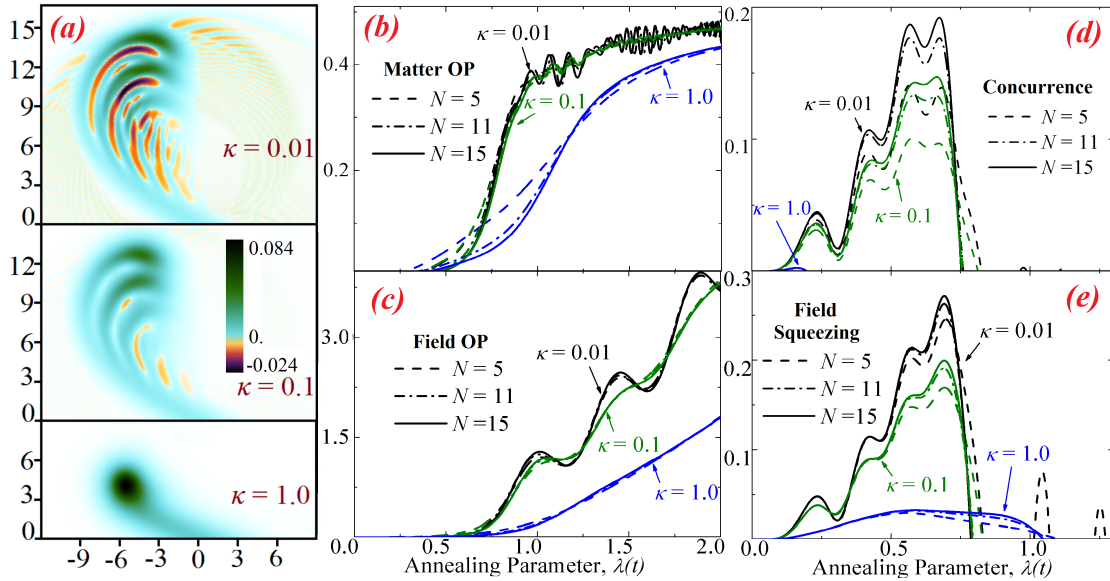


**Figure 5.** Effect of a leaky field cavity (expressed in terms of cavity decay rate  $\kappa$ ) on the dynamical enhancement of quantum properties. (a) Wigner distribution for  $AV \log_2 v = -1.58$ ,  $N = 15$  qubits at instant  $\lambda = 2$ . (b-e) Different field and matter properties as function of time for  $\log_2 v = -3.86$ , and three different system sizes. Quantum chaos signatures (sub-Planckian structures, negative Wigner distributions, and oscillations in OPs) are highly sensitive to dissipative perturbations. On the other hand, squeezing and internal entanglement effects are far more robust, especially for field squeezing. In all figures  $\bar{n} = 0$ .

The robustness of quantum correlations suggests that some of the effects described in this paper may be accessible under current experimental realizations of the DM. In particular, Klinder et al. have proven that the kind of control described here as  $\lambda(t)$  can be realized as a pump laser power increasing over time, and that the noise present in current experiments (nearly analogous to our  $\kappa = 0.1$  case) is small enough that the squeezing related quantum correlations predicted in our work could be experimentally assessed [43]. As field squeezing is the most robust quantum correlation (see Fig. 5e) and it is experimentally accessible thanks to a leaky mirror, tomographic techniques and photon statistics could be the first front for experimental comparisons with our predictions [3]. Other tomographic techniques could also analyze properties of the matter subsystem state [44]. Given the specific degrees of freedom forming the qubit states in current realizations (basically matter wave modes) [43], suitable equivalences of those state resolving techniques to this kind of degrees of freedom should be devised.

#### 4.2. Scaling of results

Our results exhibit substantial size invariance, as the insets of Figs. 1 and 2 show. Even the small system sizes in lossy cavity results in Figs. 5b-e are highly size independent,

which justifies our claim that the conclusions drawn there can be taken as general trends. Figures 6a-b show that the onset point of the dynamical regime occurs at points  $\lambda_d$  following a power law,  $(\lambda_d - \lambda_c) \propto v^{2/3}$ . This kind of scaling relation is typical in QPT critical properties [2]. This scaling laws extends our previous results on adiabatic scaling theory [15] to the fast regime. Even though we have used the same kind of scaling variables as in the near adiabatic case, many results in the dynamic regime collapse very well without any re-scaling of  $\lambda$ .

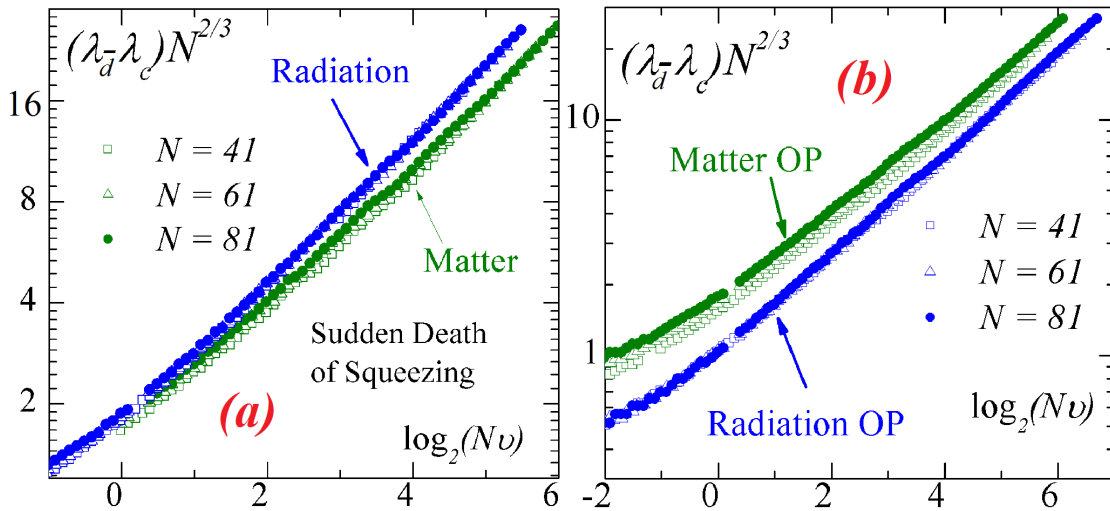


**Figure 6.** Size-independence of the instant  $\lambda_d$  when field and qubits organize in a combined light-matter excited state. (a) Instant of a sudden death of squeezing, in both matter and radiation subsystems. (b) Instant when each system reaches a significant value of its OP. These values are  $\langle \hat{J}_z \rangle / N + 1/2 = 0.1$  and  $\langle \hat{a}^\dagger \hat{a} \rangle / N = 0.0123$ . At sufficiently high AVs, all the instances chosen are related by the same scaling power law relation  $(\lambda_d - \lambda_c) \propto v^{2/3}$ .

The origin of the scaling exponent can be understood in a rather simple way, using concepts from the Kibble-Zurek mechanism [1]. The scaled time is the instant where the healing time of the system (as measured by the inverse mean energy gap in the spectrum  $\delta^{-1}$ ) has the same order of magnitude, i.e. when  $t\delta \approx 1$ . As  $\delta \propto (\lambda_d - \lambda_c)^{1/2}$  in the ordered phase [10], and  $t \propto (\lambda_d - \lambda_c)v^{-1}$ , we get the exponent  $2/3$  present in all lines of Figs. 6a-b. The fact that equilibrium critical exponents have been used reveals that, even though the emergence of the dynamical regime is well inside the  $\lambda > 0.5$  range, its mechanism is still related to the QPT, and so many critical phenomena get dynamically enhanced. On the other hand, the fact that the evolutions are very similar in the chaotic region, despite the different sizes, has to do with the relatively equal structure of the interaction well inside the superradiant phase, provided it has not bounced against the finite limits of the matter subsystem.

## 5. Conclusions

We investigated the details of the microscopic properties of both matter and light subsystems of the DM when macroscopically driven into the superradiant phase from an initial non-interacting equilibrium state. We have found that, in between the traditional driving schemes (either near-adiabatic or sudden quench), a previously unnoticed intermediate annealing regime emerges, and that this regime can be seen as advantageous for many quantum control processes. The onset of this intermediate phase is marked by induced non-linear self-interactions in both matter and field subsystems, developing squeezed states in each of them that are related to internal entanglement. This squeezing process is much stronger than what can be achieved in near-adiabatic evolutions, since the internal entanglement does not have to compete against the matter-field entanglement that arises in later stages.

We have also found that the dynamical squeezing mechanism is succeeded by the development of a chaotic and entangled radiation-matter dynamical phase. Clear signatures of quantum chaos such as fragmented Wigner functions, have been identified in this phase. This stage has its own dynamically enhanced properties such as superradiance, phase order, and sensibility to weak forces. We have established the robustness of all the quantum enhancing processes under dispersive conditions and its invariance to system size. We have shown that this last invariance condenses into a power-law relation associated with critical exponents. We hope this understanding will prove important for developing schemes to generate squeezed and other entangled states, as have been proposed in the contexts of quantum metrology and quantum information processing.

## 6. Acknowledgements

O.L.A., L.Q. and F.J.R. acknowledge financial support from Proyectos Semilla-Facultad de Ciencias at Universidad de los Andes (2010-2014) and project *Quantum control of non-equilibrium hybrid systems*, UniAndes-2013. O. L. A. acknowledges financial support from Colciencias, Convocatoria 511.

## References

- [1] Dziarmaga J 2010 *Adv. Phys.* **59** 1063–1189
- [2] Sachdev S 2011 *Quantum Phase Transitions* (Cambridge University Press)
- [3] Lvovsky A I 2009 *Rev. Mod. Phys.* **81** 299–332
- [4] McConnell R, Zhang H, Hu J, Ćuk S and Vuletić V 2015 *Nature* **519** 439–442
- [5] Dicke R H 1954 *Phys. Rev.* **93** 99–110
- [6] Emary C and Brandes T 2003 *Phys. Rev. Lett.* **90** 044101  
Emary C and Brandes T 2003 *Phys. Rev. E* **67** 066203
- [7] Nataf P and Ciuti C 2010 *Nature Comm.* **1** 1  
Viehmann O, von Delft J and Marquardt F 2011 *Phys. Rev. Lett.* **107** 113602

## Robust quantum correlations in out-of-equilibrium matter-light systems

14

- [8] Baumann K, Guerlin C, Brennecke F and Esslinger T 2010 *Nature* **464** 1301–1306  
Hammer C, Qu C, Zhang Y, Chang J, Gong M, Zhang C and Engels P 2014 *Nature Comm.* **5** 4023  
Baden M P, Arnold K J, Grimsmo A L, Parkins S and Barrett M D 2014 *Phys. Rev. Lett.* **113** 020408
- [9] Lambert N, Emary C and Brandes T 2004 *Phys. Rev. Lett.* **92** 073602
- [10] Reslen J, Quiroga L and Johnson N F 2005 *Europhys. Lett.* **69** 8
- [11] Vidal J and Dusuel S 2006 *Europhys. Lett.* **74** 817
- [12] Wang T L, Wu L N, Yang W, Jin G R, Lambert N and Nori F 2014 *New J. Phys.* **16** 063039
- [13] Jarrett T C, Olaya-Castro A and Johnson N F 2007 *Europhys. Lett.* **77** 34001
- [14] Bastidas V M, Emary C, Regler B and Brandes T 2012 *Phys. Rev. Lett.* **108** 043003
- [15] Acevedo O L, Quiroga L, Rodríguez F J and Johnson N F 2014 *Phys. Rev. Lett.* **112** 030403
- [16] Kitagawa M and Ueda M 1993 *Phys. Rev. A* **47** 5138
- [17] Kirchmair G, Vlastakis B, Leghtas Z, Nigg S E, Paik H, Ginossar E, Mirrahimi M, Frunzio L, Girvin S M and Schoelkopf R J 2013 *Nature* **495** 205–09
- [18] Stobińska M, Milburn G and Wódkiewicz K 2008 *Phys. Rev. A* **78** 013810
- [19] Law C, Ng H and Leung P 2001 *Phys. Rev. A* **63** 055601
- [20] Wang X and Mølmer K 2002 *Europ. Phys. J. D* **18** 385–391
- [21] Giovannetti V, Lloyd S and Maccone L 2011 *Nature Photon.* **5** 222–229  
Schnabel R, Mavalvala N, McClelland D E and Lam P K 2010 *Nature Comm.* **1** 121  
Rey A M, Jiang L and Lukin M 2007 *Phys. Rev. A* **76** 053617
- [22] Braunstein S L 2005 *Rev. Mod. Phys.* **77** 513–577  
Amico L, Osterloh A and Vedral V 2008 *Rev. Mod. Phys.* **80** 517–576
- [23] Altland A and Haake F 2012 *New J. Phys.* **14** 073011
- [24] Alvermann A, Bakemeier L and Fehske H 2012 *Phys. Rev. A* **85** 043803
- [25] Bakemeier L, Alvermann A and Fehske H 2013 *Phys. Rev. A* **88** 043835
- [26] Furuya K, Nemes M and Pellegrino G 1998 *Phys. Rev. Lett.* **80** 5524  
Song L, Yan D, Ma J and Wang X 2009 *Phys. Rev. E* **79** 046220
- [27] Grimsmo A L, Parkins A S and Skagerstam B S 2014 *New J. Phys.* **16** 065004  
Kopylov W, Emary C, Schöll E and Brandes T 2015 *New J. Phys.* **17** 013040
- [28] Acevedo O L, Quiroga L, Rodríguez F J and Johnson N F 2015 (*Preprint* [arXiv:1503.05470](https://arxiv.org/abs/1503.05470) [quant-ph])
- [29] Breuer H P and Petruccione F 2007 *The Theory of Open Quantum Systems* (Oxford University Press)
- [30] Wootters W K 1998 *Phys. Rev. Lett.* **80** 2245
- [31] Ma J, Wang X, Sun C and Nori F 2011 *Phys. Rep.* **509** 89–165
- [32] Wang X and Sanders B 2003 *Phys. Rev. A* **68** 012101
- [33] Koashi M and Winter A 2004 *Phys. Rev. A* **69** 022309
- [34] Dowling J, Agarwal G and Schleich W 1994 *Phys. Rev. A* **49** 4101
- [35] Walls D and Milburn G J 2008 *Quantum Optics* (Springer)
- [36] Fuchs S, Ankerhold J, Blencowe M and Kubala B 2015 (*Preprint* [arXiv:1501.07841](https://arxiv.org/abs/1501.07841) [quant-ph])
- [37] Walls D F 1983 *Nature* **306** 141–146
- [38] Bakemeier L, Alvermann A and Fehske H 2012 *Phys. Rev. A* **85** 043821
- [39] Hepp K and Lieb E H 1973 *Ann. Phys.* **76** 360–404
- [40] Zurek W H 2001 *Nature* **412** 712–717
- [41] Qin P, Wang W g, Benenti G and Casati G 2014 *Phys. Rev. E* **89** 032120
- [42] Toscano F, Dalvit D, Davidovich L and Zurek W 2006 *Phys. Rev. A* **73** 023803
- [43] Klinder J, Keßler H, Wolke M, Mathey L and Hemmerich A 2015 *Proc. Natl. Acad. Sci. U. S. A.* **112**(11) 3290–3295
- [44] Schmied R and Treutlein P 2011 *New J. Phys.* **13** 065019

# Appendix E

## Support of Chapter 4

### E.1 Deduction of mean field equation

There are many procedures to deduce Eqs. 4.12. One way is to start with the expectation value version of the Heisenberg equations,

$$\frac{d\langle\hat{T}_{i,\alpha}\rangle}{dt} = i\langle[\hat{H},\hat{T}_{i,\alpha}]\rangle = \sum_{l,\beta,k,\gamma} h_{i,\alpha}^{l,\beta,k,\gamma}\langle\hat{T}_{l,\beta}\hat{T}_{k,\gamma}\rangle + \sum_{l,\beta} h_{i,\alpha}^{l,\beta}\langle\hat{T}_{l,\beta}\rangle. \quad (\text{E.1})$$

Here, indexes  $i, l, k \in \{1, 2\}$ , while  $\alpha, \beta, \gamma \in \{x, y, z\}$ . The last equation is possible because operators  $\hat{T}_{i,\alpha}$  form a closed algebra under commutations, and Hamiltonian has terms of quadratic order at most. In terms of single particle operators,

$$\langle\hat{T}_{i,\alpha}\hat{T}_{l,\beta}\rangle = \sum_{j=1}^N \langle\hat{\rho}^j \hat{t}_{i,\alpha}^j \hat{t}_{l,\beta}^j\rangle + \sum_{j=1}^N \langle\hat{\rho}^{j_1, j_2} \hat{t}_{i,\alpha}^j \hat{t}_{l,\beta}^j\rangle = \frac{N}{4}\pi_i \delta_{i,l} \delta_{\alpha,\beta} + \sum_{j_1 \neq j_2}^N \langle\hat{\rho}^{j_1, j_2} \hat{t}_{i,\alpha}^{j_1} \hat{t}_{l,\beta}^{j_2}\rangle. \quad (\text{E.2})$$

An operator like  $\hat{\rho}^{j_1, j_2}$  is the reduced density matrix of to the two particles  $j_1$  and  $j_2$ . The last substitution stands from orthogonality properties of Pauli matrices,

$$\frac{1}{2}\{\hat{t}_{i,\alpha}^j, \hat{t}_{l,\beta}^j\} = \frac{1}{4}\hat{\pi}_i^j \delta_{\alpha,\beta} \delta_{i,l}, \quad (\text{E.3})$$

where  $\hat{\pi}_i^j$  is the projection onto nuclear state  $i$ . We can replace  $\langle\hat{\pi}_i^j\rangle = \pi_i$ , which is the probability of being in nuclear state  $i$ . In the initial condition of Eq. 4.10,  $\pi_2 = \sin^2 \frac{\beta}{2}$ , while  $\pi_1 = 1 - \pi_2$ .

So far, the formulae we have written are exact. Now it is time to apply the mean field approximation. It is based on the assumption that the total density matrix can be approximated

as,

$$\hat{\rho} \approx \bigotimes_{j=1}^N \hat{\rho}^j, \quad (\text{E.4})$$

i.e., that the state has no correlations among particles. Under such assumption, formula E.2 is reduced to,

$$\langle \hat{T}_{i,\alpha} \hat{T}_{l,\beta} \rangle \approx \frac{T_l}{2} \delta_{\alpha,\beta} \delta_{i,l} + \frac{N(N-1)}{N^2} \langle \hat{T}_{i,\alpha} \rangle \langle \hat{T}_{l,\beta} \rangle. \quad (\text{E.5})$$

We have supposed the all-to-all case, where all  $\hat{t}_{l,\beta}^j$  are independent of the particle  $j$ . Even if the all-to-all case did not hold, the term  $\langle \hat{T}_{i,\alpha} \rangle$  would represent the expected value average over all particles while  $\langle \hat{T}_{i,\alpha} \hat{T}_{l,\beta} \rangle$  would be the average over all pair of particles. Notice that if  $\langle \hat{T}_{i,\alpha} \rangle$  is of order  $N$ , and the last expression is divided by  $N^2$ , there will remain some terms of order  $1/N$  in the approximation. They can be thought as a first order correction on an expansion of  $\hat{\rho}$  where the perturbation parameter is  $1/N$ . As such, under the zero order mean field approximation, these terms are ignored. That is, one simply make the replacement  $\langle \hat{T}_{l,\alpha} \hat{T}_{k,\beta} \rangle \approx \langle \hat{T}_{l,\alpha} \rangle \langle \hat{T}_{l,\beta} \rangle$ . In order to be consistent, linear terms are also corrected by doing  $(N-1) \langle \hat{T}_{i,\alpha} \rangle \approx N \langle \hat{T}_{i,\alpha} \rangle$ . When these replacements are made on all the Heisenberg equations, Eqs. 4.12 are obtained.

Alternatively, the MFE could have also been derived by assuming that the state of the system is always expressible as the direct product of two coherent states [168], one for each nuclear state. So, the mean field approximation can be stated as,

$$|\psi(t)\rangle \approx |\mathbf{n}_1\rangle \otimes |\mathbf{n}_2\rangle, \quad (\text{E.6})$$

where each  $\mathbf{n}$  is a unit three dimensional vector in the Bloch sphere. A spin coherent state can be written as,

$$|\mathbf{n}(\theta, \phi)\rangle = e^{\zeta \hat{T}_+ - \zeta^* \hat{T}_-} |T, -T\rangle, \quad (\text{E.7})$$

where  $\zeta = \frac{\theta}{2} e^{-i\phi}$  is expressed in terms of the spherical coordinates of  $\mathbf{n}$ . Simply said, a spin coherent state is the zero excitations state along  $-z$  rotated so that it points to a general direction  $\mathbf{n}$ . However, initial condition in Eq. 4.10 is *not* an example of such a product of spin coherent states. A state like Eq. E.6 requires that it should be possible to separate  $s$  atoms in nuclear state 2 and  $N-s$  atoms in nuclear state 1. But symmetrization of the GDM precludes that, since each atom is in a coherent superposition of both states. Despite of that, in terms of MFE, the picture of two Bloch vectors, common to Eq. E.6 and Fig. 4.3, should hold correct, as all the correlations caused by the symmetrization in the GDM are ignored. But this would imply that in order to correctly compare MFE predictions with the quantum ones, one should do a weighted average in the MFE analogous to that of Eq. 4.11. That is, one should compute MFE solutions for each possible value of  $s$ , which is equivalent to have vectors  $\mathbf{t}_1$  and  $\mathbf{t}_2$  having different lengths  $\frac{1}{2}(1-p_s)$  and  $\frac{1}{2}p_s$  respectively, with  $p_s = \frac{s}{N}$ .

## E.2 Computing expectation values up to second order

The analysis made during chapter 4 has been pursued by taking as basic information the expectation values of the form  $\langle \hat{T}_{i,\alpha} \rangle$  and  $\langle \{ \hat{T}_{i,\alpha}, \hat{T}_{l,\beta} \} \rangle$ , where  $\alpha, \beta \in \{x, y, z\}$  and  $i, l \in \{1, 2\}$ . Thus, all the analysis is made up to second order expectation values. Then, in principle one would need to compute the expectation value of 21 anti-commutators and six linear terms of the form  $\hat{T}_{j,\alpha}$ . This small section specifies a simplified way to compute all this entries. It starts by recalling the following useful relations, which are entirely based on the  $SU(2)$  algebra of operators  $\hat{T}_{i,\alpha}$ ,

$$\hat{T}_{j,+} = \hat{T}_{j,x} + i\hat{T}_{j,y}, \quad (\text{E.8a})$$

$$\hat{T}_{j,z}\hat{T}_{l,+} - \frac{1}{2}\delta_{j,l}\hat{T}_{j,+} = \frac{1}{2}\{\hat{T}_{l,x}, \hat{T}_{j,z}\} + \frac{i}{2}\{\hat{T}_{l,y}, \hat{T}_{j,z}\}, \quad (\text{E.8b})$$

$$\hat{T}_{j,+}^2 = \hat{T}_{j,x}^2 - \hat{T}_{j,y}^2 + i\{\hat{T}_{j,x}, \hat{T}_{j,y}\}, \quad (\text{E.8c})$$

$$\frac{1}{2}(\hat{T}_{1,+}\hat{T}_{2,-} - \hat{T}_{1,+}\hat{T}_{2,+}) = \hat{T}_{1,y}\hat{T}_{2,y} - i\hat{T}_{2,y}\hat{T}_{1,x}, \quad (\text{E.8d})$$

$$\frac{1}{2}(\hat{T}_{1,+}\hat{T}_{2,-} + \hat{T}_{1,+}\hat{T}_{2,+}) = \hat{T}_{1,x}\hat{T}_{2,x} + i\hat{T}_{1,y}\hat{T}_{2,x}. \quad (\text{E.8e})$$

As all terms in the right side are hermitic, the real and imaginary parts of the expectation value of the left side provide twice the information in terms of real numbers. Also, formulae for those complex numbers are usually easier, and they transform very simply under rotations around the  $z$  axis, easing transformations between rotating frames. With the ten complex expectation values in Eqs. E.8, and the seven real expectation values of the form  $\langle \hat{\mathbf{T}}_j^2 \rangle$ ,  $\langle \hat{T}_{j,z}\hat{T}_{l,z} \rangle$  and  $\langle \hat{T}_{j,z} \rangle$ , one can compute all the 27 real entries for the full set of covariances.

There are other 8 expectations values important for some microscopic aspects of the results. These are, the six  $\langle \hat{S}_z\hat{T}_{l,\alpha} \rangle$ , and  $\langle \hat{S}_z \rangle = -\frac{N}{2}\cos\beta$  and  $\langle \hat{S}_z^2 \rangle = \frac{N}{8}[N+1+(N-1)\cos(2\beta)]$ . The last two terms have been computed with the initial conditions in Eq. 4.10.

## E.3 The squeezing parameter

In chapter 3 we used a squeezing parameter that is only good at assessing entanglement when the system is in the maximum multiplicity manifold, i.e., in the maximum eigenvalue of  $\hat{\mathbf{T}}^2$ . Here we generalize the squeezing parameter for other cases as defined in Ref. [169]. Let us start by defining **covariance**, which is a measure of correlations, both quantum and classical, between two observables. The covariance between operators  $\hat{A}$  and  $\hat{B}$  is,

$$\text{cov}(\hat{A}, \hat{B}) \equiv \frac{1}{2}\langle \{ \hat{A}, \hat{B} \} \rangle - \langle \hat{A} \rangle \langle \hat{B} \rangle. \quad (\text{E.9})$$

The procedure for obtaining the squeezing parameter useful for chapter 4 starts by computing  $(\mathbb{A})_{\alpha,\beta} = \text{cov}(\hat{T}_\alpha, \hat{T}_\beta)$ , i.e., the  $3 \times 3$  matrix of macroscopic covariances. Next, let  $\mathbb{P}$  be the projector onto the plane perpendicular to the expected value vector  $\langle \hat{\mathbf{T}} \rangle$ , i.e.,

$$(\mathbb{P})_{\alpha,\beta} = \delta_{\alpha,\beta} - \frac{\langle \hat{\mathbf{T}}_\alpha \rangle \langle \hat{\mathbf{T}}_\beta \rangle}{|\langle \hat{\mathbf{T}} \rangle|^2}. \quad (\text{E.10})$$

Notice, that if  $\mathbf{n}$  is a 3D unit vector, the number  $\mathbf{n}^T \mathbb{A} \mathbf{n}$  gives the variance  $\Delta T_{\mathbf{n}}$  of operator  $\hat{T}_{\mathbf{n}}$  along the direction  $\mathbf{n}$ . If we define the matrix  $\mathbb{X} = \mathbb{P} \mathbb{A} \mathbb{P}$ , then its second greatest eigenvalue can be called  $x_2$ . The squeezing parameter is,

$$\xi^2 = \frac{N x_2}{|\langle \hat{\mathbf{T}} \rangle|^2} = \frac{N \min_{\mathbf{n}_\perp} (\Delta T_{\mathbf{n}_\perp})}{|\langle \hat{\mathbf{T}} \rangle|^2}. \quad (\text{E.11})$$

In other words, it expresses the normalized minimal variance in any direction perpendicular to  $\langle \hat{\mathbf{T}} \rangle$ . As usual with squeezing parameters, whenever this parameter is less than unity, there is multi-qubit entanglement in the system [169]. This squeezing parameter coincides with the definition of Wineland *et al.* [166], and it is associated to phase sensitivity of the clock. If we substitute  $\hat{T}_\alpha$  with its projections  $\hat{T}_{i,\alpha}$  onto each nuclear state, we can speak about a squeezing parameter associated to each projection  $\xi_1$  and  $\xi_2$ .

## E.4 Expectation values: from macro to micro

In order to compute microscopic correlations and 2-qubit concurrences one needs to compute microscopic expectations values like  $\langle \hat{t}_{i,\alpha}^{j_1} \hat{t}_{i,\beta}^{j_2} \rangle$ . However, in section E.2 only macroscopic expectation values have been specified. This section explains how we can go from those macroscopic values to the microscopic ones. It happens that Eq. E.2 already hints at the following equivalence,

$$\langle \hat{t}_{i,\alpha}^1 \hat{t}_{i,\beta}^2 \rangle N(N-1) = \frac{1}{2} \left\langle \left\{ \hat{T}_{i,\alpha}, \hat{T}_{i,\beta} \right\} \right\rangle - \frac{N}{4} \pi_i \delta_{i,l} \delta_{\alpha,\beta}, \quad (\text{E.12})$$

where we have computed the value for the pair of particles 1, 2, since any pair of different particles would yield the same result for our all-to-all system. Also, by definition of collective operators,

$$\langle \hat{t}_{i,\alpha}^j \rangle N = \langle \hat{T}_{i,\alpha}^j \rangle \quad (\text{E.13})$$

Finally, if we notice that  $\hat{\pi}_2^j = \frac{1}{2} + \hat{s}_z^j$  and  $\hat{\pi}_1^j = \frac{1}{2} - \hat{s}_z^j$ , we can deduce the following equivalences,

$$\langle \hat{\pi}_1^1 \hat{t}_{l,\beta}^2 \rangle N(N-1) = \left(\frac{N}{2} - \delta_{1,l}\right) \langle \hat{T}_{l,\beta} \rangle - \langle \hat{S}_z \hat{T}_{l,\beta} \rangle, \quad (\text{E.14a})$$

$$\langle \hat{\pi}_2^1 \hat{t}_{l,\beta}^2 \rangle N(N-1) = \left(\frac{N}{2} - \delta_{2,l}\right) \langle \hat{T}_{l,\beta} \rangle + \langle \hat{S}_z \hat{T}_{l,\beta} \rangle, \quad (\text{E.14b})$$

$$\langle \hat{\pi}_2^1 \hat{\pi}_2^2 \rangle N(N-1) = \frac{N^2}{4} + N \langle \hat{S}_z \rangle + \langle \hat{S}_z^2 \rangle - N\pi_2, \quad (\text{E.14c})$$

$$\langle \hat{\pi}_1^1 \hat{\pi}_1^2 \rangle N(N-1) = \frac{N^2}{4} - N \langle \hat{S}_z \rangle + \langle \hat{S}_z^2 \rangle - N\pi_1. \quad (\text{E.14d})$$

In the particular case of being in the nuclear state Dicke Manifold, one can prove that  $\langle \hat{\pi}_i^1 \hat{\pi}_l^2 \rangle \equiv \pi_{i,l} = \pi_i \pi_l$ . These are all the formulas needed to accomplish the microscopical analysis of correlations and concurrence between any pair of particles.

## E.5 Failure of MFE: correlations and concurrence

The mean field approximation has as a consequence that, if it is true, then there must be zero correlations between different particles. In terms of covariance (which is a measure of linear correlation), if approximation in Eq. E.4 holds, then one must have  $\text{cov}(\hat{t}_{i,\alpha}^{j_1}, \hat{t}_{l,\beta}^{j_2 \neq j_1}) = 0$ , whenever  $j_1 \neq j_2$ . We can use the converse of this proposition in order to establish a measure of how the actual equations of motion deviate from the MFE. If we can establish particularly big covariances between a pair of microscopic observables associated to different particles, we should expect the involved macroscopic observables to be poorly represented by the MFE. In order to do that, let us define the  $6 \times 6$  real symmetric matrix defined by all the microscopic particle covariances,

$$(\mathbb{K})_{i,\alpha;l,\beta} = \text{cov}(\hat{t}_{i,\alpha}^{j_1}, \hat{t}_{l,\beta}^{j_2 \neq j_1}). \quad (\text{E.15})$$

This matrix has all its entries equal to zero whenever the mean field approximation holds exact, either in the form of Eq. E.4 or Eq. E.6. This means that, if we define a matrix distance from  $\mathbb{K}$  to the zero matrix, then we would have a measure of the breaking down of the MFE. Let us use the matrix norm,

$$K = \|\mathbb{K}\|_1 = \max_{\mathbf{n}} |\mathbf{n}^T \mathbb{K} \mathbf{n}|, \quad (\text{E.16})$$

which is defined as the maximum eigenvalue of  $\mathbb{K}$  in terms of absolute value. Despite this correlation parameter  $K$  is a good measure of the failure of the MFE, it has the disadvantage of not having a straightforward physical meaning. Instead, if we concentrate on specific parts of matrix  $\mathbb{K}$ , we could have correlation parameters with clearer interpretations. For example, if we take  $K_T = \|\mathbb{K}_T\|_1$ , where  $(\mathbb{K}_T)_{\alpha,\beta}$  is the  $3 \times 3$  correlation matrix with no distinction of nuclear states, then  $K_T$  can be seen as the maximum covariance between two particles in terms of Bloch vector  $\hat{\mathbf{t}}$ . Furthermore, the normalized eigenvector  $\mathbf{n}_T$  associated to that maximum eigenvalue gives the direction along which this maximum covariance occurs. The sign of the eigenvalue

would have also physical meaning, with positive indicating ferromagnetic order, and negative implying anti-ferromagnetic order. Similar parameters can be defined with  $K_i = \|\mathbb{K}_i\|_1$ , i.e., with respect to the covariance matrix where the Bloch vector examined for both particles is  $\hat{\mathbf{t}}_i$ . Finally, if we take the total  $\mathbb{K}$  matrix, and set the  $\mathbb{K}_i$  parts to zero, the parameter of the remaining matrix  $K_R = \|\mathbb{K}_R\|_1$  gives the maximum covariance between Bloch vector  $\hat{\mathbf{t}}_1$  of first particle and  $\hat{\mathbf{t}}_2$  of second one. Three components of the 6dimension eigenvector of  $\mathbb{K}_{12}$  give the 3D direction along which  $\hat{\mathbf{t}}_1$  must be pointed in order to have this maximum correlation, and the other three do the same with  $\hat{\mathbf{t}}_2$ .

Correlation parameters are good indicators that the system cannot longer be seen as a set of independent particles. However, they have the disadvantage of not distinguishing between classical correlations and the quantum ones. The former can be reproduced by a suitable statistical ensemble where every member have particles with all their expected values well defined. The latter cannot be reproduced that way, and can be witnessed through quantum entanglement. In order to assess the existence of actual *quantum* magnetism in our AEA system, we need to investigate the existence of such quantum correlations. As we have focused on the microscopic system of two identical particles, Wootters concurrence is a natural choice to accomplish that task. Thus,  $c_W(\hat{\rho}_t^{1,2})$  is the object of study, when  $\hat{\rho}_t^{1,2}$  is a  $4 \times 4$  matrix formed by the clock states of both articles. Notwithstanding, the actual density matrix  $\hat{\rho}^{1,2}$  of two particles includes also the nuclear states, and so it is  $16 \times 16$  in size. Those nuclear states must be traced, and it turns out that different density matrices can be selected depending on the nuclear states we want to deal with. In general we have five  $\hat{\rho}_t^{1,2}$  density matrices, related as follows,

$$\hat{\rho}_T^{1,2} = \sum_{i,l=1}^2 \pi_{i,l} \hat{\rho}_{i,l}^{1,2} = \sum_{i,l=1}^2 \pi_{i,l} \langle i, l | \hat{\rho}^{1,2} | i, l \rangle :, \quad (\text{E.17})$$

where each  $\hat{\rho}_{i,l}^{1,2}$  can be extracted from microscopic expected values as those explained in section E.4,

$$\langle \hat{t}_{i,\alpha}^1 \hat{t}_{l,\beta}^2 \rangle = \pi_{i,l} \text{tr} \left\{ \hat{t}_{\alpha}^1 \hat{t}_{\beta}^2 \hat{\rho}_{i,l}^{1,2} \right\}, \quad \langle \hat{t}_{i,\alpha}^1 \hat{\pi}_l^2 \rangle = \pi_{i,l} \text{tr} \left\{ \hat{t}_{\alpha}^1 \hat{\rho}_{i,l}^{12} \right\}. \quad (\text{E.18})$$

Concurrence  $c_W(\hat{\rho}_{1,2}^{1,2}) = c_W(\hat{\rho}_{2,1}^{1,2})$ , therefore, in general, we will deal with four different concurrences: namely  $c_W^T$ ,  $c_W^{1,1}$ ,  $c_W^{2,2}$ , and  $c_W^{1,2}$ . The existence of two particle concurrence is associated to the presence of quantum noise. Measuring that kind of fluctuations require full experimental access to the quantum regime, something that have been recently achieved in the  $^{87}\text{Sr}$  lattice clock [170].

## E.6 Analytic solutions under zero magnetic field

Hamiltonian in Eq. 4.9 under zero magnetic field ( $a = 0$ ) is integrable under the *total* basis  $\{|s, l, J\rangle_2\}$  (see definition after Eq. 4.10). Using the initial condition in Eq. 4.10 one can

compute the expected value of every *total* operator, as they all commute with  $\hat{\mathbf{T}}^2$ . For instance, the expectation value of  $\langle \hat{T}_+ \rangle$  can be computed as,

$$\langle \hat{T}_+ \rangle = -e^{ix\tau} \sum_{l_2=0}^s \sum_{l_1=0}^{N-s} \binom{N-s}{l_1} \binom{s}{l_2} \left[ (N-s-l_1) \frac{s_1}{c_1} + (s-l_2) \frac{s_2}{c_2} \right] (e^{-ix\tau} c_1^2)^{N-s-l_1} (e^{-ix\tau} c_2^2)^{s-l_2} (e^{ix\tau} s_2^2)^{l_2} (e^{ix\tau} s_1^2)^{l_1}, \quad (\text{E.19})$$

where  $s_i$  and  $c_i$  are sine and cosine of each angle respectively, and  $\tau$  and  $x$  are those of the MFE in Eqs. 4.12. By using binomial formulas like  $\sum_{k=0}^n k \binom{n}{k} a^k b^{n-k} = an(a+b)^{n-1}$  one can deduce all the following expectation values, which are relevant for computing covariance matrices and squeezing parameters,

$$\langle \hat{T}_z \rangle = -\frac{s}{2} \cos \theta_2 - \frac{N-s}{2} \cos \theta_1, \quad (\text{E.20a})$$

$$\langle \hat{T}_z^2 \rangle = \frac{s^2}{4} \cos^2 \theta_2 + \frac{s}{4} \sin^2 \theta_2 + \frac{(N-s)^2}{4} \cos^2 \theta_1 + \frac{N-s}{4} \sin^2 \theta_1 + \frac{s(N-s)}{2} \cos \theta_1 \cos \theta_2, \quad (\text{E.20b})$$

$$\langle \hat{\mathbf{T}}_1 \cdot \hat{\mathbf{T}}_2 \rangle = \frac{s(N-s)}{4} \cos(\theta_2 - \theta_1), \quad (\text{E.20c})$$

$$\langle \hat{T}_+ \rangle = -W_{2,1}^{s-1} W_{1,1}^{N-s-1} \left[ \frac{N-s}{2} \sin \theta_1 W_{2,1} + \frac{s}{2} \sin \theta_2 W_{1,1} \right], \quad (\text{E.20d})$$

$$\langle \hat{T}_z \hat{T}_+ \rangle = W_{2,1}^{s-2} W_{1,1}^{N-s-2} \left\{ \frac{s}{4} \sin \theta_2 W_{1,1} [(s-1)Q_2 W_{1,1} - W_{2,1} W_{1,1} + (N-s)Q_1 W_{2,1}] + \frac{N-s}{4} \sin \theta_1 W_{2,1} [(N-s-1)Q_1 W_{2,1} - W_{1,1} W_{2,1} + sQ_2 W_{1,1}] \right\}, \quad (\text{E.20e})$$

$$\langle \hat{T}_+^2 \rangle = W_{2,2}^{s-2} W_{1,2}^{N-s-2} \left[ \frac{(N-s)(N-s-1)}{4} W_{2,2}^2 \sin^2 \theta_1 + \frac{s(s-1)}{4} W_{1,2}^2 \sin^2 \theta_2 + \frac{s(N-s)}{2} W_{2,2} W_{1,2} \sin \theta_1 \sin \theta_2 \right], \quad (\text{E.20f})$$

where,

$$W_{i,n} = e^{-inx\tau} \cos^2(\theta_i/2) + e^{inx\tau} \sin^2(\theta_i/2). \quad (\text{E.21})$$

Also, terms  $Q_i$  in Eq. E.20e are,

$$Q_i = e^{-inx\tau} \cos^2(\theta_i/2) - e^{inx\tau} \sin^2(\theta_i/2). \quad (\text{E.22})$$

If  $\theta_1 = \theta_2$ , some of these expressions reduce to some previously found [20], where the nuclear degrees of freedom are not taken into account, because the initial state is in the Dicke maximum manifold, i.e.,  $\hat{\mathbf{T}}^2 = J(J+1)$  with  $J = N/2$ .